COMPARISON OF DELAYED CONTRAST-ENHANCED MAGNETIC RESONANCE IMAGING OF MYOCARDIAL VIABILITY AT 1.5 AND 3 TESLA

A Thesis
Presented to
The Academic Faculty

By

Puneet Sharma

In Partial Fulfillment
Of the Requirements for the Degree
Doctor of Philosophy in the
School of Biomedical Engineering

Georgia Institute of Technology
May, 2005

COMPARISON OF DELAYED CONTRAST-ENHANCED MAGNETIC RESONANCE IMAGING OF MYOCARDIAL VIABILITY AT 1.5 AND 3 TESLA

Approved by:

Dr. John N. Oshinski, Advisor
School of Biomedical Engineering
Georgia Institute of Technology

Dr. W. Thomas Dixon
GE Medical Systems

Dr. Paul Benkeser
School of Biomedical Engineering
Georgia Institute of Technology

Dr. Roderic I. Pettigrew
National Institute of Health

Dr. Xioping Hu
School of Biomedical Engineering
Georgia Institute of Technology

Date Approved: April 1, 2005

There is something fascinating about science. One gets such wholesale returns of conjecture out of such a trifling investment of fact.

- Mark Twain, *Life on the Mississippi* (1883)

ACKNOWLEDGEMENTS

Where to begin? The appreciation I have for the many people surrounding me throughout this journey is far-reaching. It extends beyond the able guidance of my mentors, both academic and familial; but also encompasses my sometimes surreptitious friends and confidants, who have helped keep me sane throughout these years! Therefore, I share this space with all of these people, and I hope even the casual reader will find reason to take this step with me.

My academic advisor, Dr. John Oshinski, deserves ample recognition for his superior guidance and teaching. His humor and pleasant nature, combined with extensive knowledge of magnetic resonance imaging and engineering, has indeed motivated me to pursue new ways to look at problems, while never forgetting the delicate balance between whimsical ideas and clinical practicality. I once mentioned to someone that Dr. Oshinski is almost like a "partner-in-crime", whereby the relationship felt more like an even-handed partnership in the pursuit for scientific answers, rather than the customary multi-tiered student-mentor relationship. I thank him for this method, since we were able to see all aspects of the problem and easily convey creative ideas.

In this vein, I must also recognize Dr. Roderic Pettigrew, who gave me the opportunity to work in the MRI lab at Emory, and Dr. W. Thomas Dixon, who was my first MR teacher. I will never forget their bountiful teachings and creative minds. Furthermore, special recognition must be given to other clinical faculty who not only helped me in some aspect of this project, but were also great friends and advisors

themselves. Namely, I must acknowledge Dr. Salil Patel, Dr. Josh Socolow, Dr. Mushabbar Syed, and Dr. Stam Lerakis. Also, much appreciation to my other MRI brethren in the Frederik Philips Lab: Dr. Hui Mao, Dr. Marijn Brummer and Dr. Robert Long, from whom I benefited from many MR-related conversations. I also thank the research support given by Philips Medical Systems and Siemens Medical Solutions.

My growth into the person I am today could not be mentioned without acknowledging my parents, Puja and Dharam Sharma. It is their gift of encouragement and guidance that I will cherish in my continued pursuit of all career and life goals.

Where to end? There are still many I could thank in this space. The people I have met during this process have all added pieces to the overall puzzle, however small. The contributions are all worthy of the spotlight, and I acknowledge them all. Thank you.

TABLE OF CONTENTS

LIST OF TABLES

LIST OF FIGURES

LIST OF SYMBOLS AND ABBREVIATIONS

α_{opt}	Optimal flip angle (along with TI_{opt}) producing maximum $T_{1contrast}$
α	RF excitation flip angle
TR	RF excitation repetition time
TI_{zero}	Inversion time that produced no $T_{1contrast}$ between infarct and normal myocardium
TI_{opt}	Optimal inversion time (along with α_{opt}) producing maximum $T_{1contrast}$
TI_{null}	Inversion time needed to produce zero signal for normal myocardium
TI	Inversion time. Duration between 180 pulse and the center of k-space.
TF	Duration of "free T_1 relaxation" between the end of the acquisition segment to the beginning of the next inversion pulse or segment.
TE	Time from the excitation pulse to the center of the echo signal
T_2*	Effective spin-spin relaxation time (due to field inhomogeneities).
T_2	Spin-spin relaxation time.
$T_{1contrast}$	Estimated transverse magnetization difference (contrast) determined by simulations.
T_1	Spin-lattice relaxation time.
T	Tesla (= 10,000 gauss)
SNR	Image signal-to-noise ratio
RR	Duration between successive R-waves in an ECG.
RF	Radiofrequency
R_1	Relaxation rate (= $1/T_1$)

r_1	contrast agent relaxivity
NSA	Number of signal averages
M_z	Longitudinal magnetization (parallel to the main magnetic field)
M_{xy}	Transverse magnetization (perpendicular to main magnetic field)
M_0	Equilibrium longitudinal magnetization
IR	Inversion Recovery
FOV	field-of-view
FLASH	Fast Low Angle Shot (spoiled (coherent) gradient echo pulse sequence)
EPI	Echo planar imaging
CNR	Image contrast-to-noise ratio
b-SSFP	Balanced Steady-State Free Precession (non-spoiled (incoherent) gradient echo pulse sequence
B_{1trans}	RF excitation field
B_0	Main magnetic field strength
Δf	Off-resonance frequency
ω_0	Larmor frequency
λ	Partition coefficient
ϕ	Magnetization phase
γ	Gyromagnetic ratio (42.6 MHz/T for ^{1}H)
M_{xy}^-, M_z^-	Magnetization just prior to RF excitation.
M_{xy}^+, M_z^+	Magnetization just following RF excitation.
M_{ss}	Steady-state magnetization
${}_sM_z$	Longitudinal magnetization during segment *s*.

SUMMARY

Imaging of myocardial viability using the delayed enhancement technique currently provides high image contrast between infarcted and normal tissue with the aid of a magnetization prepared fast gradient echo pulse sequence following the administration of an extracellular contrast agent. However, there exists a degree of image contrast variability and subjectivity due to contrast agent kinetics and user-specified imaging parameters. Also, the technique has not been explored at higher field strengths (3T), which offer greater inherent signal-to-noise ratio. The overall goal of this study is to compare magnetic resonance delayed contrast enhancement of myocardial infarction at 1.5T and 3T.

The analysis was conducted by first developing a comprehensive mathematical simulation of the imaging sequence, which allowed modification of various imaging parameters. Simulations were performed to optimize the sequence for flip angle and inversion time, as well as to evaluate the influence of other image parameters that affected contrast. These theoretical results were validated experimentally with phantoms.

In vivo post-contrast T_1 measurements at 1.5T and 3T from normal volunteers (n=10) and patients (n=5) provided more precise input into mathematical optimization simulations. In both populations, longer T_1 values were found at 3T compared to 1.5T for normal (pre-contrast: 1.24 ± .06s vs. 1.07 ± .05s; post-contrast: 0.34-0.59 vs. 0.33-0.54s, n=15) and infarcted myocardium (pre-contrast: 1.27 ± .06s vs. 1.04 ± .06s; post-contrast:

0.25-0.37s vs. 0.23-0.32s, n=5). Corresponding simulations using these T_1 values revealed an infarct-to-normal tissue contrast gain at 3T of approximately 25%. *In vivo* image contrast between infarcted and normal tissue following contrast administration was also higher at 3T by approximately 37%.

In conclusion, there was good correlation between mathematical simulations of delayed enhancement and experimental results, enabling parameters to be compared and optimized offline given input T_1 values. Although contrast-enhanced viability imaging at 3T suffered from artifacts due to field, RF, and inversion pulse inhomogeneity, these results suggest that 3T offers higher contrast-to-noise ratio than 1.5T for this application.

CHAPTER 1

INTRODUCTION

Introduction

The identification of viable myocardium following an ischemic event is critically important for determining if cardiac tissue can recover function after appropriate treatment strategies. Recently, magnetic resonance imaging (MRI) has become a significant tool for detecting myocardial viability in patients with chronic ischemic heart disease. Regions of dysfunction can be accurately assessed with MRI, and subsequently correlated with newly developed contrast-enhanced MRI, termed "delayed enhancement imaging", which depicts areas of ("bright") myocardial scarring. Delayed enhancement magnetic resonance imaging has diagnostic relevance in its ability to visually separate reversible from irreversible ischemic injury independent of infarct age or wall motion, and distinguish areas of the heart that will benefit from revascularization therapies. Qualitative "matching" of scar regions with dysfunction is evidence of irreversible myocardium, which is known to have low prognosis for improvement following surgical intervention. Therefore, there is a need to identify patients who will most benefit from surgical therapy, and those who present a higher risk and are more suitable for pharmaceutical therapy.

Delayed enhancement imaging has been performed almost exclusively at 1.5 Tesla (T) magnetic field strengths, and has demonstrated high sensitivity, specificity and repeatability in clinical settings. However, *this application has not been explored on*

higher field systems such as 3T, despite clinical interest and the potential for higher signal-to-noise ratio resulting in finer depiction of infarct regions.

Motivation

The science of the delayed enhancement technique is still developing, and the potential benefits it provides in the treatment-planning and prognosis of ischemic heart disease support the need to fully investigate its technical advantages and disadvantages, and how they relate to inherent MR properties, such as tissue relaxation and hardware parameter settings. With this knowledge, the technique can be implemented optimally and efficiently to provide better image quality. Though studies have revealed the high repeatability of delayed enhancement, the method traditionally requires a high degree of user expertise to produce images of diagnostic image quality. As the technique becomes more widespread, many institutions will rely on recommendations for optimizing the sequence, with little fore-knowledge. But an oft forgotten truth is that an underlying scientific process exists, which has yet to be brought together as a single entity for the strict purpose of optimization. This fact is the central motivation for this project.

There are several factors that play important roles in the study of this technique. The sequence itself is well described and understood, albeit superficially. However, the delayed enhancement pulse sequence can be described mathematically, opening the door for optimization. But does the mathematical theory agree with imaging results? If so, image contrast (between tissues of varying T_1 and T_2) can be studied and optimized off-line, not only for the traditional inversion-recovery (IR) based delayed enhancement

technique used currently, but also for new variants of the technique, such as those utilizing a combination of preparation pulses or different acquisition strategies.

If optimization through mathematical means is tenable, the field strength at which the experiment takes place can also be considered important. Mathematics aside, an increase in field strength has several positive and negative consequences to image quality. On the positive side, increased sensitivity of proton spins allow signal-to-noise (SNR) to increase linearly with field strength. The net gain in SNR can be used to increase resolution, or decrease imaging time. Where this advantage has been observed in brain imaging, the same benefits may not be as apparent in cardiac imaging. Cardiac imaging is more sensitive to the disadvantages of high field imaging than neuro-imaging since the imaging time is greatly reduced to accommodate cardiac motion and patient breathing. Field inhomogeneity presents a difficulty in some imaging sequences, and efficient magnetic field corrections (or, "shimming") must be implemented to suppress banding and susceptibility artifacts. There are also deficiencies in radiofrequency (RF) homogeneity/penetration depth, tissue power deposition (SAR), reception coil sensitivity, acoustic noise, and ECG-triggering compared to 1.5T. A question this thesis will explore is: are these factors too significant for efficient delayed enhancement patient imaging at 3T?

The Problem Statement

What are the implications of viability imaging at 3T? This specific topic has not been fully explored. The compounding factors of contrast media pharmacokinetics (and the influence on T_1), high field strength challenges, and viability assessment have not

been treated concisely. Therefore, *this thesis intends to outline the design criteria necessary for developing optimized pulse sequences for delayed enhancement imaging and compare delayed enhancement imaging at two imaging field strengths, 1.5T and 3T.*

Approach

The use of the term "optimization" implies the search of the best set of imaging parameters given certain constraints. This formulation is best determined mathematically, since, once a general expression is established, multiple variables can be easily modified to describe many different trends and relationships. Hence, *the overriding approach to address delayed enhancement image contrast optimization at 1.5T and 3T is to represent the image contrast mathematically using basic MR theory*. From this basis, a general understanding can be realized of the expected image contrast behavior. However, any simplistic theoretical development such as this is innately a "stripped-down" representation of realistic MR image contrast, which is further complicated due to electromagnetic field variations, hardware limitations, safety constraints, efficiency losses, thermal noise, and, of course, the impedance of the human subject. Therefore, a theoretical analysis warrants experimental validation, which can best be achieved with imaging *phantoms*—a tool in which the object's MR properties (T_1 and T_2) can be conveniently customized to correlate with specific mathematical simulations. Not only will this set the stage for predicting image contrast behavior of delayed enhancement imaging at 1.5T and 3T given *in vivo* myocardial and infarct T_1 values, but it will also provide a measure of the systematic error (if any) between theoretical and experimental results.

Recreating the nature of a delayed enhancement imaging sequence with a mathematical model is useful for analyzing image contrast behavior, but it is blind to the key electromagnetic differences that distinguish 3T from 1.5T. It is next important to quantify these practical field strength-related differences. This will provide a level of "awareness", which will ultimately place limitations on specific MR imaging parameters, and possibly pose recommendations for alternative pulse sequence designs.

Next, it is essential to acquire *in vivo* T_1 information at 1.5T and 3T in the tissues of interest, namely blood, healthy (or viable) myocardium, and infarcted myocardium. This will serve as input into the developed mathematical formulations of delayed enhancement. From this, recommendations can be made about the optimum flip angle and inversion time, which theoretically produces the highest image contrast. Concomitantly, this knowledge can be compared to current knowledge and implementation of the delayed enhancement technique and, more importantly, be used to assess whether image contrast between infarcted and normal myocardium will improve at 3T.

Thesis Organization

The organization of the pages to follow closely adheres to the progression described above. Each chapter is essentially a "stand-alone" collection of related experiments, with standard subject headings typical to most research papers. This text book-like composition seemed the most logical arrangement for this thesis given the plurality of topics. In this manner, it was hoped that proper discussion could be spent on each problem as it pertains to the thesis as a whole.

Chapter 2 provides the reader with additional background of myocardial viability from a clinical and technical standpoint. It covers key findings from previous research investigations and gives an overview of current methods of assessing myocardial viability. It finally discusses MRI's current role in viability imaging, along with specific technical features pertinent to this project.

Chapter 3 covers the theoretical background of the image contrast simulations that will be validated and completed in future chapters. It formulates the mathematical expressions that describe delayed enhancement imaging (as it is used today) from basic spin-relaxation physics. The figure-of-merit for image contrast is then defined, and the mathematical development is analyzed for behavioral trends as a function of various MR sequence parameters. The chapter also discusses T_1 measurement techniques from a mathematical standpoint for *in vivo* application. The chapter concludes with general recommendations for optimum image contrast in delayed enhancement imaging.

Chapter 4 involves phantom imaging validation of the theoretical development of Chapter 3. This entails segmented inversion recovery and T_1 measurement techniques. Then, a thorough treatment of image contrast in specific T_1 phantoms is conducted and correlated with prediction from the theory.

Chapter 5 is an analysis of field strength-related issues at 3T that may hamper cardiac imaging. These include field (main and transmit) inhomogeneity analysis, inversion pulse efficacy, and sensitivity gain at 3T.

Chapter 6 and 7 both involve *in vivo* imaging at 1.5T and 3T. Chapter 6 concerns imaging with normal (healthy) volunteers, while Chapter 7 investigates MR imaging in patients with chronic myocardial infarction. The overriding goal of each chapter is to

measure T_1 of myocardial tissue and blood to serve as input into the theoretical treatment of earlier chapters. From this, sequence design recommendations are discussed. Concurrently, image signal- and contrast-to-noise of delayed enhancement imaging is measured in the patients to assess potential benefits at 3T.

Scope of the Document

It is presumed the reader has some previous familiarity with magnetic resonance imaging. A detailed explanation of spin dynamics, electromagnetism, and the process of MR image formation will not be covered. Some general MRI principles are covered as they are discussed in each section, and some relevant terms and abbreviations are summarized in the List of Symbols and Abbreviations page for reference. For more dedicated descriptions of MRI, the reader is directed to reference books by Haacke (1999) and Vlaardingerbroek (2003), and a more basic reference for the novice, Elster (2001).

CHAPTER 2

CLINICAL BACKGROUND AND LITERATURE REVIEW

Introduction

Impairment of left ventricular function due to ischemic heart disease reduces ejection fraction and may lead to heart failure. However, left ventricular dysfunction is not necessarily an irreversible process. Therefore, the term *myocardial viability* implies myocardial cells have undergone *reversible damage due to ischemic injury, without cellular necrosis (or cell death)*. In addition, the determination of *viable myocardium* increases the potential for local or global improvement of ventricular dysfunction following appropriate therapeutic intervention. Ideally, determining myocardial viability in preoperative patients with coronary artery disease would serve as an essential element in *risk stratification*, particularly when deciding between medical or surgical intervention. Specifically, if cellular necrosis or scar tissue occupies the majority of the dysfunctional segment, such as with *transmural infarction*, surgical intervention to restore oxygen supply will not improve ventricular function, since cell death is an irreversible process. However, if necrosis occupies only a small subendocardial layer, reperfusion of the segment will likely result in functional improvement

The discussion of viability assessment with MRI necessitates a thorough treatment of the many physiological and technical aspects of the technique. Still in its youth, determining viability with MRI has been received with increasing promise throughout both the MRI and medical community due to its superior spatial resolution and reproducibility. The past few years have seen MRI manufacturers provide the

capability for fast cardiac scanning, which has made MRI an increasingly robust and cost-effective modality. Concurrently, a growing number of researchers worldwide continue to investigate and develop new hardware and imaging routines to solidify a permanent place in the future for assessing myocardial viability with MRI.

There are three major areas pertaining to this research that will be discussed in this background chapter: 1) the evolution of MRI pulse sequences for differentiating myocardial necrosis (infarction) from viable tissue; 2) the use of paramagnetic contrast agents (e.g. Gd-DTPA-BMA) for the enhancement of myocardial infarction; and 3) the potential clinical benefits of high field imaging (3T). This chapter will also discuss other imaging modalities used for non-invasive viability assessment, as well as other MRI techniques used to complement the findings of contrast-enhanced viability imaging ("delayed enhancement"). First, though, a discussion of the facets of ischemic heart disease is needed.

Definition of Viability

An initial ischemic insult extending from a reduction of myocardial blood flow causes a subsequent down-regulation of myocardial metabolism within the first few minutes. Despite structural changes and the disruption of normal cellular activity, myocytes have the potential to remain viable if adequate collateral flow meets the minimum oxygen requirements for sustained cell life [Flameng et al 1981, Depre et al. 1995]. This maintenance leads to functional recovery following restoration of normal oxygen supply. Hence, there is impetus to reestablish normal blood flow before irreversible cellular necrosis and ventricular dysfunction occurs.

In the setting of ischemic heart disease, *viability is defined as the maintenance of cellular integrity despite contractile dysfunction* [Dilsizian 2000]. If the duration of severe ischemia is significant, cell death occurs within the first hour via necrosis or apoptosis, whereby functional recovery is no longer salvageable, even after reperfusion. However, during mild ischemia, myocytes have shown the ability to adapt their functionality indefinitely and remain viable. But the compromised region is still subject to further ischemia and necrosis, and is thus considered an *"area-at-risk"*. Therapeutic measures to improve oxygen supply and cardiac function in the area-at-risk correlate well with positive left ventricular remodeling and increased patient survival [Alderman et al. 1983, Brundage et al. 1984, Elefteriades et al. 1993, Christian et al. 1997]. *There is motivation, therefore, to determine the extent of viable myocardium prospectively.*

Currently, two terms are used to define viable myocardium within regions of contractile dysfunction: "stunning" and "hibernation". Both conditions are characteristic of *reversible ventricular dysfunction*, but are contrasted by the state of coronary blood flow. *Stunning is associated with acute ischemic insults, while hibernation is characterized by a chronic state of reduced blood flow.*

Myocardial Stunning

Ventricular dysfunction may persist following successful reperfusion of the affected ventricular segment. This state of *delayed functional recovery after a transient period of ischemia* was initially noted by Heyndrickx in dogs [Heyndrickx et al. 1975] and was later termed "stunning" by Braunwald and Kloner [Braunwald et al. 1982]. The persistence of reduced contractile function in this circumstance is thought to be caused by

subsequent myocardial injury from both post-ischemic reperfusion ("reperfusion injury") and the initial ischemic insult [Bolli 1992]. The eventual recovery of function depends on the extent of the myocardial injury; however, if ventricular function is critically reduced due to stunning, the recovery process can be encouraged by pharmacologic stimuli. This elucidation of "contractile reserve" has often been used to differentiate viable (stunned) myocardium from nonviable (infarcted) myocardium [Bolli et al. 1985, Becker et al. 1986], leading to viability assessment with non-invasive echocardiography imaging techniques [Pierard et al. 1990]. The exact mechanism for post-ischemic ventricular dysfunction remains unclear despite numerous genetic and cellular theories. But, in any case, the time for cellular processes to revert back to the pre-ischemic state is far from a spontaneous process, and may take days to weeks before function returns to normal. *The key feature of myocardial stunning includes normal or near-normal myocardial blood flow*, which is the basis for the frequently used definition that there is a blood flow-contraction "mis-match" in stunned myocardium.

Myocardial Hibernation

In contrast to myocardial stunning*, hibernation represents a blood flow-contraction "matching"*, meaning that hibernating myocardium is in a state of *chronically reduced blood flow*. First characterized by Rahimtoola, the term technically refers to the recovery of ventricular function following the successful reestablishment of normal blood flow with surgical revascularization [Rahimtoola et al. 1989]. The initial down-regulation of blood flow is thought to cause an adaptive response in myocardium, whereby the metabolic and contractile processes are depreciated in light of reduced

oxygen supply. This inherent adaptability of the supply-demand ratio exists in the absence of clinically evident stunning and ischemia [Marban 1991]. Myocytes do incur structural changes in hibernating myocardium, which may lead to irreversible damage if adequate perfusion is not eventually established. Thus, the adaptability of the hibernating myocardium is a temporary process.

Evidence of hibernation has been found experimentally. Animal studies have confirmed the adaptive response of the myocardium under prolonged reduction of coronary perfusion [Fedele et al. 1988, Ross 1991] -- the poignant degradation of ventricular function was complemented by the absence of ischemic-induced metabolic changes. However, there is an inherent difficulty modeling chronic hibernation experimentally due to the challenge of maintaining a chronic stenosis without myocardial fibrosis or the development of overwhelming collateral perfusion (leading to flow-contraction "mismatch", i.e. stunning) [Shen et al. 1995]. Recently, models for hibernation have involved porcine models with a partially occluded coronary artery and maintenance of moderate flow to the region of interest [Chen et al. 1996, Fallavollita et al. 1997]. In a clinical setting, the prognostic repercussions of a reduced contractile match are noteworthy: although hibernation can be reversed by adrenergic stimulation, as with stunning [Schulz et al. 1992], the ventricular segment is left vulnerable to recurrent episodes of ischemia due to the chronic state of reduced *resting* blood flow. Therefore, surgical intervention is the primary method to reestablish normal resting perfusion permanently.

Myocardial Necrosis

Even though myocytes can adaptively maintain viability when perfusion is low, complete coronary occlusion results in *irreversible cell necrosis* (myocardial infarction) within the first hours via a progressive "wavefront" originating in the subendocardial layer of the myocardium [Reimer et al 1979]. The degree of infarction is directly related to the occlusion time and stenosis location, with proximal stenosis being the most severe. The transmural dependence of infarct generation is a direct implication of the systolic pressure gradient within the myocardial wall, which reduces coronary flow to the endocardium relative to the epicardium in stenotic vessels during stress [Gallagher et al. 1983]. Histologically, it is believed that cell death occurs in patches, with the cardinal effectors being loss of energy stores (ATP) and a rise in cellular acidity. Additionally, disruption of cellular integrity is indicative of significant microvascular injury (local swelling and plugging), which limits re-flow even when perfusion is restored. Though it has been shown that early reperfusion of a severely ischemic "area-at-risk" may cause additional (albeit preventable) myocardial injury related to the sudden availability of oxygen and blood flow [Hearse 1991], *the most effective long-term means of limiting infarct size is reperfusing the occluded coronary artery*, due to the strong correlation between occlusion time and extent of cell necrosis. In addition to necrosis, cell loss also occurs through apoptosis (programmed cell death).

The post-infarction period involves activation of inflammatory cells (neutrophils and macrophages) and the elimination of necrotic myocytes. Over the course of 4-12 weeks, the infarct tissue is replaced by fibrous *scar tissue*, which is typically smaller in

size than the infarct due to tissue shrinkage and thinning of the ventricular wall [Masseri 1995, Chareonthaitawee 1995].

Methods of Viability Detection

Common clinical markers to test for myocardial infarction include elevation of myocardial enzymes, particularly creatine kinase (since these enzymes originate exclusively from myocardial cells), abnormal electrocardiographic findings, coronary stenosis, and poor ventricular function. The size of the infarct using these clinical markers can be determined by the relative significance of these tests, but remains semi-quantitative at best. Furthermore, information about the extent of viable myocardium remains difficult to assess using these indicators.

Regional contractile reserve is the increase in ventricular function of hypokinetic myocardium under increased workload. It is possible to detect residual contractile reserve in viable myocardium with positive inotropic stimulation. One such catecholamine is dobutamine, which, when used at relatively low doses (4-8 ug/kg per minute) increases myocardial oxygen demand and blood flow, enabling visualization of contractile reserve with echocardiography, as seen in Figure 2.1. Nonviable myocardium (scar) exhibits no contractile response to dobutamine. High dobutamine doses elicit an ischemic response in poorly perfused dysfunctional segments such as hibernating myocardium, which depresses function in these segments and provides potential distinction from stunned myocardium. Since the beginning of the 1990s, dobutamine stress echocardiography has progressively gained acceptance for prospectively predicting functional recovery in both acute and chronic ischemic heart disease [Barilla et al 1991, Cigarroa et al. 1993, Salustri

et al 1994, Smart 1994], with an overall predictive accuracy between 77 and 95%. There is also evidence to support the quantification of infarct size with stress echocardiography [Watada et al. 1994].

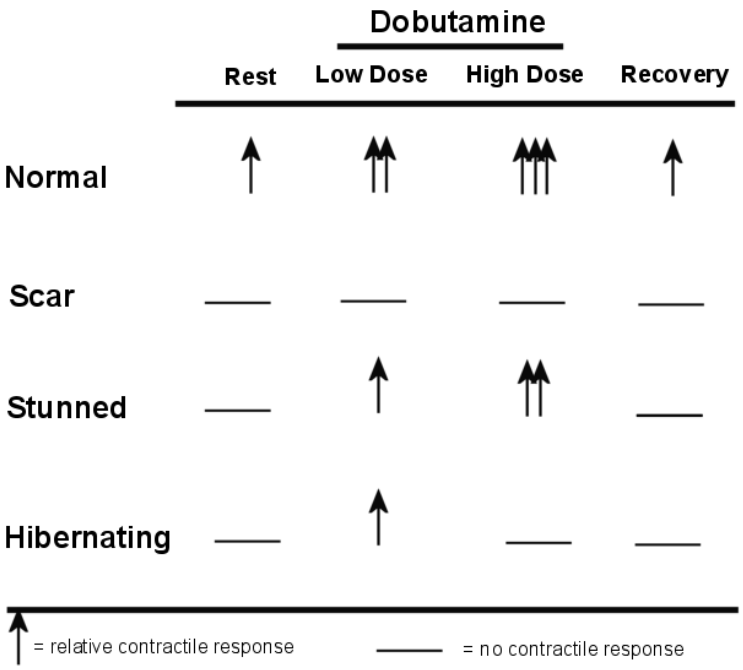

Figure 2.1. *Myocardium response to low/high dose dobutamine.*

Nuclear imaging techniques, such as single proton emission computed tomography (SPECT) and positron emission tomography (PET), have also shown value for determining myocardial viability. Thallium-201 (^{201}Tl) SPECT imaging characterizes myocardial perfusion to intact cells during the first-pass. The redistribution stage of thallium-201 (after 15 minutes and lasting 3-4 hours) is not related to flow, but has the potential to differentiate irreversible from reversible ischemic injury due to differential washout kinetics [Okada 1984]. Conversely, technetium-99m-labeled (^{99m}Tc) SPECT imaging (e.g. sestamibi), which can be used at higher doses, characterizes perfusion with

minimal redistribution, making late images similar to the first-pass state. Uptake is passive across mitochondrial membranes, and is proportional to myocardial blood flow [Dilsizian 2000]. Both ^{99m}Tc and ^{201}Tl can be performed during stress to determine coronary flow reserve and approximate perfusion defect size; however, due to differences in tracer kinetics, it has been shown that ^{99m}Tc underestimates ischemia and viability compared to thallium-201 imaging. Clinically, the two techniques have been used in combination to enhance the favorable properties of ^{201}Tl and ^{99m}Tc (rest-redistribution ^{201}Tl and stress ^{99m}Tc) [Berman et al. 1993].

In addition to perfusion imaging, nuclear imaging has been used to assess metabolism via PET. Metabolic activity can be visualized using ^{18}F-2-deoxyglucose (FDG) radionuclide, which is essentially "trapped" within *viable* myocytes during the initial stages of cellular glucose metabolism. A common protocol involves the evaluation of both myocardial blood flow (by ^{13}N-amonia, NH_3) and glucose metabolism (by FDG). The subsequent patterns of radionuclide uptake in regions of LV dysfunction provide substantial insight into viability, and allow delineation between stunning, hibernation, and myocardial necrosis. Specifically, stunning is characterized by dysfunctional segments with normal FDG and NH_3 uptake ("normal"), while hibernating myocardium shows patterns of normal FDG but reduced NH_3 ("mis-match"). Myocardial necrosis reveals both reduced FDG and NH_3 ("match") and normal functioning segments have normal FDG and perfusion uptake [Segall 2002]. These distinct uptake patterns allow PET to be considered the gold-standard in viability imaging, with a sensitivity and specificity of over 80%.

Comparative Analysis between Imaging Modalities

One of the hallmark measures of viability assessment is the improvement of ventricular function following revascularization. Even though other contributing measures are relevant (incidence of arrhythmias or recurrent ischemia), positive contractile response based on prospective evaluation of viability is a generally accepted prognosis for patient survival. The discussed techniques have been evaluated in the literature on the basis of functional recovery following surgical revascularization. A recent article has pooled data from many studies in order to analyze the sensitivity and specificities of available viability techniques [Bax et al. 1997]. Even though the data is presented exclusively for chronic dysfunction, it gives a good overview of the predictive accuracy of each modality. Table 2.1 summarizes the data from this report.

Table 2.1. Comparison of Sensitivities and Specificities of Viability Imaging Techniques.

	No. of Pts	Sens. (%)	Spec. (%)
^{99m}Tc	207	83	69
LD Echo	448	84	81
^{201}Tl stress-reinjection	209	86	47
FDG PET	332	88	73
^{201}Tl rest-redistribution	145	90	54

Sens = sensitivity; Spec = specificity; ^{99m}Tc = technetium 99m labeled SPECT; LD Echo = low-dose dobutamine echocardiography; ^{201}Tl = thallium 201 imaging; FDG PET = fluorodeoxyglucose PET. Data summarized from Bax et al. 1997.

From the pooled analysis, all modalities for detecting viability have high sensitivities that are not significantly different. However, dobutamine echocardiography has an apparent advantage in specificity over the nuclear imaging techniques. Newer strategies for stress-echocardiography involve high-dose dobutamine analysis in combination with the vasodilator agent, dipryridamole [Sicari et al. 1999], which may

further improve the accuracy. Specificity is particularly low for ^{201}Tl imaging, suggesting this technique potentially overestimates the recovery of dysfunctional segments. Improved specificity was found for technetium-99m perfusion tracers, but resulted in a slight decrease in sensitivity. Positron emission tomography is commonly viewed as the "gold standard" for viability assessment. As noted by Bax, many of the PET studies in the analysis did not include perfusion data, which may increase specificity.

Limitations of Current Techniques

The predictive benefits of dobutamine echocardiography are complimented by its widespread availability, low-cost, and convenient portability. However, the value of the technique is dependent on the positioning/interpreting expertise of the user, and may be prone to inter-observer variability. Much of this variability can be attributed to the inherent low image quality, and the limited range of the acoustic window. In many instances, transesophageal echocardiography is used to improve visualization of certain cardiac structures, but this procedure is less accepted by patients and requires mild sedation. Recently, ultrasonic contrast agents have been developed to increase wall motion visibility [Porter et al. 1994].

The drawbacks of nuclear imaging techniques include poor spatial resolution and the deleterious effect of radioactive tracers. Resolution of the images is a function of the collimator size of the detection cameras, which is inversely related to the signal-to-noise ratio. Therefore, in order to provide more spatial resolution to detect small, non-transmural infarcts, detection cameras must be equipped with smaller collimator sizes. By increasing the efficiency of the scintillation crystals used to capture emitted tracer

radiation (with materials such as sodium iodide and bismuth germanate), the trade-off of signal-to-noise ratio can be limited. Another characteristic artifact is signal attenuation, arising from body tissues. The resulting signal drop-out may potentially reveal a false defect. Currently, there is on-going investigation with attenuation correction in SPECT and PET imaging. With PET scanners, the institution adopts a significant cost burden, which limits its widespread availability. Furthermore, due to the short half-life of the radionuclides used in PET, an in-house cyclotron must be established to provide rapid access to the radioisotopes use for imaging.

The Prognostic Value of Determining Viability

Predominantly, the improvement of prognosis in patients with coronary artery disease is associated with the improvement of left ventricular ejection fraction [Alderman 1983], with the most significance being in patients with very low ejection fraction prior to therapeutic intervention. Current therapeutic alternatives range from pharmacological treatment to coronary revascularization and heart transplantation. Comparatively, coronary revascularization surgery has greater long-term benefits than medical therapy [Alderman et al. 1983, Almman et al. 2002]. However, *question remains as to whom coronary revascularization will benefit the most*, since in addition to the associated risk of bypass surgery despite improvements in anesthesia and medical technology, not all patients are eligible to undergo surgery (due to unsuitable target vessels, accompanying diseases, or age). Furthermore, if myocardial necrosis or scar tissue occupies the complete wall of the myocardium (transmural infarction), coronary revascularization has a minimal chance of improving ventricular function; whereas it will most benefit those

patients who exhibit only small subendocardial infarcts with surrounding myocardium defined as viable [Allman et al. 2002]. From this standpoint, ethical and economic concerns arise about the risk-benefit ratio influencing which therapeutic approach will best serve the patient. *By determining the transmural extent of viable myocardium in a given myocardial segment, appropriate therapeutic decisions can be better served.*

Clinical Outcomes

Regardless of whether viable myocardium is stunned or hibernating, the determination of contractile reserve or positive metabolic processes in dysfunctional segments using imaging techniques is highly predictive of functional recovery following successful reperfusion. Evidence of this outcome is reflected in the high sensitivities of the imaging modalities discussed above. The ultimate value of a diagnostic technique, however, would be its ability to affect the use of different treatment modalities (pharmacological or surgical). Compared to patients who did not reveal contractile reserve with echocardiography, Chaudry recently showed that patients who exhibited contractile reserve following low-dose dobutamine had higher survival rates following revascularization [Chaudry et al. 1999]. This distinction could not have been made with baseline assessment of ventricular function. In another investigation of the prognostic implication of viability assessment, Arfidi evaluated the mortality rate of patients with and without viable myocardium (as assessed by dobutamine echocardiography) who either underwent revascularization or did not [Arfidi et al. 1998]. The study found that the patient group with viable segments who underwent revascularization had the lowest death rate after 36 months (6%), while patients with viable segments who were not

revascularized had significantly higher death rates (20%). In patients without viable myocardium, the death rate was approximately 20% regardless of whether the patient underwent revascularization.

Similar prognostic implications were found using PET viability assessment. Specifically, retrospective studies have shown that functional improvement and long-term patient survival following coronary revascularization were most significant when "mismatch" (hibernating myocardium) was defined by PET [Di Carli et al. 1994, Eitzman et al. 1992, Lee et al. 1994]. These positive prognoses were relative to treatment with medical therapy.

Outcomes of studies such as these reinforce the idea that revascularization therapy to improve ventricular function is most beneficial to patients who not only reveal viable myocardium, but also who have poor left ventricular ejection fraction. *Therefore, the detection of myocardial viability, combined with appropriate therapeutic intervention, is critical for long-term patient prognosis.*

Viability Imaging with MRI

As discussed, there are several imaging modalities and procedures that provide highly predictive information about myocardial viability. However, due to the many aspects of viability assessment (ventricular function, contractile reserve, perfusion, metabolism, and infarct size/location), each technique must be used in combination as part of the overall clinical evaluation. Recently, magnetic resonance imaging (MRI) has become an attractive tool for the assessment of viability, since it provides the potential to image the many aspects of viability assessment in *one setting*. MRI is well-suited for

evaluating cardiac morphology and function due to its excellent spatial and temporal resolution, and high soft tissue contrast. Additionally, MRI provides the capability of imaging any tomographic plane without interference from surrounding tissue, such as lung or bones.

The following sections outline the current role of MRI in viability assessment. This relatively new field of MRI has progressed immensely in recent years, and has become increasingly more commonplace in the clinical algorithm for evaluating ischemic heart disease. There are three applications of MRI that have relevance in viability assessment which will be discussed here. The first two are *functional* and *perfusion imaging*, which have similar clinical objectives as echocardiography and PET/SPECT, respectively. The third, which is the primary focus of these sections and this thesis, is a new MRI technique termed "delayed enhancement". *This technique allows the potential to differentiate viable and non-viable myocardium directly by using an extracellular-specific paramagnetic contrast agent that enhances the signal from infarcted myocardium.* As a result, one is able to easily delineate infarcted (non-viable) from non-infarcted (viable) myocardium, with the potential to also quantify infarct size.

Functional and perfusion imaging with MRI will be briefly discussed first, followed by the clinical and technical aspects of delayed enhancement as they pertain to this research. These topics include a description of the delayed enhancement pulse sequence, contrast agent kinetics, and the potential implications of a higher magnetic field strength.

Determining Ventricular Dysfunction with Cine MRI

The capability for fast cardiac imaging with modern MRI scanners has enabled functional assessment of the left ventricle within a short breath hold period. By imaging multiple phases of the cardiac cycle over several heartbeats, cine loops can be displayed in a continuous format. Cine MRI offers superior spatial resolution and image contrast for accurate delineation of myocardial wall thickness and thickening, which are vital indicators of akinesis, dyskinesis and contractile reserve. Contrast between blood and myocardium allows determination of ventricular volumes and ejection fractions with high accuracy and reproducibility compared with echocardiography [Grothues et al 2002].

Image contrast in MRI is primarily a function of the excitation flip angle (α), the excitation repetition time (TR), and the time from the excitation to the reception of the echo signal (TE). Since many frames within the cardiac cycle need to be acquired in a relatively short time, the acquisition method needs to contain short TR and TE while still generating adequate signal-to-noise. These requirements lend themselves to gradient echo sequences, and more recently, the *balanced steady-state free precession sequence* (b-SSFP), which is now considered the state-of-the-art in MR functional imaging [Bundy et al 1999, Fang et al 2000, Plein et al 2001]. The physics of b-SSFP will be discussed in more detail in Chapter 3. In brief, b-SSFP is a non-spoiled, gradient echo sequence in which there is no net phase accumulation (by spatial gradients) over one TR period [Haacke 1999]. As a result, magnetization is "re-used" throughout the scan, enabling heightened signal compared to spoiled, *un*balanced gradient echo techniques (like Fast Low Angle SHot, FLASH) [Haase et al. 1986, Barkhausen et al 2001]. This trait also maintains uniform blood signal throughout the cardiac cycle, which, in FLASH cine

imaging, is normally lost in regions of high shear, turbulent flow, or stationary flow. The benefits of b-SSFP methods in functional assessment translate to reduced inter-observer variability and the detection of functional improvements following surgical intervention.

As in echocardiography, pharmacological stress can be used with MRI to detect contractile reserve. Several studies have validated the close correlation between stress echocardiography and cine MRI [Pennel et al 1992, Nagel et al 1999]. Furthermore, stress MRI provides added diagnostic accuracy when echocardiography results in poor image quality [Hundley et al 2002]. The key drawbacks of stress MRI are the associated risks of administering dobutamine in the magnet (where patient ECG cannot be directly monitored) and the inherent degradation of MR image quality in individuals with fast heart rates. The latter limitation has been reduced with the advent of b-SSFP and parallel imaging techniques [Pruessmann et al. 1999].

First-Pass Myocardial Perfusion Imaging

Regional perfusion can be evaluated using MRI with the aid of a chelated paramagnetic contrast agent, such as gadolinium diethylenetriaminepentaacetic acid (Gd-DTPA). Relevant ischemic information is only accurate during the *first-pass* of the contrast agent. Thereafter, signal intensity in ischemic regions is affected by recirculation and diffusion mechanics. Using PET and coronary angiography as the standard of reference, myocardial perfusion MRI has been shown to produce sensitivities and specificities over 85% in detecting >50% vessel stenosis [Schwitter et al 2001], but the variability from study to study is high [Wilke et al 1999].

First-pass perfusion imaging requires high temporal resolution, which is satisfied in MRI by acquiring multi-slice, single-phase images dynamically every heartbeat. The transit of contrast media lowers tissue T_1, increasing the local signal intensity, which can be displayed as a function of time via a time-signal intensity curve. Image contrast between perfused and ischemic regions is accentuated by suppressing the signal from myocardial tissue before the contrast-injection, using an appropriately-timed inversion pulse (180°) or, more recently, saturation pulse (90°). The advantage of saturation recovery over inversion recovery regimes is the ability to use short recovery delay times for suppression (enabling more slices per heartbeat), and limiting changes in image contrast between slices due to variations in heart rate. Each dynamic image is acquired in a "single-shot" using an ultra-fast T_1-weighted sequence with short TR and TE, such as spoiled gradient echo (FLASH), echo-planar imaging (EPI), b-SSFP, or hybrid techniques (FLASH-EPI). Due to the need for high temporal resolution, current protocols sacrifice spatial resolution so data can be acquired quickly with minimal motion artifacts. This may lead to an underestimation of the size of ischemic region. Recent advances in parallel imaging have also benefited first-pass perfusion imaging by reducing scan times or increasing in-plane resolution.

Perfusion MRI has the ability to detect hypoperfused myocardium due to occluded coronary arteries. The clinical impact of perfusion defects revealed *at rest* is only relevant for high-grade coronary stenosis, since smaller coronary occlusions will not elicit significant signal intensity differences between normal and jeopardized myocardium. Other perfusion defects due to myocardial ischemia can only be detected under physiological stress using dipryridamole or adenosine, which cause vasodilatation

and increased blood flow. Since vessels with stenosis do not respond to external vasodilators, a significant difference in signal intensity can be observed between hypoperfused and normal myocardium. Determining the *myocardial perfusion reserve* (defined as the ratio between maximal perfusion at stress and maximal perfusion at rest) has been shown to be a useful indicator to distinguish "at-risk" myocardial regions supplied by a stenotic coronary artery (> 75% stenosis) [Al-Saadi et al 2001]. However, the method is limited by its inability to detect significant perfusion defects if the coronary occlusion is small (< 50%). In addition, perfusion MRI can yield negative results despite confirmed coronary stenosis. Despite the discrepancy, this finding may be indicative of adequate collateral blood supply, a feature not directly observed with coronary angiography.

The potential significance of perfusion MRI is its ability to detect *subendocardial perfusion defects* that are not observed with thallium SPECT or perfusion PET. This finding may be an indication of microvascular obstructions at the myocardial level, even when larger epicardial arteries appear patent [Panting et al 2002].

Delayed Enhancement Imaging

A more insightful MRI technique is "delayed enhancement imaging", which is performed approximately 10 minutes following the administration of a T_1-enhancing gadolinium-based contrast agent, such as Gd-DTPA. The term refers to the "delayed" uptake (~10 minutes) of the contrast agent in infarcted myocardium relative to normal myocardium, while "enhancement" refers to the increase in signal intensity in the infarct tissue compared to non-infarcted myocardium. *Delayed enhancement imaging allows*

direct visualization of infarcted myocardium with a resolution that exceeds PET or SPECT, which is relevant for the quantification of infarct size and location.

In this discussion of delayed enhancement imaging, a brief history of the technique and current clinical outcomes will be initially discussed. This will be followed by a more rigorous discussion of the technical aspects of current DE-MRI pulse sequences. The section will conclude with the impact of contrast agent kinetics and the implications of magnetic field strength on delayed enhancement imaging.

Background

In the absence of contrast agents, reports have shown a prolongation of T_1 (spin-lattice relaxation time) in infarcted myocardium [Frank et al. 1976, Williams et al. 1980, Wesbey et al. 1984, de Roos et al. 1988, Been et al. 1988, Kim et al. 1996]; however, the increase is only approximately 23% at 2T [Saeed et al. 2000], making differentiation difficult. It was initially recognized by Wesbey that both the uptake and washout mechanisms of the contrast agent were "delayed" in infarcted myocardium relative to normal myocardium at 5 minutes post-injection [Wesbey et al. 1984]. The potential for contrast agents to delineate infarcted myocardium in this manner allowed a more careful investigation into characterizing the effects of injury type on enhancement patterns, since it was unclear whether differences could be seen between necrotic tissue and tissue that was possibly recoverable. Using a T_1-weighted spin echo (SE) sequence, McNamara noted marked signal increase in areas of irreversible injury with the aid of Gd-DTPA in nine dogs [McNamara et al. 1986]. These early imaging sequences were compromised by their relatively long acquisition times, which introduce artifacts due to respiratory and

cardiac motion. Subsequent improvements in the technique involved reducing scan times to the duration of a breath hold by using segmented *k*-space and gradient echo sequences, and increasing contrast-to-noise ratio with inversion recovery preparation. Despite reports disputing the precise relationship between enhancement and cellular necrosis in acute settings [Saeed et al. 1992], it is currently accepted that delayed enhancement is related to irreversible injury [Kim et al 1999]. These initial findings, combined with technical advancements, have led to more comprehensive validation studies.

Clinical Results in Delayed Enhancement Imaging

Studies in clinical settings have shown that delayed enhancement MRI is able to distinguish reversible from irreversible myocardial injury, even in situations where gross LV dysfunction clouds the possible presence of viable tissue. Kim recently studied fifty patients who were scheduled to undergo revascularization due to ischemic heart disease [Kim et al. 2000]. The investigators compared the extent of delayed enhancement before revascularization in relation to functional LV abnormalities. They revealed that if a region was dysfunctional without or < 25% transmural enhancement prior to treatment, revascularization lead to 80-100% functional improvement. In a similar light, *the transmural extent of enhancement before surgical intervention was inversely related to contractile improvement*, with > 75% transmural enhancement resulting in functional recovery in just 1 of 58 segments (2%). This conclusion was supported by other studies in both animals and humans [Hillenbrand et al 2000, Choi et al 2001], and revealed the ability of MRI to distinguish irreversible myocardial injury from surrounding tissue that could benefit from revascularization. This outcome was present for both acute [Choi et al

2001, Gerber et al 2002] and chronic [Kim et al 2000] ischemic settings; but there is evidence pointing to a decrease in the enhanced zone in acute settings compared to chronic settings when follow-up delayed enhancement imaging is performed after several months [Ingkanisorn et al 2004]. Currently, imaging sequences cannot differentiate acute infarction from chronic scar tissue.

A particular benefit of delayed enhancement is the detection of *subendocardial infarcts*. In a recent study by Wagner, myocardial viability was compared between delayed enhancement MRI and thallium SPECT in both animals and humans [Wagner et al 2003]. Both techniques were able to detect all segments with >75% transmural infarcts, but SPECT only detected 28% (animals) and 47% (humans) of subendocardial infarcts identified by delayed enhancement MRI. Patients with missed infarcts and normal perfusion by SPECT may be classified as "normal", when indeed there is evidence of subendocardial infarction detected by delayed enhancement MRI. Evidence of infarction in this circumstance would encourage treatment measures to prevent secondary cardiac events and increase patient prognosis.

MR Pulse Sequences for Delayed Enhancement

The high degree of sensitivity of delayed enhancement imaging ultimately depends on the ability of the MRI pulse sequence to use the available magnetization efficiently in order to provide high image contrast. Delayed contrast enhancement in infarct regions is a direct result of T_1 shortening caused by the accumulation of contrast material and the impaired washout mechanics of the infarct zone [Wesbey et al. 1984, de Roos et al. 1988, Judd et al. 1995, Kim et al. 1996]. Early development of delayed

enhancement utilized T_1-weighted SE sequences without breath holding [de Roos et al. 1988, de Roos et al. 1989, van Dijkman et al. 1991]; however, they have largely been replaced by inversion recovery (IR) gradient echo techniques, which are triggered with the cardiac cycle and provide imaging times on the order of a breath hold [Kim et al. 1999, Kim et al. 2000, Simonetti et al. 2001]. The IR pulse is timed to *null* (or "suppress") the signal from normal myocardium post-contrast, and provides high sensitivity to T_1 differences in the myocardium. Simonetti provides a thorough comparison of several imaging methods for delayed enhancement MRI and concludes that *a 2D segmented IR-prepared, low flip angle gradient echo technique (IR-FLASH) is superior to previous SE and single shot gradient echo methods* [Simonetti et al. 2001]. Specifically, the sequence yields over 1000% signal increase of infarct in canines and close to 500% increase in human studies. The significant difference between this pulse sequence and other similar gradient echo techniques is the "segmented" *k*-space acquisition strategy to provide high T_1-sensitivity over single shot methods [Edelmann et al. 1990], and accurate suppression of post-contrast myocardium by IR preparation (inversion delay time, *TI*, of 200-400ms). The benefit gained by segmented data acquisitions may be compromised, however, in situations when arrhythmia and tachycardia act to vary and shorten the cardiac cycle, causing inconsistent or insufficient recovery time for the magnetization between data acquisition segments, which results in inaccurate nulling of normal myocardium. This issue is remedied by skipping 2 or more heartbeats before the next *k*-space segment is acquired.

3D Techniques

Delayed enhancement imaging is normally executed with 2D imaging techniques, requiring the acquisition of slices from apex to base, each performed in a breath hold. However, due to advances in gradient performance and parallel imaging methods, 3D delayed enhancement has gained more acceptance. 3D acquisition methods allow the full coverage of left ventricle in one breath hold [Kuhl et al 2004, Foo et al. 2004]. A significant difference with 2D methods is that imaging is performed every heart beat, which necessitates a reduction in *TI* to impart suppression. Since slice thickness is usually <5mm in 3D methods (compared to 8-10mm with 2D methods), partial volume errors of infarct size are reduced. However, this results in a reduction in in-plane resolution to keep the acquisition time within a breath hold.

Suppressing Normal Myocardium

As mentioned, heightened visualization of infarcted tissue depends on effectively suppressing the signal from normal myocardium using an appropriate inversion delay time, *TI*. Although the science of suppressing T_1 values of interest with inversion recovery follows the solution of the Bloch equations, these theoretical results do not always translate to optimal suppression in practice. The primary causes of the discrepancy include additional magnetization disturbances from readout excitation pulses, and insufficient relaxation prior to the next inversion pulse. The challenge is exacerbated in delayed enhancement imaging since the T_1 value of normal myocardium varies over time due to contrast agent washout. Currently, implementation of delayed enhancement relies heavily on user-expertise, with *TI* selections made based on the time

post-contrast, the contrast agent dose, the patient heart rate, and the interval time between inversion pulses (1- or 2-heartbeats). Nevertheless, efforts have been made to elucidate the temporal dependency of inversion times based on T_1 knowledge [Mahrholdt et al. 2002, Sharma et al 2003]. However, *a thorough mathematical treatment of the delayed enhancement technique for the purpose of both optimizing TI and understanding the mechanisms of contrast enhancement has not been presented in the literature.* Detailing this relationship and correlating the results with practical imaging sequences is one of the efforts of this project.

Recent advances have attempted to reduce the complexity of *TI* selection. One example is to use a "*TI*-scout" image series. Rather than acquire one image at a distinct inversion time, several images can be acquired following a single inversion pulse and analyzed to determine which image in the series provides the best normal myocardium suppression. The corresponding *TI* is used in a subsequent delayed enhancement image. This "*TI*-scout" image is a modified "Look-Locker" technique, whereby a series of images are acquired following a single inversion pulse [Look et al 1970]. Often, rapid acquisition methods are used in tandem with the *TI*-scout, which limits the SNR and spatial resolution of the technique for use as a stand-alone delayed enhancement technique. It should be noted that the *TI*-scout readout module (2D FLASH-EPI, b-SSFP, etc.) may differ from the acquisition method used for delayed enhancement (2D or 3D FLASH), leading to potential deviations in the *TI* value.

Another promising technique is the phase-sensitive reconstruction method [Kellman et al. 2002]. This technique was motivated by the idea that delayed enhancement images, which are normally displayed as *magnitude* images, are not able to

distinguish positive magnetization from negative magnetization, causing certain images, at specific *TI* values, to appear to have no image contrast. By preserving the sign of the magnetization, the technique offers a larger range of *TI* values that produce high image contrast. This reduces the number of additional scans needed to locate the optimal inversion time using conventional techniques.

Contrast Agents and R_1 Kinetics

Gadolinium-based contrast agents, such as Gd-DTPA, can significantly increase signal on T_1-weighted images [Hendrick et al. 1993]. The contrast agent greatly reduces the T_1 of blood and tissue immediately after venous injection [Kim et al. 1996, Saeed et al. 2000], but tissue with inadequate perfusion will experience a delayed accumulation usually through collateral circulation or slow diffusion mechanics [Kim et al. 1996, Rehwald et al. 2002]. Furthermore, cell membrane disruption increases interstitial free water access for Gd-DTPA, which is normally excluded from the intracellular space [Jennings et al. 1990, Judd et al. 1995]. Normally, the presence of contrast media in healthy tissue is short-lived, since most is efficiently washed out by venous return. However, edematous tissue from cell damage may cause compression of venous capillaries, effectively diminishing the expulsion rate of the contrast agent [McNamara et al. 1986]. As a result, normal tissue returns to equilibrium in less than an hour, but impaired washout properties cause preferential accumulation in chronic infarction.

It is often more convenient to use relaxation *rates* ($R_1 = 1/T_1$) to express a contrast agent's affect on T_1, since their mechanisms simply add to a sample's nominal R_1 value. At any given time point after injection, the effect of the contrast agent on R_1 varies with

respect to the concentration present in the extracellular space of the tissue [Tweedle et al. 1991, Rehwald et al. 2002]. If washout is highly efficient, as in normal tissue, one will expect a sharp return to pre-contrast R_1 values following the initial rise immediately after injection. Blood and healthy tissue rank high in having efficient washout mechanics, with a time constant of 1.5 hours, but this is dependent on glomerular filtration and species type [Oksendal et al. 1993]. Injured tissue, such as infarct, has poor uptake and washout, making the return to equilibrium values much slower [Kim et al. 1996]. *The relevant uncertainty lies in the R_1 values of normal myocardium, since IR pulses are timed to null this tissue.* Though the R_1 trend is known, guaranteeing all patients exhibit the same washout mechanics for contrast material is highly unlikely.

Field Strength

The utility of high field imaging (3T) is already extensive for functional and anatomical imaging of the brain. *The primary advantage of 3T MRI over 1.5T is its higher signal sensitivity* due to the increased splitting of energy spin states. This allows a greater amount of bulk magnetization to be sampled during an experiment, effectively increasing the relative SNR. Another direct benefit of higher fields is increased chemical sensitivity and separation, creating new potential for advances in clinical MR spectroscopy.

Investigations into the broad clinical relevance of 3T systems are still ongoing. Since 1.5T systems have been the norm in most clinical institutions for more than a decade, they represent a sound reference of comparison as 3T systems become more widespread. High field whole body MRI systems present some inherent challenges which

must be overcome before acceptance. The technical challenges are related to need to design new receiver and transmit coils, which become increasingly cumbersome due to inhomogeneity effects imposed by the higher resonant frequency. A larger resonant frequency also results in greater power deposition in the patient, and increased susceptibility-induced signal loss. Other challenges include increased operating costs.

The feasibility of cardiac imaging at 3T was shown in the late 1990s [Wen et al. 1997, Noeske et al. 2000]. Although the investigations reported increased SNR relative to lower field strengths [Wen et al. 1997], several important observations were concurrently revealed that could potentially degrade SNR gains. The use of surface coils, which are inherently sensitive to signal drop-off for deep body tissues, is further limited by a reduction of penetration depths of the radiofrequency (RF) transmit field, making signal- and contrast-to-noise ratio a strong function of spatial position. There is also a greater propensity for motion artifacts at higher fields due to greater field inhomogeneities, especially for pulse sequences highly sensitive to field perturbations, such as balanced steady-state free precession, which is a very important sequence for evaluating myocardial function. This places greater emphasis on optimizing shimming routines beyond the first- and second-order, or accurate determination of resonant frequency off-set for the particular scan.

The overall limitation to high field imaging is imposed by the maximum allowable power deposition, or specific absorption rate (SAR), of the experiment. Federal guidelines have set the maximum SAR at 8 W/kg [International Electrotechnical Comission 1995]. The selected scan parameters play a direct role in determining the SAR of the scan, which in turn, place limits on allowable scan parameters. SAR is also field-

dependent, increasing by approximately the square of the magnetic field. The ultimate outcome is restrictions on the maximum allowable flip angle and the shortest allowable *TR*.

Spin-Lattice Relaxation, T_1

Another key difference at high fields is the lengthening of T_1 relaxation times [Block et al. 1974, Bottomley et al. 1988]. This increase may have great significance in infarct imaging using delayed enhancement MRI. The use and effect of contrast agents at high fields have been studied [Rinck et al. 1988, 1999], but *an accurate documentation of how relaxation rates at 3T may change relative to values at 1.5T has yet to be investigated*. From a theoretical basis [Bloembergen et al 1948], the relaxation rate ($R_1 = 1/T_1$) of a tissue is proportional to its correlation time (τ_c), or the "dwell time" associated with the movement of water. This means that relaxation is roughly dependent on the extent of the "bound" *and* "free" water in tissue. This two-phase system has been studied extensively [Koenig et al. 1969]. Relaxation rates are also influenced by the magnetic field strength. Specifically, depending on the tissue type, *T_1 will increase at higher fields*. This is highly relevant for tissue organs (solid/viscous liquid), but fluids such as cerebrospinal fluid will experience little or no change since it has an equal proportion of molecules tumbling at a broad range of frequencies.

For paramagnetic contrast agents, the quantitative measure of effectiveness is *relaxivity* (r_1), which is defined as *the change in relaxation rate per unit concentration of contrast agent*. For Gd-DTPA, relaxivity is essentially constant at high fields (>1T) [Bousquet et al. 1988], but does exhibit a minor reduction with field strength. It has also

been shown that r_1 has some dependency on the molecular environment [Stanisz et al 2000]. This may cause certain tissues to experience more *net* enhancement relative to other tissues.

The most important characteristics influencing R_1 values of infarcted and normal myocardium at 3T following contrast agent administration are: 1) baseline R_1 values before contrast injection; 2) the relaxivity of the contrast agent; 3) the dose of contrast agent administered; 4) the molecular environment of the tissue; 5) the degree of extracellular space (distribution volume); and 6) the elimination (or "washout") mechanics of the agent. Many of these factors are *independent of field strength*, namely, Gd-DTPA dose administered, distribution volume, washout mechanics. Therefore, baseline R_1 values and contrast agent r_1 are the primary determinants of tissue R_1 values post-contrast. For very small r_1 changes between field strengths, baseline R_1 values are the most significant factor contributing to signal intensity. Therefore, determining the relative change in baseline R_1 between 1.5T and 3T can lead to general approximations of the expected image contrast.

The difference in field dependency between solids and liquids may have some relevance for imaging infarcted myocardium at 3T. There is increased water content in infarcted myocardium relative to normal myocardium due to edema. This leads to infarct tissue T_1 being higher than normal myocardium T_1 [Klein et al. 2004]. This may also cause the infarcted myocardium R_1 to change less significantly with field strength than normal myocardium. If this occurs, the R_1 difference post-contrast (and hence image contrast) between infarct and normal myocardium will increase at 3T, assuming relaxivity and contrast concentration do not change (Figure 2.2).

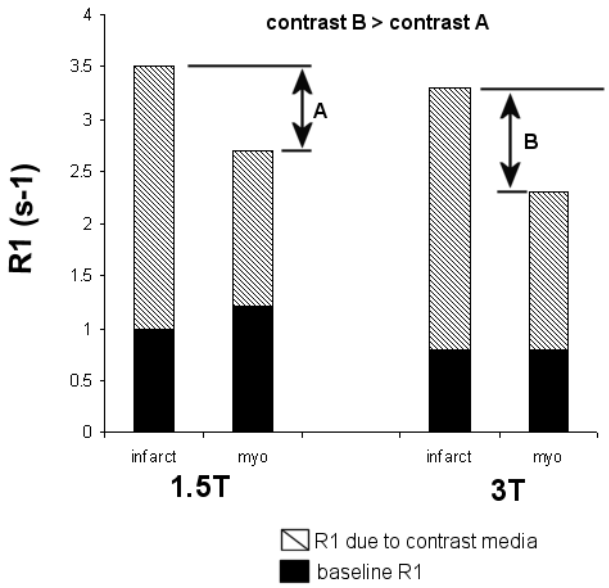

Figure2.2. *Hypothetical image contrast increase at 3T due to minimal baseline infarct R_1 change between 1.5T and 3T.*

Conclusions

This chapter has reviewed the clinical aspects of myocardial viability and the need to prospectively assess the degree of necrosis following an ischemic event. Many clinical tests are currently available to quantify left ventricular function, perfusion, and metabolic state due to regional ischemia. A new contrast-enhanced MRI technique, called delayed enhancement, is now available that provides heightened image quality for infarct tissue detection and allows more precise quantification of infarct size. There are still some technical issues related to the technique that challenge its robust use in clinical practice. Moreover, a formal presentation analyzing contrast optimization of the technique has not been fully investigated. Also, due to the inherent benefits (SNR) afforded by higher field MRI, particular advantages, such as increased infarct resolution, need to be described along with potential pitfalls.

CHAPTER 3

THEORETICAL BACKGROUND AND T_1 CONTRAST SIMULATIONS

Introduction

This chapter focuses on providing a comprehensive mathematical framework of the imaging methods used in this document. This examination is necessary for optimizing and analyzing many of the pulse sequences used in cardiac MRI. Moreover, for the extension of conventional delayed enhancement sequences to high fields, it is convenient to define the expected signal behavior with mathematical models, before resorting to trial-and-error-based experimentation at the scanner console. From this stance, simulations can be carried out to confirm or predict scientific findings in a clinical or experimental setting.

Before outlining the specific mathematical models used to simulate the delayed enhancement sequence, it will be necessary to introduced commonly known signal expressions, such as inversion recovery (IR), spoiled gradient-echo imaging (Fast Low-Angle SHot, i.e. FLASH), and balanced steady-state free precession (b-SSFP). Mathematical expressions for these models are commonly seen in the literature relating the signal intensity to common MR parameters such as T_1, T_2, TR, and flip angle (α). In this treatise, the complete signal expressions will be developed in a general sense; initially without direction to a particular application. Then, as these foundations are built, more assumptions and practical imaging scenarios will be introduced, culminating to the final expressions used to model the techniques included in this chapter, such as T_1 measurements and delayed enhancement imaging (IR-FLASH). As a result, this chapter

will serve as a useful reference in the chapters to follow. Note that many of the symbols are summarized in "List of Symbols and Abbreviations" at the beginning of this thesis.

The theory developed in this chapter will be revisited in Chapter 4, as T_1-"phantoms" are used to validate some of the techniques developed here. All simulations were performed with Mathematica 5.0 (Wolfram) and Matlab 6.5 (MathWorks, Natick, MA) software with the aide of references [Hanicke et al. 1990, Jivan et al. 1997, Hargreaves et al. 2001, Scheffler et al. 2001, Scheffler 2003, Haacke 1999]. This chapter is topically divided into three parts. The first topic will review the mathematical expressions of magnetization relaxation due to spin inversion and saturation. Then, a survey of the FLASH and b-SSFP sequence will conclude with contrast optimization simulations using hypothetical scan parameters (this topic will be revisited in Chapter 6 and 7 when *in vivo* T_1 data is obtained). The final portion of the chapter is dedicated to an explanation of the T_1 measurement sequences used in the following chapters, namely a 2-point ratio method, and a 4-point single shot technique.

Magnetization Response

It is assumed that the reader is familiar with nuclear induction by an external magnetic field. Simply stated, the initial condition for the discussions in this chapter is the presence of *net equilibrium magnetization* (M_0) in the direction of the main magnetic field, B_0. The mathematical expressions developed in this chapter estimate the expected amplitude of magnetization in longitudinal (M_z) and transverse (M_{xy}) direction assuming the repetitive action of radiofrequency (RF) excitation pulses of infinitesimal width. RF excitation at a frequency $\omega_0 = \gamma B_0$ (where γ is the gyromagnetic ratio of hydrogen, 42.6

MHz/T) causes the magnetization vector to be tipped away from equilibrium (in the rotating frame of reference) through an angle $\alpha = \gamma B_{1trans}\tau$ (where B_{1trans} is the RF field strength and τ is the pulse width). Thereafter, energy is released by the system as equilibrium is reestablished via characteristic relaxation times T_1 and T_2. The calculations of M_z and M_{xy} in this treatment do not represent the actual voltage signal detected by the receiver system, and no concessions are made to include noise in the simulations (for a full treatment, see [Hanicke et al. 1990, Vlaardingerbroek 2003]). However, these calculations are *proportional* to the expected signal, enabling predictions of image contrast (given user-defined scan parameters and tissue relaxation values).

Also, it should be prefaced that these expressions represent *the magnetization amplitude at a particular point in time*, meaning that a plot of the data at specific time intervals would be a series of discrete points. For visual purposes, all plots were joined to create smoothed curves.

Expression for a 180 pulse

This section develops a general expression for longitudinal recovery of magnetization following an inversion (180°) pulse using a *classical mechanics* methodology. The state of magnetization following an RF excitation pulse can be simulated by the Bloch equation of motion [Bloch et al. 1946]. For simplicity, we will consider excitation and relaxation in the *rotating frame of reference*, and ignore off-resonance effects. The derivation begins with a differential equation describing relaxation of magnetization toward equilibrium (M_0) following excitation:

$$\frac{dM_z(t)}{dt} = -\frac{M_z - M_0}{T_1}. \qquad [1]$$

The characteristic relaxation time for M_z is T_1, the *spin-lattice relaxation time*. This differential equation can be solved easily using separation of variables:

$$\frac{dM_z(t)}{M_z - M_0} = -\frac{dt}{T_1}$$
$$\ln\left(M_z(t) - M_0\right) = -\frac{t}{T_1} + C_1 \qquad [2]$$

where C_1 is a constant of integration. It remains only to solve for M_z. Taking the exponential of both sides:

$$M_z(t) - M_0 = C_2 \exp\left(-\frac{t}{T_1}\right), \qquad [3]$$

which produces a second constant, C_2. The final step is to move M_0 to the right hand side of the equation. The constant preceding the exponential is determined by applying the initial condition, $M_z(0) = M_z^- \cos\alpha$. This condition represents an excitation of angle α at time zero, and M_z^- represents the amount of magnetization *just prior* to the pulse. Solving for C_2 reveals, $C_2 = M_z^- \cos\alpha - M_0$. Note that the angle of nutation, α, is not restricted to only inversion, but can be *any angle*. The general equation, therefore, for longitudinal magnetization at time *t*, subject to a flip angle α, is:

$$M_z(t) = M_0\left(1 - \exp(-t/T_1)\right) + M_z^- \cos\alpha \exp(-t/T_1). \qquad [4]$$

An important outcome is that the flip angle, α, operates exclusively on M_z^-, which is not necessarily equivalent to M_0, as we will see when the FLASH sequence is considered. When α is 90°, the magnitude of M_z^- is inconsequential since the second term of Eq. [4] becomes zero. Alternatively, if α is 180° (spin inversion), the value of M_z^- is very significant. Often, the general form of the inversion recovery equation assumes the

magnetization prior to inversion is at equilibrium ($M_z^- = M_0$), which allows further simplification of Eq. [4]. These conditions lead to the general forms of the inversion recovery equation, which are summarized as follows (with corresponding delay time, *TI*):

$$M_z(TI) = M_0\left(1 - 2\exp(-TI / T_1\right) \qquad [5]$$

Image contrast is obtained by modifying *TI* appropriately. This equation forms the foundation of many methods of contrast enhancement in cardiac MRI, and will be used throughout this chapter.

Short-TR, Gradient Echo Imaging

This section focuses on Fast Low-Angle Shot (FLASH) imaging, which falls under the classification of gradient echo imaging and is the most common sequence used with delayed enhancement imaging. A sequence diagram is shown in Figure 3.1. This pulse sequence is implemented with equally-spaced low-flip angle pulses ($\alpha < 90°$) and short repetition times (TR), which enable data to be sampled very quickly (compared to spin echo sequences). The purpose of this section is to formulate a mathematical expression for *inversion recovery* FLASH imaging (IR-FLASH), which will subsequently be used in contrast optimization simulations pertaining to delayed enhancement imaging. To achieve this final expression, the general magnetization equations developed in the previous section will be carried through this discussion and modified to the requirements of delayed enhancement imaging. To complete this process, we must consider the repercussions of repetitive RF excitation on magnetization, which strongly saturates the available magnetization (since magnetization can not recover sufficiently if $T_1 << TR$), and develops a steady-state magnetization level (M_{zss}) *lower* than the equilibrium level,

M_0. This occurrence motivates the prescription of "optimal" flip angles (such as the well-known *Ernst angle*), or other implementation strategies to lessen the saturation effect ("variable flip angle sweep"). Additionally, we must address the effects of *image segmentation*, a prescribed data acquisition method that acquires image data in parts (or "segments"), which is necessary to compensate for cardiac motion. Finally, we must address the impact of magnetization preparation into our mathematical treatment of FLASH (inversion preparation). This section topically deals with each of these important issues, and also provides simulation figures to aid in the understanding of each formulation.

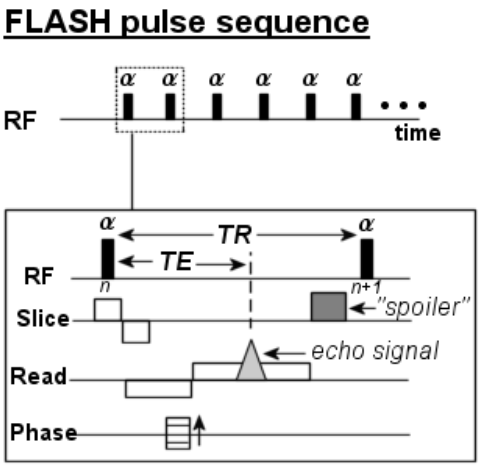

Figure 3.1. *Diagram of FLASH pulse sequence*

FLASH is an imaging technique that is largely T_1-weighted. The T_2 influence on FLASH is negligible, since: 1) TR and the echo time, TE, are very short compared to T_2; and 2) techniques are used to "spoil" residual transverse magnetization before each RF pulse. "Spoiling" refers to purposely destroying the transverse magnetization such that there are no transverse components present in the magnetization prior to each new RF

pulse. This is achieved either by applying an additional gradient, or, more commonly, by *RF phase cycling*, in which the excitation phase (or "direction") is advanced from pulse to pulse in a defined manner [Haase et al. 1986]. This also helps cancel out spurious echoes (such as "stimulated" echoes) that arise due to closely-spaced excitation pulses.

Figure 3.2a-c shows the number of pulses needed to achieve *steady-state* in various imaging scenarios. Analytical expressions are left out for the time being for a more qualitative understanding. The transition of magnetization from equilibrium (pulse = 0) to a constant steady-state value (termed the *transient response*) follows clear trends. Steady-state is achieved quickly for low T_1s, high flip angles and long TRs. The most dominant effect, however, appears to be flip angle (for a given TR and T_1). Although steady-state is achieved much faster for $\alpha = 45°$ compared to 7° (Figure 3.2a), the steady-state magnetization level is very low, which may result in undesirably low signal.

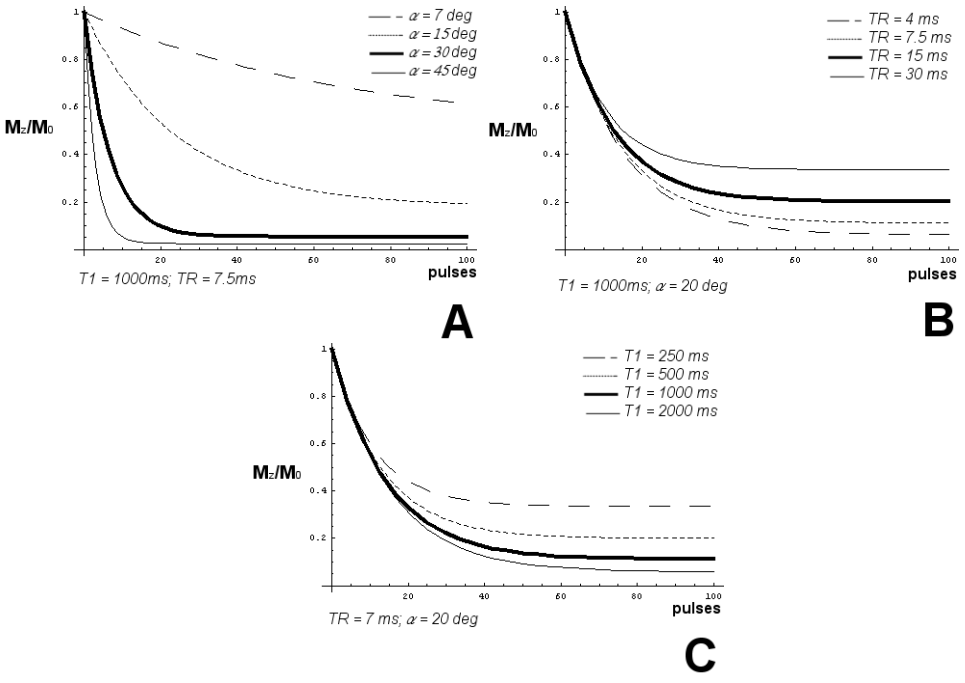

Figure 3.2. *Transition of M_z FLASH to steady-state*

The destruction of (available) magnetization in Figure 3.2 due repetitive pulses has repercussions in the final reconstructed image. Since each pulse number is associated with a measured *echo signal*, the changing echo amplitude may make certain features in the image distorted, depending how *k-space* is filled. *K*-space contains the frequency and phase information from every measured echo signal (which is subsequently Fourier transformed to produce a reconstructed image): high frequency (and phase) information describes *edge information* in reconstructed images, while low frequency (and phase) describes *general image contrast* and *homogeneous regions*. Therefore, the degree of signal change during the transient response and which area of *k*-space is acquired first will both dictate how artifacts present themselves in the final image (namely, edge artifacts, blurry edges and ghosting).

Longitudinal Magnetization

The longitudinal magnetization just prior to the *first* RF pulse of the FLASH acquisition segment (also termed "readout") is represented by M_{z1}^{-}. Without IR or SR preparation, M_{z1}^{-} is equivalent to M_0. Following the first RF pulse, which reduces the longitudinal magnetization by a factor $\cos(\alpha)$, the system relaxes with T_1 until the next RF pulse. Hence, the magnetization just prior to the *second* RF pulse (M_{z2}^{-}) can be described using Eq. [4] of the previous section by substituting TR (the RF pulse repetition time) for *t*:

$$M_{z2}^{-} = M_0\left(1-\exp(TR/T_1)\right) + M_{z1}^{-}\cos(\alpha)\exp(-TR/T_1)\,. \qquad [6]$$

It is important to note that $M_{z1}^{-}\cos(\alpha)$ is equivalent to M_{z1}^{+}, the magnetization immediately *after* the first pulse. With the flip angle held *constant*, the magnetization just prior to the *third* pulse is:

$$M_{z3}^{-} = M_0\left(1-\exp(TR/T_1)\right) + M_{z2}^{-}\cos(\alpha)\exp(-TR/T_1). \qquad [7]$$

This magnetization can be expressed in terms of M_{z1}^{-} by substituting Eq. [6] into Eq. [7]. This is convenient since it relates the current magnetization amplitude (M_{z3}^{-}) with the initial magnetization (M_{z1}^{-}), which is often known or assigned. Performing this substitution and using simpler notation, $ER = \exp(-TR/T_1)$, the magnetization prior to the third RF pulse is simplified to:

$$M_{z3}^{-} = M_0\left(1-ER\right)\left[1+ER\cos\alpha\right] + M_{z1}^{-}\left(ER\cos\alpha\right)^2. \qquad [8]$$

The determination of M_{zn}^{-} can be determined recursively, and the final solution can be written in terms of the initial magnetization before readout, M_{z1}^{-}. Hence, the magnetization just prior to the n^{th} RF pulse is:

$$M_{zn}^{-} = M_0\left(1-ER\right)\sum_{k=0}^{n-2}(ER\cos\alpha)^k + M_{z1}^{-}\left(ER\cos\alpha\right)^{n-1}. \qquad [9]$$

Equation [9] can be simplified into a more concise form, since the first summation term is a geometric series:

$$M_{zn}^{-} = M_0\left(1-ER\right)\left[\frac{(ER\cos\alpha)^{n-1}-1}{ER\cos\alpha-1}\right] + M_{z1}^{-}\left(ER\cos\alpha\right)^{n-1}. \qquad [10]$$

This is the general equation for FLASH imaging for n pulses. The *image signal intensity* following the n^{th} pulse is proportional to $M_{zn}^{-}\sin(\alpha)\exp(-TE/T_2^*)$, which is the magnitude of *transverse magnetization* ($M_{xyn}^{+} = M_{zn}^{-}\sin(\alpha)$) scaled by T_2^* decay. T_2^* is

the transverse magnetization decay time constant associated with *gradient echo imaging*. It has two components: natural T_2 decay (spin-spin relaxation) *and* dephasing due to inherent main field inhomogeneities. The impact of this decay on M_{xyn}^{+} is small since normally TE<<T_2*. In high susceptibility regions, T_2* decay is prominent and TE may be on the same order as T_2*. However in this analysis the derivations and calculations ignore the influence of T_2* on the magnitude of transverse magnetization, since the FLASH pulse sequence contains very short TEs.

Steady-State Magnetization

Before analyzing the general models for longitudinal and transverse magnetizations in FLASH, it is important to consider the limiting case of Eq. [10] as *n* becomes large. Recall form Figure 3.2 that a steady-state value was achieved after a finite number of RF pulses. This phenomenon occurs since $(ER\cos\alpha)^n$ goes to zero for large *n*. As a result, the steady-state value (M_{zss}) of Eq. [10] becomes:

$$M_{zss} = M_0 \frac{(1-ER)}{1-ER\cos\alpha}. \qquad [11]$$

Note that the steady state value is *not* dependent on the initial magnetization prior to the first pulse (M_{z1}^{-}), meaning that the tissue of interest will always converge to a single magnetization level, *even if it begins in the inverted state*. This is shown in Figure 3.3a, using the parameters from Figure 3.2a (*TR* = 7.5ms; T_1 = 1000ms; α = 30°), and two initial states: M_{z1}^{-} = 1 and M_{z1}^{-} = -1. The *rate* of convergence to the steady state value is inversely proportional to $ER\cos\alpha$, which is always less than one. However, given the small values of TR used in FLASH (TR < 10ms), *ER* is approximately 1.0 for

physiologic T_1s (500ms to 1500ms), making $\cos(\alpha)$ the more dominant factor influencing the approach to steady state. It is also apparent from Figure 3.3a that the *negative* magnetization approaches M_{zss} at a faster rate than the *positive* magnetization. The difference lies in that the recovery of initially inverted magnetization is *accelerated* by RF excitation (assuming the phase of excitation does not change), because the $\cos(\alpha)$ factor will complement natural T_1 recovery of negative longitudinal magnetization toward zero. Figure 3b shows a plot of the absolute rate of M_{zn}^{-} (dM_{zn}^{-}/dn) for the parameters used earlier. The plot reveals that dM_{zn}^{-}/dn is greater for the M_{z1}^{-} = -1 initial condition in the range of *n* shown. This result has significance in inversion recovery FLASH sequences, particularly if magnetization is sampled when it still has negative sign. The outcome will be a steeper saturation effect during the transient period toward M_{zss}, potentially causing image artifacts.

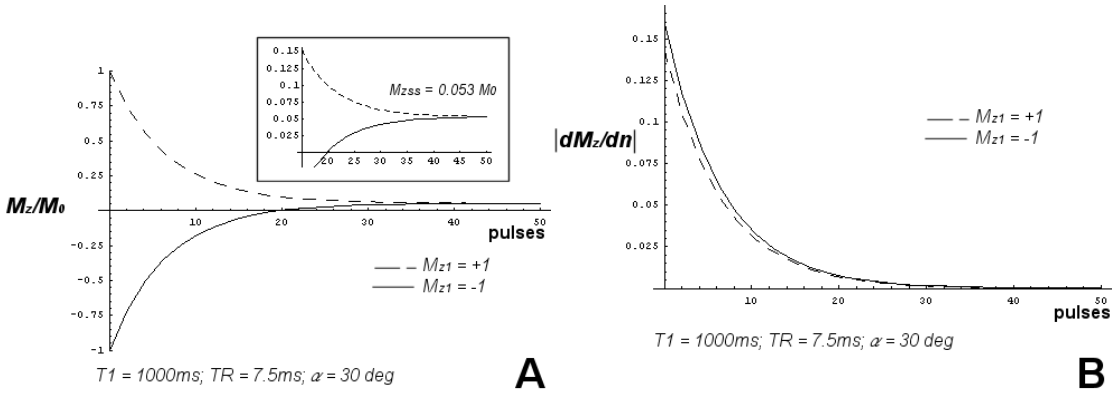

Figure 3.3. *Rate of convergence of magnetization to steady-state from the inverted and non-inverted initial condition.*

Transverse Magnetization and the Ernst Angle

A more precise representation of the expected signal as a function of RF pulse number is the magnitude of *transverse magnetization* following the n^{th} pulse, M_{xyn}^{+}. As mentioned, the transverse magnetization, assuming TE<<T_2*, is:

$$M_{xyn}^{+} = M_{zn}^{-} \sin\alpha \,. \qquad [12]$$

Figure 3.4 shows the magnitude of M_{xyn}^{+} for the same parameters given in Figure 3.3a. The magnitude of M_{xyss} is only 0.027 of M_0 compared to 0.053 in Figure 3.3a. Notice there is still a significant change in M_{xyn}^{+} during the transient phase (from M_{xy1}^{+} to $\sim M_{xy40}^{+}$), meaning that the echo amplitudes after the initial RF pulses are larger than those during the steady-state. In a practical setting, it is prudent to acquire the image data close to steady magnetization in order to avoid these significant signal fluctuations during the transient phase, which may cause blurring or ghosting artifacts in the phase encode direction.

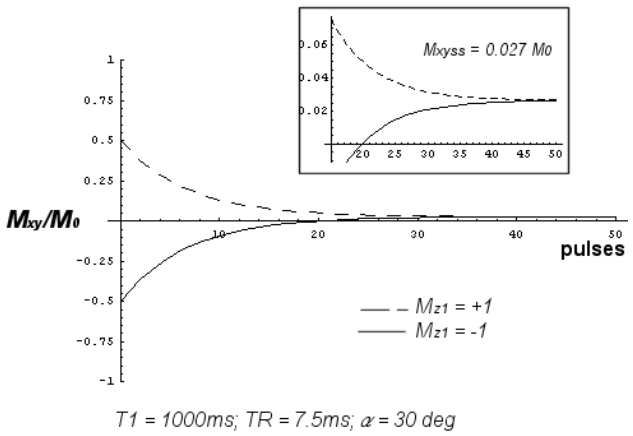

Figure 3.4. *Convergence to steady-state transverse magnetization for positive and negative initial conditions.*

Noting that M_{xyss} is small, there is a motivation to somehow maximize M_{xyss}. This is accomplished by determining a flip angle that produces the maximum M_{xyss} for a given TR and T_1. This flip angle is called the *Ernst angle*, and is commonly less than 90°. The Ernst angle, in terms of TR and T_1, is determined first by differentiating:

$$M^{+}_{xyss} = M^{-}_{zss} \sin\alpha = \frac{M_0 \sin\alpha(1-ER)}{(1-ER\cos\alpha)} \qquad [13]$$

with respect to the flip angle, which yields:

$$\begin{aligned} \frac{dM^{+}_{xyss}}{d\alpha} &= \frac{(1-ER)\cos\alpha}{1-ER\cos\alpha} - \frac{(1-ER)ER\sin^2\alpha}{(1-ER\cos\alpha)^2} \\ &= \frac{(ER-1)(ER-\cos\alpha)}{(ER\cos\alpha-1)^2} \end{aligned} \quad . \qquad [14]$$

The root of Eq. [14] is determined by setting the numerator equal to zero. The trivial solution is $ER = 1$, which means $T_1 = \infty$ or TR = 0. Hence, we equate $ER - \cos\alpha = 0$, which yields a simple relationship between the optimum flip angle and TR and T_1. Therefore, the Ernst angle (α_E) for FLASH imaging is:

$$\alpha_E = \cos^{-1}(\exp(-TR/T_1)) \, . \qquad [15]$$

This value represents the flip angle at which the *maximum steady state signal* is achieved. Theoretically, the Ernst angle is small for very low TRs, and high for low T_1, as shown in the plots of Figure 3.5. Usually, TR < 10ms in cardiac applications and T_1 is roughly 1000ms for heart tissue, making the Ernst angle much less than 20°. The use of contrast agents, which lowers T_1, affords using higher flip angles. Figure 3.6a and b shows M^{-}_{zn} and M^{+}_{xyn} using the Ernst angle (α_E = 8°; TR = 10ms; T_1 = 1000ms). The magnetization amplitudes are relatively constant due to the low flip angle, but both functions are still decreasing after 60 pulses, meaning that the steady-state has not been

reached. But since the slope of the curves are very low (compared to the examples shown in Figure 3.2), image degradation due to fluctuating echo amplitude from pulse to pulse is expected to be minor. The steady state value in this case is 0.50 for M_{zn}^{-} and 0.07 for M_{xyn}^{+}.

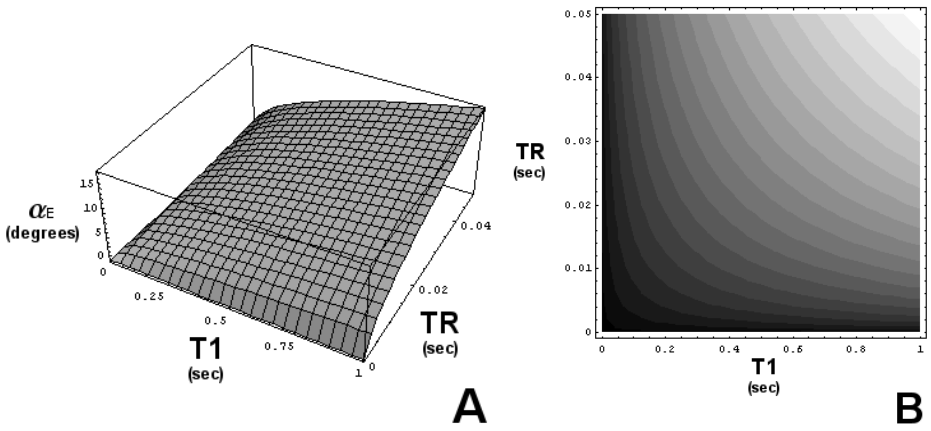

Figure 3.5. *The Ernst angle as a function of TR and T_1.*

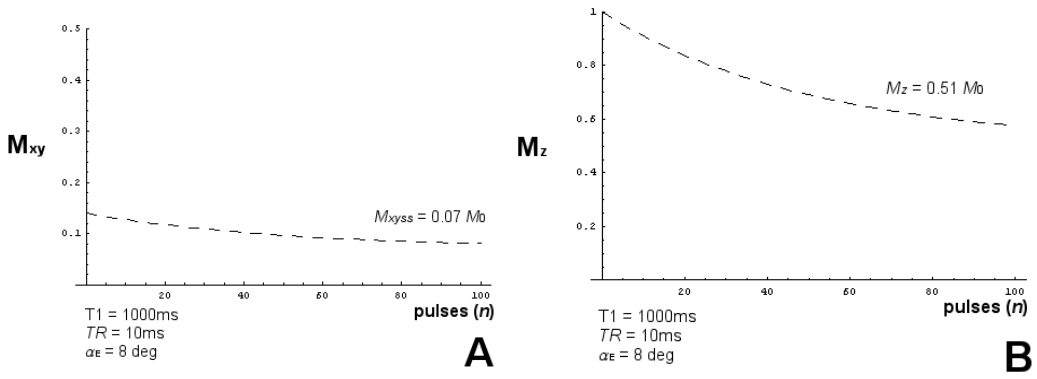

Figure 3.6. *Magnetization profiles as a function of pulse number using the Ernst angle.*

Variable Flip Angle

Determining the nature of the set of flip angles in an imaging sequence is critical for optimizing sequences through mathematical models. The magnetization response is

quite different between methods that use constant flip angles and those that use variable flip angles. Constant transverse magnetization from pulse-to-pulse can only be obtained by varying the RF excitation angle from pulse-to-pulse. This scheme is relevant when it is known *a priori* the steady-state can not be reached. The condition that needs to be satisfied is:

$$M_{xyn}^{+} = M_{xy(n-1)}^{+}. \qquad [16]$$

A recursive formula that relates the current flip angle, α_n, to both the previous, α_{n-1}, and first flip angle, α_0, can be calculated using the stipulation $M_0 \sin\alpha_0 = M_{zn}^{-} \sin\alpha_n$. It can be shown that this relationship involves TR and T_1:

$$\frac{ER \sin\alpha_0}{\tan\alpha_{n-1}} + (1 - ER) = \frac{\sin\alpha_0}{\sin\alpha_n} \quad . \qquad [17]$$

The complete derivation is given in Appendix A. The terminal flip angle in this scheme is usually 90°. Of course, constant transverse magnetization after each RF pulse is only possible if the flip angle is less than or equal to 90°, since if the recovery of longitudinal magnetization during TR is *less* than the desired transverse magnetization, even a flip angle of 90° is not enough to provide sufficient M_{xyn}^{+} to satisfy Eq. [16].

Variable flip angles during the FLASH readout are a common implementation for most MRI scanners. As a result, Eq. [10] no longer describes the magnetization response. Rather, the derivation must take each flip angle, α_n, into consideration. The expression becomes more complicated than before, but it can be written concisely if M_{zn}^{+} is expressed instead of M_{zn}^{-} or M_{xyn}^{+}. Therefore, applying Eq. [6] recursively for a unique set of α_n, the result is:

$$M_{zn}^{+} = M_0\left(1-ER\right)\left(\sum_{i=0}^{n-2} ER^i\left(\prod_{j=0}^{i}\cos\alpha_{n-j}\right)\right) + M_{z1}^{-}ER^{n-1}\left(\prod_{k=0}^{n}\cos\alpha_k\right), \qquad [18]$$

which represents the longitudinal magnetization just *after* the n^{th} pulse. To obtain the more familiar M_{zn}^{-}, Eq. [18] can be divided by $\cos\alpha_n$. The complete derivation of Eq. [18] is given in the Appendix B. The corresponding transverse magnetization is related to Eq. [18] by:

$$M_{xyn}^{+} = M_{zn}^{+}\tan\alpha_n . \qquad [19]$$

As an example, the flip angles needed to produce *constant transverse magnetization* was determined iteratively using Eq. [17] and the parameters: TR = 10ms, T_1 = 1000ms, and α_0=12°. The result of the simulation is shown in Figure 3.7a. The simulation produces a unique flip angle, in this case, as long as the number of RF pulses is less than 26. If the pulse train continues beyond 26 pulses, the transverse magnetization will *not* be the same as the previous RF pulses, even if the flip angle is 90° (which rotates 100% of longitudinal magnetization into the transverse plane). The reason there is a limit on the number of pulses is because of the marked saturation of longitudinal magnetization, as shown in Figure 3.7b. This dissolution of M_z is starkly different than the typical transient response seen in Figure 3.2, which attains a steady-state value. Though constant transverse magnetization is produced using this strategy, a steady-state M_z is *not attained*. Zero longitudinal magnetization by the 26th pulse is not troublesome if the experiment concludes following the last pulse; however, if more data is to be collected (as in segmented acquisitions), the user must allow for adequate spin relaxation to take place, so that subsequent acquisitions are consistent with the first.

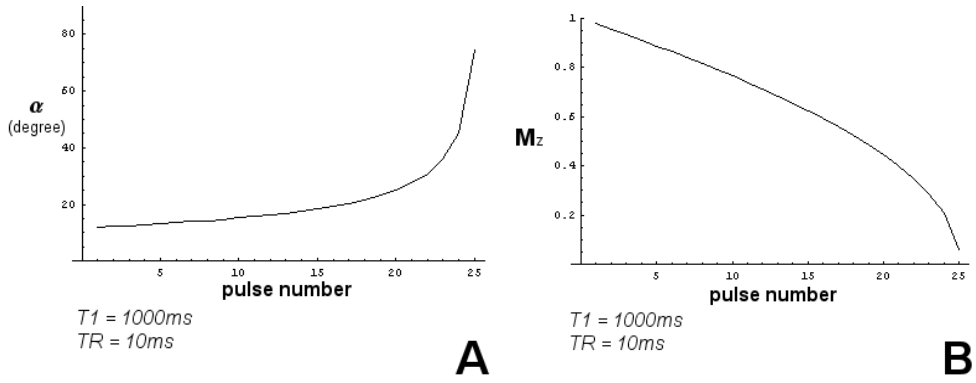

Figure 3.7. a) *The flip angles needed to produce constant M_{xy}, and* ***b)*** *the availability of longitudinal magnetization.*

Analysis of Flip Angles in FLASH Imaging

In order to verify that the MRI system used in this research implements variable flip angle routines to maintain constant transverse magnetization based on the above theory, measurements were made on the pulse amplitudes during a typical FLASH imaging sequence. These measurements were made with the scanner software GraphicalViewer v. 1.0 (Philips Intera, Best, The Netherlands), which enables users to view a detailed graphic of a pulse sequence's time course. Relevant sequence parameters included: TR = 6.4ms, $n = 21$, $\alpha = 20°$, and a *linear* k-space ordering (phase encoding is incremented each TR from $+k_{max}$ to $-k_{max}$, with the center of k-space, $k_y = 0$, occurring at $n / 2$). In addition to the 21 pulses, the default scanner settings installed 5 "dummy pulses" (where RF pulses were executed, but no data was collected) prior to the readout period to bring the magnetization closer to steady-state.

The relative RF amplitude, which was not displayed as pulse angles in the program, was measured and linearly mapped to the flip angle assuming that the maximum measured amplitude was equivalent to the user-defined flip angle (20°). Figure 3.8a is a plot of the flip angle as a function of the RF pulse number, which reveals a

gradual flip angle increase from roughly 0° to 20° (the nominal flip angle). The flip angles thereafter remain at 20°. *This flip angle profile differs from the theoretical profiles described above to maintain constant transverse magnetization*. When M_{zn}^{+} and M_{xyn}^{+} were plotted for this set of flip angles, the magnetizations were *not* constant (Figure 3.8b). It is important to note, however, that the first five pulses are "dummy pulses", used only to bring the magnetization closer to steady-state. Also indicated is where the center of *k*-space is acquired (using linear *k*-space ordering).

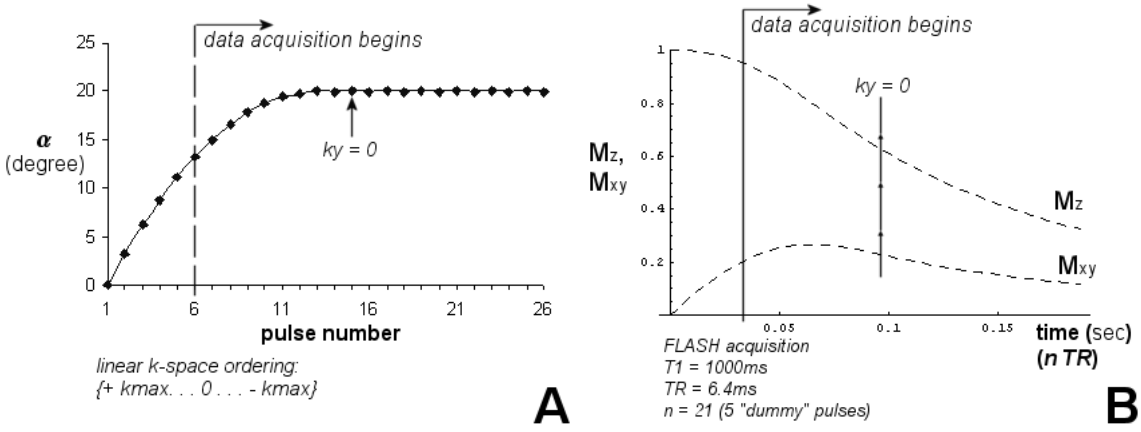

Figure 3.8. a) *Variability of the flip angle in FLASH as measured from the MR console, and* ***b)*** *the resulting magnetization response.*

The *variable flip angle sweep* shown in Figure 3.8a is quadratic in nature. To investigate this relationship, the flip angles during the increase to 20° (first 13 pulses) were mapped to the equation: $\alpha(n) = An^2 + Bn + C$. Using the following constraints: 1) $\alpha(1) = (1-f)\alpha_{\max}$ [the first pulse is some fraction, *f*, of the nominal pulse, $\alpha_{\max}$]; 2) $\alpha'(N) = 0$ [the quadratic function is increasing until pulse *N* and then remains constant];

and 3) $\alpha(N) = \alpha_{\max}$ [the final pulse in the sweep, N, is equivalent to $\alpha_{\max}$], the coefficients A, B and C are:

$$\begin{aligned} A &= -f\alpha/(1-2N+N^2) \\ B &= -2AN \\ C &= \alpha + AN^2 \end{aligned} \qquad [20]$$

where N is the number of pulses it takes (including the "dummy pulses") to reach the nominal flip angle ($\alpha_{\max}$), and f is the fractional reduction of $\alpha_{\max}$ to produce $\alpha(1)$. An f of 1 means $\alpha(1) = 0$. This quadratic expression was directly used to evaluate the set of flip angles in all IR-FLASH delayed enhancement simulations.

The MR software allows user-modification of the flip angle sweep through selection of *initial flip angle* (percent of nominal flip angle), but it does not allow customization of the way the flip angles increase to the nominal value. A constant flip angle sweep is obtained by selecting a value of $f = 0$, which means the *first* flip angle is "0% reduced from the nominal".

Segmentation

The duration of data collection is usually too long to avoid motion artifacts in cardiac MRI. Therefore, *k*-space data is "segmented" into several parts. This means only a small portion of the image data is acquired at a time. Since the cardiac cycle is periodic, each *segment* is acquired during the same phase of the cardiac cycle, so that a stationary "frame" of the heart can be obtained at that time point (Figure 3.9). Each RF pulse within the segment is associated with a specific *k*-space phase encoding step (k_y), which is determined by the *k*-space filling order (a "linear" acquisition is shown in Figure 3.9 where the center RF pulse is associated with $k_y = 0$). The scan time to acquire a static

image of the heart is given as a function of *heartbeats*, rather than TR. As a result, another variable is introduced that affects image contrast, namely *TF*, which is the "*T*ime for *F*ree relaxation" from the end of the current segment to the beginning of the next segment. This value can be expressed in terms of heartbeats, or the *R-wave to R-wave interval* (*RR*), and other known parameters (TR and *n*): $TF = b \cdot RR - (n-1) \cdot TR$, where the integer *b* is included to indicate the number of heartbeats between segments. Since the cardiac cycle is easily determined experimentally, we will designate segmentation interval in terms of *RR* interval and *b*.

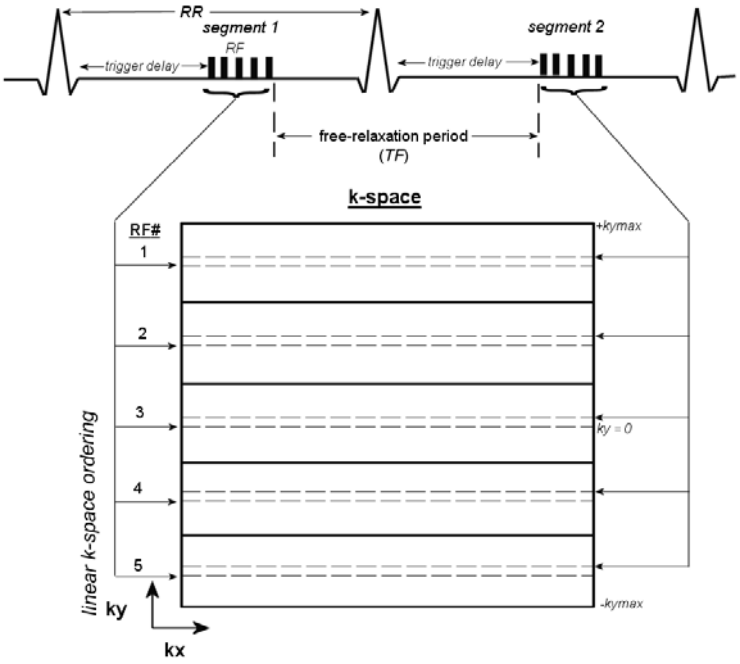

Figure 3.9. *Schematic of the nature of segmented acquisition typically used in cardiac MRI.*

Until now, the magnetization response has been investigated as a function of TR, T_1, and α for an unconstrained number of RF pulses. But in actuality, only a finite

number of RF readout pulses are applied during each segment. Thus, *each segment has a unique* M_{xyn}^{+} *and* M_{zn}^{+} *response, which is a function of the new variable, TF*.

The Effect of Segmentation on Magnetization Response

Segmentation was modeled mathematically by assigning a value for *RR* and defining the number excitations per segment (*n*). The goal was to investigate the difference in M_{xyn}^{+} and M_{zn}^{+} responses as a function of the *segment number* and the value *RR*. Since the magnetization response per segment is still defined by Eqs. [10] and [18] for constant and variable flip angles, respectively, these equations were used in a recursive fashion to determine the magnetization response for *each* segment. The key stipulation in this process was that the initial magnetization, M_{z1}^{-}, prior to first pulse of each segment must be a unique value that is dependent on *RR*. From Eqs. [10] and [18], one can determine this value by first finding the magnetization at the *end* of the readout period (of *n* pulses), and second, finding the amount of "free relaxation" the magnetization experiences until the next segment. As before, this latter process can be modeled with Eq. [1] by replacing *t* with *TF* (which can be determined from *RR* and *b*). Therefore, M_{z1}^{-} just before the beginning of the *next* segment is:

$$ {}_{s+1}M_{z1}^{-} = M_0(1-EF) + {}_{s}M_{zn}^{+} \cdot EF \,, \qquad [21] $$

where the additional subscript, *s*, designates the segment number, and $EF = \exp(-TF/T_1)$.

Simulations of segmented FLASH were performed for myocardium with the following parameters: T_{1myo} = 900ms, *TR* = 7.5ms, *RR* = 850ms, *n* = 26, segments = 8.

Two constant flip angle routines were considered: 20° and 7° (the latter of which is close to Ernst angle for myocardium). The same flip angles were used to simulate variable flip angle sweeps, assuming an $f = 1$ quadratic rise (Eq. [20]) during the first 13 pulses of the segment. Figure 3.10 shows the results for segments 1, 4, and 8 using constant flip angles (a-c), and variable flip angles (d-f). From the plots, there was a significant saturation effect of longitudinal magnetization when $\alpha = 20°$ (solid line) for both constant and variable flips, which resulted in the reduction of the initial magnetization by 40% by the 4th segment (Figure 3.10b and e). The influence on M_{xyn}^{+} was not as great. The transverse magnetization after pulse #16 ($k_y = 0$) was approximately 35% lower during the 4th segment compared to the first. And, similar to M_{zn}^{+}, this trend was observed for both constant and variable flip angle cases. The saturation effect was much less pronounced for $\alpha = 7°$ (dashed line), which caused a reduction in M_{zn}^{+} of only 10% by the 4th segment. The transverse magnetization was nearly unchanged from segment 1 to 4 due to almost complete magnetization relaxation during *RR*. Furthermore, this low flip angle created nearly constant transverse magnetization for the constant flip angle profile, and with an amplitude at $k_y = 0$ similar to variable flip angle case (0.101 and 0.104 of M_0, respectively).

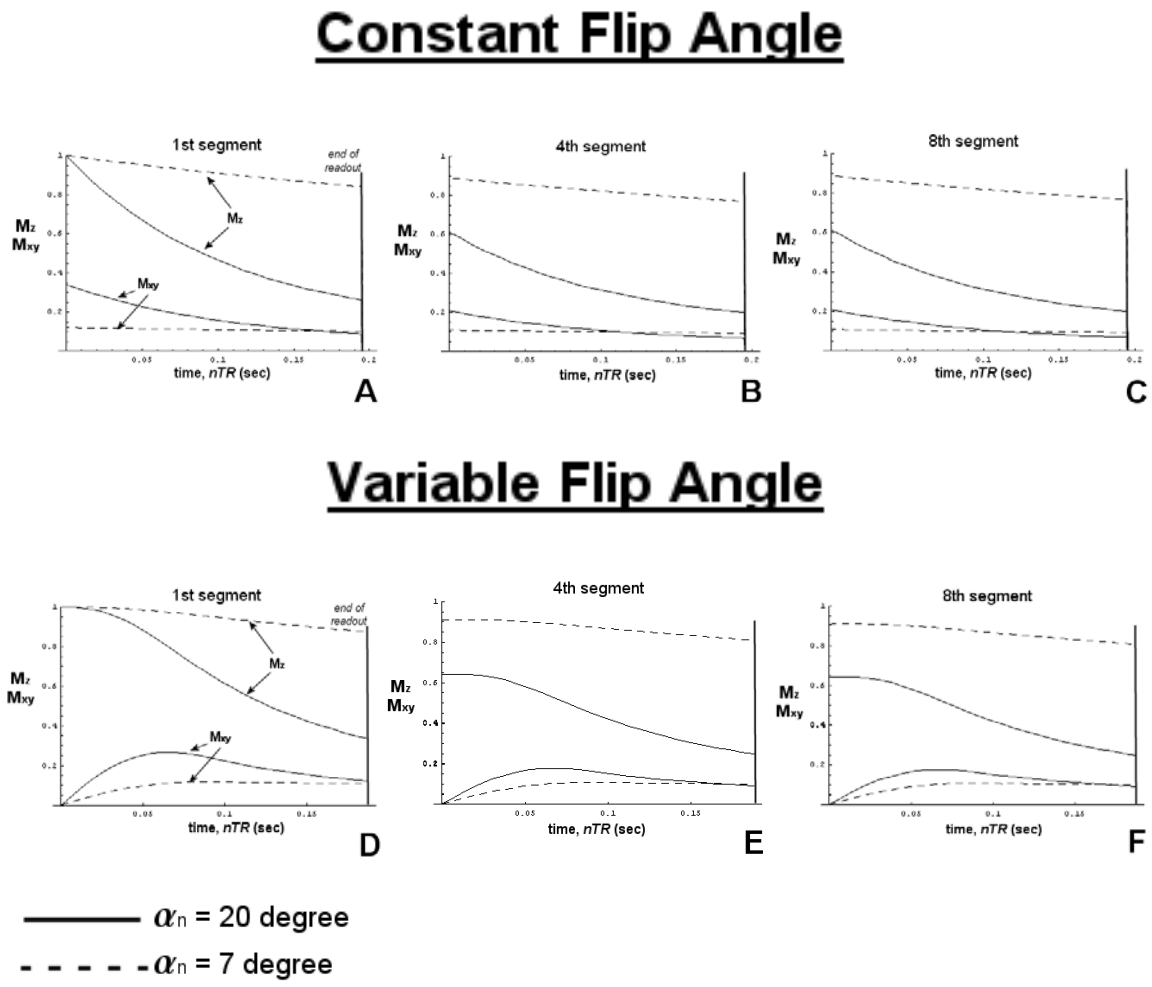

Figure 3.10. *Magnetization response for constant and variable flip angle cases over the data acquisition period, as a function of segment number and flip angle.*

Interestingly, after 8 segments (Figure 3.10c and f), the magnetization *profiles* achieve a "steady-state" of their own, as no difference was observed between the 8th segment and the 4th segment. This effect was similar to the gradual approach to steady state seen earlier for an unconstrained number of pulses (Figure 3.2), but with TR, not *TF*, as the parameter determining steady-state. This is a significant finding for reducing image artifacts due to inconsistent magnetization levels from segment-to-segment. In

practice, one may use the first few segments as preparatory, or "dummy shots", before image data is collected, just the same way "dummy pulses" are used to commence each readout period.

Magnetization-Prepared Segmented FLASH

The complete picture of the delayed enhancement sequence can now be formulated using the theories and equations of the previous sections. The final step is to combine the inversion recovery expression given in Eq. [5] with the segmented FLASH expression developed from Eqs. [10] and [18]. Consequently, the magnetization response of both M_{xyn}^{+} and M_{zn}^{+} can be plotted for a given T_1 value in order to estimate the signal intensity for a particular tissue. A schematic of inversion recovery, segmented FLASH is given in Figure 3.11 (shown for $b = 1$).

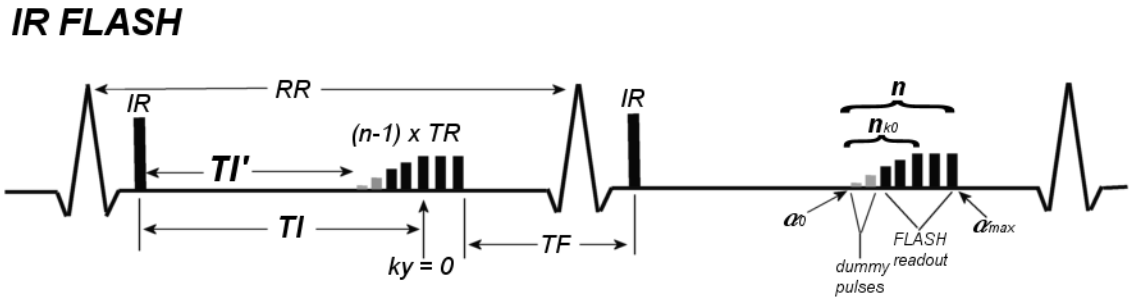

Figure 3.11. *Diagram of segmented IR-FLASH used to model delayed enhancement imaging.*

A few important points must be realized first. The magnetization preparation pulse will cause M_{z1}^{-} to be a function of *TI*. However, since *TI* is the inversion time measured to $k_y = 0$ (which is located near the center of the readout period and is the *k*-space profile associated with the majority of signal and contrast information), an adjustment must be made to define the inversion time to the *first* RF excitation: $TI' = TI - (n_{k0} - 1) \cdot TR$, where n_{k0} is the number of pulses to $k_y = 0$. Also, care must be taken when considering segmentation, since the effective *TF* time will change due to the inclusion of the *TI* time, making $TF = b \cdot RR - TI' - (n-1) \cdot TR$. The outcome is a shorter "free-relaxation period" following a particular readout segment (Figure 3.11). Note also the difference between *n* and n_{k0}: *n* is the number of pulses per segment, while n_{k0} is the number of pulses to $k_y = 0$.

Figure 3.12 shows the first three segments of M_z for a segmented IR-FLASH simulation with the following parameters: T_1 = 330ms (*dashed*) and 1000ms (*solid*), TR = 7.5ms, *n* = 26, α = 15° (constant), *TI′* = 500ms, and *RR* = 850ms (*b* = 1). The IR pulse is assumed to take place at *t* = 0 of each segment. As previously observed, the magnetization profiles achieve a steady-state of their own, depending on the T_1 values of the samples. In Figure 3.12, the 3rd segment is almost exactly the same as the second segment, meaning *a segmental "steady-state" has been achieved.*

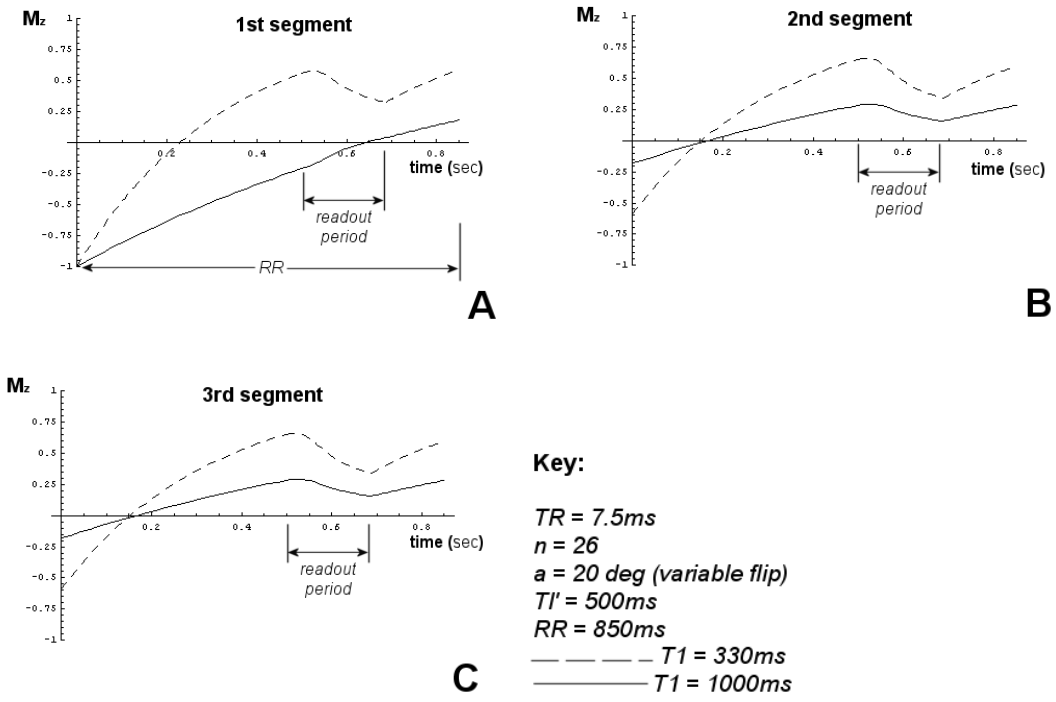

Figure 3.12. *M_z response of segmented IR-FLASH for the first three segments with T_1 of 330ms (dashed) and 1000ms (solid).*

There are some noteworthy consequences of the magnetization between the 1st segment and future segments (the segmental steady-state situation). For slow T_1 (1000ms), an *RR* interval of 850ms is too short for adequate magnetization recovery between segments, as indicated in Figure 3.12a by a magnetization value of 0.18 at the end of the first segment. This caused the *zero-crossing* during the *second* segment to occur much earlier (175ms following the IR), leading to *positive* magnetization during the readout period. This trend perpetuates to future segments until a steady-state zero-crossing is created (*TI* = 275ms at segment #5, not shown). The magnetization response for the fast T_1 (330ms) does not vary greatly in all three segments, owing to the sufficient T_1 recovery from segment-to-segment. A magnetization steady-state is achieved faster for T_1 = 330ms under these conditions.

The practical significance of these trends depends on when the $k_y = 0$ line is collected, *since this phase encode line dictates the majority of signal intensity in MRI*. For *linear* acquisition, the collection of central *k*-space lines occurs in the middle of the readout period (pulse 16, in this case), but question remains as to which *segment* acquires $k_y = 0$. Upon analysis of the segmented FLASH pulse sequence in the GraphicalViewer, the center *k*-space line was found to occur during the *first segment using inversion pulse*, which follows several "dummy" segments preformed to prepare the scan. From the data in Figure 3.12, one would suspect close to zero signal for the T_1=1000ms simulation, since this magnetization crosses zero during the readout in the 1st segment. But this may not be entirely true, since the central *k*-space lines acquired during future segments *do not* produce zero magnetization, and may actually cause a slight signal increase, coupled with blurring and ghosting due these segment-to-segment signal inconsistencies. For this reason, *it is expected that the magnetization profile created after several segments best represents the state of magnetization seen in IR-FLASH images.*

Balanced Steady-State Free Precession (b-SSFP)

Although balanced steady-state free precession imaging (b-SSFP) is not commonly used for delayed enhancement imaging, it is a powerful technique that offers heightened signal-to-noise characteristics. The technique is best known for applications in functional cardiac imaging, where its short TR and high blood-to-myocardium contrast benefit the visualization of ventricular wall dysfunction. An intricate discussion of the utility of b-SSFP is beyond the scope of this thesis; however, the technique is used for some of the T_1 measurement methods in this project, and warrants a descriptive analysis.

Also, its unique contrast characteristics offer potential to delayed enhancement imaging. In this section, the magnetization response of segmented IR b-SSFP is discussed in the context of contrast optimization in delayed enhancement imaging and the calculation of T_1 using limited sample points. This will lead the development of the 2-point T_1 measurement technique used for post-contrast studies.

Signal Evolution and Simulation Assumptions

A sequence diagram of b-SSFP is shown in Figure 3.13. Balanced-SSFP is a steady-state technique in which the *coherence of transverse spins is maintained*. This means the transverse magnetization is *not* spoiled at the end of each TR; rather it is re-used during future TRs, causing the resulting signal to be a function of T_2, in addition to T_1. Also, all *applied* gradient moments are refocused for each TR (the net gradient moment over each TR is zero, Figure 3.13), which explains the use of the term "balanced" in its description. Gradient "balancing" during each TR implies that the only net phase accumulation (β) experienced by the magnetization vector evolves from local B_0 inhomogeneities (δB_0). Since the magnetization is only influenced by these "natural" field perturbations, the spins are said to undergo "free precession" during TR. It has been shown that by alternating the phase of each RF pulse by 180°, the steady-state signal response is maximum in the neighborhood of zero off-resonance frequency ($\beta = 0$, Figure 3.13; note that not all tissues have a flat region of high signal; it is dependent on tissue and relaxation properties) [Haacke 1999]. An RF phase of 180° is equivalent to rotating the magnetization vector by 180° about the z-axis, or alternatively, pulsing at +/- α

degrees along either the x- or y-axis. This oscillating flip angle train allows the use of higher flip angles without the repercussions of significant signal saturation.

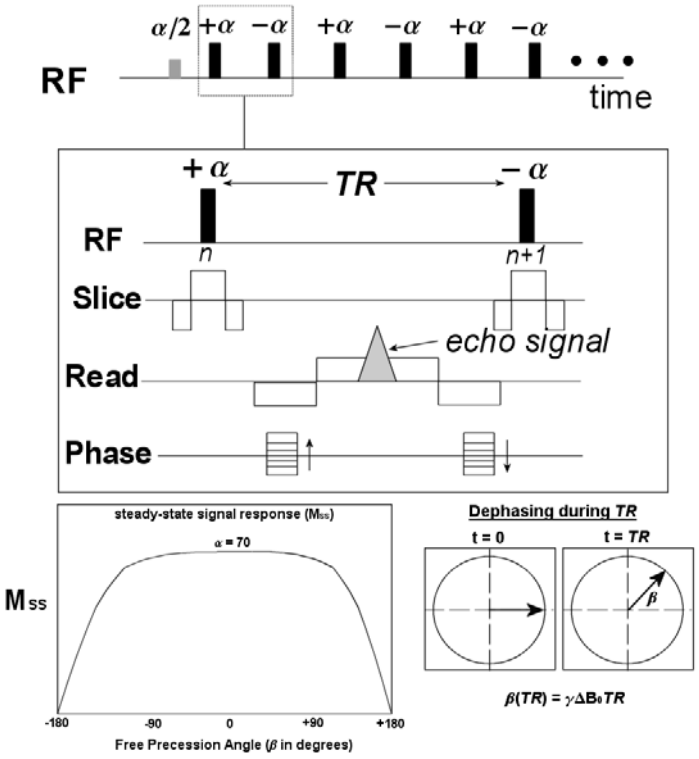

Figure 3.13. *Diagram and signal response of the balanced steady-state free precession (b-SSFP) sequence.*

As with other short-TR gradient echo methods, repetitive RF pulses cause a gradual transition of magnetization vector to a steady-state value. Previous investigators realized that the steady-state magnetization could be achieved quickly and smoothly if the magnetization was prepared prior to the readout [Deimling et al. 1994]. For a series of alternating α-pulses, a preparation of $\alpha/2$ conveniently brings the magnetization closer to steady-state if it is applied TR/2 before the first readout pulse. Other techniques are available, but this is the most common preparation method used to date.

Since the analysis of b-SSFP involves all three magnetization components, M_x, M_y, and M_z, representing its transient phase with matrices is required [Hargreaves et al. 2001]. If the current pulse is indicated by n, the state of the magnetization vector at pulse n+1 due to rotation, precession and relaxation can be described by:

$$\vec{\mathbf{M}}_{n+1} = \mathbf{A}\vec{\mathbf{M}}_n + \vec{\mathbf{B}} \qquad [22]$$

where **A** is a 3x3 matrix and **B** is a 3D vector. The values of **A** and **B** are *constant* for a given experiment, but can be determined as a function of various imaging parameters, depending of the pulse sequence considered. The derivation of **A** and **B** for b-SSFP is given in [Hargreaves et al. 2001]. For simplicity, the off-set frequency, β/TR, will be set to zero, but it should be stressed that the signal intensity is a function of this off-resonant angle (Figure 3.13). Since the magnetization is prepared with a $\alpha/2$ pulse prior to the first alternating RF pulse, $\vec{\mathbf{M}}_0$ must be determined first. From the discussions of FLASH, this is also dependent on the amount of magnetization *prior* to the $\alpha/2$ pulse itself, which can be a function of inversion recovery decay and the *RR* interval time. Therefore, the first vector state of **M** is:

$$\vec{\mathbf{M}}_0 = \begin{pmatrix} 0 \\ M_{z0}^{-}\sin(\alpha/2) \\ M_{z0}^{-}\cos(\alpha/2) \end{pmatrix} \qquad [23]$$

where M_{z0}^{-} is the amount of longitudinal magnetization just prior to the $\alpha/2$ pulse. With rotation assumed around the x-axis, the x-component of **M** is always zero if the free-precession angle over TR is assumed to be zero. Though achieving zero precession is virtually impossible due to local field homogeneities, the effect can be reduced by keeping TR short. In this treatment, TR was assumed to be 5ms.

From the initial condition of Eq. [23], the recursive formula of Eq. [22] yields the transient response magnetization vector as a function of n. As with the FLASH analysis, the simulation may include the effects of segmentation and M_z preparation, but the only consequence of these options is the subsequent modification of M_{z0}^{-} in Eq. [22].

Comparison of IR b-SSFP with IR-FLASH

Magnetization-prepared b-SSFP can be compared with IR-FLASH. Figure 3.14 shows the magnetization time course of post-contrast infarct and normal myocardium T_1 (200 and 400ms, respectively; T_2 assumed to be 40ms) using both IR b-SSFP and IR-FLASH (1st segment). A greater saturation effect is visible for IR-FLASH during the readout period, which lowers the signal at 16th pulse ($k_y = 0$) for normal myocardium by 31%. Although it has been shown that this is ameliorated by variable flip angle sweeps, it still is not comparable to the apparent T_1 recovery of IR b-SSFP, which is dampened only slightly by the train of RF pulses. *The ability for b-SSFP to be relatively insensitive to T_1 recovery in inversion recovery experiments is the most significant difference between IR b-SSFP and IR-FLASH.*

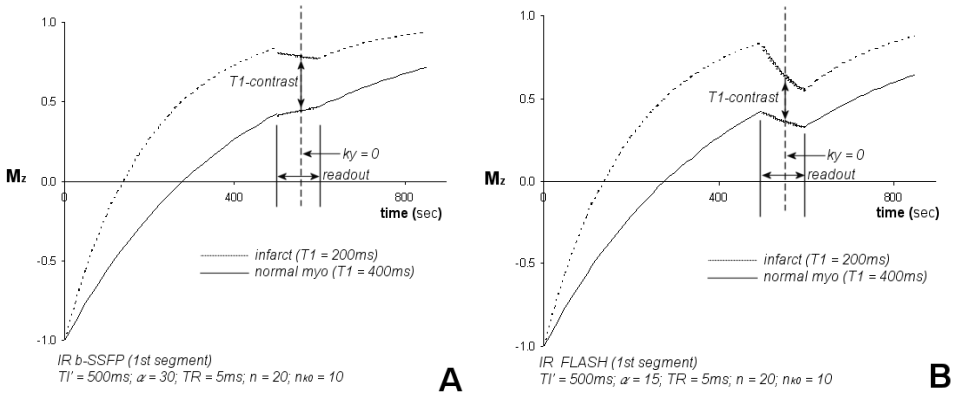

Figure 3.14. *Comparison of the M_z response of **a)** IR b-SSFP and **b)** IR-FLASH for T_1 = 200ms (dashed) and 400ms (solid).*

T_1 Contrast Simulations

This section details the theoretical contrast magnetization response of IR-FLASH and IR b-SSFP. The goal of this simulation is to determine the "$T_{1contrast}$" of the delayed enhancement sequence in order to optimize the imaging parameters, particularly *TI* and α. The term $T_{1contrast}$ is used to distinguish signal contrast estimations using mathematical models from true contrast-to-noise measurements taken *in vivo* (Chapter 6 and 7). Two inversion times will be distinguished: TI_{opt}, the inversion times that produces the maximum $T_{1contrast}$; and TI_{null}, the inversion time that suppresses "normal myocardium" T_1. IR-FLASH simulations require assumptions of infarct and normal myocardium T_1 values, while IR b-SSFP requires T_1 and T_2 information. A general overview of the simulation methodology is given first, followed by results from the two imaging scenarios.

Methodology Overview

Using the theories developed, contrast between two T_1s in segmented IR-FLASH and b-SSFP can be determined as a function of *TI*, *RR*, TR and α for given T_1 and T_2 values, and subsequently, these parameters can be optimized for use experimentally. The simulations presented here will consider tissue contrast using an *absolute difference relationship* of corresponding *transverse* magnetizations:

$$T_{1\text{contrast}} = Abs\begin{pmatrix} M_{xy}\left(seg, TR, TI', RR, \alpha, n, n_{k0}, T_{1a}, T_{2a}, M_{0a}\right) \\ -M_{xy}\left(seg, TR, TI', RR, \alpha, n, n_{k0}, T_{1b}, T_{2b}, M_{0b}\right) \end{pmatrix}. \qquad [24]$$

The *difference in signal responses* was considered rather than a ratio to avoid asymptotes that would be created when $M_{xy} \to 0$. Ratios would not provide distinction between TI_{opt}

and TI_{null} since the optimal TI would always coincide with TI_{null}, making the analysis trivial. The absolute value in Eq. [24] ensures that the difference is always positive (as in magnitude images). The tissue parameters $T_{1a,b}$, $T_{2a,b}$ and $M_{0a,b}$ are the only differences between the two M_{xy} expressions, while TR, TI, RR, α, n, n_{k0}, and seg (segments) are known parameters. To provide a consistent standard of comparison, *the $T_{1contrast}$ in all simulations was determined at n_{k0}, which is number of pulses until the $k_y = 0$ line.* The following constraints were applied to both sequences: $TR < 7.5$ms, $n > 16$ (with 5 "dummy pulses" for IR-FLASH), linear acquisition (FLASH: $n_{k0} = \left(\left(n+5\right)/2\right)+5$; b-SSFP: $n_{k0} = n/2$), and two segment interval scenarios using $RR = 850$ms ("1 heartbeat interval", $b = 1$) and 1700ms ("2 heartbeat interval", $b = 2$). Additionally, seg was varied from 1 to 6, and the subsequent change in $T_{1contrast}$ at n_{k0} was noted. Since several segment repetitions are needed to establish a steady-state response, the $T_{1contrast}$ at $seg = 6$ was assumed to represent the final $T_{1contrast}$ of the imaging sequence. Further sequence-specific methodology is discussed below.

Segmented IR-FLASH

IR-FLASH contrast simulations were performed in Mathematica 5.0 software by building functions of the variable flip angle equations discussed earlier (Eq. [18]). Since there is an ensemble of relationships between parameters in IR-FLASH, there is reason to initially assume values for some variables, such as the number of lines/segment, n, before determining the parameters that produce the maximum contrast. Therefore, initially, $n = 16$ (including 5 "dummy" pulses), which is the limit assigned to keep breath hold scan time reasonably short (< 18 heartbeats). The IR-FLASH description requires knowledge

of T_1 and M_0 of infarct tissue and remote (or "normal") myocardium post-contrast at both 1.5T and 3T. Note that the T_1 of infarct and normal myocardium are known to change with time post-contrast injection, so that solutions generated for one particular scenario may not be robust solutions for all T_1 combinations. Therefore, simulations were performed assuming $T_{1inf} = 0.25T_{1myo}$, $0.50T_{1myo}$, and $0.75T_{1myo}$ to assess the T_1 dependency of IR-FLASH. Since TE was assumed short, and transverse magnetization is spoiled, T_2 effects were not considered in IR-FLASH. M_0 was initially set to unity.

Segmented IR b-SSFP

Matrix simulations of IR b-SSFP were performed in Matlab 6.5 software to determine the optimal flip angle and *TI*. The same T_1 values for infarct and normal myocardium were assumed to assess T_1 dependency ($T_{1inf} = 0.25T_{1myo}$, $0.5T_{1myo}$, and $0.75T_{1myo}$). However, as seen in Eq. [23] and elsewhere [Hargreaves et al. 2001], there is also a T_2 dependency on the b-SSFP signal. The T_2 of myocardium is approximately 50ms at 1.5T [Walker et al. 1993], which is expected to decrease after the administration of contrast agent, but not as significantly as T_1. For these simulations, T_2 was related to T_1 by the assumption: $1/T_2 = 1/T_{2pre} + (1/T_{1m} - 1/T_{1pre})$, where $T_{2pre} = 0.05s$, $T_{1pre} = 1.0s$, and T_{1m} was the T_1 assigned to either normal myocardium or infarct tissue. This simplistic contrast agent equation assumes the r_2 relaxivity of the contrast agent is equivalent to r_1 relaxivity. In determining the optimal *TI*, the accuracy of the T_2 values is not as important as the T_1 if $T_2 << T_1$, as in myocardium.

Relationships between imaging parameters were performed analogous to IR-FLASH to determine specific parameter sets that produced high $T_{1contrast}$. Particularly, TR

was constrained to be less than 5ms (since b-SSFP is sensitive to off-resonance), RF phase = 180° (alternating RF pulses), and one "dummy" preparation pulse was used to bring magnetization closer to steady-state, namely $\alpha/2$ (see IR b-SSFP theory). With these simulations, IR b-SSFP was compared to IR-FLASH in terms of $T_{1contrast}$, TI_{opt}, α_{opt}, and TI_{null}.

Simulation Results and Discussion

Optimal results from these simulations were determined from 2D-, or 3D-plots using various parameter settings. Since absolute value equations for $T_{1contrast}$ were used, the plots of IR-FLASH and IR b-SSFP contained distinctive features. Particularly, there existed a point of "zero-contrast" for the selected T_1 values that occurred at the inversion time (TI_{zero}) when both T_1 values resulted in the *same transverse magnetization values (hence, the difference is zero)*. It is noteworthy that if the *sign* of the magnetization is conserved, a point of zero-contrast will not exist, and the $T_{1contrast}$ will become continuous for all *TI*.

Segmented IR-FLASH

Distinction between Optimal and Null-Point TI

The $T_{1contrast}$ between two T_1 values with IR-FLASH produced two critical points of interest: optimal *TI* (TI_{opt}) and the null-point *TI* (TI_{null}). Figure 3.15 shows examples of the distinction between these two points-of-interest, using T_{1inf} = 200ms and T_{1myo} = 400ms. The *solid line* in Figure 3.15 represents the $T_{1contrast}$ (signal difference) between "infarct" and "normal myocardium", while the *dashed line* is the "normal myocardium"

transverse magnetization (T_1 = 400ms). In Figure 3.15a, normal myocardium T_1 passes through a null-point at TI'_{null} = 221ms (TI_{null} = 271ms). The optimal *TI* (obtained from the maximum of the *solid curve*), however, is TI'_{opt} = 228ms (TI_{opt} = 278ms). Therefore, it is evident that $TI_{opt} \neq TI_{null}$. Although it may seem that the difference is negligible (in addition to the corresponding $T_{1contrast}$ being essentially equivalent), another example, Figure 3.15b, shows a starkly different result: TI_{opt} = 289ms and TI_{null} = 216ms, with modifications to α, *RR*, *n* (and n_{k0}). However, the $T_{1contrast}$ in Figure 3.15b corresponding to TI_{null} and TI_{opt} remained essentially equivalent to one another (0.082 and 0.086, respectively). This suggests that even though certain parameter settings (α, TR, *RR*, *n*, n_{k0}) indelibly changes the maximum attainable $T_{1contrast}$ *and* the difference between TI_{opt} and TI_{null}, the relative difference in $T_{1contrast}$ between these two *TI*s of interest remains essentially the same (within 10%).

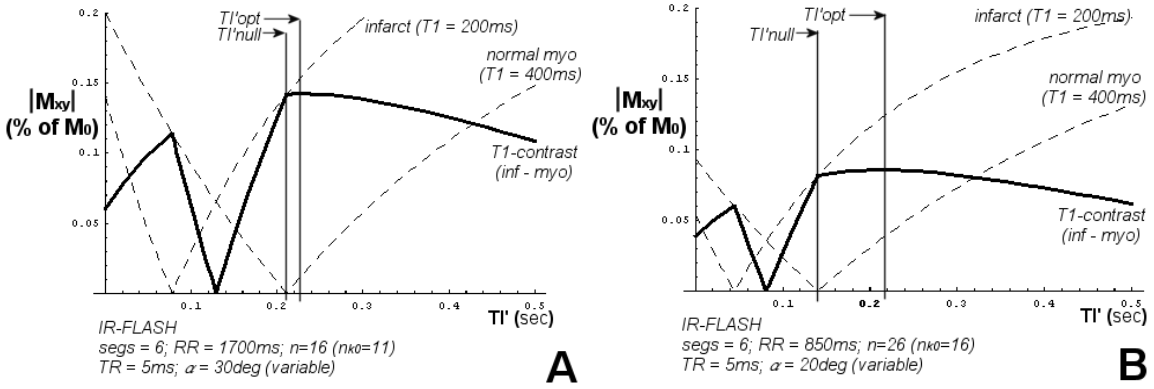

Figure 3.15. *Definition of important parameters in segmented IR-FLASH simulation results for a) 1-heartbeat interval and b) 2-heartbeat interval.*

Segment Number Dependency

The contrast profiles of Figure 3.15 were computed for *seg* = 6; but there was a degree of profile variation from the 1st segment to future segments. This variation in the $T_{1contrast}$ profile was primarily dependent on the duration of the *RR* interval and the amount of magnetization saturation during the IR-FLASH readout. The 1st segment and the 6th segment are shown in Figure 3.16 for the same parameters as Figure 3.15. As seen, when the *RR* interval is long and the readout duration is short (Figure 3.16a), the $T_{1contrast}$ profile changes only subtly between the 1st and 6th segment, maintaining the similarity between TI_{opt} and TI_{null} solutions. However, when the *RR* interval is short and the duration to n_{k0} is long (Figure 3.16b), the $T_{1contrast}$ profile during the 1st segment is significantly larger than the 6th segment. Moreover, value of TI_{opt} and TI_{null} increases relative to the 1st segment. Note also the decrease in maximum $T_{1contrast}$ as a function of segment number in Figure 3.16b. This trend is directly related to length of the readout period (which is related to magnetization saturation) and the duration between inversion pulses, or "free relaxation period". Variation in $T_{1contrast}$ profiles among imaging segments may cause image blurring.

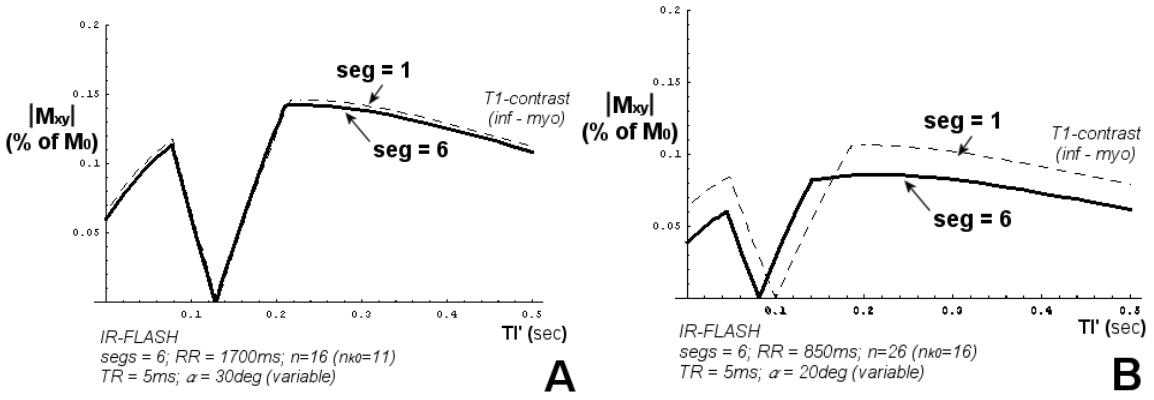

Figure 3.16. *Difference in $T_{1contrast}$ profiles for seg = 1 and 6 using* ***a)*** *2-heartbeat intervals and* ***b)*** *1-heartbeat intervals.*

Relationship between Flip Angle and Lines per Segment

Prescribing $n = 16$ for Figure 3.15a allowed a larger flip angle ($\alpha = 30°$) to be used without compromising $T_{1contrast}$. As n was increased to 26 (Figure 3.15b), a lower flip angle of $\alpha = 20°$ seemed detrimental to $T_{1contrast}$. Since a reduction in $T_{1contrast}$ is also attributable to the *RR* interval, the optimal flip angle was determined as a function of n for both *RR* interval cases (*RR* = 850ms and *RR* = 1700ms), using TI_{opt}, TR and the T_1 values used earlier. It was found that the optimal flip angle (α_{opt}) was virtually *insensitive* to *RR*. The trend of α_{opt} as a function of n is shown in Figure 3.17a. It is apparent that the optimal flip angle in IR-FLASH decreases as the number of lines per segment increases. This follows from the realization that as the duration of the readout period increases, the greater the potential for magnetization saturation, even with a variable flip angle sweep installed. Figure 3.17b shows the corresponding maximum $T_{1contrast}$ as a function of n. The largest $T_{1contrast}$ in this scenario was obtained using the shortest possible n ($n = 16$), and the longest *RR* (2-beat interval, *RR* = 1700ms). Under these circumstances, $\alpha_{opt} = 28°$, $TI_{opt} = 279$ms, $TI_{null} = 212$ms, and $T_{1contrast} = 0.142\ M_0$.

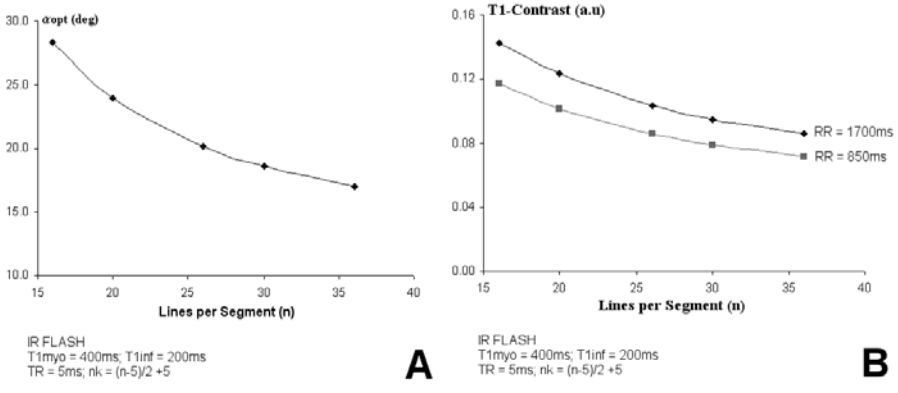

Figure 3.17. a) *Variation of the optimal flip angle with lines per segment and* ***b)*** *the corresponding $T_{1contrast}$ produced for 1- and 2-heartbeat intervals*

Modulation of TI_{null} with Flip Angle

It has been shown that even though $TI_{opt} \neq TI_{null}$, the resulting $T_{1contrast}$ is essentially equivalent (Figure 3.15). By definition, there exists only *one set* of α_{opt} and TI_{opt} that yields the maximum $T_{1contrast}$, for a given set of parameters and T_1 values. Conversely, TI_{null} simply defines the inversion time needed to suppress a prescribed T_1 value (normal myocardium) and is "blind" to the magnetization state of the other T_1 value (infarct tissue, in this case). Hence, TI_{null} can vary in a given experiment if the user decides to increase or decrease the flip angle. Using n =16 and TR = 5ms, Figure 3.18 shows the relationship between TI_{null} and flip angle for three T_1 values expected to represent normal myocardium post-contrast. As shown, there is only minor dependency of TI_{null} on α, even though the curves exhibit a slight decrease with increasing flip angle. In all cases, TI_{null} decreased approximately 22ms by changing the flip angle from 10 to 40°. For larger values of n, the curves exhibit a more noticeable decrease (not shown). A more relevant result occurred when changing the experiment from 1-beat segment intervals to 2-beat intervals (Figure 3.18b to 3.18a). As seen, TI_{null} became longer as a result of this transition, and was dependent on the T_1 value of interest. For the T_1 values shown, TI_{null} increased by 3ms (2.2%), 39ms (17.7%), and 96ms (34.8%) for T_1 = 200, 400, and 600ms, respectively.

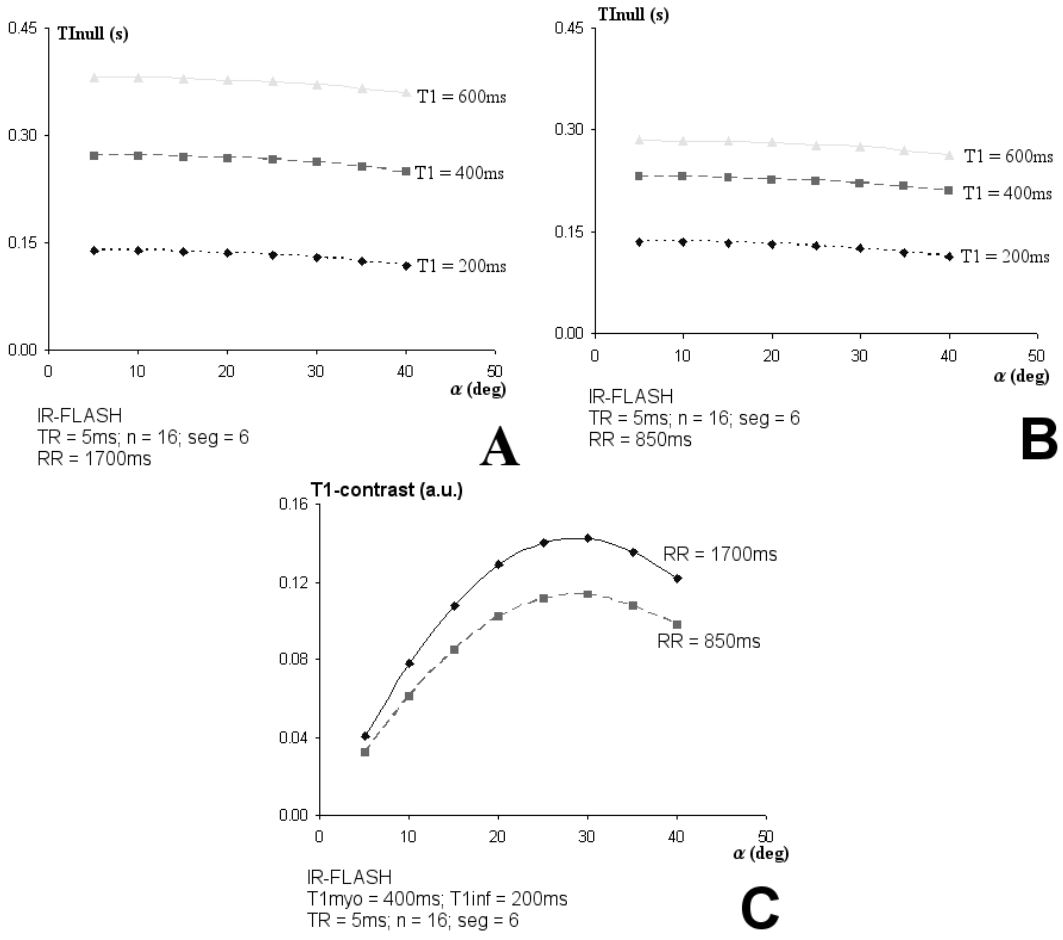

Figure 3.18. a-b) *Dependency of TI_{null} on user-defined flip angle for given T_1; and* ***c)*** *corresponding $T_{1contrast}$ using T_{1myo} = 400ms and T_{1inf} = 200ms.*

A value for $T_{1contrast}$ can be determined using TI_{null} if another T_1 value (infarct tissue) is defined. Using an infarct T_1 = 200ms, $T_{1contrast}$ is maximum at approximately the same flip angle found to maximize TI_{opt} ($\alpha_{opt} \approx 28°$) (Figure 3.18c). In other words, α_{opt} can be used with either TI_{opt} or TI_{null} to garner maximum $T_{1contrast}$ in a given experiment.

TR Dependency

Thus far, a TR of 5ms has been assumed for all parameter relationships, which falls within the short-TR, cardiac MR requirements. However, it is worth relating TR to α_{opt}, TI_{opt}, TI_{null}, and maximum $T_{1contrast}$. Specific results using different TRs are given in Table 3.1 assuming T_{1myo} = 400ms and T_{1inf} = 200ms. The number of lines per segment, n, was chosen as 16 since this value produced high $T_{1contrast}$ at n_{k0} (see Figure 3.17). As seen, the gain in $T_{1contrast}$ with longer TR is essentially negligible (~4%), especially for the chosen scenario (low n and n_{k0}), suggesting that a decrease in TR (to reduce the acquisition window) results in minor effects on $T_{1contrast}$, if TI_{opt} or TI_{null} is applied.

Table 3.1. Relationship of TR and $T_{1contrast}$ for selected IR-FLASH parameters[a].

	TR (ms)	n / n_{k0}	α_{opt} (°)	TI_{opt} (ms)	$T_{1contrast}$[b]
1-bt	2.5	16/11	27.6	290 (228)	0.115 (0.110)
	5.0	16/11	28.4	289 (223)	0.118 (0.113)
	7.5	16/11	29.2	288 (218)	0.120 (0.115)
2-bt	2.5	16/11	27.7	279 (267)	0.140 (0.140)
	5.0	16/11	28.4	279 (262)	0.143 (0.142)
	7.5	16/11	29.0	279 (257)	0.146 (0.145)

[a] TI_{null} results given in parentheses. [b] maximum T_1-contrast evaluated for T_{1myo} = 400, T_{1inf} = 200ms, expressed as % of M_0.

T_1 Dependency

The simulated $T_{1contrast}$ results are ultimately dependent on the T_1 values for normal myocardium and infarct tissue. Until now, assumptions were made for these values to elucidate the relationships among other user-defined parameters. It is obvious that the physiologic T_1 values that determine image contrast are beyond the user's control. As such, this final analysis deals with the effect of T_1 values, in a general sense, on the *maximum* $T_{1contrast}$ in IR-FLASH. In addition, it is important to reveal the dependency of TI_{opt} and TI_{null} on various combinations of normal myocardium and infarct T_1 values.

As a first glimpse into the T_1 dependency of critical parameters such as α_{opt}, TI_{opt}, and TI_{null}, consider the hypothetical situation where T_1 increases by 25% from 1.5T to 3T (actual measured values will be discussed in Chapter 6 and 7). Hence, if we assume post-contrast 1.5T T_1 values of 400 and 200ms for normal myocardium and infarct tissue, respectively, the 3T values will become 500 and 250ms. Under these circumstances, the results of the previous sub-sections can be applied to determine the *change* in maximum $T_{1contrast}$ (using α_{opt} and TI_{opt}) and TI_{null} as one goes from 1.5T to 3T field strengths. For this simulation, n/n_{k0} = 16/11, TR = 5ms, RR = 1700ms, seg = 6, and M_0 = 1.

The results were displayed as 3D contour plots (Figure 3.19), with α and TI' being the independent variables. Maximum $T_{1contrast}$ from the 3D contour plot was determined from the *maximum value* in Figure 3.19a ("1.5T") and Figure 3.19c ("3T"), while TI_{null} was determined from the *minimum value* in Figure 3.19b ("1.5T") and Figure 3.19d ("3T") using a flip angle of α_{opt}. Notice the dark, band-like region of "zero-

contrast" at TI_{zero} (the inversion time that produces $T_{1contrast} = 0$) in Figures 3.19a-c, which occurs due to the use of *modulus images*.

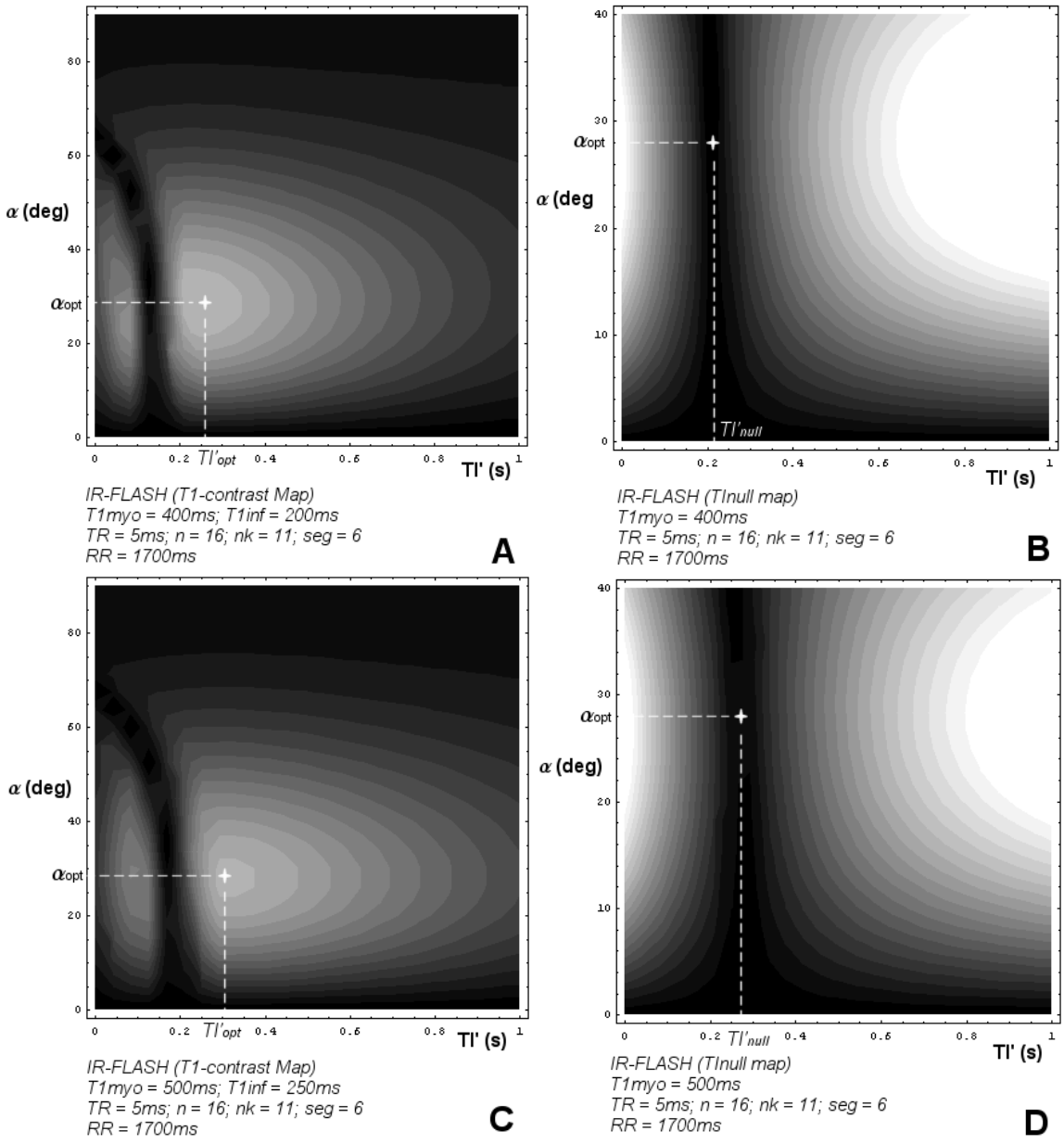

Figure 3.19. *3D contour maps showing $T_{1contrast}$ at* ***a-b)*** *1.5T and* ***c-d)*** *3T for the parameters shown. TI_{null} exists for every α, but markings are shown for α_{opt}.*

The differences are subtle, but the maximum $T_{1contrast}$ decreased in the 3T case (Figures 3.19c) by 5% relative to the 1.5T case (Figures 3.19a). This was also dependent

on the assumed imaging parameters (TR, *n*, *RR*, etc.). Also note a *broad region of relatively high* $T_{1contrast}$ around TI_{opt} and α_{opt} in Figure 3.19. This suggests that there may be some 'leeway' in *TI* selection in delayed enhancement imaging. But it must also be asserted that only *one* inversion time (TI_{null}) results in a suppressed normal myocardium signal. If this broad span of *TI* in Figure 3.19 can somehow be adapted to null normal myocardium signal (like TI_{null}), then delayed enhancement imaging will be able to benefit from *TI*-insensitivity (since there will leeway in *TI* selection) *and* high $T_{1contrast}$.

From this simple example, the difference in maximum $T_{1contrast}$ was primarily dependent on the relationship between infarct and normal myocardium T_1 values. To extend the analysis, Figure 3.20 shows the maximum $T_{1contrast}$ for three infarct/normal myocardium T_1 relationships: $T_{1inf} = 0.25T_{1myo}$, $0.5T_{1myo}$, and $0.75T_{1myo}$. T_{1myo} was assumed to span 200ms to 800ms, which is the expected T_1 range seen post-contrast at 1.5T [Klein et al 2004] (for the time being, 3T T_1 values can be assumed to be in this range as well). By determining the maximum value in 3D plots like Figure 3.19, it was found that the optimal flip angle (α_{opt}) ranged between 26 and 30°, which reflected the optimal flip angle's insensitivity to T_1 and the *RR* interval. From Figure 3.20a (*RR* = 1700ms), the plots of TI_{null} and TI_{opt} overlap, which implies that the maximum $T_{1contrast}$ among all three infarct-to-normal myocardium T_1 scenarios was *equivalent* regardless of whether TI_{opt} or TI_{null} was used in the simulation. This result occurred despite the dissimilarity between the actual TI_{opt} and TI_{null} values (except for $T_{1inf} = 0.25T_{1myo}$), as shown in Figure 3.20c. For shorter segment interval times (*RR* = 850ms), $T_{1contrast}$ was *lower* using TI_{null} compared to simulations with TI_{opt} (Figure 3.20b). The difference in $T_{1contrast}$ in this case was most likely due to the large difference between TI_{opt} and TI_{null}

(Figure 3.20d), suggesting the difference between these two inversion times eventually leads to large changes in $T_{1contrast}$. One of the most important differences between TI_{opt} and TI_{null} is their proximity to TI_{zero}, which is the *TI* that produces $T_{1contrast} = 0$. The null-point inversion time was consistently found to be relatively close to the TI_{zero} compared to TI_{opt}, such that slight reductions in TI_{null} would result in equivalent signal intensity for normal myocardium and infarct tissue, since *modulus images* do not distinguish between positive and negative signal.

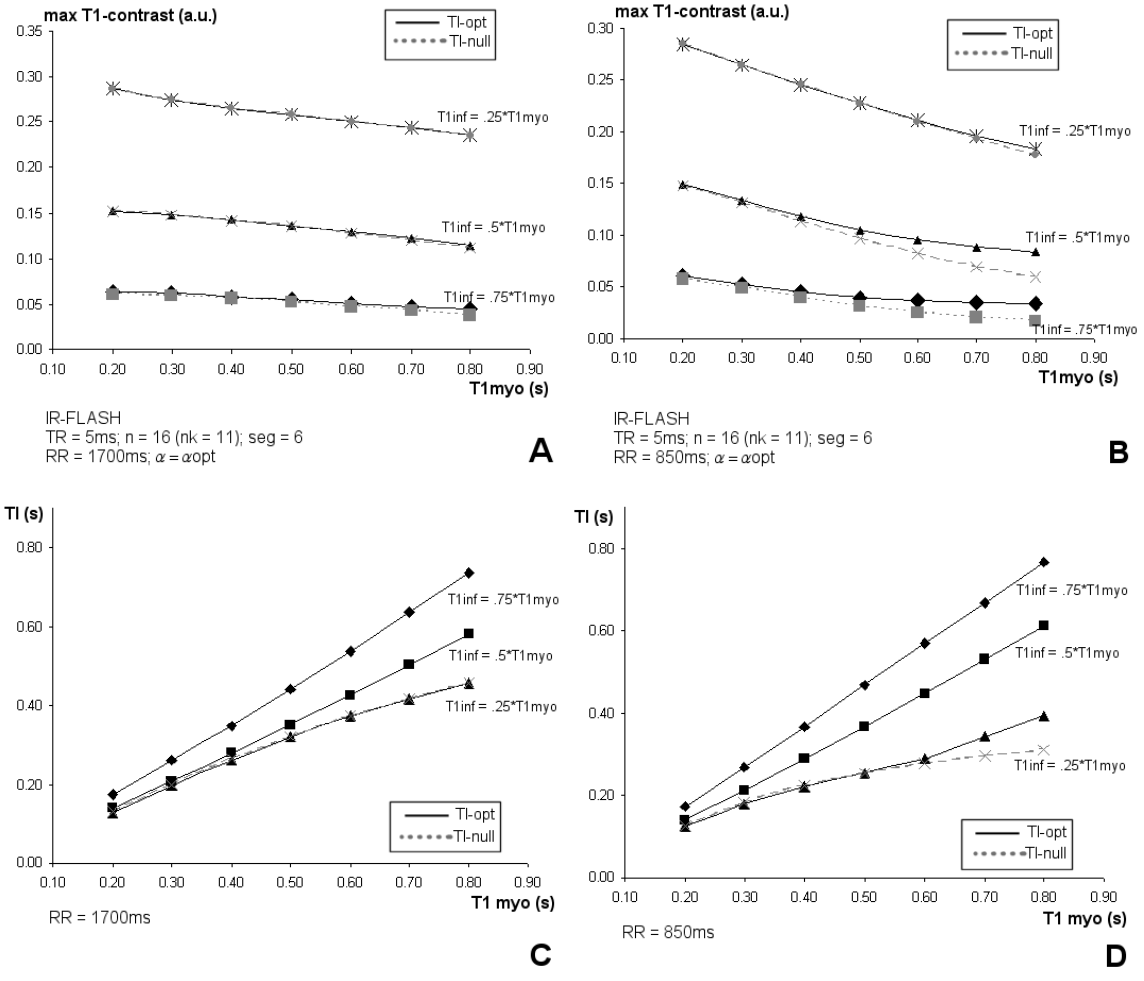

Figure 3.20. *The maximum $T_{1contrast}$ as a function of T_{1myo} and T_{1inf} using TI_{opt} and TI_{null} with* ***a)*** *RR = 1700ms and* ***b)*** *RR = 850ms. The change in TI with T_1 is shown in* ***c)*** *and* ***d)****.*

The largest $T_{1contrast}$ was obtained for the case when $T_{1inf} = 0.25T_{1myo}$ (Figures 3.20a-b). Therefore, *smaller T_1 ratios between infarct and normal myocardium (T_{1inf}/T_{1myo}) lead to greater $T_{1contrast}$*. In practice, the T_{1inf}/T_{1myo} ratio is beyond the user's control, and is dependent entirely on contrast agent kinetics and tissue properties. In Chapter 7, values of T_{1myo} and T_{1inf} will be measured at 1.5T and 3T in patients.

Equilibrium Magnetization (M_0)

The simulations to this point have only considered $M_0 = 1$, since this was a convenient normalization strategy for describing the parameter relationships above. However, even if one assumes $M_0 = 1$ for all tissues at 1.5T, one can not assume that the same is true as one increases the field strength, since the equilibrium magnetization is related to the observed proton sensitivity and, hence, intrinsic signal-to-noise ratio, which is known to increase at high filed strengths [Wen 1997]. Therefore, there must be a relationship describing M_0 between 1.5T and 3T. Theoretically, the sensitivity of an MR experiment is proportional to its field strength (the details of which are introduced in Chapter 5). Precise estimations of the ratio of M_0 between 3T and 1.5T will be quantified experimentally later (Chapter 4 and 5).

The influence of M_0 on $T_{1contrast}$ is instructive. For the parameters shown in Figure 3.19, the M_0-ratio between 3T and 1.5T was varied from 1.0 to 2.5. The increase in maximum $T_{1contrast}$ with M_0 is depicted in Figure 3.21 for two T_1 scenarios. As seen, the effective $T_{1contrast}$ increase is linear, such that a doubling of M_0 at 3T resulted in a doubling of $T_{1contrast}$. These theoretical results are expected to *overestimate* imaging results, since noise and field homogeneity effects were not considered.

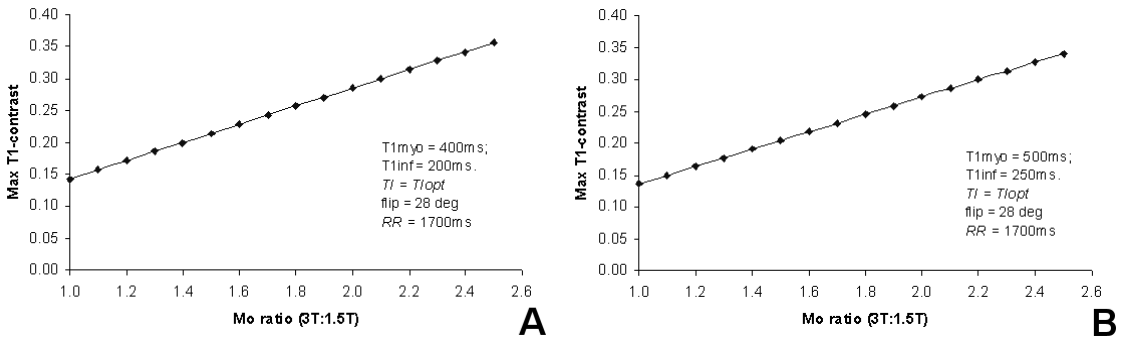

Figure 3.21. *Increase in maximum $T_{1contrast}$ as a function of relative M_0 increase at 3T for* ***a)*** *low T_1 and* ***b)*** *high T_1.*

Segmented IR b-SSFP

The 3D contour plots of segmented IR b-SSFP were similar in appearance to segmented IR-FLASH, as shown in Figure 3.22. A dark band of zero contrast (at TI_{zero}) still existed at particular *TI*s. However, this area of zero-contrast was more vertical in nature, meaning that a specific range of *TI*s resulted in zero-contrast, regardless of the flip angle used. This is because there is less magnetization saturation in IR b-SSFP for a broad range of flip angles. When the optimal flip angle and inversion time was determined from the contour plot, it was found that TI_{opt} was similar to the IR-FLASH results.

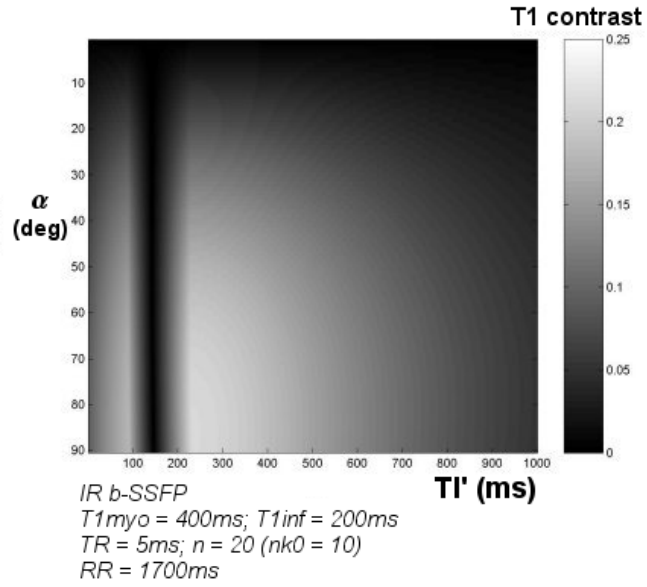

Figure 3.22. *3D contour plot of segmented IR b-SSFP for the evaluation of TI_{opt}, α_{opt} and maximum $T_{1contrast}$.*

Parameter Comparison with IR-FLASH

The parameter relationships discussed for IR-FLASH can be extended to IR b-SSFP. Particularly, high $T_{1contrast}$ was obtained when n (and n_{k0}) was small, but the choice of n was not as important in IR b-SSFP, since it was found that the $T_{1contrast}$ decreased only 15% between n = 10 and 36, compared to 40% for IR-FLASH (2-heartbeat intervals). Since b-SSFP also requires very short TR (to limit off-resonance dephasing), the duration of the data acquisition window can be much shorter than IR-FLASH using similar values of n. The ultimate choice of TR and n is dependent on available scan time and the user's choice of segment interval time (usually 2 heart beats per segment).

The reduction in maximum $T_{1contrast}$ from the 1st to 6th segment in IR b-SSFP, assuming T_{1myo} = 400ms, T_{1inf} = 200ms, TR = 4ms, α = 50°, and n = 20 (n_{k0} = 10), was 0.5% compared to 2.6% in IR-FLASH. As *RR* was reduced to 1-heartbeat intervals, this

reduction increased to 3.7%, which was still less than IR-FLASH (18.9%), meaning that there may be less segment-to-segment $T_{1contrast}$ variation with IR b-SSFP, and less potential for image blurring artifacts.

Optimal Flip Angle

As mentioned, IR b-SSFP affords the use of higher flip angles than IR-FLASH. From 3D contour plots such as Figure 3.22, it was found that the optimal flip angle was generally greater than 80°. Despite higher optimal flip angles for b-SSFP, the practical implementation of these high B_{1trans} fields is limited by specific absorption rate (SAR) constraints. This is a valid concern if segmented IR b-SSFP is performed at higher fields and, typically, flip angles above 50° are avoided because of these limitations. The results of these simulations, therefore, must be analyzed in light of SAR constraints. The decrease in maximum $T_{1contrast}$ using a flip angle of 50° was approximately 20% compared to α_{opt} (>80°), assuming the parameters of the previous section. Reducing the flip angle did not significantly change the TI_{opt} and TI_{null} results.

T_1 Dependence

Figure 3.23 shows the $T_{1contrast}$ (for 1- and 2-beat imaging scenarios) using IR b-SSFP for three T_1 relationships (and T_2 = 50ms), as well as the dissimilarity between TI_{opt} and TI_{null} as T_{1myo} is varied. The trends of these curves were analogous to IR-FLASH (Figure 3.20). The largest $T_{1contrast}$ was obtained when $T_{1inf} = 0.25T_{1myo}$ (Figure 3.23a-b), which was consistent with IR-FLASH results. However, compared to IR-FLASH,

$T_{1contrast}$ using IR b-SSFP was 24 ± 4% greater using TI_{opt} and 22 ± 3% greater using TI_{null}.

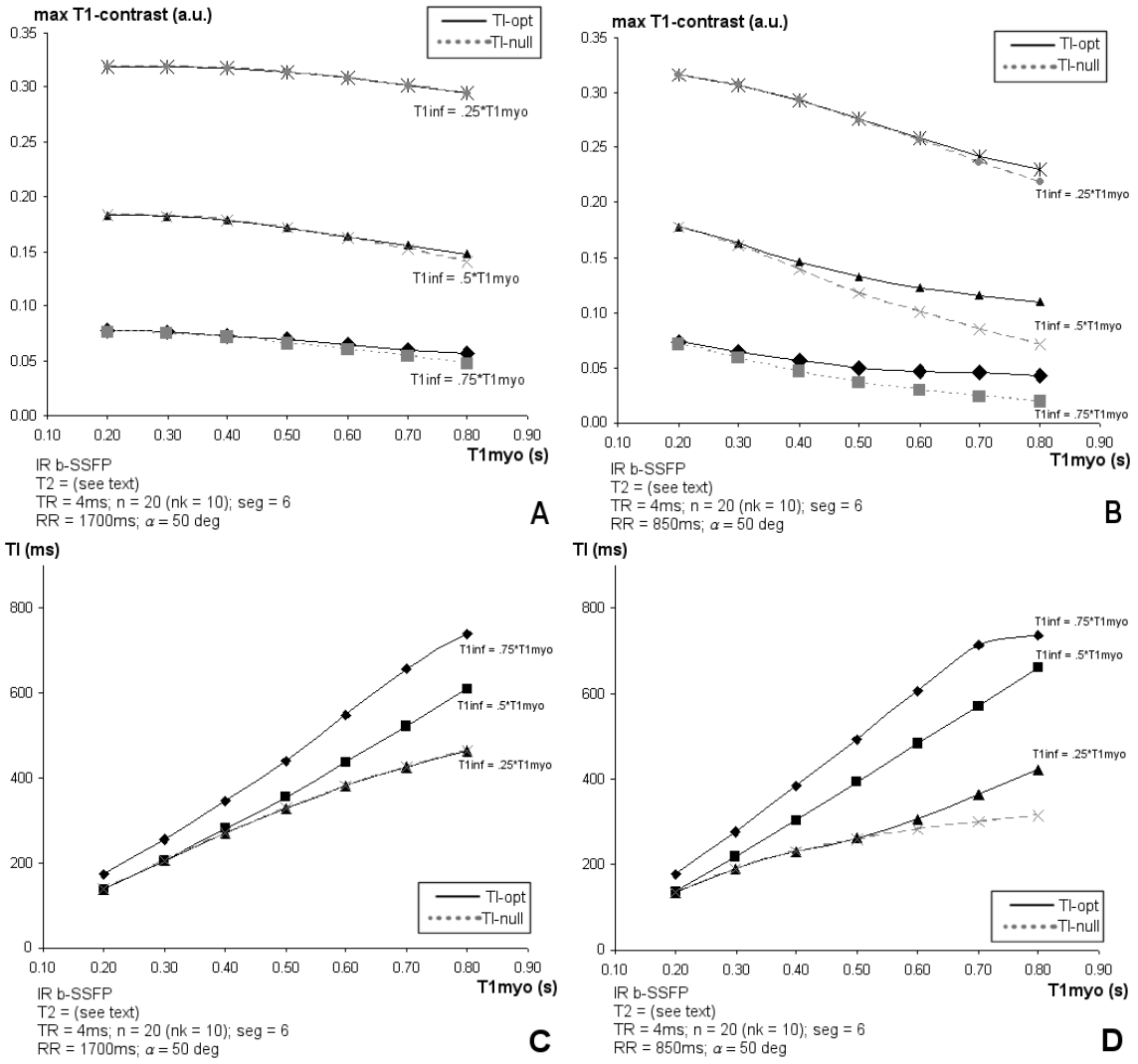

Figure 3.23. a-b) *The maximum $T_{1contrast}$ in IR b-SSFP as a function of T_{1myo} and T_{1inf}; and* ***c-d)*** *the change in TI as a function of T_{1myo} and T_{1inf}.*

As with IR-FLASH, $T_{1contrast}$ was generally equivalent using either TI_{opt} or TI_{null} when the segment interval was two heartbeats (RR = 1700ms), as shown in Figure 3.23a. Except for the $T_{1inf} = 0.25T_{1myo}$ case, this occurred despite TI_{opt} being increasingly larger

than TI_{null} as T_{1myo} became large (Figure 3.23c). For the 1-heartbeat segment interval case, $T_{1contrast}$ using TI_{opt} and TI_{null} began to diverge for large T_{1myo} (Figure 3.23b). As seen with the IR-FLASH results, this divergence was reflected by the large difference (> 300ms) between TI_{opt} and TI_{null} (Figure 3.23d). Overall, it was found that the decrease in $T_{1contrast}$ between using TI_{opt} and TI_{null} was greater with IR b-SSFP than IR-FLASH.

T_2 Dependence

The calculated $T_{1contrast}$ revealed some T_2 dependency in the simulations. For T_1 related by $T_{1inf} = 0.5T_{1myo}$ and T_{2myo} held constant, the $T_{1contrast}$ in IR b-SSFP *increased as the T_2 of infarct was increased*. The degree of this rise in $T_{1contrast}$ was minor (<10%) and only played a significant role when the T_{1myo} was large or the segment interval was short. Furthermore, the optimal inversion time, TI_{opt}, became longer as T_2 increased. Since the magnitude of T_2 decrease in myocardium after contrast injection (Gd-DTPA) is significantly less than T_1 decrease, the primary contributor to image contrast in IR b-SSFP is the relationship between T_{1myo} and T_{1inf} (as observed in the previous section). With knowledge of post-contrast T_2 values of infarct and normal myocardium, this sequence can be further optimized. However, post-contrast T_2 measurements are beyond the scope of this project.

Steady-State Magnetization in IR b-SSFP

It was observed that a steady-state magnetization was *not* achieved during the readout period. The steady state magnetization of b-SSFP, using the matrix notation of Eq. [22], is given by [Hargreaves et al 2001]:

$$\mathbf{M}_{ss} = (\mathbf{I} - \mathbf{A})^{-1}\mathbf{B} \qquad [24]$$

which, for normal myocardium ($T1_{1.5T}$ = 400 and $T1_{3T}$ = 500ms) and a flip angle of 30°, results in $\{M_y, M_z\}_{1.5T} = \{0.16, 0.58\}M_0$ and $\{M_y, M_z\}_{3T} = \{0.14, 0.53\}M_0$. From Eq. [24], it is obvious the steady-state is *not* a function of magnetization preparation. Because there is no dependency on *TI* when the steady-state exists, *the transient magnetization response must be considered in all simulations of delayed enhancement imaging.* The optimal flip angle, assuming steady-state magnetization, is approximately 68° using the $T_{1inf} = 0.5T_{1myo}$ relationship.

Summary of Findings and Relevance for Delayed Enhancement

Findings from the numerical simulations of $T_{1contrast}$ for IR b-SSFP and IR-FLASH include: 1) the optimal *TI* (where the infarct-normal myocardium signal difference is greatest) was consistently longer than the null-point *TI*, especially for 1-beat segment intervals; 2) the separation of TI_{opt} and TI_{null} was largest when segment intervals were short or when T_1 was long; 3) $T_{1contrast}$ was essentially equivalent for TI_{opt} and TI_{null} (<10% difference); 4) optimal flip angle does not increase with higher T_1 values (but maybe limited by SAR); 5) $T_{1contrast}$ was largest for low T_{1inf}/T_{1myo} ratios (T_{1inf} = $025T_{1myo}$), but also when T_{1myo} was short; and 6) $T_{1contrast}$ was greater for IR b-SSFP than IR-FLASH due to less signal saturation during readout.

The use of an inversion preparation provides more $T_{1contrast}$ than simulations without preparation (or a 90° preparation). From the 3D contour plots (Figure 3.19), there was a *broad region of relatively high* $T_{1contrast}$. This suggested that a *large span of TI* (which includes TI_{opt} and TI_{null}) will produce large (and equivalent) $T_{1contrast}$. It is well

accepted that an inversion time near the null-point of normal myocardium subjectively creates the highest image quality for diagnostic assessment in delayed enhancement [Simonetti et al. 2001]. If this *span of TI* can be adapted to "null" normal myocardium, then the delayed enhancement sequence can be executed consistently with *high T_1-contrast and TI-insensitivity*, addressing the two current issues that limit its utility in clinical practice. Caution should be observed in *TI* selection, however, since underestimating the optimal *TI* results in *zero-contrast* between infarct and normal myocardium. This is more important if TI_{null} is used since, from the data presented, $TI_{null} < TI_{opt}$.

It should be emphasized that the maximum $T_{1contrast}$ in these simulations was determined assuming a *linear k-space acquisition scheme*, with $k_y = 0$ encountered near the middle of the acquisition segment. In fact, simulations can be performed and optimized assuming any pulse number for $k_y = 0$. Additionally, the number of lines per segment plays a major role in image contrast, particularly in IR-FLASH (Figure 3.17). Shortening the number of readout pulses per segment will reduce signal saturation and artifacts during the transient phase, but the scan time will be increased.

T_1 Measurement Calibration

In this section, the IR b-SSFP technique will be analyzed for measuring T_1. There are two relevant scenarios for application of T_1 measurements in this project: 1) before contrast administration, and 2) after contrast administration. Both situations require unique methods for determining T_1 values in the heart, which are constrained by several intrinsic factors. With the present discussion, specific T_1 measurement protocols will be

developed for efficient use *in vivo*. The additional trade-offs and limitations that affect accuracy and precision will also be discussed.

This discussion is relevant since these specific methods have not appeared previously in the literature. Common techniques used for T_1 measurements are inversion recovery techniques with numerous sample points and lengthy T_1 recovery times. These methods are not conducive to cardiac imaging. Faster T_1 methods, like the "Look-Locker" method, can be utilized *in vivo* with appropriate correction algorithms [Look et al. 1970, Diechmann et al. 1991, Pickup et al. 2004]. Due to some specific technical requirements (a long segment interval time is needed to reestablish M_0), technique is difficult to implement and customize for cardiac imaging, despite recent success [Klein et al. 2004]. A thorough discussion of this method is beyond the scope of this section; however, the method will be revisited in Chapter 4, when the current techniques are validated experimentally, and in Chapter 7, when the Look-Locker is used *in vivo*.

The proposed T_1 measurement techniques are not limited to use with IR b-SSFP. IR-FLASH can be used in cases when IR b-SSFP results in severe off-resonance artifacts, which may occur at 3T. It will be seen that IR-FLASH also has associated problems, such as image blurring.

Pre-Contrast T_1 Measurement: Multi-point Technique

The conventional method to measure T_1, which requires many separate images at different *TI*s, is a time-consuming process. For this reason, effort will be made to reduce the number of sample points to accurately measure T_1. This can be done as long as the chosen sample points provide enough information about the T_1 recovery process. More

importantly in this application, however, is the customization of the T_1 measurement technique for implementation in cardiac T_1 applications, which is influenced by periodic motion and breathing artifacts.

There are three important factors to consider when measuring blood and myocardial T_1 pre-contrast injection: 1) T_1 is on the order of one heartbeat; 2) the inversion repetition time must be five times greater than T_1 (to allow adequate relaxation back to equilibrium); and 3) imaging must account for breathing and cardiac motion. The last item is easily overcome in cardiac MRI by breath hold imaging and applying a consistent trigger delay relative to the R-wave. However, since the T_1 is on the order of a heartbeat (~1000ms), the trigger delay must extend into the second heart beat to accommodate *TI* values *greater* than one heartbeat. These long *TI*s (coupled with shorter *TI*s) are necessary to distinguish negative magnetization from positive magnetization in magnitude images. This requirement on the trigger delay causes increased demands on the breath hold time, which further exacerbates the fact that the inversion repetition time must be approximately 5 heartbeats to allow magnetization recovery. The implementation of conventional segmented IR sequences, therefore, may require other compensatory measures to account for breathing.

The combination of factors against using conventional segmented T_1 measurement techniques for pre-contrast T_1 calculations motivates the use of "single-shot" methods. "Single-shot" imaging means that *the entire k-space data set is acquired in one segment*. Therefore, the entire scan can be performed in one heartbeat. By triggering the scan to the diastolic period of the *second* heartbeat, the entire *k*-space (~100 lines) can be acquired following the inversion delay time, which can range from 0 to

~1800ms. Also, with the short TR values used in cardiac imaging, the single-shot technique is short enough to limit or completely avoid breath hold requirements. Despite the improvements in efficiency by using single-shot methods, the duration of the data collection window is often greater than 200ms, depending on TR. As a result, it is necessary to implement the sequence in late diastole, when heart motion is relatively stationary. The long data acquisition window also saturates magnetization more significantly due to the high number of repetitive excitation pulses. Therefore, the flip angle must be kept small.

Comparison of Single-Shot IR b-SSFP with Ideal Inversion Recovery

Using the mathematical framework of b-SSFP, it is relevant to simulate the expected signal intensity of single-shot IR b-SSFP using various *TI*s, and compare them to the ideal inversion recovery values (Eq. [5]). This comparison will reveal the effects of the readout pulses on the precision of the T_1 measurement. For the simulation, a T_1 and T_2 of 1000ms and 100ms, respectively, will be assumed, and *TI* values will range from 200ms to 1600ms in 100ms steps. The single-shot b-SSFP readout consisted of 95 RF pulses of 40°, separated by a TR of 3ms. The expected signal intensity was calculated from Eq. [22], with the majority on the signal strength assumed to occur following the 48^{th} pulse ($k_y = 0$) (linear *k*-space ordering). The acquisition window in this case is 285ms.

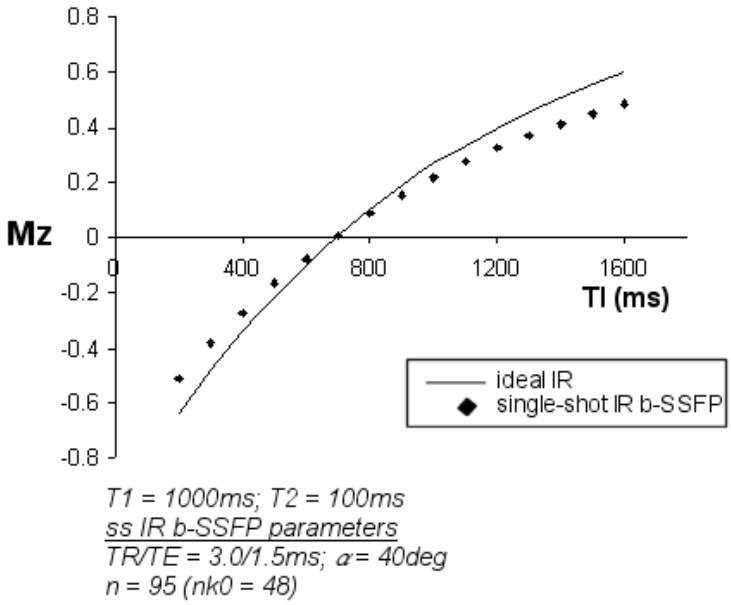

Figure 3.24. *Comparison of IR b-SSFP (single-shot) with ideal T_1 recovery for the parameters shown.*

Figure 3.24 shows a comparison of a simulated single-shot IR b-SSFP using Eq. [22] and the ideal inversion recovery curve (T_1=1000ms). The estimated T_1 from the simulation data points using a least-squares approximation yielded T_1=994ms, with an M_0 estimation of 0.81. The high accuracy of the fit was due to the precise estimation of the zero-crossing, which lead to the correct T_1 value. However, a meaningful imprecision occurred for M_0 estimation, which was about 20% lower than the "true" M_0 of 1.0. This result arose due to the poor correlation with ideal T_1 recovery at low and high *TI* values. During these *TI*s, the magnetization is far from its steady-state value. Once the readout excitations begin, the magnetization is saturated more so than if *TI* was near its natural null-point. Therefore, the estimated magnetization (and hence the signal intensity) is lower than the ideal magnetization level. A more precise approximation of highly negative or positive magnetization during inversion recovery would benefit from a short

readout duration, which does not disturb the inherent T_1 recovery as much as longer readout durations. This would provide a more accurate measure of M_0.

Reduction of Sample Points

The primary goal, however, is to measure pre-contrast T_1 (in the range of 700 to 1700ms). If only a limited amount of *TI* points around the zero-crossing were acquired, can T_1 still be measured precisely? For instance, if the same T_1-mapping simulation was executed using *TI*s of 400, 600, 800, and 1000ms, will the results be the same as before? After applying this limited set of *TI*s, the least-squares approximation of T_1 and M_0 also resulted in approximately T_1 = 994ms and M_0 = 0.80. The zero-crossing *TI* value was purposely excluded from this example since usually it is unknown prior to the experiment. But, clearly, T_1 using single-shot IR b-SSFP was able to approximate T_1 with high precision using a limited number of *TI* values.

Protocol for Mapping T_1

In the examples above, the longitudinal magnetization, M_z, was considered in the T_1 approximation. In actuality, the image signal intensity is proportional to the *transverse magnetization,* M_{xy}. However, this fact is inconsequential for approximating T_1, since mapping the transverse magnetization to the inversion recovery curve will still result in the correct T_1 estimation due to the precise approximation of the zero-crossing. The main difference will lie with the M_0 estimation. These mapping technicalities raise a consistency issue: if the signal intensity of IR images is used to approximate M_0, it affords mapping the values to the expected *transverse* magnetization given by the *full b-*

SSFP equation, using appropriate inputs for flip angle, TR, etc. However, if only T_1 is sought, mapping signal intensity values to the general inversion recovery curve suffices. In the specific protocol developed for *in vivo* pre-contrast T_1 measurements, only the T_1 value will be measured.

From the simulations above, it was shown that T_1 can be approximated using a limited number of *TI* values, as long as the zero-crossing is estimated correctly. This is due to its simple tie to T_1 ($T_1 = TI_0/\ln(2)$, where TI_0 is the *TI* to the zero-crossing). Using the knowledge from this discussion, *TI* values will be selected in the neighborhood of the (expected) zero-crossing of the tissue.

Post-Contrast T_1 Measurement: 2-point Ratio Method

There is a greater demand for a fast T_1 sampling scheme in the heart post-injection. Apart from the previously outlined reasons for fast imaging in the heart, there are two dominant motives for reducing the temporal resolution of the measurement: circulating contrast media causes 1) a large reduction of the native T_1 value, and 2) the T_1 values change over time. This situation places a constraint on the time allocated for an accurate measurement, since the value of T_1 may be changing over the course of several inversion recovery scans needed to sample the T_1 relaxation, possibly resulting in poor curve fits or overestimated values. Although this demand becomes less stringent over time post-contrast (since most of the contrast media evacuates the system in less than an hour), the effective time to acquire the set of images for the T_1 measurement should be kept as small as possible.

In the previous section, it was shown that T_1 could be estimated using a limited number of individual *TI* scans, as long as they were informative. For post-contrast measurements, we will consider a *2-point ratio technique*, which has been used previously [Sharma et al. 2003]. Even though approximating T_1 with 2 *TI* values is subject to more error in T_1 estimates, it will be shown that specific *TI* times can be selected to mitigate the uncertainty. This section will explore the theory of the 2-point ratio method, and reveal both its advantages and disadvantages. Simulations with b-SSFP will be used to assess the accuracy of the technique.

General Theory

The general theory of the ratio method can be considered without resorting to the lengthy description of b-SSFP or FLASH. Comparisons with these expressions will be addressed later. For an initial understanding, it suffices to begin with the transverse magnetization at the echo time (TE), following longitudinal recovery due to spin inversion:

$$M_{xy}(TI,TE) = M_0\left(1-2\exp(-TI/T_1\right)\cdot\sin(\alpha)\cdot\exp(-TE/T_2)\,. \qquad [25]$$

Decay due to flip angle and T_2 effects can be eliminated from the equation if a second image is obtained at a different *TI*, using identical *TE* and α. The equilibrium magnetization of the tissue, M_0, which is related to the proton density of the tissue, also cancels (Figure 3.25):

$$S(TI_a,TI_b) \equiv \frac{M_{xy}(TI_a)}{M_{xy}(TI_b)} = \frac{1-2\exp(-TI_a/T_1)}{1-2\exp(-TI_b/T_1)}\ . \qquad [26]$$

The result is a ratio value, *S*, that is a function of two *TI* values, TI_a and TI_b. The value of *S* can be determined on a pixel-by-pixel basis, if both images are registered and identically scaled. This process will be discussed when performing phantom and in vivo experiments.

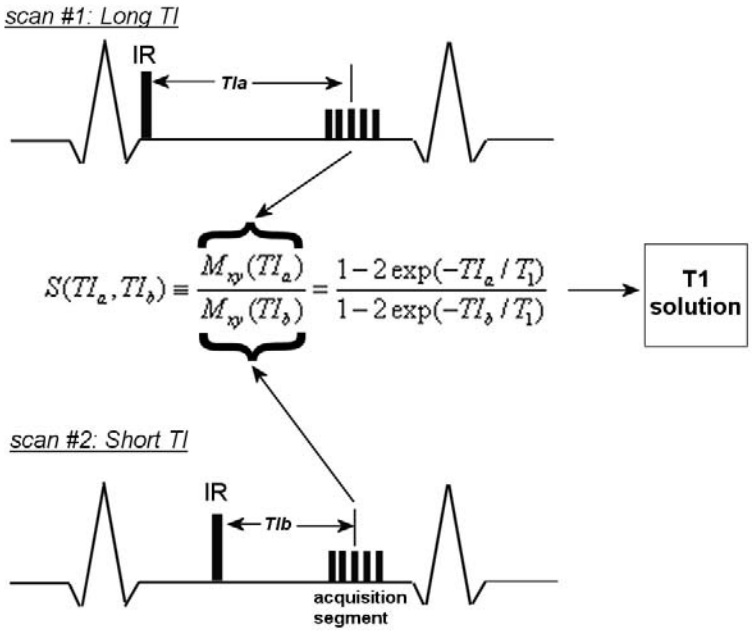

Figure 3.25. *The 2-pt ratio method for determining T_1 values post-contrast.*

With the simplistic relationship of Eq. [26], knowledge of *S* results in one equation with one unknown, which is computationally attractive. But since the experiment utilized IR preparation, the sign of the magnetization becomes relevant for determining the sign of *S*. This issue is problematic since the images produced using cardiac phase-array coils contain exclusively modulus (positive) intensities. Therefore, the actual sign of *S* is uncertain, and both positive and negative variants must be considered in T_1 calculation. Both the positive and negative values for *S* result in *two*

unique T_1 solutions, and necessitate a decision criterion for determining the correct T_1 value. Often, knowledge of the *expected* T_1 is known beforehand, and one solution can be easily eliminated. But if both solutions are very similar, it becomes difficult to dismiss one solution. The simplest method to overcome these difficulties is to observe the trend of T_1 change over time post-injection, which is characterized by a gradual increase in T_1 due to contrast agent elimination. Though effective, one still has to subjectively choose the correct T_1 solution, and there are instances when the procedure fails. The method can be improved if the T_1 solutions themselves are highly distinct. In the following sections, some specific features of the 2-point ratio method will be presented, and strategies will be outlined to maximize the *distinction* between the two T_1 solutions.

Cardinal Features of the Ratio Method

Since the value of *S* is the ratio of signal intensities from inversion recovery scans, a problem arises when the signal intensity from either IR scan is close to zero. When the ratio Eq. [26] is evaluated, this situation translates to a very low (approaching zero) or a very high (approaching infinity) value for *S*.

To view this unique relationship between the *S* and T_1 solutions, it is convenient to generate a look-up table. It can be shown that there is a unique relationship between T_1 and *S* depending on the chosen *TI* times. Two examples are shown in Figure 3.26. The plots show the *absolute value* of *S* (which is realistic considering the two source IR scans are modulus images). It also assumes $TI_a > TI_b$, but this is not a strict requirement. There are two points of interest in the plots, namely the *asymptote* and the *zero-point*. These points occur when the chosen *TI*s null their corresponding T_1 values, which, for the *TI*s

shown (TI_a/TI_b = 100/500ms and 200/400ms), are 159/721ms and 288/577ms, respectively.

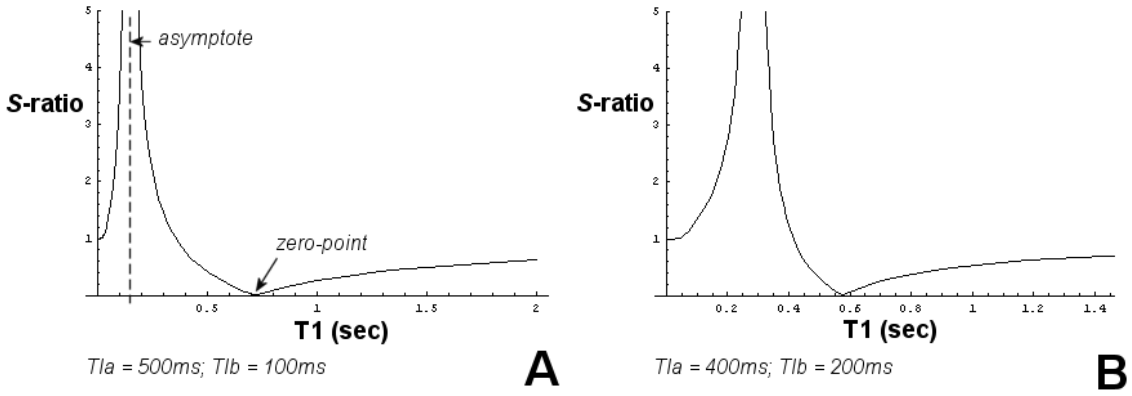

Figure 3.26. *Relationship between S and T_1 in the 2-pt ratio technique.*

There are other key features in the plots of Figure 3.26. First, the slope of the curve is very high for low T_1s. This is because of an asymptote relatively close to $T_1 = 0$, but it also implies that a large change in the value of *S* does not cause a significant change in T_1. For instance, there is a certain error associated with *S*, which is caused by noise in the two source images. This error will result in an error in T_1. But since the slope of the curve is large for small T_1, the error in T_1 will be small in comparison to *S*. For longer T_1s, a significant error in *S* will result in a significant error in T_1, which is not desired. For measuring longer T_1s, therefore, it is recommended that a different *TI* pair be used for calculating T_1.

Secondly, note that for any value of *S*, there are two distinct T_1 solutions, as mentioned earlier. The relative difference between these two T_1 solutions is dictated by the value of *S* and the *TI*s of the scans. Ideally, the T_1 solutions should be very *different* from one another so that one value can be easily eliminated. But at what point do the T_1

solutions become different enough from each other to deem one solution as trivial? One answer is to base the decision on the *expected standard deviation of the measurement*. For measuring post-contrast T_1 values in blood, myocardium, and infarct, it has been shown that the standard deviation at each time point post-injection is at most 0.10 seconds [Klein et al 2004]. Therefore, one can propose a criterion that *if two T_1 solutions are less than this threshold value, the method is not specific enough to determine the correct T_1*.

The *difference* in the T_1 solutions at a particular *S* value and *TI* pair can be shown graphically. Using a threshold constraint of 100ms as a measure of the success of the 2-point technique, an array of *TI* pairs can be found that avoid *S* values resulting in "indistinguishable" T_1 solutions. Figure 3.27 shows plots of three *TI* pairs, 650/150ms, 400/200ms, and 500/300ms; chosen such that each *TI* is less than one *RR* interval. The curves do not provide any information on the values of the T_1 solutions themselves, but rather the *difference* between the two T_1 solutions. As shown, the T_1 solutions are *below* the threshold value for very low or very high values of *S*. Specifically, for the 650/150ms *TI* pair (Figure 3.27a), this occurs when *S* is less than 0.1 or exceeds 5.6. For closely separated *TI* pairs, like 400/200ms (Figure 3.27b), the maximum possible *S* is lower (4.2), while the minimum is slightly higher (0.2). This implies that if *S* is beyond these boundaries, the difference in the two T_1 solutions will be too small to confidently select the correct T_1. A similar result exists for the 500/300ms *TI* pair (Figure 3.27c).

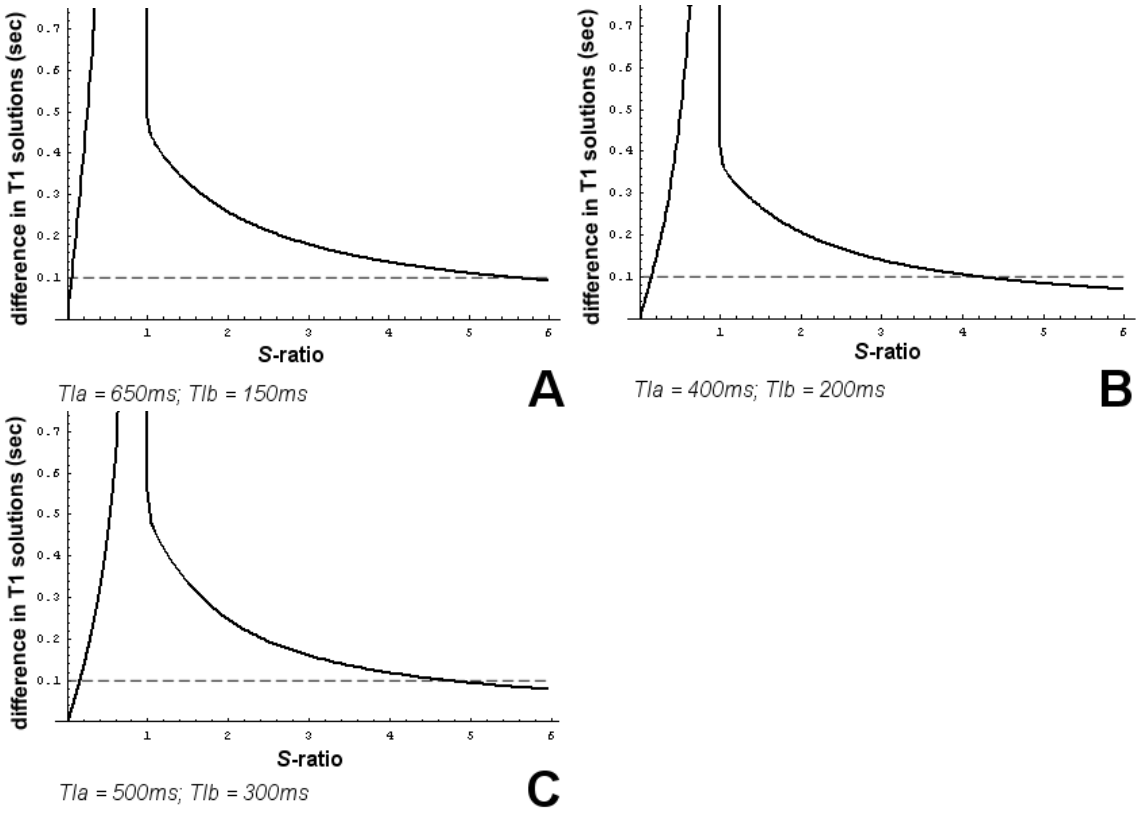

Figure 3.27. *The difference in T_1 solutions for selected TI-pairs.*

Selecting Appropriate TI values for the 2-Point Method

The boundaries of *S* in the analysis above are dependent on the selected *TI* pair. Figure 3.27 showed that the region above the threshold (*S* for which the T_1 solutions are greater than 100ms) was larger for the 650/150ms *TI*-pair than for the other two *TI*-pairs. Thus, when the difference in the selected *TI*s is large, there is a greater chance that the resulting T_1 solutions are very distinct from one another, making the elimination of an erroneous T_1 easier. To visualize this trend more clearly, Figure 3.28 compares the T_1 solution *difference* of three *TI*-pairs, in which the lower *TI* is held constant at 150ms, while the larger *TI* is increased from 350ms to 950ms. All three curves give maximum values at $S = 1$, but for $S > 1$, the curve decreases more sharply when the larger *TI* is

small. It is similarly true when $S < 1$, as the 350/150ms curve rises slower than the other two *TI*-pairs. The end result is a wider acceptable T_1-solution region (area under the curve) when the difference in the selected *TI*s is large.

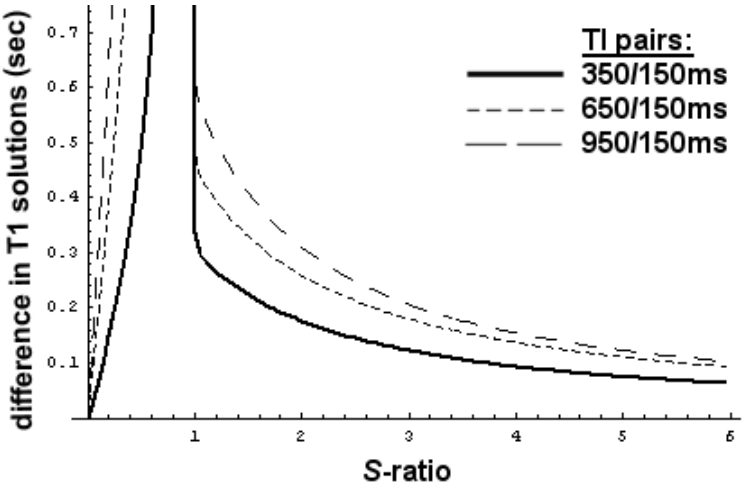

Figure 3.28. *Comparison of the difference in T_1 solutions when the low TI is constrained to TI = 150ms.*

The idea that the *TI* difference of the two IR images should be large is constrained by the length of the *RR* window, which is related to the heart rate (*HR*) by *RR* = 60/*HR* (sec), and the length of the readout window. These factors limit the maximum allowable *TI*. In a practical setting, the smaller *TI* is limited by the duration from the first readout pulse to $k_y = 0$, which is dependent on the number of lines per segment and the *k*-space acquisition order. The best strategy for selecting appropriate *TI* values is to choose a relatively low *TI* (< 150ms) and a large *TI* that is contained within the *RR* interval. These two *TI* values will represent signal intensities from sufficiently different parts of the T_1 relaxation curve. For post-contrast T_1 measurements, a very low *TI* is needed, since the scan must also avoid completely nulling the tissue of interest.

A large part of measuring T_1s post-injection is to have a reasonable idea about the expected T_1 value. The expected range of T_1 values of healthy myocardium at both 1.5T and 3T are assumed to be less than 600ms over a 30 minute post-injection period. For blood and infarcted myocardium, the maximum expected T_1 is much lower, likely no more that 400ms. It is clear that this knowledge will aid the decision-making process in instances when one of the two T_1 solutions is found to be greater than 1000ms. In summary, therefore, *maximizing the T_1 solution difference*, and *having a reasonable idea of expected solutions and trends*, will most benefit the 2-point ratio method.

Comparison with IR b-SSFP and IR-FLASH

In the previous analysis, a simplistic expression was presented for the 2-point ratio method (Eq. [26]). However, it affords to compare the *S* values generated by Eq. [26] with the *full* expressions for IR b-SSFP and IR-FLASH, which better represent the expected signal intensity of the individual IR scans. In this comparison, the magnetization profile during the 1st segment will be initially assumed since the *TF* will be considered large (3 *RR* intervals) relative to post-contrast T_1 values ($T_1 < 600$ms). Other relevant simulations parameters include: (b-SSFP) $\alpha = 30°$; TR = 3ms; $n_{k0} = 21$; $T_2 = T_1/3$; and (FLASH) $\alpha = 15°$ (constant and variable flip); TR = 5ms; $n_{k0} = 21$.

The saturation effect present with IR-FLASH modulated the ratio values, *S*, in comparison to the theoretical values from Eq. [26]. This was true even for relatively small flip angles of 15°. However, as shown in Figure 3.29b, the theoretical predictions of the simplistic expression of Eq. [26] were closely matched when a variable flip sweep was used. This was due to the smaller flip angles during the initial portion of the readout,

thereby limiting the amount of longitudinal saturation, and making the magnetization at $k_y = 0$ almost equivalent in magnitude to an ideal inversion recovery experiment. Excluding the values in the immediate neighborhood of the asymptote and zero-point, the difference between IR-FLASH with variable flip angles and Eq. [26] was less than 15%, with the majority of the error occurring in the region between the asymptote and the zero-point. The approximation of the zero-point using the full IR-FLASH analysis was 0.96sec compared to 0.94sec using Eq. [26].

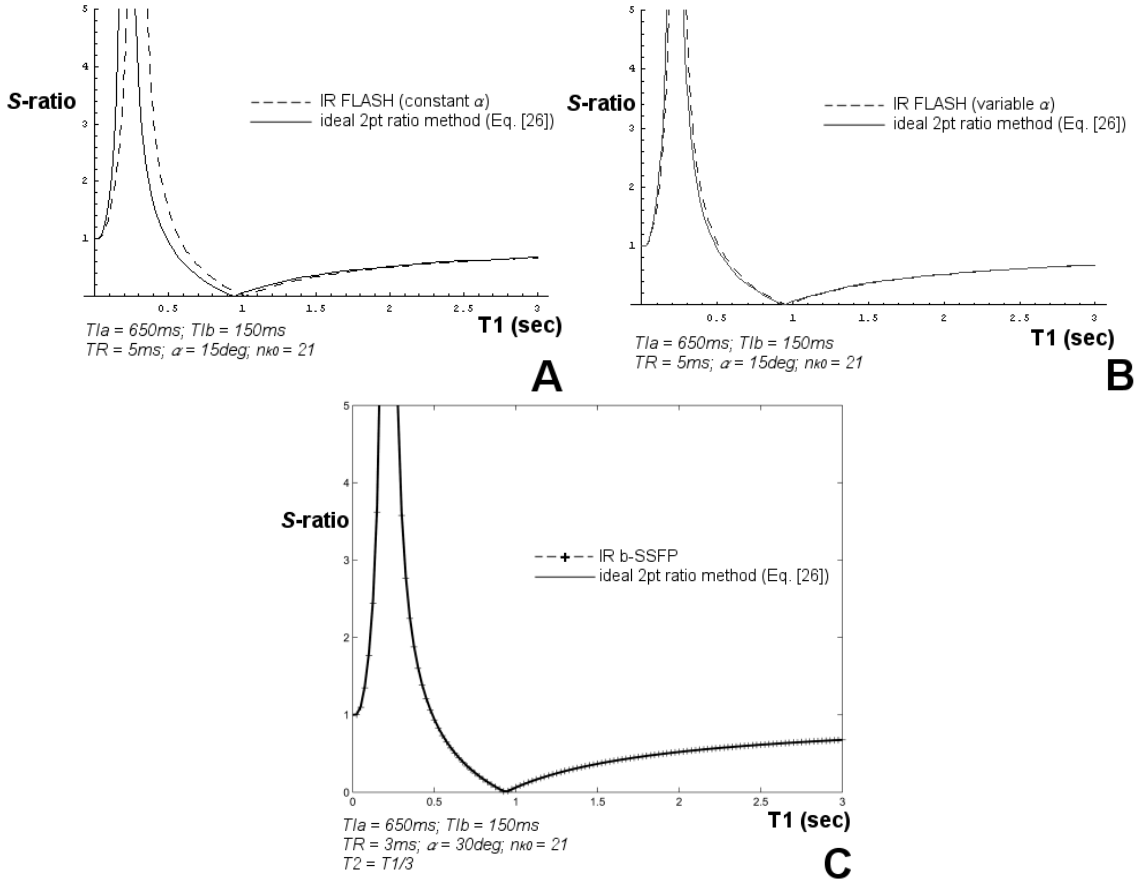

Figure 3.29. *Correlation of ideal 2-pt ratio method with full* ***a-b)*** *IR-FLASH and* ***c)*** *IR b-SSFP expressions.*

The error was larger when variable flip angles were not used, as shown in Figure 3.29a. In this case, the approximation of the zero-point was 1.02sec, and there was a

severe overestimation (~45%) of *S* between the two critical points. This result is particularly relevant since this region contains T_1 values typically seen post-contrast in the heart (200 to 600ms), which casts doubt about the utility of IR-FLASH (constant flip angles) for the 2-point ratio method. This inaccuracy can only be remedied by shortening the readout period, lowering the flip angle, or using "centric" (low-to-high) *k*-space ordering.

When compared to Eq. [26], high correlation was found using the full IR b-SSFP simulation (Figure 3.29c). The difference between the two approximations was less than 5% (excluding values near the asymptote and zero-crossing). Moreover, the estimated zero-point using IR b-SSFP was 0.96sec, which was equivalent to the value predicted using Eq. [26]. The course of longitudinal magnetization of IR b-SSFP was shown in Figure 3.14 in comparison to IR-FLASH. Clearly, the magnetization prior to data acquisition in FLASH was driven lower once readout commenced, while it changed only subtly in IR b-SSFP. This characteristic of b-SSFP enabled the magnetization at $k_y = 0$ to be similar to theoretical predictions. The T_2 component of the SSFP signal did not effect the ratio values until $T_2 < 0.1T_1$. Evidently, this is in the neighborhood of T_2 values expected in post-contrast myocardium. However, it was still found that IR b-SSFP was superior than IR-FLASH in its prediction of Eq. [26], with an error consistently <10%.

A critical factor in the accuracy of the 2-point method is the *segment interval time* of the two IR scans. Equation [26] is the ideal scenario, where it is assumed that the magnetization preceding the IR pulses is M_0. Of course, this may not be true if the segment interval, *TF*, is $< 5*T_1$. The forth-coming *in vivo* studies utilize segment interval times of 3 heartbeats, but it is important to see the effects of this interval time on the ratio

S values. Figure 3.30 compares IR b-SSFP and IR-FLASH (variable case) for an interval time of 3 heartbeats (~3000ms) using the same parameters above. The third segment is shown along with the predicted curve given by Eq. [26]. There is a clear misregistration between predicted and simulated curves, which is more dominant in the FLASH case. Particularly, longer T_1 values will be underestimated. This effect is less pronounced for b-SSFP, where errors begin to arise for T_1 values greater than 0.7s.

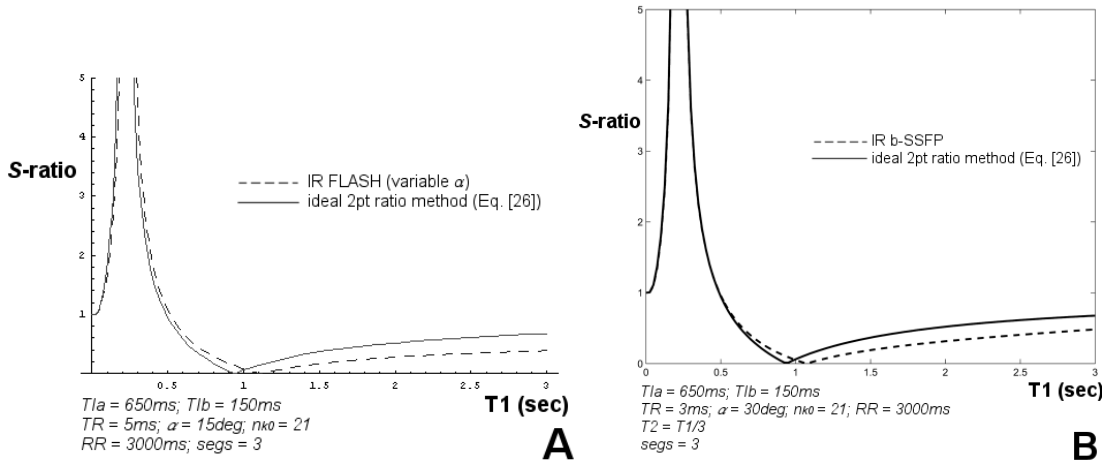

Figure 3.30. *Correlation of 2-pt method Eq. [26] with* ***a)*** *IR-FLASH and* ***b)*** *IR b-SSFP assuming 3RR intervals.*

Summary of Findings: Post-Contrast T_1 Measurement Technique

The comparison of Eq. [26] with IR-FLASH and IR b-SSFP was performed to quantify the error between the simplistic expression given in the general theory and the fuller imaging expressions, which predict signal intensity. From the simulations, it was found that IR b-SSFP closely correlated to Eq. [26] when long segment intervals (≥ 3 heartbeats) were used. This allowed the use of the reduced Eq. [26] for determination of T_1 instead of the more complex expression of IR b-SSFP. When the segment interval is

less than 3 heartbeats (< 3000ms), errors in post-contrast T_1 estimation will occur if Eq [26] is used. In this case, lengthening the segment interval or utilizing single-shot methods will improve the correlation. Appendix C details the process for determining both T_1 solutions using the Newton-Rapshon numerical method, and the generation of a T_1-map.

Conclusion

This chapter outlined the theoretical framework contained within the project. The mathematical discussion of image contrast mechanisms is crucial for the study of delayed enhancement optimization criteria at both 1.5T and 3T. The framework provides the ability to experiment with various parameters and optimize the sequence in light of changing tissue properties at high fields. From the simulation results, the following points are most important:

1. Three distinct inversion times are noteworthy: a) TI_{zero}, the inversion time that produces *zero* $T_{1contrast}$ between infarct and normal myocardium; b) TI_{null}, the inversion time that produces *zero signal from normal myocardium*; and c) TI_{opt}, the inversion time that produces the *maximum* $T_{1contrast}$. These three inversion times are related in time by: $TI_{zero} < TI_{null} < TI_{opt}$. Therefore, in selecting TI_{null}, one should err on the side > TI_{null} to avoid TI_{zero}.
2. TI_{null} converges to TI_{opt} as the T_1 difference between infarct and normal myocardium increases *and* as T_1 of infarct tissue decreases.

3. Though TI_{opt} produces the maximum $T_{1contrast}$ (and is generally much greater than TI_{null}), the gain in $T_{1contrast}$ is less than 10%, suggesting a broad region of high $T_{1contrast}$ and large range of possible *TI* values for delayed enhancement.
4. The optimal flip angle (α_{opt}) is approximately 26-30°, but should be < 40° to avoid significant signal saturation (driven equilibrium), and > 10° to avoid low signal amplitude (low SNR).

Also, for equivalent sequence parameters, the $T_{1contrast}$ increased as the segment interval delay (or, equivalently, the R-to-R wave interval) increased.

The longitudinal insensitivity of the b-SSFP sequence enabled its use with T_1 measurement routines. It was found that the single-shot version of IR b-SSFP correlated well with the expected longitudinal magnetization from an ideal inversion recovery, provided the *TI*s were chosen to span the particular tissue's zero-crossing. This high correlation with the inversion recovery equation was also shown for a 2-point segmented IR b-SSFP ratio technique. The theoretical ratio values (Eq. [26]) did not differ significantly from the simulated values from the full b-SSFP equation, whereas large deviations were present with FLASH simulations when large flip angles and long readouts were used. It was also shown that the finite segment interval time caused a significant inaccuracy for measuring long T_1s.

As more knowledge of myocardial and infarct T_1 values at 1.5T and 3T become known, the contrast optimization routines presented in the chapter can be refined for the delayed enhancement technique. Many of the techniques and concepts in this chapter will be revisited throughout the analysis of future experiments.

CHAPTER 4

PHANTOM EXPERIMENTS

Introduction

The study of image contrast mechanisms in FLASH and b-SSFP is critical for understanding and optimizing cardiac MRI sequences at 1.5T and 3T. Until now, image contrast has been described in terms of the expected signal *difference* using mathematical models of FLASH and b-SSFP (see Chapter 3). From that description, optimization strategies were developed based on assumptions for T_1 and T_2. The primary objective, however, is to extend the methods and results produced by mathematical simulations to practical imaging scenarios. Moreover, the validation of such simulations requires experimental confirmation. Only then will the mathematical models be useful for predicting image contrast *in vivo*.

A "phantom" is any MR sample that substitutes for the human body during imaging. It provides a convenient tool for experimental testing prior to *in vivo* imaging. With MR phantoms, one can adapt the sample to particular T_1 values, and subsequently analyze the image contrast in a controlled setting. The primary criteria of a *contrast phantom* are: 1) homogeneous T_1 information that span a broad spectrum of values; and 2) a manageable size such that the sample can be contained within the magnet's sphere of homogeneity. The latter requirement is adopted to avoid signal loss (due to inhomogeneous fields) and excessively large field-of-views (FOV).

The purpose of this chapter is to use a series of T_1 phantoms to evaluate the imaging techniques used in this project and confirm the accuracy of the mathematical

simulations. These techniques include: 1) the T_1 measurement techniques (single-shot and 2-point ratio methods); and 2) the delayed enhancement technique (IR-FLASH). Before considering these two main areas, it will be first necessary to subject the T_1 phantoms to cursory imaging scenarios discussed previously with mathematics, namely, inversion recovery (IR), flip angle sweeps, constant flip angles, and imaging during the transient approach to steady-state. *These initial studies will help to validate the theory developed, lend insight into variances with mathematical predictions, and validate the accuracy of methods which will be used in vivo*. Emphasis will then be placed on IR-FLASH, the most common technique used in delayed enhancement imaging. Phantoms will be used to characterize the suppression and enhancement performance of the sequence in terms of *signal intensity differences*. These results will be compared to the results determined from the simulation studies (Chapter 3).

Methods

Following an overview of T_1 phantom preparation method, there are 3 main areas of experiments that will be described: 1) T_1 measurement validation; 2) Correlation between experimental FLASH and b-SSFP imaging with mathematical simulation; and 3) delayed enhancement image contrast experiments.

Scaling of Images

Throughout these experiments, the signal intensity from MR images will be compared (and correlated) with simulation results. The simulation results are scaled from 0.0 to M_0, where M_0, the equilibrium *longitudinal* magnetization, is normalized to 1.0.

This assumption was made for convenience, since an exact value for M_0 is not explicit in MR images, even though it is known to vary among tissues and field strengths. Therefore, to allow comparisons to be made between experimental and simulation results, *a single nominal scaling value must be established*. In this chapter, this nominal scaling value was obtained via a "reference image scan" (such as a scan without an IR pulse in IR experiments), against which the scan under analysis is normalized. This provides MR signal intensities on a scale from 0 to 1. To match this scale, the simulation results were also similarly normalized against an additional "reference" simulation. Figure 4.1 depicts example signal intensities and simulations undergoing this normalization, where each quadrant in the diagram represents a different tissue signal.

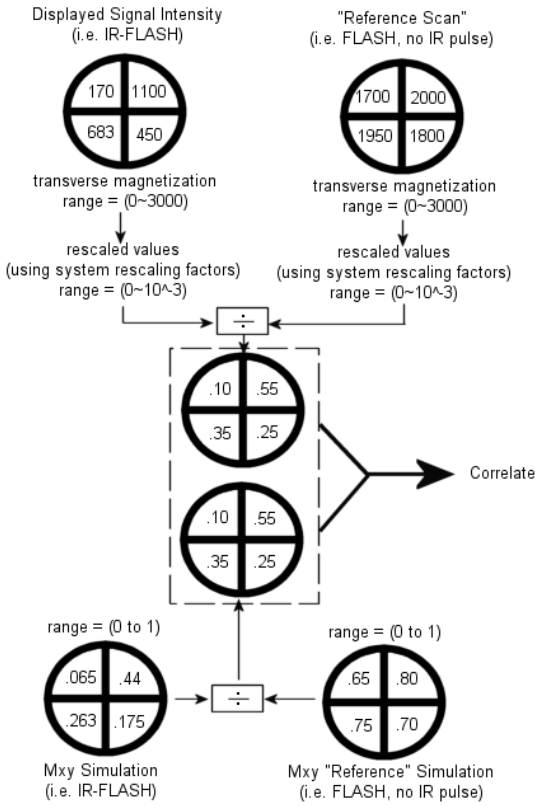

Figure 4.1. *Diagram of scaling method for correlating imaging with simulation results*

T_1 Phantom Preparation

All T_1 phantoms were contained within 50mL plastic test-tubes during imaging. Each sample was created with varying concentrations of gadodiamide contrast agent (Gd-DTPA-BMA, Amersham, molec wt. 537g/mol) to lower T_1. To prepare physiological T_1s (T_1>100ms), a stock solution was prepared by adding 1mL of 0.5M Gd-DTPA-BMA to 250mL of 0.9% saline and mixed, producing a contrast agent concentration of 2mM. To prepare the individual T_1 samples, a specific amount was taken from the 2mM stock solution and diluted further to a desired concentration. The following calculation determined *the amount of stock solution to dilute in 50mL*:

$$\text{Stock Solution}: \frac{1\,\text{mL Gd - DTPA - BMA}}{0.25\,\text{L H}_2\text{O}} = 2mM \;\; \textit{Gd-DTPA-BMA}$$

$$\text{Desired Solution}: X\ \text{mM Gd - DTPA - BMA}$$

$$\text{Amount of Stock Solution to add}: Y\ \text{L} = \frac{0.25\text{L} \times X\ \text{mM} \times 0.05\text{L}}{0.5\text{mmol}}$$

Hence, for a 0.2mM Gd-DTPA-BMA concentration in 50mL of saline, 5mL of the 2mM stock solution is needed.

Samples for some studies were prepared with agar, since viscous gels offer different T_1 and T_2 relaxation properties over pure saline. To produce a mixture of 4% concentration (by weight), 4mg of solid agar was added per 10mL Gd-DTPA-BMA/saline solution. The solutions were mixed well such that the solids dissolved. The mixtures were then placed in a water bath and heated for 5 minutes at approximately 80°C to promote a thoroughly dissolved mixture. The samples were checked for air bubbles and sedentary particles, poured into the 50mL plastic tube and cooled. Since Gd-DTPA-BMA is known to be sensitive to light, the samples were wrapped in aluminum

foil when not in use. The actual T_1s prepared in this chapter are given under each experiment below.

Contrast Agent Relaxivity in Macromolecular Solutions

Contrast agent relaxivity, r_1, is defined as the change in relaxation rate per unit contrast agent concentration ($mM^{-1}\ s^{-1}$). It is the inherent ability of the contrast agent to promote relaxation in tissue. Even though the chemical environment of the phantoms used in this experiment may differ from the *in vivo* extracellular distribution space, *this investigation will predict whether the relaxivity of the contrast agent will change depending on the density of the macromolecular environment or field strength*.

In the present work, two agar gel samples were prepared (1% and 4%) and one milk powder sample (6%) in a total volume of 25mL. Four concentrations were prepared in this experiment: 0.2mM, 0.4mM, 0.8mM, and 1.2mM, in addition to one sample with 0mM gadolinium. The samples were prepared using 0.9% saline as the base solvent.

All samples were imaged at 1.5T (Philips Intera), 3T (Philips Intera), and 4.7T (Varian Spectrometer) within 5-10 days. The T_1 of each sample was measured using conventional inversion recovery techniques; however, because of the different protocols available on each scanner, the sequence parameters varied slightly. At 1.5T and 3T, an adiabatic inversion pulse was followed by a spin echo acquisition (to limit B_0 inhomogeneity), which collected data (2 echoes per TR) using an in-plane resolution of $1.5mm^2$ (~$200mm^2$ FOV, 128 matrix) and an echo time (TE) of 4-6ms. The total scan duration for each inversion time *(TI)* scan was 8.5mins. At 4.7T, an adiabatic inversion was followed (after *TI* ms) by a 90° excitation pulse, after which the free induction decay

signal was sampled, Fourier transformed, phase corrected, and measured. It was known that the span of T_1 was approximately 150ms (highest Gd sample) to 2500ms (pure saline), which necessitated TR to be very high (at least 5 times T_1) to accommodate the longest T_1. Thus, the TR was set to 10-15 sec. Since it was expected that many of the samples have T_1 less than 1000ms, a greater density of inversion times were selected between 100-800ms. More specific *TI*s (greater than 1000ms) were used for T_1 samples greater than 1000ms. In all cases, at least 15 *TI*s were used to characterize T_1. A very long *TI* (near TR) was also measured to confirm longitudinal recovery back to equilibrium before the next inversion pulse.

A least-squares fitting algorithm was used to determined T_1 and M_0 based input quantities S_m and TI_m (where S_m is the mean signal intensity measured from an ROI of the *m*th sample):

$$S_m = M_0\left(1 - 2\exp\left(-TI_m / T_1\right)\right). \qquad [1]$$

The T_1 data from each sample and field strength was converted to relaxation rates ($R_1 = 1/T_1$) for relaxivity calculations. Gd-DTPA-BMA relaxivity was determined from the slope of R_1 and contrast agent concentration ([Gd]) for each macromolecular sample. This was based on the assumption that [Tweedle et al. 1991]:

$$R_1 = R_{1_{pre}} + r_1\left[Gd\right], \qquad [2]$$

where it can be seen that R_1 and R_{1pre} are related linearly by r_1, the relaxivity, given by $(\text{mM s})^{-1}$. Relative error was given by the r^2 value.

T_1 Measurements

The T_1 measurement techniques introduced in Chapter 3 (multipoint single-shot IR b-SSFP and 2-point ratio method IR b-SSFP) were validated with MR phantoms. Thirteen 50mL plastic test tubes containing 0.9% saline were made with varying concentrations of Gd-DTPA-BMA contrast media (0mM Gd to 1.2mM Gd). The tubes were arranged in a head coil at 3T (Philips Intera, Best, The Netherlands).

Reference T_1 Measurements

Reference T_1 relaxation times were measured using a segmented IR FLASH-echo planar (EPI) hybrid sequence with 31 inversion times (*TI*), spanning 50ms to 2500ms. A FLASH-EPI sequence diagram is shown in Figure E.1 of Appendix E. Parameters for the sequence were $270\times270mm^2$ FOV, 128×128 matrix, TR/TE/α =12,000ms/5.4ms/15°, 3 EPI lines/TR, and 8mm slice thickness. Scan time was 5.75 min.

"Pre-Contrast" T_1 Measurement

The 4-point single-shot IR method (proposed for pre-contrast T_1 measurements, abbreviated here as "IR-ss") was used to measure the T_1 of the same 13 tubes at 3T. For the pre-contrast IR-ss, 4 *TI*s were used (500, 800, 1100, and 1500ms), which are values that theoretically span the zero-crossing of blood, infarct and myocardium T_1 *pre*-contrast. These inversion times were used in this confirmation despite the broad range of T_1 values of the phantoms. As a result, this approach will reveal the ability of this selection of *TI*s to measure T_1 values *outside* "expected" range of blood and myocardium, such as very low T_1 values. All scans were ECG-gated to a physiologic simulator set to

75 beats per minute (bpm). Even though the phantom styrofoam tray was motionless, a trigger delay was supplied to permit imaging during the same phase of the cardiac cycle, as would be the scenario for *in vivo* imaging. Since some *TI*s were greater than the *RR* interval (*RR* = 850ms), the trigger delay was set to the "diastolic" period of the *subsequent* "heartbeat". Other IR-ss (b-SSFP) sequence parameters were: FOV: 300×285mm, 112 lines (single-shot), 256 reconstruction matrix, 8mm thickness, and TR/TE/α = 2.5ms/1ms/40°. A maximum bandwidth was used, and scan time was 2 seconds.

"Post-Contrast" T_1 Measurement

The 2-point segmented IR method (proposed for *post*-contrast T_1 measurements, abbreviated here as "2pt-IR") was validated on the T_1 phantoms at 3T using a *TI*-pair that satisfied the conclusions observed in the mathematical simulations of the sequence (see Chapter 3). Particularly, large T_1 solution differences, which made the elimination of one solution an easier task, occurred when *the inversion times were very different from one another*. For this validation, a *TI*-pair of 650 and 150ms was used since it provided a long *TI* (650ms, that is also shorter than a typical *RR* interval), and a short *TI* (150ms) that allows *linear* k-space ordering. All scans were gated to a 75 bpm ECG physiologic simulator and trigger delays enabled imaging during the same phase of the *RR* window. Other 2pt-IR (b-SSFP) sequence parameters were: FOV: 300 × 285mm, 196 × 256 matrix, 42 lines/segment, 8mm thickness, TR/TE/α = 3.1ms/1.5ms/40°, and 3 *RR* segment intervals to allow sufficient relaxation. Scan time was 15 "heart beats".

Look-Locker T_1 Measurement

T_1 values were also measured at 3T using a multi-image IR sequence (also known as a "Look-Locker" sequence [Look et al 1970]), which has been used in other investigations of T_1 [Kay et al. 1990, Diechmann et al. 1991, Pickup et al. 2004, Klein et al. 2004]. This technique is commonly implemented by performing an inversion pulse once per trigger period prior to a multi-frame (cine) readout (see Figure E.2, Appendix E). Since the scan acquires 20 to 50 sequential images per inversion preparation, each frame (or image) is associated with a different inversion time and, hence, has unique image contrast. Therefore, the scan is similar to acquiring many separate images with different *TI* times, but with the convenience of acquiring all these images in one scan. This is a very time-efficient method for T_1 approximation; however, the technique is not commonly available on all scanners or field strengths. Furthermore, the T_1 obtained from these data sets are typically not equivalent to the *true* T_1, and necessitates appropriate corrections (see Results). The Look-Locker sequence in this experiment was programmed to acquire images at approximately 40ms intervals using two different segment interval lengths: 2-"heartbeat" interval (*RR* = 2000ms) and 3-"heartbeat" interval (*RR* = 3000ms). In both cases, the first image had an effective *TI* equivalent to roughly 6.5ms, and the overall data acquisition lengths were 1000ms and 2000ms, respectively, which left 1000ms for unperturbed longitudinal magnetization recovery before the next inversion pulse. Data acquisition was performed with a FLASH-EPI hybrid sequence with the following sequence parameters: $270\times270mm^2$ FOV, 128×128 matrix, TR/TE/α = 40ms/5.4ms/10°, 8mm slice thickness, 7 EPI lines/TR, and bandwidth 125 Hz per pixel.

Calculation of T_1 values

Post-processing of all T_1 scans involved obtaining the appropriate scaling factors for each image (ImageExportTool, Philips Medical Systems, Best, The Netherlands), which enabled comparison of signal intensities between scans. For IR-ss, each pixel T_1 value was determined with Matlab 6.5 (MathWorks, Natick, MA) from a two parameter fit of a mono-exponential inversion recovery curve, which is described in Appendix C. The goodness of the fit was expressed with the correlation coefficient, r^2. Appendix C also provides the method for determining T_1 using the 2-pt IR method, which was less computationally demanding. Recall that 2pt- IR yields *two solutions*. T_1-maps using both T_1 solutions were computed, and one solution was eliminated based on the results of the reference T_1 calculations.

For the Look-Locker data, T_1* was determined from a 3-parameter fit to: $M(nTR) = A(1 - B\exp(-nTR / T_1^*))$, where $M(nTR)$ and nTR are, respectively, the mean signal intensities and image time intervals of each frame, and A, B, and T_1* are the fit parameters. Appropriate corrections were made to determine T_1 from T_1* [Look et al. 1970, Diechmann et al. 1991, Pickup et al. 2004].

The percent difference of each T_1 measurement technique relative to the reference measurements was determined from: $\%diff = (T_{1obs} - T_{1ref}) / T_{1ref}$, where T_{1obs} is the observed T_1 using the proposed techniques. The homogeneity of the measurement was determined from the standard deviation of the measurement ROI taken from the T_1-map.

FLASH and SSFP Theory Validation

Before delayed enhancement contrast experiments were performed with T_1 phantoms and correlated with simulation results, the theoretical equations of FLASH and b-SSFP utilized in Chapter 3 were validated with imaging experiments. The confirmation of the transient approach to steady-state magnetization (which is relevant in delayed enhancement imaging and T_1 measurement protocols) and the signal amplitude of IR-FLASH as a function of T_1 are outlined in the two sub-sections below.

The Transient Approach to Steady-State in FLASH and b-SSFP

The transient state of FLASH and b-SSFP was determined with five T_1 phantoms. The phantoms were constructed individually using 4% agar gel made with 0, 0.2, 0.4, 0.8, and 1.2mM of Gd-DTPA-BMA in 50mL plastic test tubes. Before the experiment, the T_1 values were determined with inversion recovery techniques to be 165, 242, 430, 749, and 1883ms at 1.5T. These T_1s are expected physiologic values seen *in vivo*.

To measure the effect of a series of RF pulses on signal intensity, the excitation flip angle (α) was kept constant, and a defined number of start-up, or "dummy", RF pulses were executed *prior* to data acquisition (Figure E.3, Appendix E). These "dummy" pulses were executed without spatial encoding gradients, so no data was acquired. By varying the number of "dummy" pulses, it was possible to estimate the *signal reduction as a function of RF pulse number*, which is analogous to describing the transition to steady-state as mathematically presented in Chapter 3.

The experiment was implemented at 1.5T (Philips Intera, Best, The Netherlands) using a segmented FLASH sequence. Sequence parameters were: 300×300 mm FOV,

256×256 matrix (177 phase encoding steps), 10mm slice thickness, 5 lines/segment, TR/TE/α = 5.5ms/2.6ms/20°, and a 6000ms segment interval to provide sufficient T_1 relaxation. The *k*-space profile order was made *centric* to allow the $k_y = 0$ phase-encode line to be acquired immediately following the series of "dummy" excitations. Since TE was very short and transverse magnetization was "spoiled" each TR, T_2 effects were considered negligible in the final FLASH images. The number of "dummy" pulses used in each scan was 0, 10, 30, 60, 80, and 100 (maximum allowable).

The experiment was repeated with different TRs and the flip angles. Keeping the other parameters constant, the TR was varied among 5, 20 and 40ms. Likewise, α was modified among 10, 20, and 40°. Since the assigned flip angle is known to vary across the slice profile, an average flip angle ($\bar{\alpha}$) was used in the mathematical simulations: $\bar{\alpha} = 0.7\alpha$ [Diechmann et al. 1992, Haacke 1999]. However, it must be noted that this value is an assumption and may not be precisely true at 3T. But it was important to make this estimation since numerous consecutive excitations were being used to describe the transient state, such that an error in the flip angle propagates throughout the "dummy" RF pulse train, causing significant disagreement with experimental results. The efficacy was determined from a correlation coefficient, r^2.

The transient phase of b-SSFP was examined with the same T_1 phantoms using a strategy similar to the FLASH experiment. The imaging protocol was: 300×300mm^2 FOV, 256×256 matrix, 10mm slice thickness, 5 lines/segment, TR/TE/α = 3.5ms/1.75ms/20°, and 6000ms segment intervals. "Dummy" RF pulses (10, 30, 60, 80, 100) were used prior to centric *k*-space image acquisition to approximate the transient phase. Since resonance offset is influenced by TR in b-SSFP, the repetition time was kept

as short as possible and not varied. The flip angle was modified among 20, 50, and 70° to determine α-dependency on the transient state. The three data sets were normalized and compared to mathematical b-SSFP simulations using the same imaging parameters. This comparison necessitated knowledge of T_2 values (for b-SSFP only), which were determined prior to the experiment (with a standard multi-spin echo experiment) to be 91, 80, 78, 57, and 52ms, respectively for the T_1 values listed above. The correlation was determined from the r^2 value.

IR-FLASH Phantom Imaging with Variable Flip Angle Sweep

The agreement between theoretical and experimental results of the *segmented IR-FLASH pulse sequence* was validated with eleven Gd-doped aqueous T_1 phantoms spanning from 124ms to 2381ms ($R_1 = 0.42s^{-1}$ to $8.08s^{-1}$) at 1.5T. The scan was triggered to a physiology simulator set to 75 bpm (850ms *RR* window), and a *variable flip angle sweep* was used to sample data. Imaging parameters for the IR-FLASH sequence were: 300×300 mm^2 FOV, TR/TE/α = 7.5 ms/3.8 ms/15°, 256×256 imaging matrix, 32 lines/segment, and 8mm slice thickness. Two segment interval times were defined ("1-heartbeat" and "2-heartbeat") in order to compare the influence of *post-acquisition unperturbed relaxation* (*TF*) on signal intensity. For this comparison with mathematical simulations, the inversion time, *TI*, was held constant at 250ms. A second scan was performed without the inversion preparation pulse to serve as a signal intensity reference.

Normalized signal intensity was recorded from each vial (ROI ≥ 20 pixels). These values were compared to theoretical simulations, as described earlier (Chapter 3), using appropriate adjustments for a *variable flip angle sweep* and *linear k-space ordering*. The

results were expressed as *normalized signal intensity versus* R_1. Correlation between imaging and simulations was expressed with the r^2 value.

Determination of a "Suppressed" Signal Threshold

This experiment sought to determine *the magnetization/signal threshold value below which* T_1 *samples were considered void of signal, or "suppressed"*. Motivation for this assessment evolved from the idea that certain MRI signal intensities appear "suppressed" to the naked eye despite having values one or two standard deviations *above* the background noise. Since no concessions were made to monitor noise level with the simulation studies, the only indication of tissue suppression with these simulations was a magnetization value of *zero*, which can not be precisely achieved in practice. "Zero" signal also causes a singularity point (division by zero) in signal ratio calculations. With knowledge of a *signal intensity threshold* that indicates "perceived" tissue suppression experimentally, one can determine the *range* of T_1 values suppressed in a single inversion recovery experiment using simulation routines.

To determine the level of signal intensity that appears "suppressed" due single inversion recovery, a set of 11 saline T_1 phantoms spanning 240ms to 775ms were imaged using IR-FLASH (using the parameters from above) with 1-, 2-, 3-, and 10-"heartbeat" segment intervals. The experiment with 1-, 2-, and 3-heartbeat intervals (TI = 250ms) intended to show the *sensitivity of the range of tissue suppression* to heartbeat interval time in sequences typically implemented *in vivo*. The 10-heartbeat experiment was performed to explicitly establish a "suppression" threshold value, since in this case, the magnetization will be able to fully recovery to equilibrium and therefore better mimic

a true inversion recovery experiment. In establishing the threshold value, specific T_1 phantoms were "suppressed" using inversion recovery (*TI* = 250ms), and then the *TI* was varied without disrupting the suppression. This tactic allowed subtle changes in signal intensity to be monitored while the T_1 phantoms appeared "suppressed" to the naked eye. The inversion time was varied from 220ms to 270ms in 10ms steps. The normalized data was used to subjectively determine the threshold between values that were considered "suppressed" on IR-FLASH images and those that revealed perceived signal elevation. The final threshold value was chosen such that all signal intensities below were unanimously "suppressed". The subjective grading of images was assisted by 3 MR-experienced reviewers who chose whether the phantom appeared "suppressed" or not.

Delayed Enhancement at 1.5T and 3T in Phantoms

Segmented IR-FLASH was assessed with T_1 phantoms that closely approximated the expected *in vivo* infarct and normal myocardium T_1 values at 1.5T and 3T. To simulate field and time dependency post-contrast, a *unique* set of 6 T_1 phantoms each were used to represent infarct and normal myocardium at each field, 1.5T and 3T. For "infarct" phantoms, the T_1 values at 1.5T were 217, 240, and 269ms; while at 3T the T_1 phantoms were 240, 269, and 309ms. For "normal myocardium", the T_1 values at 1.5T were 358, 430, and 535ms; while at 3T the T_1 phantoms were 430, 535, and 726ms. Thus, a total of *eight* T_1 phantoms were prepared for this experiment.

The implementation of the IR-FLASH imaging protocol was similar to the delayed enhancement protocol used routinely in clinical imaging. The number of lines per segment, which will affect the comparison of signal intensity with mathematical

simulations, was kept constant at 26 between field strengths, and *k*-space profile order was always set to *linear*. Other primary imaging parameters were also kept the same, namely FOV (300×300 mm^2), matrix size (256×256), slice thickness (8mm), and segment interval (1-heartbeat). The TR and TE values were set to "shortest" (4.4ms and 2.2ms, respectively) using a bandwidth of 300 Hz/pixel.

Without changing the flip angle, the *TI* of IR-FLASH was varied from 100 to 500ms in 25ms steps, which spans the inversion times typically used in clinical practice. The variation in *TI* was repeated for "2-heartbeat" segment intervals using a physiology simulator set to 75 bpm (850ms *RR* window). An additional scan without inversion preparation was also obtained to serve as a signal intensity reference (see Figure 4.1). The flip angle for FLASH was initially set to 20° and a variable sweep was used during the readout. To determine the sensitivity of image contrast to higher flip angles, an additional experiment was performed with a flip angle of 60°.

The imaging parameters for IR-FLASH served as input for the mathematical simulation of T_1 contrast as described in Chapter 3. For the simulation, a flip angle of $\bar{\alpha} = 0.7\alpha$ was used to compensate for variations within the slice, as before. The imaging results were compared to simulation results, and assessed on the basis of displaying similar trends with flip angle and inversion time, particularly the *zero-contrast* (TI_{zero}) and *null-point TI* (TI_{null}). For the simulation, the number of segments was set to 6, which allowed the contrast signal response curve to be stable for the calculation. From an analysis of the FLASH imaging sequence using a graphical viewer (GraphicalViewer v.1., Philips Medical Systems), it was determined that 5 "dummy" excitations *preceded*

data acquisition, and that the central phase encode step ($k_y = 0$) occurred after the 18^{th} excitation of the readout.

Results

Contrast Agent Relaxivity in Macromolecular Solutions

Figure 4.2 graphically displays the calculated relaxation rates at each field strength, along with the linear fit equation and correlation coefficient. The resulting relaxivities, taken from the slope of the linear fits, are given in Table 4.1 for each macromolecular solution. From the data*, Gd-DTPA-BMA relaxivity increases as the percentage of solid concentration increases when field strength is held constant*. This trend has been shown previously at 1.5T [Stanisz et al. 2000]. However, the rate of increase in r_1 with compartmental solid concentration, which was non-linear, was higher in this study compared to Stanisz et al, possibly since gels were created in this study. As the field strength was increased from 1.5T to 3T and 4.7T, the Gd-relaxivity as a function of macromolecular content had a smaller overall range: at 1.5T the relaxivity difference between saline and 6% milk powder samples was 2.15mM^{-1} s^{-1}, while this difference decreased to 1.65mM^{-1} s^{-1} and 0.96mM^{-1} s^{-1}, at 3T and 4.7T respectively. Relaxivity is known to decrease with temperature [Lauffer 1987, Pickup et al. 2005], thus physiologic tissues will have lower r_1 than presented here. Plots such as Figure 4.1 aid in T_1 phantom preparation at various field strengths.

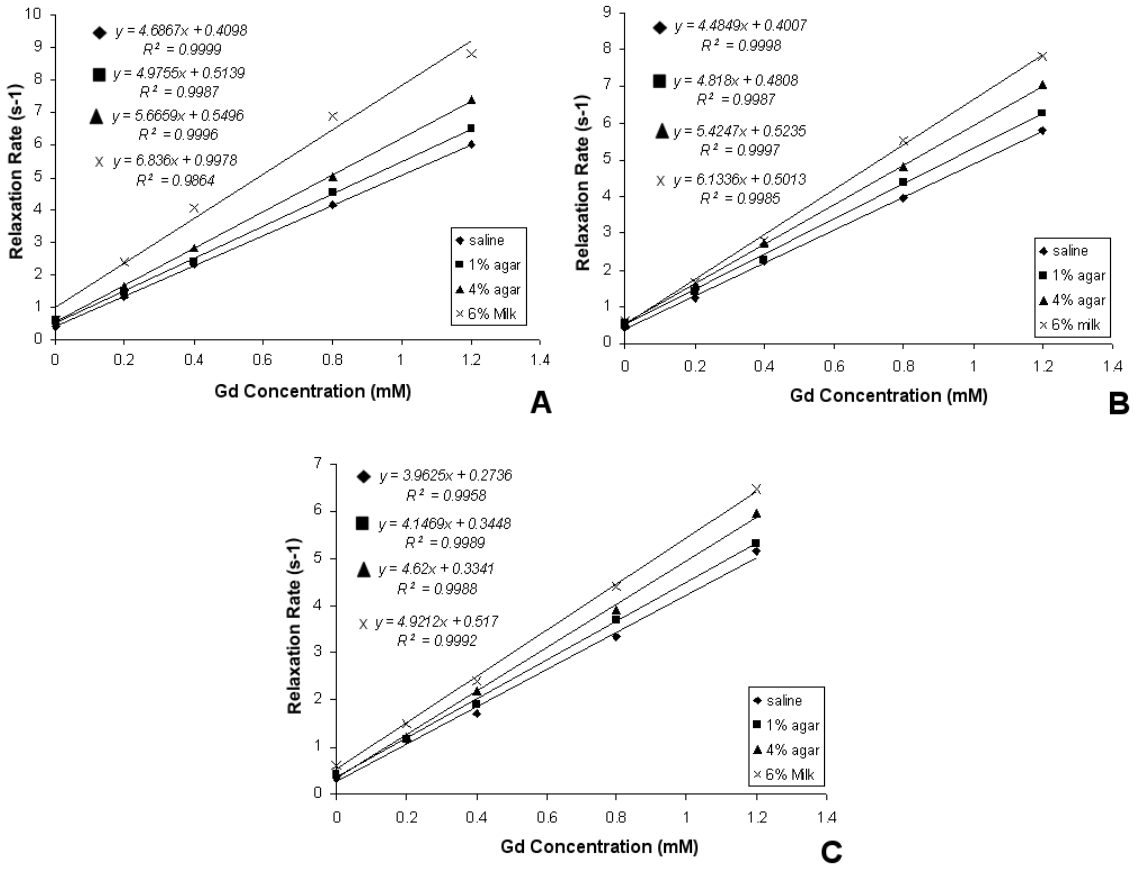

Figure 4.2. *Relaxation rate as a function of Gd concentration for saline, 1% agar, 4% agar and 6% milk powder at* ***a)*** *1.5T,* ***b)*** *3T, and* ***c)*** *4.7T.*

Table 4.1. Gadolinium Relaxivity in Various Solid Concentrations at Room Temperature

sample	% solid conc.	Gd r_1 (mM s)$^{-1}$			Range (from 1.5T to 4.7T)
		1.5T	3T	4.7T	
Saline	0%	4.67	4.48	3.96	0.72
Agar	1%	4.98	4.82	4.15	0.83
Agar	4%	5.66	5.42	4.62	1.04
Milk powder	6%	6.83	6.13	4.92	1.91
Range (from 0% to 6%)		2.15	1.65	0.96	

It can also be surmised from the data above that *the gadolinium relaxivity in various solutions becomes increasingly similar at higher fields, irrespective to the macromolecular content.* However, as shown in Table 4.1, the degree of this decrease, expressed as the overall r_1 range between 1.5T and 4.7T for each sample individually, was largest when the solid concentration was large ($1.91 mM^{-1}s^{-1}$ for 6% milk powder and $0.79\ mM^{-1}s^{-1}$ for saline). In other words, as the medium in which Gd-DTPA-BMA resides becomes more *viscous*, the relaxivity becomes more sensitive to field change.

T_1 Measurement Confirmation

Measurements from the all three T_1 measurement techniques (IR-ss, 2-pt IR, and Look-Locker ("2-beat" and "3-beat")) are shown in Table 4.2, and compared to the reference T_1 measurements in the phantoms. Two-parameter T_1 fitting to the IR-ss scans were determined with low error (relative to reference measurements), particularly for long T_1s (> 500ms) (<5% difference), which span the T_1 values seen pre-contrast *in vivo*. Accuracy for measuring low T_1s using the IR-ss technique was also accurate even though the null-point was not sampled with the chosen *TI*s. However, the 95% confidence interval (CI) was larger in these instances (approximately ±20ms), making the measurement subject to variability when T_1 is low (T_1 < 500ms). The 2-pt IR method yielded low error when T_1 values were low (T_1 < 550ms, <5% difference), which resemble T_1 values seen post-contrast *in vivo*. Accuracy for measuring long T_1s was compromised by the finite segment interval length (3 *RR* intervals). The image quality of 2pt-IR was much higher than IR-ss, owing to less blurring (due to a greater number of data sampling points) and a shorter data acquisition window. As a result, use of IR-ss

post-contrast for low T_1 measurement should only be used for localization or when patient breath-holding becomes difficult.

Table 4.2. Comparison of T_1 Measurement Methods.

[Gd] mM	T_{1ref} (ms)[a]	IR-ss 4pt (ms)		IR 2pt (ms)		LookLocker 2bt (*RR* = 2000ms)[d] (ms)			LookLocker 3bt (*RR* = 3000ms)[e] (ms)		
		T_1[b]	%diff	T_1	%diff	T_1*[c]	T_1	%diff	T_1*[c]	T_1	%diff
0	2831	2881	1.8%	1526	-46.1%	1683	4626	63.4%	1233	2309	-18.4%
.05	1844	1827	-0.9%	1281	-30.5%	1096	1871	1.5%	973	1538	-16.6%
.10	1314	1324	0.8%	1065	-19.0%	831	1212	-7.8%	781	1108	-15.7%
.15	1054	1046	-0.8%	974	-7.5%	707	965	-8.5%	677	910	-13.7%
.20	923	905	-1.9%	818	-11.3%	652	866	-6.2%	621	811	-12.1%
.25	748	699	-6.5%	693	-7.3%	570	726	-2.9%	543	683	-8.6%
.35	557	585	5.0%	528	-5.1%	444	534	-4.1%	434	519	-6.7%
.40	517	535	3.4%	516	-0.3%	430	514	-0.7%	425	506	-2.3%
.55	348	351	0.7%	336	-3.6%	305	345	-1.0%	304	344	-1.2%
.65	317	317	0.2%	307	-3.0%	276	308	-2.9%	275	307	-3.0%
.80	296	300	1.1%	285	-3.8%	265	294	-0.6%	263	292	-1.6%
1.0	209	208	-0.2%	198	-5.0%	192	206	-1.0%	192	207	-0.9%
1.2	202	199	-1.7%	192	-4.8%	187	201	-0.6%	187	201	-0.3%

[a]Measurement 95% confidence interval (CI) ±10ms; [b]Measurement 95% CI approx. ±10-20ms; [c]Measurement 95% CI approx ±5-15ms; [d]data acquisition window (dacq) = 1000ms; [e]dacq = 2000ms.

Two variations of the Look-Locker method are shown in Table 4.2, which differ only in the length of data acquisition widow. A 3-parameter fit of the data sets produced an *apparent* T_1 relaxation time, given by T_1*, which is related to the true T_1 value by:

$$E_1^* = E_1 \cos(\alpha), \qquad [3]$$

where $E_1^* = \exp(-TR / T_1^*)$, and α is the excitation angle. This relationship, which was briefly introduced earlier (see Eq. [3.11]), occurs because magnetization during the multi-

pulse Look-Locker sequence is being driven to steady-state (see Figure 3.2) rather than recovering freely to its equilibrium value, M_0. Consequently, the conventional inversion recovery equation (Eq. [3.5]) does not accurately describe T_1 relaxation. From Table 4.2, the Look-Locker method (after correction) was more accurate for low T_1. This occurred because $T_1^* \approx T_1$ for a broad range of α for low T_1. Furthermore, following data acquisition, these low T_1s were more likely to recover completely back to equilibrium, a requirement noted previously to produce accurate results [Pickup et al. 2004]. There was no advantage gained when the data acquisition window was increased to 3000ms, despite the increase in sample points. The possible benefit of long data acquisition windows, however, was that the steady-state value was better approximated during the 3-parameter fit, making T_1^* more reproducible.

FLASH and b-SSFP Theory Validation

The Transient Approach to Steady-State in FLASH and b-SSFP

The transient approach to steady state in FLASH and b-SSFP sequences were approximated with constant flip angle "dummy" pulses prior to data acquisition. Correlation coefficients greater than 0.98 were measured between simulation and experimental results, meaning that *both data sets exhibited similar trends during the transient approach to steady-state*. In all cases, the simulation results were able to accurately predict the TR- and flip angle-dependent transition to steady state as a function of different T_1 values.

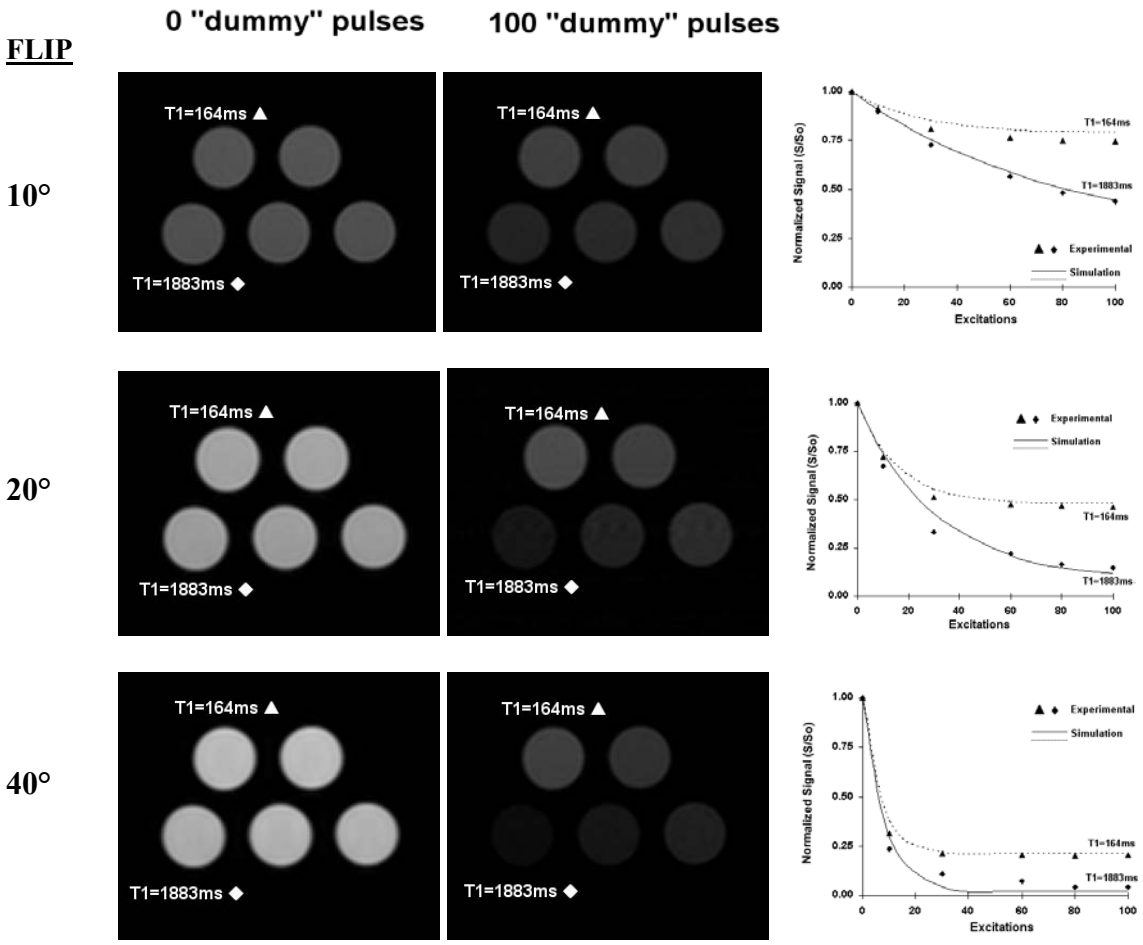

Figure 4.3. *Correlation between simulation and phantom imaging of the transient state in FLASH imaging with TR = 5ms.*

FLASH imaging results comparing the signal intensity after 0 and 100 "dummy" RF pulses are shown in Figure 4.3 for flip angles 10, 20 and 40° and a TR of 5ms. Also shown are the normalized signal intensities for selected T_1 phantoms with corresponding mathematical simulation results (other T_1 phantom data were not included in the plot for visualization purposes). An increase in flip angle resulted in a greater saturation effect and a faster approach to steady state, which was predicted by the mathematical simulations in Chapter 3 (see Figure 3.1), and also shown by the curves adjacent to the images in Figure 4.3. Moreover, a comparison among the different flip angle experiments

revealed that the signal intensities from the scan *without* "dummy" pulses were related by *exactly* the sine of the corresponding flip angle. This result further confirms a close correlation with mathematical results. Except for the 40° case, only the short T_1 phantoms (T_1 = 165, 242, and 430ms) exhibited signal intensities near their steady-state value after 100 "dummy" excitations, while the two remaining phantoms (T_1 = 749 and 1883ms) still showed evidence of being in the transient state. The lack of image contrast for "dummy" excitations < 30 is the reason that *unprepared* FLASH imaging is *not* used in delayed enhancement imaging.

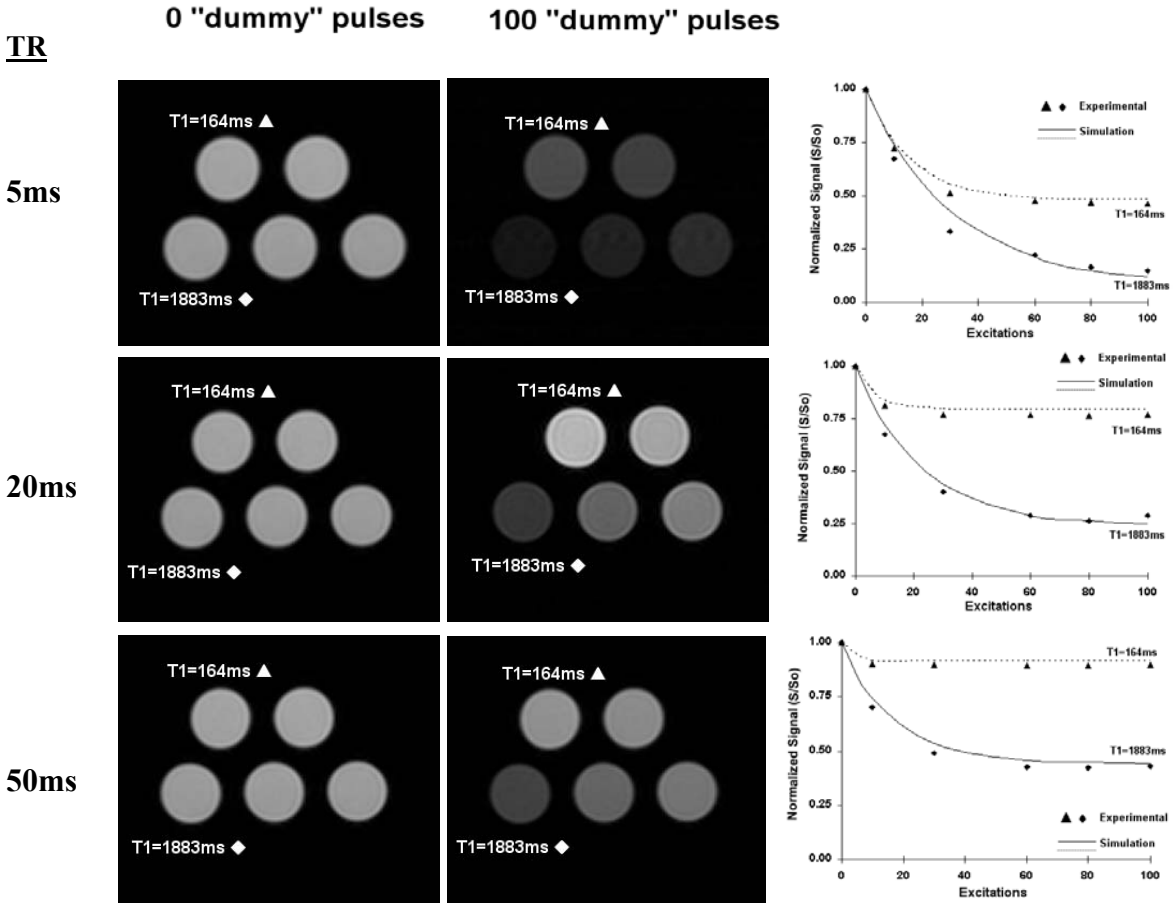

Figure 4.4. *Correlation between simulation and phantom imaging of the transient state in FLASH imaging with α = 20°.*

The dependency of the approach to steady-state on TR is shown in Figure 4.4 for the 0 and 100 "dummy" pulse scans using a constant flip angle of 20°. It was found that the normalized signal intensity from the T_1 phantoms was much larger as TR increased, which was consistent with the predictions of the FLASH simulation ($r^2 = 0.99$). A TR of 50ms not only produced a faster approach to steady-state, but also greater steady-state signal intensities than the other two TR scenarios (+34 ± 14% vs. TR = 20ms; +156 ± 46% vs. TR = 5ms). Among the T_1 values, the approach to steady-state was fastest for low T_1 values.

Imaging the transient phase of b-SSFP is depicted in Figure 4.5, along with imaging examples of 0 and 100 "dummy" excitations. The flip angle was varied among 20, 50 and 70° while keeping TR and TE fixed at 3.5ms and 1.7ms, respectively. Figure 4.5 reveals minor signal saturation (compared to FLASH), and is more distinctive for long T_1 values (T_1 = 1883ms). The percent reduction of signal intensity between 0 and 100 "dummy" excitations was only 16% for T_1 = 1883ms and 9% for T_1 = 165ms when the flip angle was 20°. This relatively small reduction in normalized signal intensity after 100 excitations made T_1 distinction difficult both visually and quantitatively, as indicated by the proximity of the simulation and experimental curves. Image contrast between the selected T_1 values remained low as α was increased to 50 and 70°; however, the correlation coefficients between simulation and experimental results were very high ($r^2 >$ 0.98). The phantoms had a broad range of T_2/T_1 ratios (0.05-0.31) and similar M_0, which, according to steady-state b-SSFP theory, should provide significant signal contrast between the phantoms. However, since the steady-state magnetization was *not* achieved

during the experiment, the signal intensities given in Figure 4.5 could not be compared on the basis of T_2/T_1 ratios.

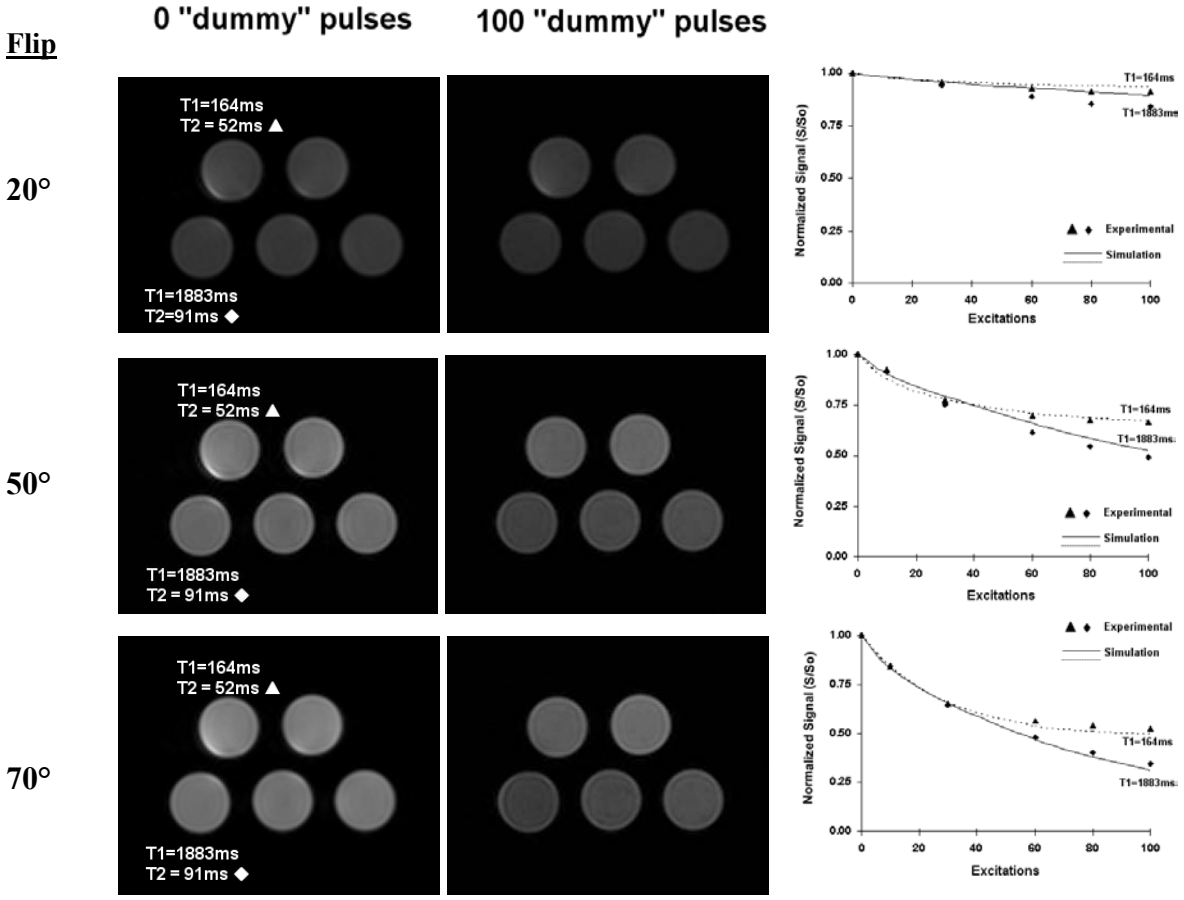

Figure 4.5. *Flip angle dependence of b-SSFP transient response (TR = 5ms).*

IR-FLASH Imaging in Phantoms with Variable Flip Angle Sweep

Figure 4.6 shows a comparison between a T_1 phantom image and a mathematical simulation for IR-FLASH (*TI* = 250ms) as a function of R_1. The display convention has R_1 increasing from left to right (bottom row), then from right to left (middle), finally from right to left (topmost). Normalized signal intensities were measured and plotted for 11 R_1 tubes spanning $0.42s^{-1}$ to $8.08s^{-1}$ (The T_1s of the two remaining tubes were not

accurately measured due to their very high Gd concentration). The predicted curves were a close approximation of the signal measurements obtained from the images, as shown by the corresponding correlation coefficients ($r^2 > 0.96$). Sources of error due to imperfect pulse angles with finite duration were not accounted for in the simulation.

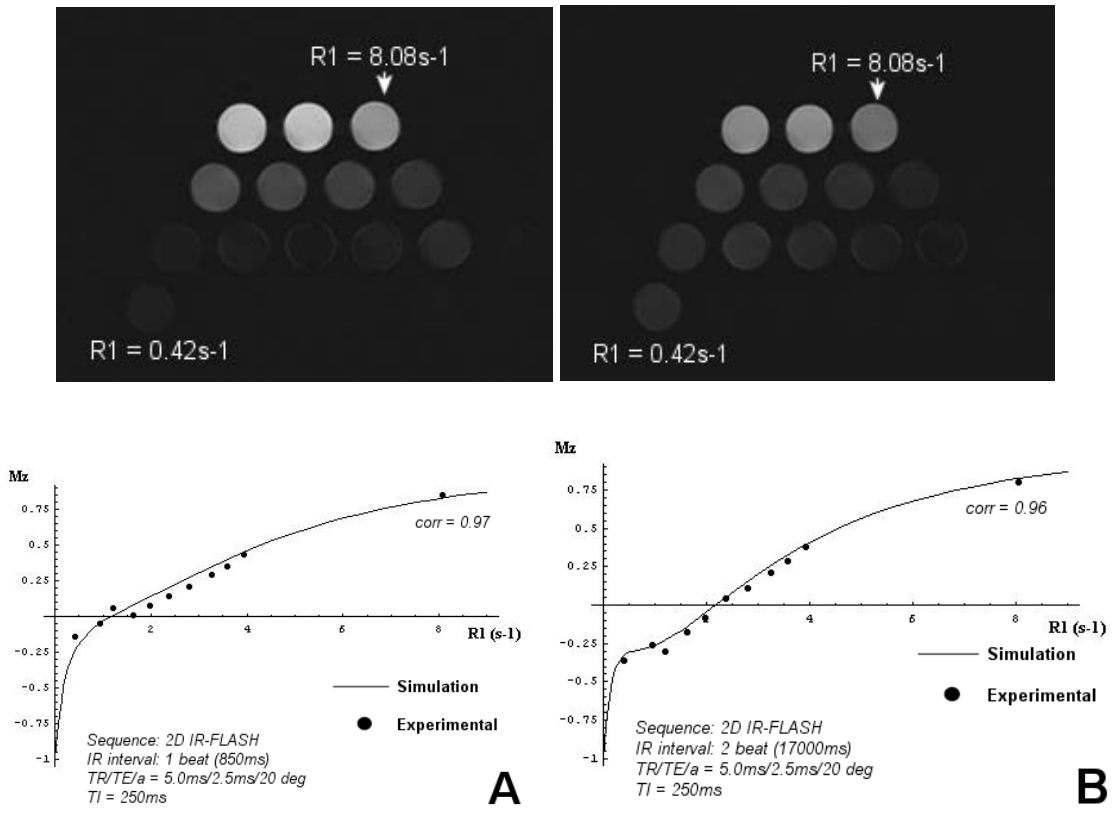

Figure 4.6. *Correlation of IR-FLASH imaging and simulation as a function of R_1 for* ***a)*** *RR = 850ms and* ***b)*** *RR = 1700ms.*

Ideally, an inversion time of 250ms would cause a zero-crossing to occur at $R_1 = 2.77s^{-1}$, which would occur assuming perfect spin inversion, mono-exponential relaxation, and no RF acquisition pulses. However, because of a finite segment interval time (*RR* = 850 and 1700ms) and the progressive saturation of magnetization due to RF excitation during the acquisition period, the observed R_1 "zero-crossing" was lower than

if the acquisition had not been taken into account. This trend existed both mathematically and experimentally with the data in Figure 4.6. For 1-heartbeat intervals (*RR* = 850ms), the inversion time of 250ms imparted signal suppression of R_1 values in the range $0.95s^{-1}$ to $1.98s^{-1}$. The precise zero-crossing (determined mathematically) occurs at approximately $R_1 = 1.25s^{-1}$. Compared to the 1-heartbeat case, an increase in *TF* (2-heartbeat interval) caused a smaller range of T_1 phantoms to be near zero signal intensity ($1.98s^{-1}$ to $2.38s^{-1}$, Figure 4.6b), with a mathematically determined zero-crossing at approximately $R_1 = 2.25s^{-1}$. With longer *TF* (or *RR* interval), the zero-crossing tends to converge to the value of $R_1 = 2.77s^{-1}$. Additionally, the observation that the suppression range *decreases* as *TF* becomes large makes the 2-heartbeat sequence more *TI* sensitive. *These results imply that the same TI would not impart the same infarct-to-normal myocardium contrast in both 1-beat and 2-beat sequences.*

Determination of a "Suppressed" Signal Threshold

Figure 4.7 shows IR-FLASH with 1-, 2-, and 3-heartbeat intervals for *TI* = 250ms. White arrows indicate the specific T_1 phantoms considered "suppressed" by visual inspection from 3 reviewer evaluations. The number of suppressed T_1 phantoms decreased as the number of heartbeat intervals increased. In each experiment, however, *single inversion FLASH imaging was able to visually suppress a range of T_1 phantoms.* Quantitatively, the measured normalized signal intensity from these "suppressed" T_1 phantoms were consistently under 0.075, or 7.5% of maximum signal (as determined from a non-prepared scan with the same parameters). Figure 4.8 reaffirms this result by plotting the normalized signal intensity of IR-FLASH with 10 heartbeat intervals and *TI*

ranging from 220ms to 270ms. The data points indicated by an *open circle* were considered "suppressed" by visual inspection from three volunteers. As with the previous observation, these normalized values were generally less than 0.10. However, *TI* = 250ms seemed to suppress T_1 = 302ms, but not T_1 = 380ms. This means some uncertainty exists even when the suppression threshold is 0.10, so a lower threshold might be recommended. For the simulation studies that parallel *in vivo* studies in Chapter 6 and 7, a suppression threshold value of 0.05 (5%) will be used.

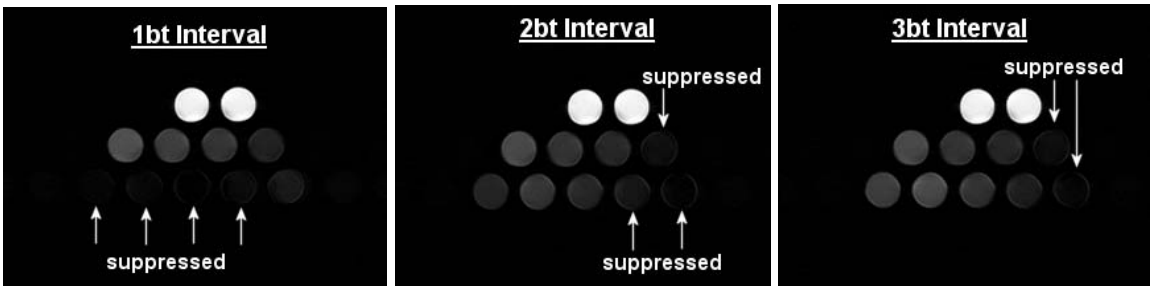

Figure 4.7. *Degree of signal suppression for TI = 250ms as a function of heartbeat interval.*

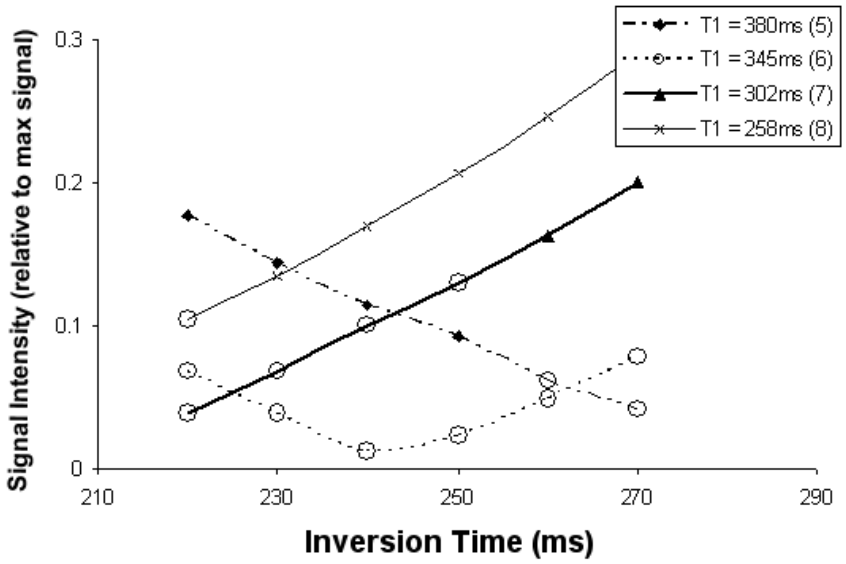

Figure 4.8. *Normalized signal intensity over a small TI range for selected T_1.*

Delayed Enhancement Imaging at 1.5T and 3T in Phantoms

The normalized signal difference between "normal myocardium" and "infarct" T_1 phantoms was used to determine image contrast as a function of inversion time. Image data was compared to simulation data using the same scan parameters (with flip angle adjustments) and T_1 values. Overall, *the correlation between simulation and experimental results exceeded 0.95*.

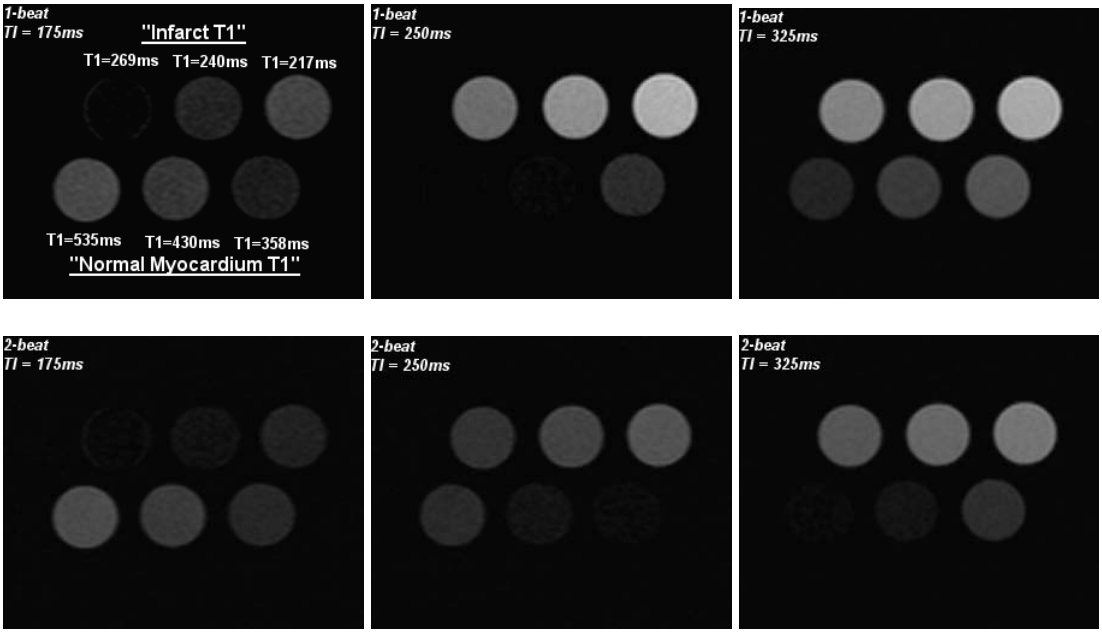

Figure 4.9. *Sample images from phantom IR-FLASH imaging at 1.5T (TI = 175, 250, 325ms) using 1- and 2-heartbeat intervals.*

Figure 4.9 and 4.10 shows sample images obtained at 1.5T and 3T using a *TI* of 175, 250, and 325ms for 1- and 2-beat IR-FLASH, respectively. Note that the signal intensities and image contrast were dissimilar between the two field strengths *only because the T_1 values of the phantoms were unique to each field* (see Methods). To be

sure, when the *same* T_1 phantoms were imaged at both field strengths, no observable difference in image contrast was measured.

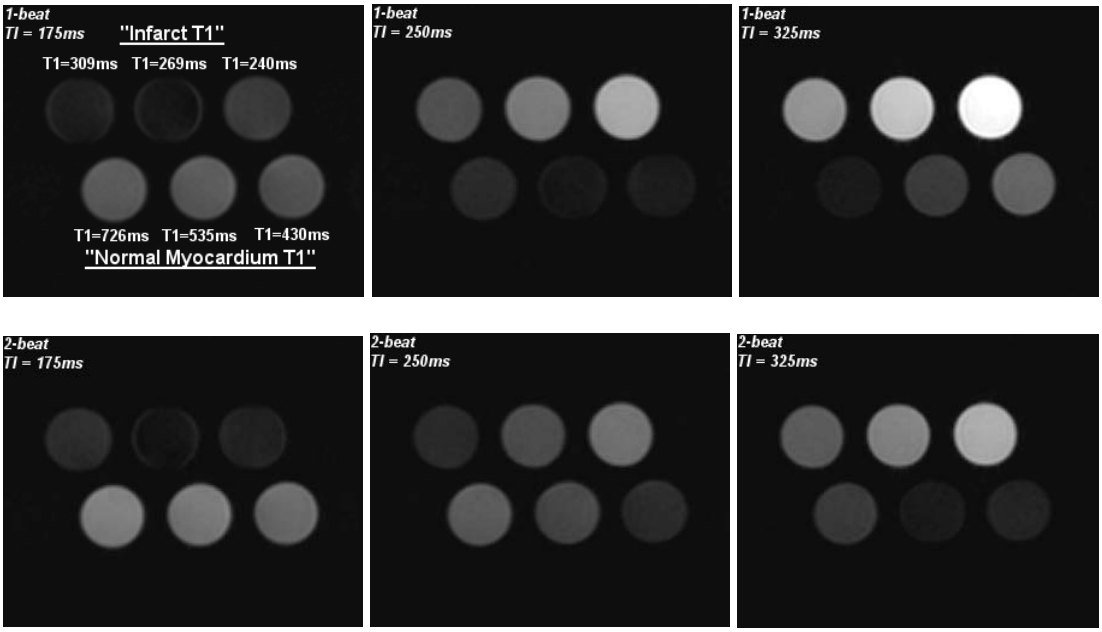

Figure 4.10. *Sample images from phantom IR-FLASH imaging at 3T (TI = 175, 250, 325ms) using 1- and 2-heartbeat intervals.*

The most revealing qualitative difference between imaging at 1.5T and 3T was the increase in re-scaled *signal intensity* at 3T for similar scan parameters and T_1 (measured from the FLASH sequence without IR preparation). The signal ratio from this comparison was 1.33 ± .08, *favoring 3T*.

Figure 4.11 shows quantitative results correlating image contrast data with simulation results, for both 1- and 2-beat imaging scenarios. Generally, high correlation was apparent between the imaging results (*symbols*) and simulation data (*line*) (Figure 4.11), which *validates the precision of the mathematical framework of Chapter 3* r^2>0.90). Since several combinations of "infarct" and "normal myocardium" T_1 values were compared in this experiment, the graphs only show results from T_{1myo} = 535ms (3T) and T_{1myo} = 430ms (1.5T) to promote readability. Each plot expresses the *difference in*

normalized signal intensity between the particular T_1 values as a function of inversion time. As shown in Figure 4.11, every curve has an associated TI_{zero} (where the T_1 values produce no signal contrast), TI_{opt} (where the highest contrast is achieved), and TI_{null} (where T_{1myo} is suppressed). The null-point *TI* was exclusively determined from the experimental results by visual inspection. 2D-plots such as these were used to determine TI_{opt} for maximal image contrast, and TI_{zero}, the point of zero-contrast. Given that the inversion time steps in this study were 25ms, the *TI* at which zero image contrast occurred correlated well with simulation results (1.5T: $r^2 = 0.83$ (1-beat); 0.96 (2-beat); 3T: $r^2 = 0.91$ (1-beat); 0.99 (2-beat)).

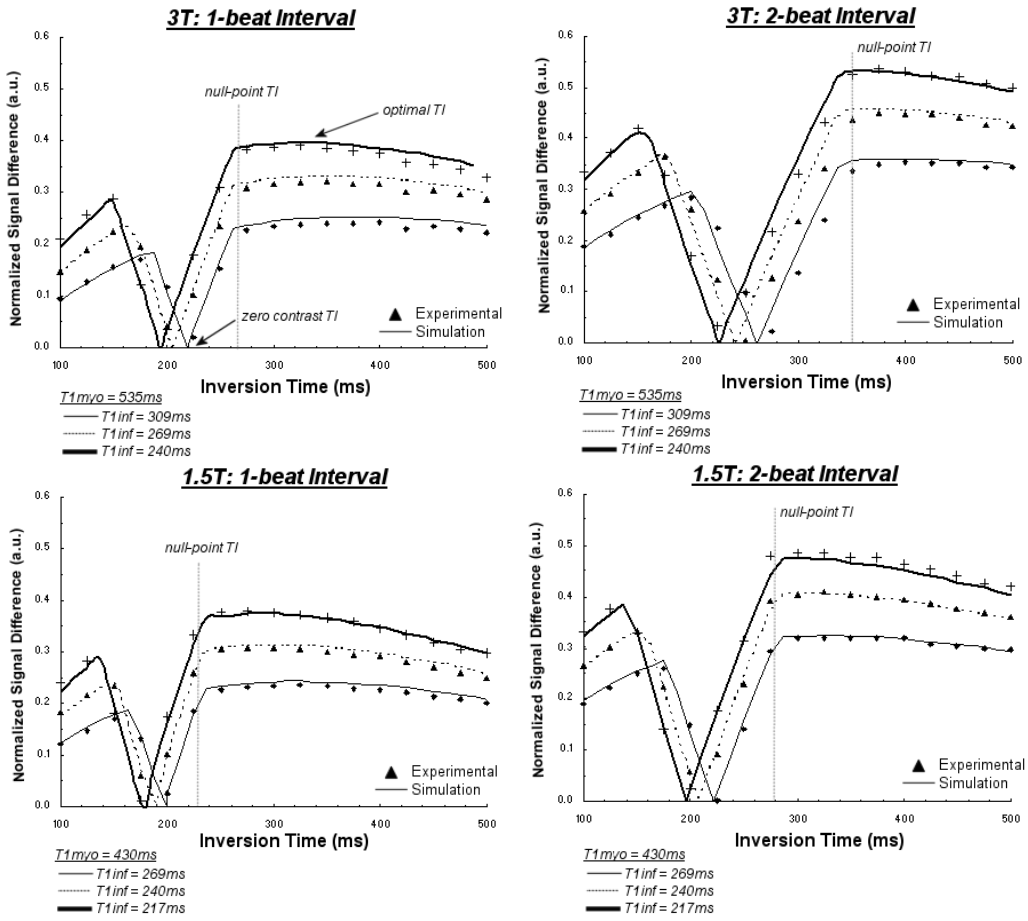

Figure 4.11. *Correlation between imaging and simulation for delayed enhancement imaging (IR-FLASH) at 1.5T and 3T.*

The maximum signal difference (found at TI_{opt}) was also equivalent between simulation and experimental results. Even so, a slight misalignment was found with the simulation results, which may have been a result of imperfect flip angle estimation or errors in T_1 approximation between field strengths. Recall that the simulation process is blind to fundamental field strength differences, such as B_0 and B_{1trans} spatial variations, are absent. Table 4.3 details the overall correlation coefficients for each comparison performed, as well as TI_{zero}.

Table 4.3. Correlation between Experimental and Simulation Results for Phantom T_1-pairs

B_0	T_{1myo} (ms)	T_{1inf} (ms)	1-beat (*RR* = 850ms)			2-beat (*RR* = 1700ms)		
			[a]r^2	Zero-contrast *TI* (ms)		[a]r^2	Zero-contrast *TI* (ms)	
				exp[b]	sim[c]		exp[b]	sim[c]
1.5T	535	269	0.999	200	206	0.997	250	242
		240	1.000	200	194	0.999	225	226
		217	0.998	175	187	0.999	225	213
	430	269	0.999	200	196	0.996	225	222
		240	0.999	175	186	0.998	200	208
		217	0.998	175	179	0.999	200	197
	358	269	0.976	175	186	0.987	200	205
		240	0.994	175	176	0.993	175	192
		217	0.986	175	170	0.994	175	182
3T	726	309	0.995	225	229	0.977	300	288
		269	0.996	225	214	0.986	275	265
		240	0.998	200	202	0.992	250	247
	535	309	0.994	225	218	0.972	275	261
		269	0.997	200	205	0.986	250	242
		240	0.999	200	193	0.993	225	226
	430	309	0.982	200	207	0.949	250	239
		269	0.992	200	195	0.983	225	222
		240	0.996	175	184	0.989	200	208

[a]r^2: overall correlation between simulation and experimental results; [b]exp: experimental results (TI resolution = 25ms); [c]sim: simulation results; RR: simulated R-to-R interval; B_0: field strength; T_{1myo}: "normal myocardium" T_1 phantom; T_{1inf}: "infarct" T_1 phantom

The T_1 *ratio* between the "infarct" and "normal myocardium" phantoms was found to be influential in predicting the magnitude of maximum $T_{1contrast}$: *as the T_1 ratio decreased, the maximum contrast increased accordingly*. This trend had no dependency on field strength (assuming $M_0 = 1$, which is not necessarily true, but was utilized here to compared simulation and experimental results). This intuitive result is expressed in Figure 4.12, which shows the maximum image contrast for 1-beat imaging scenarios (*solid bars*). Also indicated is the image contrast *gain* by using 2-beat segment intervals (*extension lines*). For the same pairs of "infarct" and "normal myocardium" T_1 phantoms, an average contrast gain of 39.6 ± 9.1% was measured for 2-beat scenarios, with the maximum benefit occurring when the T_1 of "normal myocardium" was large (T_1 = 726 ms).

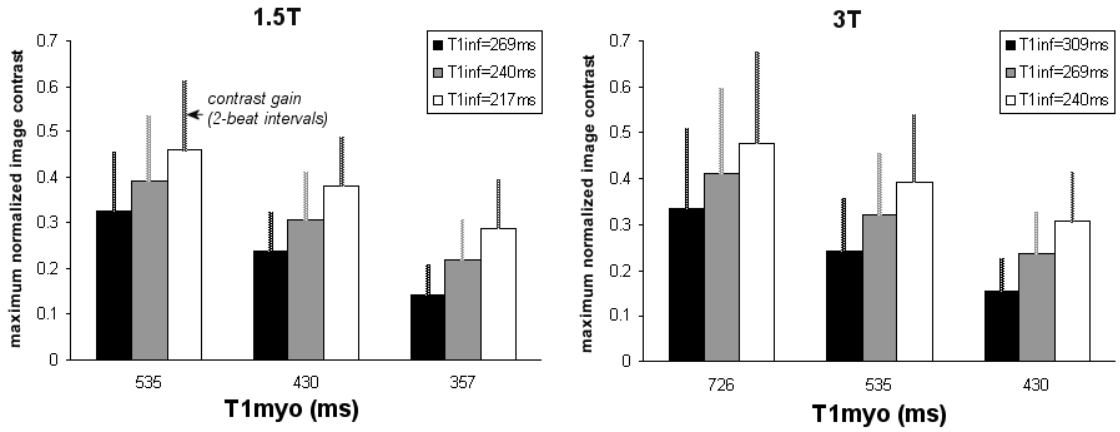

Figure 4.12. *Maximum attainable image contrast in phantom experiments using 1- and 2-beat IR-FLASH at 1.5T and 3T.*

Table 4.4. Comparison of Null-point *TI* and Optimal *TI*

B_0	T_{1myo} (ms)	T_{1inf} (ms)	1-beat (*RR*=850ms)		2-beat (*RR*=1700ms)	
			Null-point *TI*[a] (ms)	Optimal *TI*[a] (ms)	Null-point *TI*[a] (ms)	Optimal *TI*[a] (ms)
1.5T	535	269	250-275	352	350	364
		240	250-275	331	350	341
		217	250-275	313	350	341
	430	269	225	323	275	329
		240	225	304	275	309
		217	225	287	275	292
	357	269	200	298	225	302
		240	200	280	225	283
		217	200	265	225	268
3T	726	309	300	407	425	449
		269	300	379	425	428
		240	300	257	425	428
	535	309	275	367	350	393
		269	275	342	350	364
		240	275	322	350	341
	430	309	225	337	300	355
		269	225	315	300	329
		240	225	297	300	309

[a]*Corresponding contrast differed by less than 7%.*

The optimal *TI* and null-point *TI* for these experiments are given in Table 4.4. The null-point *TI* remained constant for a given T_{1myo}, while TI_{opt} was dependent on *both* T_{1myo} and T_{1inf}. In 33 of 36 comparisons (1-beat and 2-beat), the optimal *TIs* determined from the simulation results were *longer* than the null-point *TIs* determined from the phantom experiments (range: ~3-115ms). This result was also found with the simulation results in Chapter 3. TI_{opt} and TI_{null} converged as the difference in "normal" and "infarct" T_1 values increased (became more distinct). The corresponding increase in the optimal

image contrast using TI_{opt} was generally negligible compared to the contrast attained using TI_{null} (< 7%). Also note the high dependency of TI_{opt} and TI_{null} on the segment interval time (increase of ~3-125ms from 1-beat to 2-beat, Table 4.4).

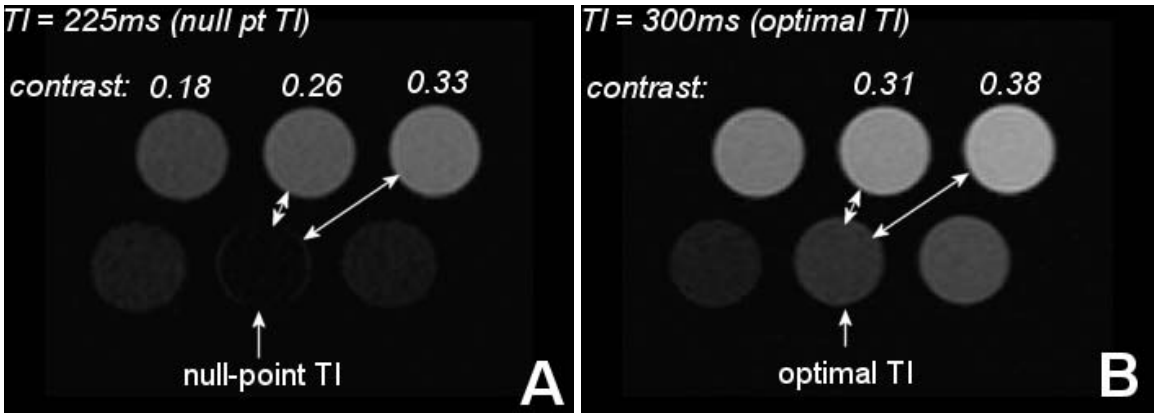

Figure 4.13. *Image contrast at 1.5T depicting the difference in* ***a)*** *null-point (TI_{null}) and* ***b)*** *optimal TI (TI_{opt}).*

An example of the difference in image contrast attained using TI_{null} and TI_{opt} is given in Figure 4.13, which was performed at 1.5T with 1-beat IR-FLASH using two *TI*s: 225ms and 300ms. With *TI* = 225ms, the middle "normal myocardium" T_1 phantom (430ms) is nulled (*arrow*), and produces specific values of image contrast with "infarct" T_1s (*top row*), as shown. The optimal *TI* for T_{1myo} = 430ms was approximately 300ms for T_{1inf} = 240ms and 217ms (Table 4.4). As displayed Figure 4.13b, it was determined that the normalized image contrast was 0.05 *higher* using TI_{opt} than TI_{null} when T_{1myo} = 430ms was compared to T_{1inf} = 240 and 217ms. Note that T_{1myo} = 430ms is not suppressed at TI_{opt}.

Figure 4.14 shows two IR-FLASH delayed enhancement phantom images at 1.5T using a flip angle of 60° and *TI*s of 300 and 500. It is clear that the relatively large flip

angle significantly reduces image contrast between the T_1 phantoms, in addition to degrading image quality. The image contrast of IR-FLASH using $\alpha = 60°$ significantly lessened the influence of the inversion pulse compared to lower flip angle IR-FLASH, which were depicted in Figures 4.9 and 4.10. This is consistent with the simulation studies of Chapter 3, which showed *constant* image contrast between two T_1 values for a wide range of *TI*s when the flip angle was increased beyond 60°. Mathematical simulations using these phantom T_1 values predicted close to *zero contrast* between "infarct" and "normal myocardium" T_1 using 60° readout pulses, even for a wide range of *TI* values. As concluded in Chapter 3, the flip angle in delayed enhancement should be between 15-30° to maintain sufficient image contrast as a function of *TI*.

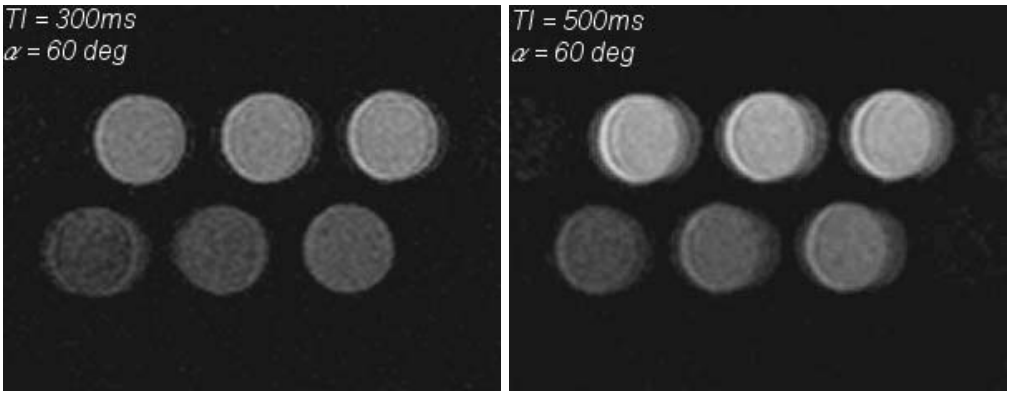

Figure 4.14. *Phantoms imaged with segmented IR-FLASH using $\alpha = 60°$, showing that image contrast becomes more insensitive to TI with high flip angle.*

Discussion

The study of image contrast with T_1 phantoms intended to provide a confirmation of the conclusions established with the mathematical results of Chapter 3, and shed light on the dependency of delayed enhancement image contrast on T_1 and inversion time, *TI*. This validation was necessary to substantiate the use of mathematical models to express

signal and contrast behavior in an experimental setting. Even though experiments with phantoms do not completely describe *in vivo* imaging, an initial impression of the change in image contrast can be realized with phantoms of particular T_1 and T_2 values. In this manner, pulse sequences can be optimized in terms of contrast-to-noise per image time, prior to implementation in clinical settings.

The phantom experiments focused on comparing mathematical and imaging data in four main areas: 1) the validation of the customized pre- and post-contrast T_1 measurement techniques in a series of phantoms with defined T_1 values; 2) the description of the approach to steady-state magnetization in FLASH and b-SSFP pulse sequences; 3) the confirmation of IR-FLASH imaging results with the expected signal intensity from corresponding simulations; and 4) the investigation of the role of varying flip angle and inversion time in delayed enhancement image contrast using specific T_1 phantoms. Before these comparisons, studies were conducted to evaluate the relaxivity of Gd-DTPA-BMA in macromolecular solutions as a function of field strength, which is important in phantom preparation and in vivo contrast studies.

Contrast Agent Relaxivity

This study found that the inherent property of Gd-DTPA-BMA, namely, the *relaxivity* r_1, varies with the macromolecular content of the solution in which it resides and the main magnetic field strength. Particularly, this data shows that *r_1 decreases with field strength and increases with macromolecular content*. There has been previous evidence of field dependence of Gd-DTPA relaxivity [Donahue et al. 1994, Rinck et al. 1999], which also demonstrates that the rate of r_1 decrease diminishes as field strength

increases. This means that for equivalent concentrations of gadolinium in the sample (or tissue), the relationship Eq. [2] predicts that the R_1 contribution from the paramagnetic contrast agent ($r_1 \times$[Gd]) reduces at higher field strengths. The decrease in contrast agent relaxivity from 1.5T to 3T has implications in contrast-enhanced MRI. Notably, for a given concentration of Gd-DTPA-BMA, the effect of the agent on R_1 is *less* at higher fields (given similar doses), leading to lower observed R_1 values. Even though this may imply lower signal strength at 3T, the concomitant increase in overall proton sensitivity may offset the presence of longer T_1 values.

T_1 Measurement Confirmation

Two customized T_1 measurement techniques were introduced in Chapter 3 for purpose of measuring pre- and post-contrast T_1 values *in vivo*. The two methods were validated by measuring the T_1 values of gadolinium-doped saline phantoms and comparing the results to reference T_1 measurements and the commonly used "Look-Locker" technique. The method proposed for pre-contrast T_1 measurements (4-point single-shot IR b-SSFP or FLASH, abbreviated "IR-ss") was implemented using a specific range of *TI* values selected to span the expected null-points of pre-contrast blood and myocardium (500, 800, 1100, and 1500ms). The measured differences in T_1 calculations from reference measurements were less than 10% for all T_1 values (Table 4.2). In the expected range of pre-contrast blood and myocardium at 1.5T and 3T (615ms to 1328ms), the IR-ss method performed well, with a difference between reference values of less than 5%. The IR-ss method also performed well for measuring post-contrast T_1 values ($T_1 < 500$ms), which is also a beneficial result. Often, a series of breath hold scans

can be difficult for some patients with complicated heart conditions associated with coronary artery disease. Providing an alternative imaging technique which does not require respiratory compensation allows the measurement to be performed conveniently with less patient-related stress. It also provides potential for real-time or dynamic T_1 measurements, which becomes increasingly important early after contrast-injection when T_1 values are changing rapidly. The use of a single-shot technique has also recently been used to assess delayed enhancement *in vivo* [Chung et al. 2003]. However, a key drawback observed with single-shot inversion recovery (compared to segmented techniques) is the lower spatial resolution and increased potential for motion-related image blurring. Also, partial voluming may hamper delineation of enhanced myocardium, or obscure the true signal intensity for T_1 calculations (which is even a potential problem in pre-contrast T_1 evaluation). As a result, single-shot inversion recovery should be performed secondarily in diagnostic settings; perhaps reserved as an initial scan for localization purposes.

The post-contrast 2-point ratio method (2-pt IR) performed well for approximating the T_1 values typical of post-contrast blood and myocardium ($T_1 <$ 550ms). As with the pre-contrast inversion times, the *TI* values for the 2-pt IR method were kept constant at 150 and 650ms, despite the wide range of T_1 values under investigation. From the results, it was observed that 2-pt IR had a larger overall percent difference with reference values, albeit lower variances, compared to IR-ss. The method also began to exhibit strong deviations from reference measurements when the T_1 values become large (46% difference for T_1 = 2831ms). Unlike IR-ss, which utilized a single-shot acquisition method, this observation has more to do with the finite segment interval

time (3 “heartbeats”) than with the choice of inversion times. This finite segment interval is too short for measuring T_1s greater than 700ms, since the efficacy of the 2-pt IR method using the simplistic relationship of Eq. [3.26] assumes that the magnetization has recovered to its equilibrium state after each imaging segment. Long T_1 values (>700ms) do not recover fully after 3 heart beat intervals (RR = ~3000ms), thereby causing greater magnetization saturation and discordance between the expected ratio value, S, and T_1.

Due to sensitivity of b-SSFP to field inhomogeneities at 3T, it can be shown that similar results can be obtained using IR-FLASH, which exhibits less image artifacts at 3T. Key modifications to sequence parameters must be made, however, to lessen the saturation effects. A parameter set that was found to be successful was (for IR-ss): TR/TE/α = 3.0ms/1.5ms/10-15°, 196 × 256 (60% scan percentage, half-scan), with a centric k-space acquisition order; and (for 2-pt IR) $TR/TE/\alpha$ = 3.0ms/1.5ms/10-15°, 196 × 256 (90% scan percentage), linear k-space order, 35 lines/segment, and 3 RR intervals.

Measuring T_1 using the “Look Locker” method also suffered inaccuracies with reference measurements, especially when corrections were not made. Since this technique tracks the recovery of longitudinal magnetization while being excited intermittently by low-flip RF pulses, the characteristic recovery time, T_1*, is *less* than the true recovery time, T_1. Moreover, if the segment interval time is not sufficient, the equilibrium magnetization will not be reached before the next inversion pulse, which further exacerbates the inaccuracies, and requires additional computational corrections. It can also be shown that the Look-Locker signal evolution converges to a sample’s *steady-state value* (see Figure 3.2). As a result, the solution determined from the Look-Locker data

requires complex corrections based on the flip angle and the assumption that magnetization does not recovery completely to equilibrium (especially for long T_1s).

Imaging of the Transient State

The gradual approach to steady-state signal values was visualized for various T_1 values with both FLASH and b-SSFP imaging. Imaging the transient state is important in delayed enhancement imaging since *data acquisition is routinely interrupted after each segment to accommodate cardiac motion reduction strategies, such as ECG-gating*.

This scan procedure was able to reveal the approach to steady-state for various T_1 values and scan parameters (TR and α). The dependency of the rate of magnetization reduction from a nominal value (which was obtained from a scan without "dummy" pulses) on TR and α was consistent with the behavior observed with simulation results (using appropriate flip angle corrections). From the FLASH imaging and simulation data (Figures 4.3 and 4.4), steady-state magnetization levels can be achieved quickly for low T_1 values and long TRs. Steady-state values were *not* achieved after 100 pulses when the flip angle was low (10°); however, the signal intensity was relatively constant in these cases, which would enable image acquisition during the transient phase without problematic image blurring as would be seen during transient imaging with large flip angles. For b-SSFP, the steady-state value (as predicted from Eq. [3.24]) was *not* achieved after 100 "dummy" excitations. But, similar to low-flip angle FLASH, the signal intensity was generally constant, as reflected with the mathematical simulations in Figure 4.5. As one increases the flip angle in b-SSFP, there is greater saturation of signal (Figure 4.5), but not as drastic as FLASH because of the alternating nature of the RF

excitation in b-SSFP. It is clear that one can use larger flip angles with b-SSFP without image degradation common to the transient state, such as ghosting.

Since precise echo amplitudes were not obtained in this experiment, and because more than 1 phase-encode line was obtained per segment, the signal intensity values measured from the FLASH and b-SSFP images were not exactly equivalent to the transverse magnetization predicted by mathematical simulations. Despite efforts of scaling and flip angle adjustments, it was found that FLASH and b-SSFP imaging of the transient phase differed from the simulation results by at most 5% (Figures 4.3-5). Many factors determine image signal intensity besides user-defined scan parameters. Imperfect T_2 spoiling or slight deviations in flip angles may have contributed magnetization to subsequent echo amplitudes.

Delayed Enhancement of T_1 phantoms

The optimal contrast in inversion recovery imaging, as determined by the relative signal intensity *difference* between two samples, occurred at an inversion time larger than the null-point *TI* (TI_{null}) in both 1- and 2-heartbeat imaging scenarios. But as the difference in the sample T_1 values grew, the optimal *TI* (TI_{opt}) became increasingly similar to TI_{null}. Despite the dissimilarity between TI_{opt} and TI_{null}, the difference in the corresponding image contrast values was minor. Quantitatively from Figure 4.11, the $T_{1contrast}$ plateaus near its peak, suggesting that a *span* of inversion times (including TI_{null}) generates relatively equivalent image contrast. Visually, however, one may *perceive* higher image contrast from TI_{null}, since one of the samples is almost completely void of signal, creating a binary-type distinction with enhanced T_1 samples. This "perceived"

optimal contrast can be appreciated between sample 2 (*arrow*) and the "infarct" samples in the top row of Figure 4.13a (in comparison to the optimal contrast shown in Figure 4.13b). The relative difference in T_1 contrast is < 7%.

Another distinct finding in the delayed enhancement simulations was the significant increase in overall $T_{1contrast}$ when 2-heartbeat segment intervals were used. The 44% average increase in image contrast correlated well with the predicted 40% increase in the simulation contrast results. The rise in image contrast was coupled with an increase in TI_{opt} and TI_{null}, compared to 1-heartbeat interval sequences. However, an observable disadvantage of the 2-heartbeat case was that it became more difficult to suppress the signal from a range of "normal myocardium" T_1 phantoms. Typically, inversion time steps greater than 50ms were needed to locate the null-point of neighboring T_1 phantoms. Practically, an increase in image contrast with 2-beat segment intervals is compromised by the increased challenge of finding TI_{null}.

The mathematical analysis of IR-FLASH alluded to a point of zero image contrast (at TI_{zero}) between infarct and normal myocardium in *magnitude images*. This finding correlated well with imaging results (1.5T: $r^2 = 0.83$ (1-beat); $r^2 = 0.96$ (2-beat); 3T: $r^2 = 0.91$ (1-beat); $r^2 = 0.99$ (2-beat)). The results also showed that TI_{zero} and TI_{null} differed by less than 100ms for 1-heartbeat segment intervals, increasing the chance of erroneous *TI* selection. Conversely, for 2-heartbeat segment intervals, the separation of these competing inversion times was typically *greater* than 100ms. But these results were heavily dependent on the difference between "infarct" and "myocardium" T_1. The implementation of 1-heartbeat imaging routines, which are common to 3D delayed

enhancement sequences, suggest one should err on the side of higher *TI* values to avoid zero-image contrast

For optimum T_1-weighting, the flip angle in IR-FLASH should be less than 30° to avoid significant image blurring. Theoretically, large flip angles produce signal intensity *independent* of the inversion time in IR-FLASH. These results, however, showed that using large flip angles lead to highly variable signal artifacts that prevented precise image contrast and geometric comparisons (Figure 4.14). Each phase-encode step samples magnetization of a non-constant magnitude, which results in amplitude changes in *k*-space. High variations in *k*-space translate to spatial variations in image space (blurring). *To obtain high quality T_1-weighted images with IR-FLASH, appropriate inversion times should be imaged with relatively low flip angle (< 30°).*

It should be emphasized that delayed enhancement imaging is *not* performed in the steady-state (see Figure 4.3-5, $\alpha < 30°$, pulses <30). The steady-state is not achieved in delayed enhancement imaging for 3 primary reasons: 1) the sequence is performed with low flip angles (15-30°); 2) a variable flip angle sweep is implemented that reduces echo amplitude variation; and 3) relatively short acquisition durations are used (<30 lines/segment). With these attributes, high image quality is possible because the magnetization prepared by the inversion pulse is perpetuated through every phase encode step (including $k_y = 0$) with insignificant variation in amplitude. The important point in this strategy is to reduce significant magnetization saturation during the course of signal detection, which is analogous to having a fast shutter speed in photography.

One of the key assumptions used in Chapter 3 in regard to contrast optimization was that the equilibrium magnetization was *unity* for the T_1 values. Hence, all contrast

calculations were on a scale of 0.0 to 1.0. Since this is not the case for physiologic tissues (or phantoms), an exact correlation between imaging and simulation results is not possible. To adjust for this inconsistency, the signal intensities from the T_1 phantoms were represented as *a fraction of the intensity values obtained without IR preparation*, which is, itself, a function of T_1. It was vital to relate the IR-FLASH imaging results to these "reference" values in order to express the signal intensity on a 0.0 to 1.0 scale. In accordance, the simulation results were also related to reference values obtained from simulated curves without IR-preparation (Figure 4.1). Inclusion of this additional scaling step may have compounded the error between simulation and imaging results, and may explain the marginal disagreement seen between the two contrast plots (Figure 4.11). The determination of precise (or relative) equilibrium magnetization of the samples under analysis will allow application of the equations of Chapter 3 directly.

Another important limitation of this scaling scheme is that it prevented a direct comparison between 1.5T and 3T delayed enhancement experiments, since the results were put on equivalent scales where 1.0 represented maximum contrast at both fields. *This was done solely to correlate imaging results to simulation results.* In actuality, it was found that the empirical signal *gain* observed at 3T (for equivalent T_1 values) was approximately 33%. Therefore, a true sense of the $T_{1contrast}$ gain seen at 3T (relative to 1.5T) can only be realized by assigning M_0 at 3T equivalent to 1.33 in the simulations. This adjustment was reserved for use in Chapter 7, when actual *in vivo* T_1 measurements are made on infarct and normal myocardium at 3T.

Delayed Enhancement Conclusions: Phantom Experiments

Performing delayed enhancement imaging studies with T_1 phantoms provides insight into image contrast behavior. Improved image quality is achieved with low flip angles (< 30°), short data acquisition durations, and variable flip angle sweeps. It has been shown that *zero* image contrast exists for particular *TI* values, which lie relatively close to the null-point and optimal *TI*s for maximum infarct-to-normal myocardium contrast. This proximity is exacerbated by using 1-heartbeat segment intervals. Although the optimal *TI* is not equivalent to null-point *TI* (but noticeably higher), the resulting image contrast is not significantly increased, allowing one to subjectively choose the null-point *TI* as the "perceived" optimal *TI*. Finally, it is easier to locate the null-point *TI* using 1-heartbeat segment intervals.

Without concessions made to M_0, increasing image contrast on delayed enhancement imaging is primarily dependent on the *maximizing the T_1 difference between infarct and normal myocardium for IR-FLASH sequences*. Given a constant T_1 difference, benefits of heightened image contrast can be realized using IR-FLASH with 2-heartbeat segment intervals. An increase in field strength shows significant improvements in signal-to-noise ratio, which enables concomitant improvement in image resolution for potentially visualizing small infarct tissue. With all other variables constant*, image contrast will benefit at 3T with an increase in M_0 and infarct-to-normal myocardium T_1 difference*.

CHAPTER 5

FIELD ANALYSIS

Introduction

The majority of magnetic resonance imaging in clinical practice employs field strengths of 1.5 Telsa (T). The utilization of superconducting materials (i.e. Nb, Ti) in modern magnet design have enabled the transition to 3T and higher. The relevancy of producing high magnetic field strengths originates from the inherent *insensitivity* of ^{1}H (hydrogen) MRI. Despite its relatively high concentration (100M) in physiological systems, the fraction of observable proton spins (n) in a magnetic field (B_0) is approximately:

$$n \simeq \gamma \pi h B_0 / kT \,, \qquad [1]$$

which is on the order of 10^{-6} (temperature (T) = 310K; B_0 = 1 Tesla) due to thermal energy (kT) far exceeding the Zeeman splitting energy ($\gamma \pi h B_0$) of the system ($\gamma \pi h B_0 << kT$). This translates to one spin in a million being oriented parallel ($n\uparrow$) to the main magnetic field for detection purposes (at 1T). It must be asserted in light of this inherent insensitivity, however, that the large population of protons per gram of tissue (6.023×10^{23}) alleviates this problem and makes hydrogen samples detectable even with field strengths as low as 0.1T. From Eq. [1], one also notices that the number of spins in excess (defined as the difference in spins parallel to B_0 versus anti-parallel: $n\uparrow$-$n\downarrow$) *increases* with B_0, making the observable spin system sensitive to the main magnetic field strength. *This fact has been the primary reason high-field systems have been pursued for both investigational and clinical purposes.*

The increased signal strength of MRI suggests that imaging should be performed at the highest possible field strength, within safety regulations. Although logical, several issues counteract the gain of signal, which may ultimately place limits on the optimum imaging field strength. Theoretically, the detected signal intensity increases with the square of the operating frequency; however, the more relevant signal-to-noise ratio (SNR) measure is predicted to increase only linearly with field strength. This results from the added noise power at higher fields, which originates from destructive interference of inhomogeneous magnetic fields on the detected echo signal. Furthermore, in addition to the inherent thermal noise produced by receiver coil, there is also considerable signal loss from the imaging sample itself, primarily due to eddy currents and field attenuation within the sample.

In this chapter, the instrumentation and pulse sequences relevant to cardiac MRI will be analyzed at 1.5T and 3T. It is the focus of this chapter to analyze the extent of these differences qualitatively and quantitatively with both MR phantoms and normal volunteers as they pertain to cardiac imaging. Several selected features of field differences will be analyzed for the purpose of explaining the potential difficulties of implementing the pulse sequences related to imaging myocardial viability. These topics are: 1) main field homogeneity; 2) transmit (B_{1trans}) field homogeneity; 3) preparation pulse accuracy and homogeneity; and 4) SNR/proton density comparisons. These topics are not a complete survey of hardware characteristics, but are relevant in regard to assessing contrast-enhanced viability imaging at 1.5T and 3T. Furthermore, it should be noted that this treatment is not intended to remedy the instrumental differences of either

field strength. Rather, the data will be used to outline the potential limitations of particular pulse sequences, while discussing the significant field-related issues at 3T.

Methods

Analysis of main field (B_0) inhomogeneity involved imaging normal volunteers, since these particular scans could be effectively performed and evaluated within a breath hold duration. The other sub-sections involved imaging with a phantom. The phantom was a 1000mL bottle of copper sulfate solution (T_1 = 300ms, 1000mL H_2O, 770mg $CuSO_4$, 2000mg NaCl). A 3000mL bottle of mineral oil was used for some experiments to contrast those performed with the copper sulfate phantom. The copper sulfate phantom, which is predominately water, has a dielectric constant (ε) of 80, which resembles biological tissue [Durney 1986]. The mineral oil phantom has dielectric properties similar to fat ($\varepsilon \approx 5$, conductivity $\sigma \approx 0.05$ Sm^{-1}) and therefore not totally reflective of *in vivo* electromagnetic properties. Imaging at 1.5T was performed on a Philips Intera system with a 60cm bore size, 1.57m length, 33 mT/mm gradient system, 160mT/mm/s slew rate, and a 5-element phased array cardiac coil. Imaging at 3T was performed on either a Philips Intera (same as 1.5T, 6 element cardiac phased array coil) or a Siemens Trio (60cm bore size, 2m length, 40mT/m gradient strength, 200mT/mm/s slew rate, 8 element torso array receive coil). What follows is a detailed outline of the methods used to assess field differences between 1.5T and 3T.

Main Field Homogeneity

Magnetic field inhomogeneity at 1.5T and 3T was quantitatively assessed spatially using a phase difference method. This technique is commonly used to measure fluid velocity (phase contrast MRI) [Bryant et al. 1984], but can be extended to describe spin dephasing across the field-of-view (FOV) due to field inhomogeneity [Reeder et al. 1998]. The accumulated phase in gradient-echo imaging is approximately (in the x-direction):

$$\phi(t) = \gamma \int \left[\delta B_0 + \delta B_e(t) + xG_x(t) \right] dt = \phi_{B_0} + \gamma \left[\int \delta B_e(t) dt + \int xG_x(t) dt \right]. \qquad [2]$$

where γ is the gyromagnetic ratio for hydrogen (42.6 MHz/T), δB_0 is the static magnetic field variation and δB_e is the field variation due to time-dependent eddy currents. The last term ($\int xG_x(t)dt$) is due to the applied gradients, and is cancelled from the expression via gradient reversal at the echo time (TE) (in gradient echo imaging). The first two terms are the *accumulated phase* that result from B_0 inhomogeneity ($\phi_{B_0} = \gamma \int \delta B_0 dt$) and eddy currents ($\gamma \int \delta B_e(t) dt$). A disadvantage of gradient echo imaging compared to spin echo sequences is that the effect of dephasing due to B_0 inhomogeneity (ϕ_{B0}) is not compensated for by the inversion of spins, as in spin-echo imaging. The phase due to eddy currents, which is time dependent, can not be compensated for by the imaging sequence, but can only be reduced through proper gradient design.

To isolate the effect of field inhomogeneity, the eddy currents in the system were assumed to be negligible, and the zero and first-order gradient moments ($\int xG_x(t)dt$) were nulled by conventional velocity compensation techniques. The frequency offset at a

particular position, $\Delta f(x,y)$, was determined by acquiring phase images at two defined echo times (TE_1 and TE_2), and subsequently applying a phase-difference algorithm:

$$\Delta f(x,y) = \frac{\gamma \delta B_0}{2\pi} = \frac{\phi_{TE_2}(x,y) - \phi_{TE_1}(x,y)}{2\pi\left(TE_2 - TE_1\right)}. \qquad [3]$$

The result is a frequency offset quantity, $\Delta f(x,y)$, given in Hertz (Hz). Two phase images are important since the measured phase from a single gradient echo phase image at TE_1 is subject to a constant phase offset [Haacke 1999]: $\phi_{TE_1} = \phi_0 + \gamma \delta B_0 \cdot TE_1$. Therefore, two phase images at unique TEs are necessary to cancel the constant phase offset. Chemical shift artifacts from fat and water can be avoided by selecting TEs that are "in-phase". The fat-water frequency shift at 3T is twice that of 1.5T (447 Hz vs 224 Hz), which makes fat and water in-phase at echo times 2.2ms, 4.4ms, 6.6ms, etc at 3T. At 1.5T, the "in-phase" echo times occur every 4.4ms, beginning with TE = 4.4ms. For this study, therefore, echo times were kept consistent at approximately $TE_1 \approx 4.5$ms and $TE_2 \approx 9.0$ms between field strength measurements. The difference in the selected TEs also has an impact on the appearance of the phase maps.

Phase maps were acquired in five healthy volunteers using the transmit/receive body coil. Slices were acquired in a mid-ventricular short-axis plane and acquisition parameters were similar between 1.5T and 3T. Two shimming routines were also compared *in vivo*: "*automatic shimming*", in which multi-order magnetic field variations are optimized throughout the entire FOV; and "*volume shimming*", where region-specific shimming can be implemented via user-specified volume elements. The user-defined volume shim element was localized to include primarily the heart, with minimal lung space to avoid air. Data acquisition was performed using an ECG-gated, segmented,

spoiled gradient echo sequence (FLASH), with the following parameters: FOV = 400mm^2; matrix = 256; slice thickness = 5mm; flip = 30°; TR = 13ms; 20 lines/segment; 2 heartbeat interval; BW/pixel = 781Hz/pixel; scan time = 9 sec. Both phase images (TE_1 and TE_2) were collected during the same scan to reduce misregistration.

The phase images were taken off-line for data processing in Matlab. The image data was linearly re-scaled from 12-bit stored values to floating point integers and B_0 inhomogeneity maps were calculated on a pixel-by-pixel basis using Eq. [3]. Due to chosen TE difference, certain regions of the phase images experienced *phase wrapping* (or "aliasing"), which is indicative of the true phase being greater than π or less than $-\pi$, relative to a reference phase. In these cases, the phase images were "unwrapped" prior to the pixel-wise calculation. The image was iteratively processed such that every phase transition greater than 2π was corrected by the following computation:

$$\phi_{wrapped} = \phi_{true} + 2\pi n\,, \qquad [4]$$

where n is an integer based on the number of phase wraps along a certain direction. When the unwrapping process began, $n = 0$ (by selecting a reference point typically near the center of the image), and adjacent pixels were conditionally analyzed for phase wrapping: if the change in phase is contained within $[-\pi, \pi)$, $n = 0$ (remains the same); however, when a phase increment was $> \pm\pi$, n was incremented by ± 1. Therefore, a complete unwrapped image was obtained by determining n at each pixel. Since this method potentially resulted in error propagation along a certain path, the unwrapping algorithm was confined to small regions at a time. More sophisticated unwrapping methods are available [Chavez et al. 2002], but are beyond the scope of this analysis.

Transmit Field Homogeneity

This section examines the spatial differences of the transmission (B_{1trans}) radiofrequency (RF) field between 1.5T and 3T in the copper sulfate phantom ($CuSO_4$). The purpose was to investigate the correlation between an applied flip angle (user-specified) and the flip angle absorbed (or, "perceived") by the sample. The methodological strategy was to use the signal intensity of an image to map the *accuracy* of the B_{1trans} field in the sample. This was accomplished by varying the flip angle, relating the spatial signal response to the known distribution of flip angles, and determining the deviation at each pixel. Ideally, this relationship should be a simple model interpreting the influence of a *single RF pulse*, and not complicated with lengthy pulse trains and T_1 and T_2 relaxation factors. This can be achieved with a "blipped" echo-planar imaging (EPI) sequence (Figure E.3, Appendix E). In this case, an explicit expression can be written that approximates the relationship between the signal intensity, $I(x,y)$, and the spatial homogeneity of the RF pulse flip angle ($a(x,y)$) [Thulborn et al. 1998]:

$$I(x,y) = \zeta M_0(x,y) B_{1rec}(x,y) \sin(\alpha(x,y)) \cdot (1 - \exp(-TR/T_1(x,y))) \exp(-TE/T_2^*(x,y)), \quad [5]$$

where M_0 is the equilibrium proton density, B_{1rec} is the receive field, α is the flip angle, TR and TE are the sequence repetition and echo time, respectively, and T_1 and T_2^* are the sample's relaxation constants (ζ is an additional scaling constant). For a homogeneous phantom using the body coil as the receive probe, the first three terms (ζ, M_0, and B_{1rec}) are assumed constant across the FOV. The influence of the relaxation factors, T_1 and T_2^*, can be reduced by setting TR very long, and TE very short. Therefore Eq. [5] can be reduced to $I(x,y) = K \cdot \sin(\alpha(x,y))$, where K is a scaling constant that contains M_0 and B_{1rec} factors. (Note that even though K is considered constant, it can be left spatially

dependent, i.e. K(x,y), for the purpose of least-squares fitting, as discussed below) A field-dependent change in K is indicative of a change in M_0 between 1.5T and 3T.

The experimental setup began by placing the sample in the isocenter of the magnet (1.5T and 3T), and initiating ECG-gating with a computer-driven physiologic simulator device available on the scanner to provide triggering to initiate the scan. The "heart rate" of the simulator was set to 75bpm. The "blipped" EPI sequence consisted of one slice-selective RF pulse followed by repeated gradient reversals in the readout direction, producing an echo train, which decayed with T_2^*. The time to the central echo ($k_y = 0$) in this train is referred to as the "effective" TE (TE_{eff}) (the point where central *k*-space lines are acquired). Using the body coil to ensure a uniform receive field (B_{1rec}), the imaging scan parameters were: 250-300mm FOV; 96 × 128 matrix; 6mm slice thickness; EPI factor = 13 (number of echoes acquired per TR), producing a TE_{eff} = 6ms; 3 heart beat TR (~2400ms); and 80-160 Hz/px bandwidth. B_0 inhomogeneity was reduced in the phantom by applying localized volume shimming over the slice-of-interest. The magnitude of the B_{1trans} field was controlled by selecting the excitation flip angle of the scan. The flip angle was varied from 1° to 150° (1, 10, 20, 40, 60, 90, 120, and 150°), producing a set of images for analysis.

B_{1trans} mapping was performed offline with a Matlab fitting algorithm. The image intensities were individually re-scaled to floating point values, as previously discussed. The routine consisted of pixel-wise nonlinear fitting of the re-scaled measurement data, $I(x,y)$, to a sinusoidal function derived from the above equation:

$$I(x,y) = \mathrm{K}(x,y) \cdot \sin(\alpha \cdot \xi(x,y)) . \qquad [6]$$

The result produced maps of $\xi(x,y)$, which is the *spatial correlation of the flip angle*, and K(x,y). Under perfect B_{1trans} field homogeneity, $\xi(x,y) = 1.0$, meaning that there is perfect correlation between α (the flip angle that was selected) and the B_{1trans} field produced (or, more importantly, the flip angle perceived by the sample). When $\xi(x,y) < 1.0$, the flip angle (and transmit field) is dampened within the sample relative to what was selected by the user. The fit also produced a map of K(x,y), which was used to assess the relative gain in proton signal sensitivity between 1.5T and 3T.

Inversion (180°) Preparation Pulse Homogeneity

Non-selective inversion (180°) preparation pulses, such as those used in delayed enhancement imaging, were assessed using a single excitation gradient echo/echo planar hybrid imaging sequence (FLASH-EPI) (Figure E.1, Appendix E). The strategy was to image the effects of the inversion pulse after a *minimal delay time,* with a short, low flip angle readout, thereby encoding the efficacy of the inversion pulse into the final image. Specifically, the signal from a low-flip (α), short-TE readout sequence with θ-prepared magnetization and transverse magnetization spoiling can be approximated by:

$$I = \mathrm{K}\left(\left(1+\left[\left(\cos\theta - 1\right)\exp\left(-TI/T_1\right)\right]\right)\sin\alpha\right) \approx \mathrm{K}\cos\theta\sin\alpha\,, \qquad [7]$$

where K is a scaling constant associated with proton density. The exponential term in Eq. [7] tends toward unity if the inversion pulse delay time, *TI*, is assumed to be very small relative to T_1.

All imaging experiments were performed in a copper sulfate phantom at 1.5T and 3T (Philips Intera) using the magnet's body coil for RF transmission and reception. This ensured the signal variations in the image were due primarily to inversion pulse

variations. Data was acquired with a FLASH-EPI sequence using a 128 × 128 matrix, 290mm^2 FOV, 10mm slice thickness, EPI factor of 3, TR/TE = 10,000ms/2.6ms, 20° flip angle, and the shortest preparation delay time, which was typically less than 10ms, depending on the type of preparation used. Data sampling was performed with a "low-to-high" acquisition order, which acquires low *k*-space lines first. As with the B_0 field homogeneity experiments, two field shimming routines were used: *automatic shimming*, and *volume shimming*. For *volume shimming*, the volume elements (shim "boxes") were placed parallel to the slice-of-interest and reduced in size to encompass exclusively the sample and slice thickness. The total scan duration was approximately 5 minutes. Following each scan with the inversion pulses, a second scan was performed *without inversion pulses* to serves as a reference scan for normalization purposes.

Three types of inversion pulses were examined: *adiabatic*, *rectangular*, and *composite* (90x-180y-90x, where the letters x and y refer to direction of the B_{1trans} field). The adiabatic inversion pulse was initially applied using the default scanner settings ($\theta \approx 1110°$), which depended linearly on the FOV and SAR limits. For a detailed description of adiabatic pulses, which are known to produce homogeneous spin excitation over a large FOV, consult Tannus [Tannus et al 1997] or Haacke [Haacke 1999]. Since larger RF field variations were expected at 3T (and not at 1.5T), further experiments were performed at 3T to explicitly test the sensitivity of the adiabatic inversion pulse by manually changing the parameter settings to 750, 850, 950 and 1300°. The composite inversion pulse consisted of a 90x-180y-90x pulse series with the middle 180° applied with a 90° phase shift. The pulses were rectangular with pulse durations of (90/180°)

0.025/0.05ms and 0.05/1.0ms at 1.5T and 3T, respectively. The pulse durations of the 180° were twice as long as the 90°, and both were lengthened at 3T to limit SAR.

Normalization involved pixel-wise division of the inversion-prepared images (I) with the reference scan (I_{ref}) to cancel the influence of proton density and readout excitation pulses. This was performed in Matlab following appropriate re-scaling of data. The ratio of intensity values (I/I_{ref}) can be related to the preparation flip angle by:

$$\frac{I}{I_{ref}} = \frac{K\cos\theta\sin\alpha}{K\sin\alpha} = \cos\theta\,, \qquad [8]$$

with T_1 and T_2 effects considered negligible. The sign of I/I_{ref} was assumed *positive* (due to the acquisition of magnitude images), so that values near unity represented *complete inversion*. Since Eq. [8] requires $I/I_{ref} < 1$, the results were expressed on a normalized scale of 0 to 1.0. The normalized images were analyzed for spatial homogeneity using intensity profiles and standard deviation measurements.

Determination of Field-Dependency of M_0

Equation 1 showed that the proton sensitivity of the MRI experiment is dependent on the static magnetic field strength (B_0). In practice, the population of spins aligned parallel to B_0 represents a bulk magnetization vector quantity, M_0, that can be measured when it is tipped completely into the transverse plane. Since the magnitude of M_0 is arbitrary in MRI, a relative quantity can be expressed between two field strengths, as long as the tip angle is consistent. This is often a more complex comparison since an MR experiment requires repeated excitations to form an image, in which the measured signal is additionally scaled by T_1 and T_2. However, under the constraint that $TR >> T_1$ and

$TE << T_2$, the observed signal intensity is proportional to the object's proton spin density, M_0.

This precondition on TR and TE was evident in several of the "reference" pulse sequences described in earlier experiments, namely a) transmit field homogeneity; b) preparation pulse homogeneity; and c) contrast agent relaxivity (Chapter 4). Furthermore, these experiments were carried out at both 1.5T and 3T, enabling the quantification of proton spin density *gain* at 3T. Additional M_0 experiments were performed with a mineral oil phantom using spin echo (TE = 7.6ms, TR = 10,000ms, $\alpha = 90°$) and gradient echo (TE = 1.25ms, TR = 10000ms, $\alpha = 20°$). The relative field-dependent M_0 data were compiled from these experiments in copper sulfate, mineral oil and agar gel. Since mineral oil has lower permittivity and conductivity compared to the copper sulfate phantom, the results from these experiments were also used to generalize the effects of dielectric properties on the nature of the B_{1trans} field in the sample.

Results

Main Field Homogeneity

Evidence of B_0 inhomogeneity throughout the FOV was apparent from the *source* phase images at 1.5T and 3T (not shown). At the corresponding TE, there were more phase-wraps (or, "aliasing") at 3T than 1.5T, which is indicative of greater spin dephasing as a function of position.

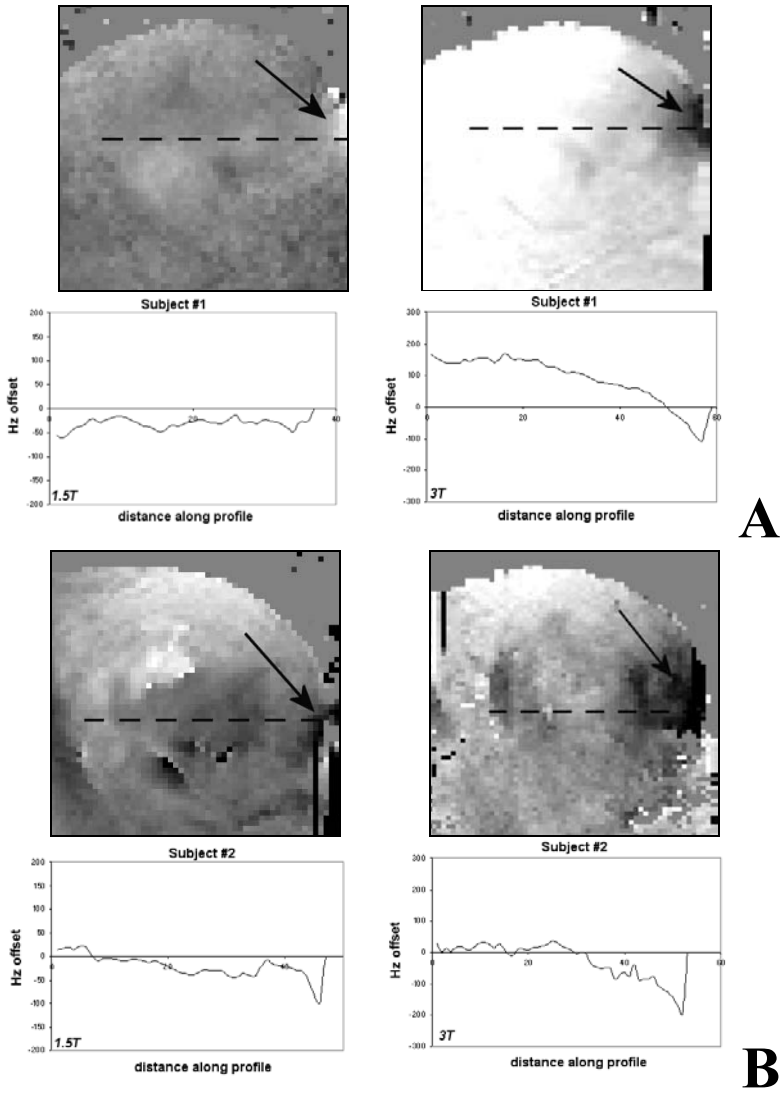

Figure 5.1. *B_0 field inhomogeneity maps from 2 volunteers*

Short-axis frequency offset maps of the heart from 2 (of the 5) volunteers are depicted in Figure 5.1. The Δf-maps ranged from +111 Hz (top white) to -111 Hz (black). At both field strengths, there was a prominent area of relatively high off-resonance near the middle and posterior cardiac vein in the lateral myocardial wall (arrow). Though the appearance of this large frequency shift (relative to the septum) was consistent in all volunteers, the *absolute magnitude* of the off-resonance was approximately 52% greater at 3T compared to 1.5T (-143.8 ± 46.4 Hz vs. -94.2 ± 25.3 Hz, n = 5). The average peak-

to-peak Δf across the left ventricle (from the septum to the lateral wall) was 89.4 ± 32.8 Hz at 1.5T and 241.3 ± 32.5 Hz at 3T. These 1.5T values were similar to previous *in vivo* investigations [Reeder et al. 1998], while the 3T values were more than double the 1.5T values.

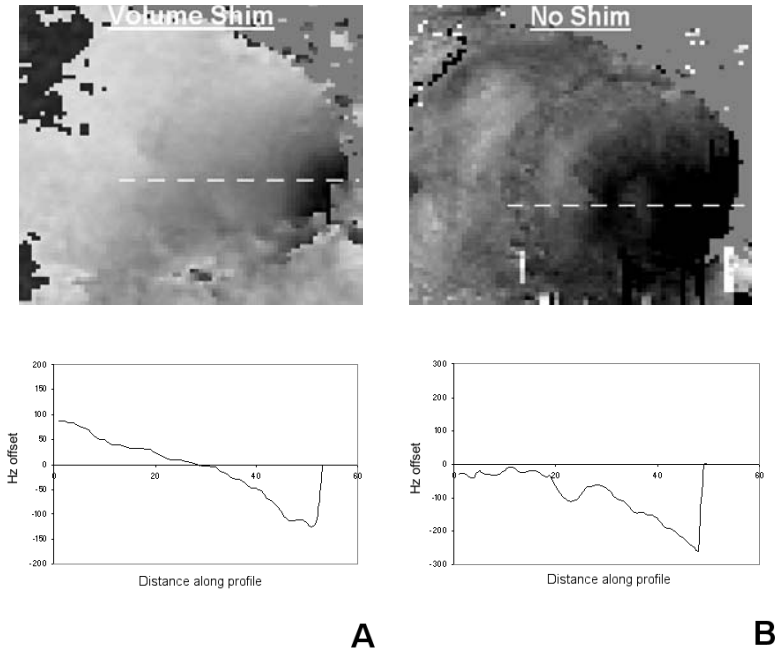

Figure 5.2. *Comparison of* ***a)*** *volume shimming and* ***b)*** *no shimming at 3T in the same volunteer.*

Implementation of manually placed *shim volumes* over the heart in the short-axis plane reduced the *absolute maximum* Δf values by about 20% at 1.5T. However, the use of shim volumes at 3T only managed to reduce the overall *average* Δf along a profile bisecting the entire heart (from 20-30Hz to almost 0Hz), while not affecting the peak-to-peak Δf. This is exemplified in Figure 5.2, which shows the same subject imaged (a) with the volume shim and (b) with no specified shimming. As seen from the profiles, the peak-to-peak Δf in Figure 5.2b is almost the same as Figure 5.2a (241.3 ± 32.5 Hz, with no

shim; 251.2 ± 2.7 Hz, with volume shim, n = 5), even though the *average value of* Δf with the shim volume is essentially zero (18.5 ± 60.3 Hz, with no shim; -0.1 ± 23.5 Hz, with volume shim, n = 5). Even though the localized volume shim reduced the average Δf in the heart at 3T, the maximum and peak-to-peak Δf was higher at 3T than 1.5T by approximately double. There was also little difference between volume and auto shimming at both fields (1.5T: 15% difference in peak-to-peak Δf; 3T: 4% difference). Also, the average peak Δf measured using both techniques were not greatly different at 3T (auto: -143 Hz vs. volume: -130 Hz). More insightful, however, were results showing that the *standard deviation* of Δf with volume shimming was (on average) almost 3-times lower than *auto shimming* routines at 3T (n = 5). The standard deviation of Δf at 1.5T was unchanged with either shimming protocol.

Transmit Field Homogeneity

The resulting $\xi(x,y)$ values in the copper sulfate phantom at 1.5T and 3T are shown as transverse and sagittal 1D plots in Figure 5.3, along with one of the source images using $\alpha = 90°$ (inset). In the transverse plane (Figure 5.3a-b), the distribution of $\xi(x,y)$ was approximately unity at the center of the phantom at both 1.5T and 3T, indicating that *the* B_{1trans} *field was most precise in this region*. However, variations from unity were apparent at each field strength near the edges of the phantom in the transverse plane, despite optimized slice shimming to minimize B_0 inhomogeneity. Specifically, $\xi(x,y)$ fell to 0.6 near the edges of the phantom at 3T (Figure 5.3b). This is an example of the "field-focusing" effect, whereby the B_{1trans} field at the isocenter (center of the bottle) is stronger than further away. The magnitude of the phenomenon seems to be field

strength dependent, as indicated by the relative spatial homogeneity at 1.5T compared to 3T, with edge $\xi(x,y)$ values greater than 0.8 (Figure 5.3a).

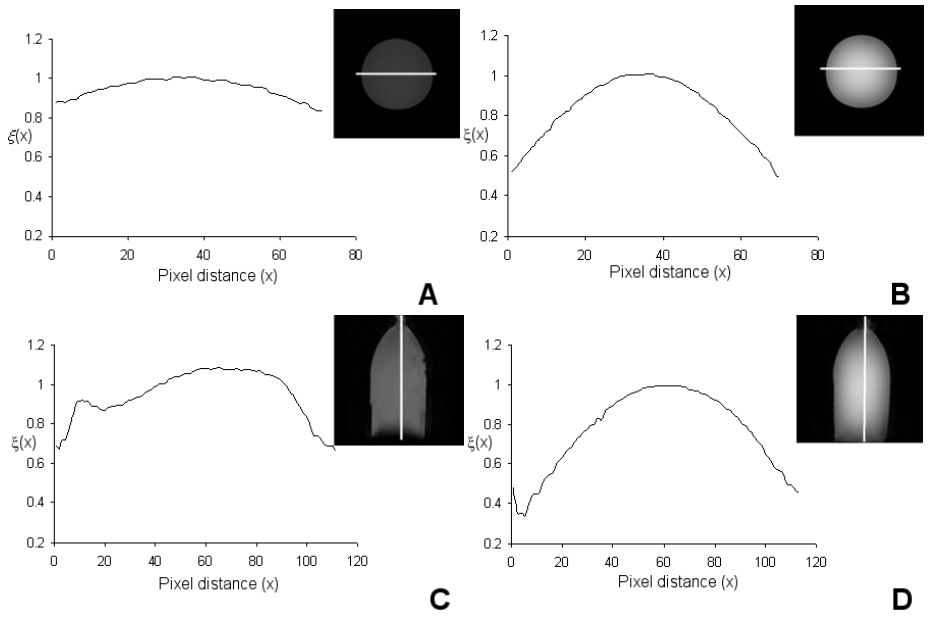

Figure 5.3. *Correlation function $\xi(x,y)$ of B_{1trans} in a $CuSO_4$ phantom at* ***a,c)*** *1.5T and* ***b,d)*** *3T.*

In the sagittal plane, the size of the sample in the foot-head (FH) direction strongly influenced the homogeneity of $\xi(x,y)$. There was a "bell-shaped" 1D $\xi(x,y)$ profile at both 1.5T and 3T in the sagittal plane (Figure 5.3c-d), with low $\xi(x,y)$ in the most caudal and basal regions of the phantom. Even though shimming was performed, B_0 inhomogeneity may have contributed to the very low $\xi(x,y)$ values (0.4-0.5 at 3T; 0.6-0.7 at 1.5T). In regions of high B_0 homogeneity (at the isocenter), both field strengths exhibited $\xi(x,y)$ profiles values close to 1.0. The field focusing phenomenon was also visible in the sagittal orientation, especially at 3T. This is indicated by the high rate of $\xi(x,y)$ decrease at 3T compared to 1.5T (1.0→0.4 at 3T; 1.0→0.6 at 1.5T) along the longitudinal axis of the bottle. *These findings are expected to influence the spatial*

homogeneity and overall quality of cardiac MR images at 3T, especially in regions away from the isocenter.

Inversion (180°) Preparation Pulse Homogeneity

Comparison of three types of non-selective inversion preparation pulses (rectangular, composite, and adiabatic) are shown in Figure 5.4 at both field strengths using *volume shimming*. For each profile, such as those in Figure 5.4, the average ratio intensities (I / I_{ref}) and standard deviations (SD) in both the foot-head (FH) and left-right (LR) direction were calculated and displayed in Figure 5.5 for both shimming protocols. Visually, spatial inversion homogeneity was greatest for adiabatic > composite > rectangular; with spatial variations more substantial at 3T. This was observed by noting a significant fall-off in inversion uniformity at 3T near the periphery of the FOV, including focal signal loss (Figure 5.4b). Therefore, *inversion pulse variations may be a critical factor at 3T, even when volume shimming and adiabatic pulses are used.*

Using the standard deviation along the intensity profiles as a measure of spatial homogeneity, the inversion variation in the FH direction was *lowest* with the adiabatic inversion pulse (1.5T: SD = 0.04; 3T: SD = 0.02) (Figure 5.5). In comparison, the composite inversion pulse resulted in SDs of 0.05 and 0.21, while the rectangular inversion had SDs of 0.10 and 0.23 at 1.5T and 3T, respectively. The trend shown in Figure 5.5 also revealed that each inversion pulse had *greater* spatial homogeneity at 1.5T; whereas, at 3T, spin inversion was only accurate with adiabatic pulses. In the LR direction, the adiabatic and composite inversion pulses were near unity in magnitude, and spatially homogeneous at *both* 1.5T and 3T.

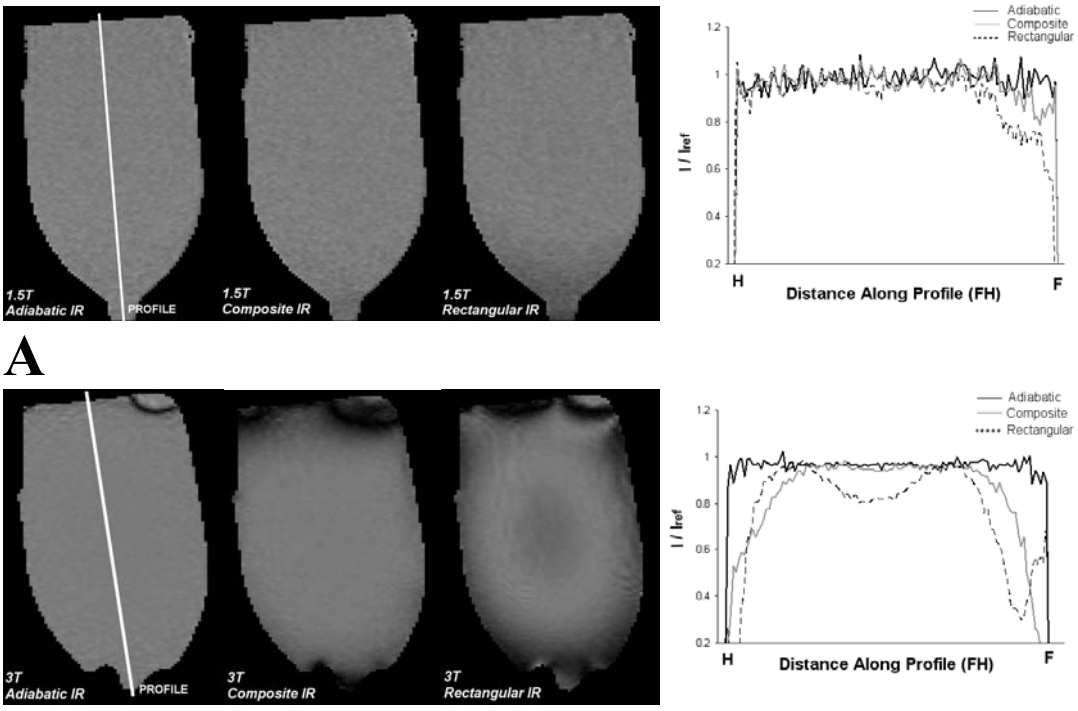

Figure 5.4. *Images and plots of 180° pulse homogeneity for specific pulse types at* ***a)*** *1.5T and* ***b)*** *3T using volume shimming.*

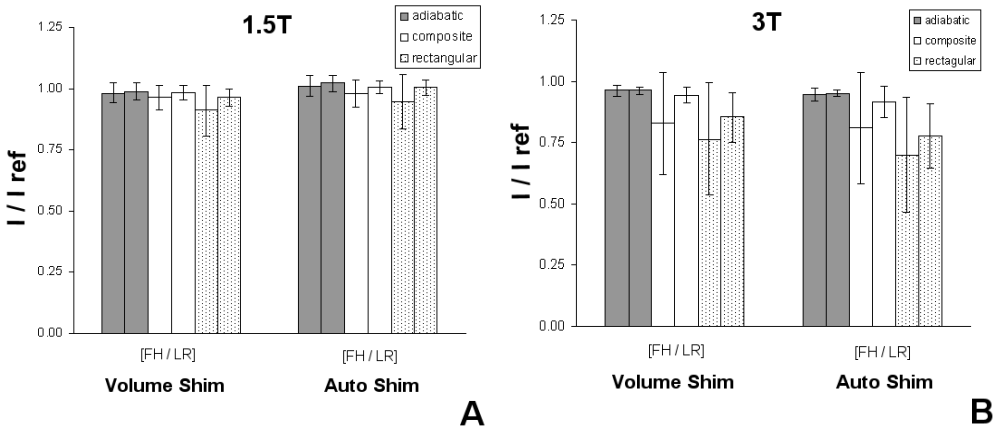

Figure 5.5. *Summary of 180° pulse efficacy and homogeneity in the foot-head (FH) and left-right (LR) direction at* ***a)*** *1.5T and* ***b)*** *3T using volume and auto shimming.*

The use of volume shimming reduced the SDs at 1.5T by 7-12% in FH direction, but there was minor effect in the LR direction. Volume shimming also did not improve I / I_{ref}, since values were already close to unity. At 3T, volume shimming greatly improved SD in the FH (4-13%) *and* LR direction (22-49%) for composite and rectangular pulses. For the adiabatic inversion, volume shimming had negligible effect. There was, however, a marginal improvement in I / I_{ref} at 3T compared to 1.5T with volume shimming (2-10%).

When the adiabatic inversion pulse angle was varied at 3T while maintaining constant FOV, it was found that the largest degree flip angle (Θ = 1300°) exhibited the greatest spatial homogeneity in the FH direction (SD = 0.02). However, it was also associated with the lowest average I / I_{ref}(0.77), which was considerably lower than the "default" adiabatic inversion shown in Figure 5.4 and 5.5 (0.96). This implies that Θ = 1300° may not completely invert the magnetization. It is believed, therefore, that the "default" flip angle of 1110° consistently provides the optimum choice for the adiabatic inversion pulse angle at 3T.

Determination of Field-Dependency of M_0

The relative gain in M_0 at 3T for various samples compiled from the reference scans are given in Table 5.1. The data reveals that there is a consistent gain in signal sensitivity at 3T compared to 1.5T (>30%), but that the gain differs among the samples. The relative M_0 ratio was highest for the copper sulfate phantom, which is mainly water. Mineral oil, conversely, has the lowest gain in M_0 at 3T, with only a 30-40% increase. Figure 5.6 compares spin echo images of the copper sulfate phantom and mineral oil at

3T. The radial variation in signal intensity in the copper sulfate phantom is apparent, and was quantified earlier with $\xi(x,y)$. Thus, the gain in M_0 reduces radially from the center to a value of approximately 1.40. In the mineral oil, however, the signal intensity is very homogeneous at 3T, which implies $\xi(x,y)$ will be close to unity throughout the FOV. Therefore, the relative gain in M_0 will be spatially uniform. This difference in spatial signal behavior follows from the distinct dielectric properties of these samples.

Table 5.1. Relative proton density (M_0) gain at 3T relative to 1.5T.

Sample	Maximum M_0 ratio (3T:1.5T)[a]	
	Spin Echo	Gradient Echo
Copper sulfate[b]	1.95	1.97
Mineral Oil	1.41	1.30
4% Agar Gel[c]	1.84	-
Saline[d]	-	1.33

[a] Maximum M_0 ratio indicates ratio values measured at the center of the FOV, where signal was maximum. [b] Copper Sulfate spin echo experiment performed separately; gradient echo experiment taken from transmit field and 180 pulse experiment. [c] M_0 measurement from contrast agent relaxivity experiment performed only with spin echo(Chapter 4). [d] Saline values from Chapter 4.

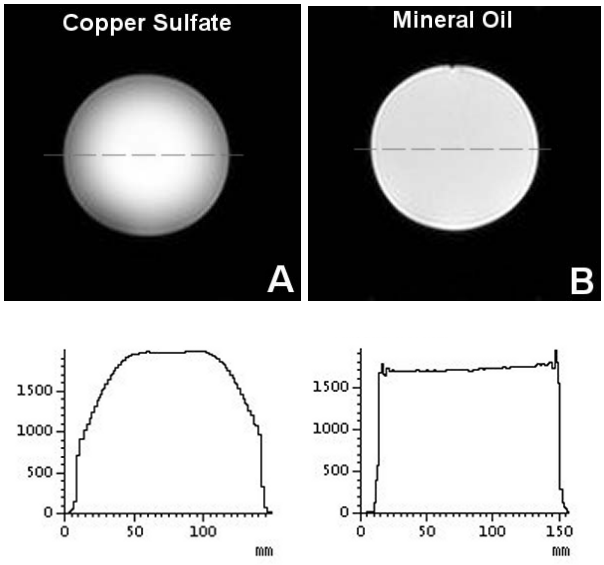

Figure 5.6. *Comparison of signal variation in transverse profiles in* ***a)*** *copper sulfate and* ***b)*** *mineral oil at 3T.*

Discussion

The goal of this chapter was to characterize the major field strength differences between 1.5T and 3T, and how they pertain to cardiac imaging, and specifically delayed enhancement imaging. The major findings of this chapter include: 1) main field inhomogeneities were more pronounced at 3T than 1.5T, particularly in the lateral and anterior wall of the left ventricle; 2) B_{1trans} field variations were greater at 3T (for high dielectric constants) such that the selected flip angle was underestimated in regions away from the center of the FOV; 3) adiabatic inversion pulse effectiveness was superior to other pulse types, particularly at 3T; 4) localized volume shimming improved inversion and average B_0 field inhomogeneities at 3T; and 5) M_0 sensitivity was at least >30% higher at 3T, but may vary spatially.

One of the most prominent difficulties when using high imaging frequencies is B_0 inhomogeneity. Perfect homogeneity is only attainable in a vacuum for an infinitely long solenoid with current windings along its axis. This is beyond practical consideration. However, if the solenoid is shortened to practical lengths (~1.5m), the bore size must be appreciably reduced as well (~0.5m) to allow, at worst, a finite homogeneous volume at the center of the magnet. This is crucial for the spatial localization of spins in 2D Fourier techniques, since a change in background magnetic field across the FOV will result in noticeable image distortions in the reconstructed image. Much of the deviation in B_0 is also due to sample loading. The presence of the homogeneous phantom or a human volunteer inherently causes the magnetic field to become inhomogeneous due to the sample's magnetic susceptibility (or inherent magnetism). Susceptibility is not only

affected by the chemical properties of the sample, but also by the magnetic field strength, becoming more significant at 3T.

Even with these restrictions, deviations in B_0 exist, due to the spatial dependency of Maxwell's equations for stationary fields. Spatial deviations can be visualized with the phase information of gradient echo images. This induced "resonance frequency off-set" (Δf) is apparent in the volunteer images shown in Figure 5.1. From the inhomogeneity maps, large field deviations at 3T were noticeable *in vivo* near high susceptibility regions like the heart-lung interface and infero- and postero-lateral wall. The use of region-based field shimming ("volume shimming") lessened the extent of field inhomogeneities at 3T by 50% (Figure 5.2). Therefore, proper shimming at 3T is crucial for artifact reduction in gradient echo images.

Many of the off-resonance frequencies measured at 1.5T did not warrant the use of volume shimming protocols to further reduce B_0 inhomogeneity. However, the >250Hz offset measured at 3T without local volume shimming (Figure 5.2b) made field shimming necessary. While the presence of large B_0 inhomogeneities at 3T in the lateral wall were consistent using both localized (volume) and unconstrained (automatic) shimming algorithms, local volume shimming performed only slightly better than automatic shimming protocols at reducing the peak Δf in this highly susceptible region. The average peak Δf measured using both techniques were not greatly different at 3T (auto: -143 Hz vs. volume: -130 Hz). Where in some cases volume shimming reduced the average Δf measured in the heart, in other cases the average Δf was *greater* (compared to automatic shimming protocol), despite effectively reducing of the peak Δf frequency. The reason for these inconsistent results with shim volumes may, in part, be due to improper

shim volume placement. Currently, a systematic approach for optimal shim volume placement is lacking. One strategic method is to limit the amount of air (lung tissue) within shim volume to confine the shim optimization to the myocardium; and another is to extend the shim volume axially such that it encompasses more than the just the slice of interest, thereby compensating for cardiac motion. There are also other on-going investigations with higher-order shim volumes to compensate for greater degrees of field inhomogeneities [Gruetter 1993, Jaffer et al. 1996].

Large field variations at 3T were not only limited to B_0, but also B_{1trans}, the RF transmission field. The results showed that the applied flip angle (which is proportional to B_{1trans}, $\alpha = \gamma B_{1trans} \tau_{RF}$, where τ_{RF} is the RF pulse duration) was spatially dependent and only accurate (according to $\xi(x,y)$) in the center of the object. This observation was more pronounced at 3T than 1.5T in both the transverse and sagittal planes (Figure 5.3). The significance of these results can only be appreciated insofar as the extent of limiting other field variations such as B_0 and B_{1rec}. Specifically, the $\xi(x,y)$ values of ~0.6 near the phantom's extreme edges may have been exacerbated by B_0 inhomogeneities, especially in the sagittal plane. To be sure, significant field variations still occur at 3T using spin echo (Figure 5.6a). Other causes of low $\xi(x,y)$ could be due to the receive field sensitivity (B_{1rec}) or inaccurate slice selection. But since the body coil was used for signal transmission and reception, B_{1rec} was assumed to be uniform over the FOV (compared to surface coils), and gave only minor deviations to the measurement of $\xi(x,y)$. The flip angle over the slice thickness, however, is inherently non-uniform since an RF pulse has finite duration. This makes its frequency content (obtained by taking the Fourier

transform of the pulse shape) inexact over a frequency range imposed by the slice-select gradient.

According to the solution to the Maxwell's Equations, there are several orders and degrees of the electric field that make up the B_{1trans} field, which also have dependency on B_0 and the electric and magnetic properties of the sample. These relationships have been elegantly analyzed by Hoult pertaining to power deposition and B_{1trans} spatial sensitivity [Hoult 2000]. It is shown that as the field strength is reduced (or the sample becomes very small), the B_{1trans} field is dominated by its *first-order* harmonic approximation. This field is uniform over the FOV and insensitive to B_0 *only in a vacuum*. In a sample with a given dielectric constant, ε, and conductivity, σ, the first-order B_{1trans} field approximation becomes spatially variable. Furthermore, this approximation only shows *radial* variation, which, from other previous investigations, is not entirely correct [Glover 1985, Hoult 2000] and requires higher order terms to describe B_{1trans} completely. It was also shown that circularly polarized RF fields cancel some higher order field terms [Hoult 2000].

The penetration and propagation behavior of these spherical harmonic waves can be analyzed with plane wave theory. The propagation of the electromagnetic wave in a conducting object is described by a propagation constant, *k*. This value is complex ($k = a + \boldsymbol{i}b$) with *a* equivalent to the wave decay constant in the sample, and *b* related to the wave velocity ($\nu = \omega_0 / b$). Both *a* and *b* are functions of the frequency ω_0 and the sample's dielectric properties (ε, σ, and μ, the permeability) [Shadowitz 1975]. For a sample at a high frequency or dielectric constant (relative to σ), the penetration decay constant is $a^{-1} = 2\varepsilon\nu / \sigma$. Conversely, in a good conductor (metals), σ is large and the electric field is limited to the surface ("skin effect"). For most body tissues (ε = 15-100

and σ = 0-1 Sm^{-1}) and MRI field strengths, the former case is more realistic. From this interpretation, therefore, the behavior of the B_{1trans} field is a combination of multi-order spherical harmonics that vary with *k* and the sample size, *r*. At high B_0, the B_{1trans} amplitude is highest in the center of the FOV (r = 0), and indicative of "field focusing" (Figure 5.3b). At lower B_0 (or very low ε or σ, i.e. fat tissue or mineral oil), the RF field is more spatially homogeneous (Figure 5.6b).

Spatial variation of RF excitation at 3T was also apparent in magnetization-prepared images, such as inversion recovery. Apart from incomplete inversion near the edge of the FOV, *the choice of inversion pulse type becomes increasingly significant at 3T* (Figure 5.5). Specifically, adiabatic inversion pulses appear to be the only pulse type that provides spatial insensitivity and accuracy throughout the FOV at 3T, while composite inversion accuracy are limited to only the isocenter.

The parameter ξ(x,y) measured in this study did not quantify the absolute *amplitude* of the B_{1trans} field, but rather the *accuracy* of the chosen flip angle over the FOV. The inhomogeneity of the transmit field at 3T raises questions about how the amplitude of the B_{1trans} field should be defined to produce a desired flip angle. For instance, one may calibrate B_{1trans} such that the *average* B_{1trans} corresponds to the desired flip angle, or one may determine the B_{1trans} field that produces the maximum free induction decay (FID) signal and assign this value to a 90° pulse. Since ξ(x,y) was close to unity at the center of the bottle (Figure 5.3), the largest signal in this region was associated with a 90° pulse (from Eq. [6], $I = \mathrm{K} \cdot \sin(90° \cdot \xi(x, y)) = \mathrm{K}$); therefore, it can be assumed that B_{1trans} was calibrated to produce an accurate field at the isocenter. Determining how the B_{1trans} field is defined in the sample leads to estimations of the

specific absorption rate (SAR) for a particular scan. Under these assumptions, it was shown by Hoult that the SAR generally increases with B_0 (and sample size), but that the region of maximum SAR is located deeper within the sample, as opposed to the sample surface, as found at lower B_0 [Hoult 2000].

The most commonly known advantage with 3T MRI is improved SNR, which is a fundamental property at high field strengths due to the increased polarization of magnetic spins (Eq. [1]). This inherent benefit has particular significance in cardiac imaging. Even though fast-gradient echo imaging of the heart in a single breath hold is capable of high quality MRI scans with current gradient strengths, they suffer from more image noise compared to neurological imaging, where physiologic motion and scan time are not as constraining. This essential MR trade-off between speed and SNR can be curbed by the improved magnetization benefits of high field imaging. It was shown in this chapter that the equilibrium proton density, M_0, sensitivity increased by 30-97% from 1.5T to 3T, which correlates well with previous estimations of sensitivity (or SNR) gain at 3T (cardiac tissue (1.50-1.60) [Wen et al. 1997]; brain tissue (1.30-2.10) [Frayne et al. 2003]). This benefit in sensitivity not only entails improved SNR, but can also potentially improve contrast-to-noise ratio (CNR). This was first made evident in Chapter 3 and 4, where it was shown that simulated CNR measures ($T_{1contrast}$) improved by virtue of larger M_0 values at 3T. This result came in light of longer T_1 at 3T, which inherently depressed signal (using constant TR and TE) and image contrast.

Particular to delayed enhancement imaging at 3T, the improved M_0 (and hence SNR) observed with these studies may result in greater *infarct tissue* SNR. A second potential merit of improved SNR at 3T in delayed enhancement imaging is that SNR can

be used to improved image resolution. *This utilization may provide more direct quantification of infarct size*, which has significance in patient prognosis.

Conclusions

From the field analysis experiments described in this chapter, a better understanding of the implications of 3T cardiac imaging was obtained. The investigation found that the immediate theoretical benefits of 3T, namely higher SNR, are humbled by several challenges specific to fast imaging protocols. Time is of the essence in cardiac imaging, such that equivalent SNR gains as neurological imaging are often difficult to achieve. But it is in this respect that the most benefit will potentially be realized in cardiac imaging at 3T. To reach that goal, however, further advancements are needed to address the issue of field inhomogeneity (both B_0 and B_{1trans}).

CHAPTER 6

IMAGING OF NORMAL VOLUNTEERS AT 1.5T AND 3T

Introduction

The study of contrast mechanisms in delayed enhancement imaging at 1.5T and 3T involves understanding contrast agent kinetics in the heart. The primary role of the contrast agent upon injection into to circulatory system is the modulation of the bulk tissue T_1 properties for the purpose of enhancing pathology. One of the indirect consequences of circulating contrast media is that the modulation in T_1 is not constant over time and among all patients. As a result, obtaining consistent image contrast post-injection is challenging. An impression of the change in T_1 over time post-injection can be realized through the study of contrast kinetics of blood and myocardium in healthy human volunteers. From a time course of T_1 change, conclusions can be made about the role of the paramagnetic agent in each of these tissue compartments. By extending the study to 3T, not only can relaxation times be compared between fields, but also the dependency of contrast media on field strength and tissue compartment. This may lead to important conclusions about the criteria necessary to optimize pulse sequences at different field strengths.

The measurement of post-contrast T_1 values also enables evaluation of the partition coefficient (λ) in tissue, which has significance in describing the pathologic state of injured myocardium [Wendland et al. 1997, Klein et al 2004]. This quantification lends insight into the biodistribution of the contrast media assuming fast-exchange between compartments (meaning that a single time constant, T_1, describes relaxation).

Since the partition coefficient is an *inherent physiological property*, its value should not be dependent on MR properties such as field strength. Even though λ measurements have been performed at 1.5T, they have not been evaluated at 3T in the same subset of people. This evaluation is important if perfusion and biodistribution studies are extended to high field strengths.

In addition, there is limited knowledge of the signal-to-noise ratio increase for common cardiac MRI sequences between 1.5T and 3T. Particularly, it has been shown earlier in this research with phantom imaging that the expected gain in bulk equilibrium magnetization sensitivity, M_0, is approximately 30-97%. However, precise *in vivo* SNR measurements of blood and myocardium have not been evaluated presently, despite evidence in literature pointing to appreciable SNR benefits at 3T for fast gradient echo sequences [Noeske et al. 2000, Stuber et al. 2002, Hinton et al. 2003, Nayak et al. 2004]. In this chapter, SNR comparisons between 1.5T and 3T will be investigated in cine balanced steady-state free precession (b-SSFP) sequences, since these are the sequences commonly used in conjunction with contrast-enhanced viability MRI to evaluate ventricular dysfunction. The analysis will also allow assessment of field effects on the quality and reproducibility of cine b-SSFP at 3T.

The primary focus of this investigation was to measure T_1 of blood and myocardium in humans at two imaging field strengths, 1.5T and 3T, before and after contrast agent injection. T_1 values and SNR measurements were determined pre-contrast injection, and T_1 values were determined every 5 minutes post-contrast for 35 minutes. In addition, this study quantitatively investigates the relative distribution of contrast media between myocardium and blood at 1.5T and 3T. From time- and field-dependent T_1

values in myocardium, strategies can also be developed to optimize tissue suppression using the mathematical models developed in Chapter 3. Motivation for this investigation is that improved image contrast for delayed enhancement of myocardial infarction at high field strengths could be realized with knowledge of field dependent T_1 changes in normal myocardium and blood.

Background Theory: Relationship of Contrast Concentration and T_1

The pharmacokinetics of gadolinium-based contrast agents (e.g. Gd-DTPA-BMA) have been well described in both animals and humans [Wienmann et al. 1984, Strich et al. 1985, Prato et al. 1988, Oksendal et al. 1993, Dedieu et al. 1999, Arheden et al. 1999], and it has been shown that determining regional contrast agent concentration is an important predictor for MR signal enhancement in pathologic regions [Strich et al. 1985, Rehwald et al. 2002]. Signal enhancement, however, is not only dependent on pharmacokinetics and imaging parameters, but also magnetic field strength (B_0), which causes the spin-lattice relaxation times (T_1) of most biological tissues to change [Block 1974, Bottomley et al. 1984, Henriksen et al. 1993, Jezzard et al. 1996, Noeske et al. 2000]. Therefore, the contrast-to-noise ratio (CNR) post-contrast may not be equal between magnetic field strengths. Questions remain as to the *magnitude* of relaxation time differences between 1.5T and 3T for blood and myocardium, and what factors may contribute to this difference post-contrast injection. There is also uncertainty whether the change in T_1 between fields seen pre-contrast is extended to post-contrast values as well.

Relaxation *rates* ($R_1=1/T_1$) are often used when describing the effect of contrast media on tissue relaxation. Many mechanisms contribute to relaxation rate and these

mechanisms can be linearly combined to express an "observed" R_1 value (R_{1obs}). As such, the contribution from contrast media can be isolated from the pre-contrast R_1 (R_{1pre}) to express meaningful information about tissue enhancement [Elster 1997] and regional distribution of the contrast agent [Tweedle et al. 1991]. The extracellular volume fraction (*fECV*) [Wendland et al. 1997, Dedieu et al. 1999, Arheden et al. 1999], contrast agent concentration ([CA]) [Strich et al. 1985, Wendland et al. 1997], and longitudinal relaxivity of the contrast agent (r_1) [Xie et al. 2001] can be characterized from R_1 information using the following linear relationships [Tweedle et al. 1991, Wendland 1997]:

$$\begin{aligned} R_{1obs} &= R_{1pre} + R_{1contrast} \\ &= R_{1pre} + r_1 [CA] \\ &= R_{1pre} + r_1 [CA]_{EC} fECV \quad . \end{aligned} \qquad [1].$$

Note that $R_{1contrast}$ is equivalent to the change in R_1 over time ($\triangle R_1(t)$), i.e. $R_{1contrast} \equiv \triangle R_1(t) = R_{1obs} - R_{1pre}$. These relationships can be used to determine the contributing factors to changes in R_{1obs} with field strength and contrast administration. The primary term in $R_{1contrast}$ that may be subject to field dependency is r_1 since [CA] and *fECV* are constant for a given dose and individual, respectively. Though it has been shown r_1 is less sensitive to field change above 1.5T [Rinck et al. 1999], other reports have shown tissue specific change in r_1 [Strich et al. 1985, Xie et al. 2001]. Additional data is needed to explain if contrast media affects relaxation uniquely at different field strengths.

An informative index of the relative distribution behavior of Gd-DTPA-BMA in myocardium and blood can be assessed with MRI by considering the *ratio* of $\triangle R_1(t)$ in

myocardium and blood. Using Eq. [1], the ratio of $\triangle R_1(t)$ in myocardium and blood ($\triangle R_{1\text{myo}} / \triangle R_{1\text{blood}}(t)$), can be written as:

$$\Delta R_{1\text{myo}} / \Delta R_{1\text{blood}}(t) = fECV / (1.0 - Hct) \times r_{1\text{myo}} / r_{1\text{blood}}(t) . \quad [2]$$

This expression has been used to determine the relative tissue distribution volume and assess the cellular integrity in ischemic and necrotic myocardium [Wendland et al. 1997, Klein et al. 2004]. Equation 2 assumes that there is fast exchange and a steady-state between compartments ($[CA]_{\text{EC-myo}} = [CA]_{\text{EC-plasma}}$), and the assumption can be supported by $\triangle R_{1\text{myo}} / \triangle R_{1\text{blood}}(t)$ being constant over time [Wendland et al. 1997, Arheden et al. 1999]. The factor *fECV* / (1.0 - *Hct*) relates the extracellular volume of distribution between myocardium and blood, and is equivalent to the *partition coefficient between myocardium and blood* (λ_{myo}). If the ratio of relaxivities ($r_{1\text{myo}} / r_{1\text{blood}}$) is unity, then $\lambda_{\text{myo}} = \triangle R_{1\text{myo}} / \triangle R_{1\text{blood}}(t)$, and should be the same between 1.5T and 3T. A measurable change in $\triangle R_{1\text{myo}} / \triangle R_{1\text{blood}}(t)$ between 1.5T and 3T may indicate a field-dependent change in $r_{1\text{myo}} / r_{1\text{blood}}$.

When analyzed over time post-contrast, the change in R_1 (ΔR_1) at a particular field strength can provide information about the relaxivity of the contrast agent (r_1) in different tissues. Using Eq. [1], the ratio of $\triangle R_1(t)$ can be determined between 1.5T and 3T in the *same individual for either blood or myocardium*:

$$\Delta R_1(t)_{1.5\text{T}} / \Delta R_1(t)_{3\text{T}} = r_{1.5\text{T}} / r_{3\text{T}} . \quad [3]$$

This expression measures the relative change in contrast agent relaxivity between 1.5T and 3T in either blood or myocardium. A value of unity would indicate no difference in contrast agent relaxivity between field strengths, while a value greater than unity would indicate the relaxivity of the contrast media is *higher* at 1.5T.

Methods

SNR of Cine b-SSFP Sequences

In order to assess the performance of b-SSFP at 1.5T and 3T, the cine sequence was implemented in 7 normal volunteers (5 males, 2 females; ages 22-37yrs) at both field strengths using a phased array surface coil (1.5T: Philips Intera System, 5-element surface array coil; 3T: Siemens Trio, 8 element torso array coil). At 3T, a non-gated manual shim was performed following the scout images on a volume encompassing the entire heart, while auto-shimming (over the entire FOV) was performed at 1.5T. The b-SSFP cine sequences were performed in the vertical long axis (VLA) and short-axis (SA) plane. Pulse sequence parameters at 1.5T and 3T were kept equivalent: 360mm FOV; 256 matrix; 8mm slice thickness; 30-40° flip angle; TR/TE=3.6/1.8ms; and approximately 16 cardiac phases (50ms phase interval).

Signal and contrast-to-noise ratios (SNR and CNR) of the b-SSFP cine sequence were compared between 1.5T and 3T in the blood pool, as well as the anterior and inferior wall of myocardium. SNR was calculated from: $SNR = SI_{ROI} / \sigma_b$, where SI_{ROI} represents the signal intensity of the measurement and σ_b is the standard deviation of the background, which, with phased-array coils, can be approximated from the mean of an ROI measurement outside the body [Constantinides 1997]. Due to manufacturer-dependent constraints on the scanners, certain parameters (such as bandwidth) were limited to specific values. To overcome this mismatch, SNR was normalized between field strengths by calculating the SNR per voxel [Haacke 1999]:

$$SNR / voxel = \Delta x \Delta y \Delta z \sqrt{N_y N_x / BW_{read}} \qquad [4]$$

where Δx, Δy, Δz constitute the voxel size, N_x and N_y are the matrix dimensions, and BW_{read} is the bandwidth per voxel in the read direction. The measured SNR was scaled by this SNR/voxel factor to account for bandwidth and voxel differences between field strengths (this factor averaged about 1.50 between 1.5T and 3T). Contrast-to-noise was estimated as the SNR difference between the blood pool and myocardium. Data was represented as mean ± standard deviation (SD). Comparisons of measurement results between 1.5T and 3T were made with a two-tailed student's t-test and deemed significant if $p<0.05$.

T_1 Measurements In Vivo

All experiments were performed using commercially available Gd-DTPA-BMA (Omniscan, Amersham, Oslo, Norway) in 20mL pre-filled syringes. Ten healthy human subjects (6 male and 4 female, age: 29.7±4.7yrs) were recruited to participate in the study. The protocol in this study was approved by Emory's Institutional Review Board, and informed consent was provided by each volunteer. Each subject underwent two MRI scans: one at 1.5T (Philips Intera, 5 element phased array receive coil) and one at 3T (Siemens Trio, 8 element phased array receive coil), both involving contrast administration of either 0.1mmol/kg (n = 5, 3 male, 2 female) or 0.2mmol/kg (n = 5, 3 male, 2 female) intravenously. The appropriate dose was determined from the subjects' weight. Subjects underwent each scan at least 3 days apart and no more than 3 weeks apart; and 1.5T and 3T scanning were performed in no particular order.

T_1 measurements were performed using the pulse sequences initially described in Chapter 3 and validated in Chapter 4. Briefly, pre-contrast T_1 values of blood and

myocardium were calculated from a set of 4 ECG-gated, inversion recovery (IR), single-shot, balanced steady-state free precession (b-SSFP) sequences ("IR-ss") (FOV: 300×285 mm, 112 lines, 256 matrix, 8 mm thickness, TR/TE/α = 2.5ms/1ms/30-40°). The inversion times (*TI*) were slightly different at both field strengths to ensure points on either side of the zero-crossing (1.5T: 400, 600, 1000, 1400 ms; 3T: 500, 800, 1100, 1500 ms). Because of the long *TI*s, a trigger delay was applied to provide imaging in diastole of the second heartbeat. Post-contrast T_1 values were calculated from two ECG-gated, segmented IR b-SSFP images ("2pt-IR") (FOV: 300×285 mm, 256 matrix, 42 lines/segment, 8 mm thickness, TR/TE/α = 3.1ms/1.05ms/30-40°, 3 R-R intervals, scan time=12 heartbeats), with *TI*s of 150ms and 650ms ("TI_{low}" and "TI_{high}", respectively). Trigger delays were set to ensure imaging of the same phase of the cardiac cycle. The temporal resolution for each measurement (two scans) was less than one minute.

Automatic shimming was performed at 1.5T. At 3T, local shim volumes were manually placed over the heart to reduce artifacts due to field inhomogeneities. T_1 measurements were performed on a mid-ventricular short-axis slice. Following the pre-contrast T_1 imaging protocols, contrast media was administered through a bolus injection in the antecubital vein, and subsequent post-contrast T_1 measurements were made every 5 minutes for 35 minutes.

To characterize the effect of field dependence on relaxation times, the T_1 difference between 1.5T and 3T was determined before and after contrast injection for blood and myocardium in each subject (T_1@3T – T_1@1.5T). This T_1 difference was averaged over all subjects at a given dose, and represented a time course of 1.5T vs. 3T T_1 *difference*, before and after contrast injection. Data was represented as mean ±

standard deviation (SD). Comparisons of measurement results between 1.5T and 3T were made with an analysis of variance (ANOVA) and deemed significant if $p<0.05$.

Contrast Agent Distribution and Relaxivities as a Function of Field Strength

The partition coefficient of a tissue is defined as the fractional distribution of contrast media in tissue relative to another tissue, usually the blood pool. It can be approximated as the ratio of ΔR_1 in each tissue compartment as outlined in Eq. [2]. $\triangle R_{1myo} / \triangle R_{1blood}(t)$ measurements were performed at each time point post-contrast by converting the T_1 information to R_1 ($R_1 = 1/T_1$). Since $\triangle R_{1myo} / \triangle R_{1blood}(t)$ was quantified temporally and between field strengths, the steady-state distribution assumption was directly assessed, along with the field-dependence of Eq. [2]. Since direct measurements of hematocrit and myocardial extracellular volume fraction were not made, the precise value of r_{1myo} and r_{1blood} could not be quantified.

The ratio of $\triangle R_1(t)$ (Eq. [3]) was similarly calculated at each time point post-contrast for blood and myocardium using the acquired T_1 information. This analysis assumed that the contrast agent concentration at each time point for each individual was the same between 1.5T and 3T. This means that a disparity of $\triangle R_1(t)$ between 1.5T and 3T could be attributable to changes in r_1.

Simulations of Myocardium Null-Point Inversion Time at 1.5T and 3T

The purpose of this analysis was to calculate and compare the null-point inversion times (TI_{null}) at 1.5T and 3T using the T_1 values measured in this study. From the time course of T_1 change in normal myocardium, the null-point TI was determined for IR-

FLASH using a similar computational procedure as introduced in Chapter 3. The magnetization as a function of inversion time was simulated with Eqs. [3.18] and [3.19] (where M_{z1}^{-} is equivalent to the magnetization following inversion time, TI'), and the series of variable flip angles were appropriately determined using Eq. [3.20]. The necessary values for myocardium T_1 at 1.5T and 3T measured in this study served as input into the simulation. The other scan parameters used to simulate IR-FLASH were identical to those used previously in Chapter 4: 20° flip angle (variable sweep), *TR* = 4.4ms, 5 "dummy" start-up excitations, 25 lines/segment, and 18 excitations to $k_y = 0$ (linear acquisition order). Hence, the entire readout period consisted of 30 excitations. The simulation was performed with 1- and 2-"heartbeat" segment intervals, assuming an *RR* interval of 850ms, and the magnetization response was determined as a function of TI' for each segment number up to segment 4. The null-point TI' (TI'_{null}) was defined as the inversion time that produced *zero* magnetization for normal myocardium T_1. Since TI'_{null} is the null-point inversion time from the inversion pulse to the *first* excitation, this value was converted to the true null-point *TI* (TI_{null}) with $TI_{null} = TI'_{null} + (n_{k0} - 1) \cdot TR$, where n_{k0} is the number of pulses to the center of *k*-space. Additionally, for each computed TI_{null}, a finite *TI* span was determined to account for the observation that suppression is maintained for a range of inversion times around TI_{null} (as shown with the phantom experiments of Chapter 4). Therefore a threshold value of ± 5% of maximum intensity indicated suppression of the particular T_1 value. Finally, for comparison, the "ideal" *TI* was determined using the simplistic equation, $TI = T_1 \times \ln(2)$, which assumes no influence from readout excitation pulses or segment interval times. The ideal *TI* is customarily used to approximate the inversion time needed to null a particular T_1 value.

Results

SNR of Cine b-SSFP Sequences

Qualitatively, image artifacts were more prevalent at 3T than 1.5T if steps were not taken to modify volume shims and reduce TR and TE. These artifacts were primarily areas of susceptibility induced signal loss located in the anterior and inferior lateral wall (Figure 6.1a). Additionally, flow induced signal dephasing and shifts were also more evident at 3T (Figure 6.1b). These artifacts were reduced when a manual shim volume was centered over the heart (Figure 6.1c). No significant artifacts were encountered at 1.5T using automatic shimming.

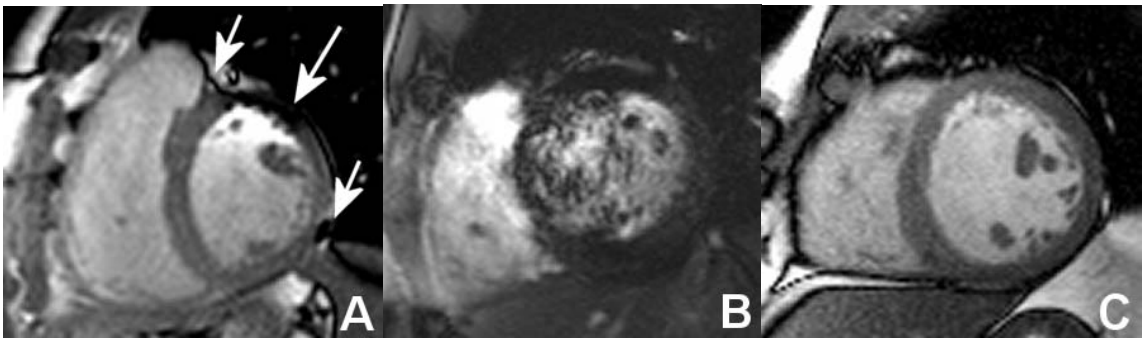

Figure 6.1. a-b) *Image artifacts in balanced steady-state cine imaging at 3T can be reduced with localized volume shimming and lowering TR as in* ***c)****.*

The SNR of the blood pool in the VLA b-SSFP images was 51±15 (a.u.) at 3T and 36±5 at 1.5T, an increase of 45% at 3T ($p=0.04$), as shown in Figure 6.2a-b. However, in the SHAX orientation (Figure 6.2c-d), the blood SNR increased only 29% ($p=0.06$). Differences in SNR between 3T and 1.5T also existed for the anterior wall of the myocardium in both the VLA (78% increase at 3T, $p=0.0005$) and SHAX (69%,

p=0.03) orientation. However, the SNR increase was less significant in the inferior myocardial wall in both the VLA (31%, p=0.002) and SHAX (30%, p=0.09).

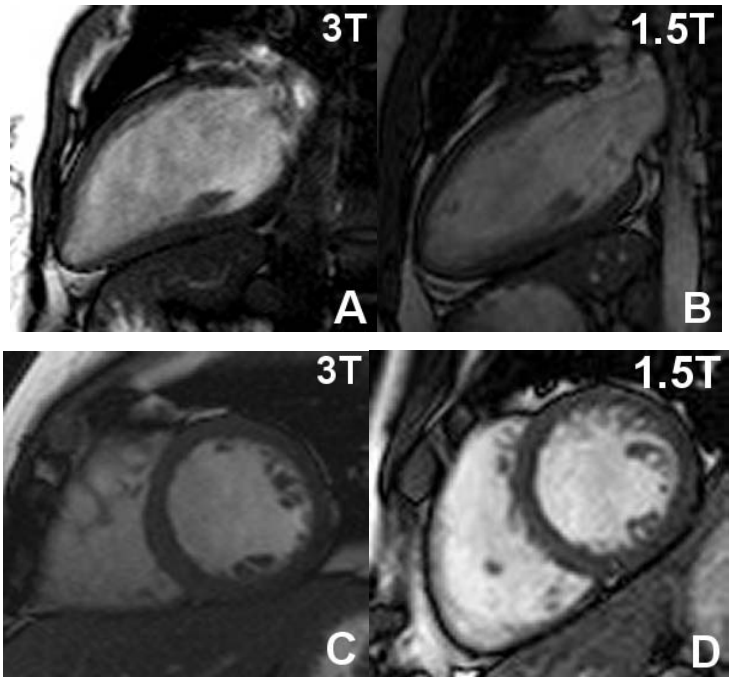

Figure 6.2. *Comparison of b-SSFP cine imaging between 1.5T and 3T in short- and long-axis views.*

Contrast-to-noise measurements between blood and myocardium were not significantly different between 1.5T and 3T, despite a mean increase at 3T. Blood-to-inferior myocardial wall contrast increased 43% at 3T in the VLA orientation (32±13 vs. 23±2, p=0.14) and 27% in the SHAX view (33±14 vs. 26±9, p=0.09), but the increase was not consistent for all subjects. The mean increase at 3T was less when blood-to-anterior wall was compared to 1.5T results (11% and 5% for VLA and SHAX views, respectively).

T_1 Calculation In Vivo

The T_1 measurement techniques were performed in all subjects without complication. An example is shown in Figure 6.3. From the 2-parameter fit of the pre-contrast T_1 measurement data, low fit errors were observed (r^2>0.95). The 2pt-IR produced T_1-maps without significant registration errors. A histogram analysis of ROI measurements from the T_1-maps (by measuring the standard deviation within each ROI) resulted in a 95% confidence interval of ±7.3 ms and ±8.0 ms, respectively, for T_1s measured using this technique [Haacke 1999].

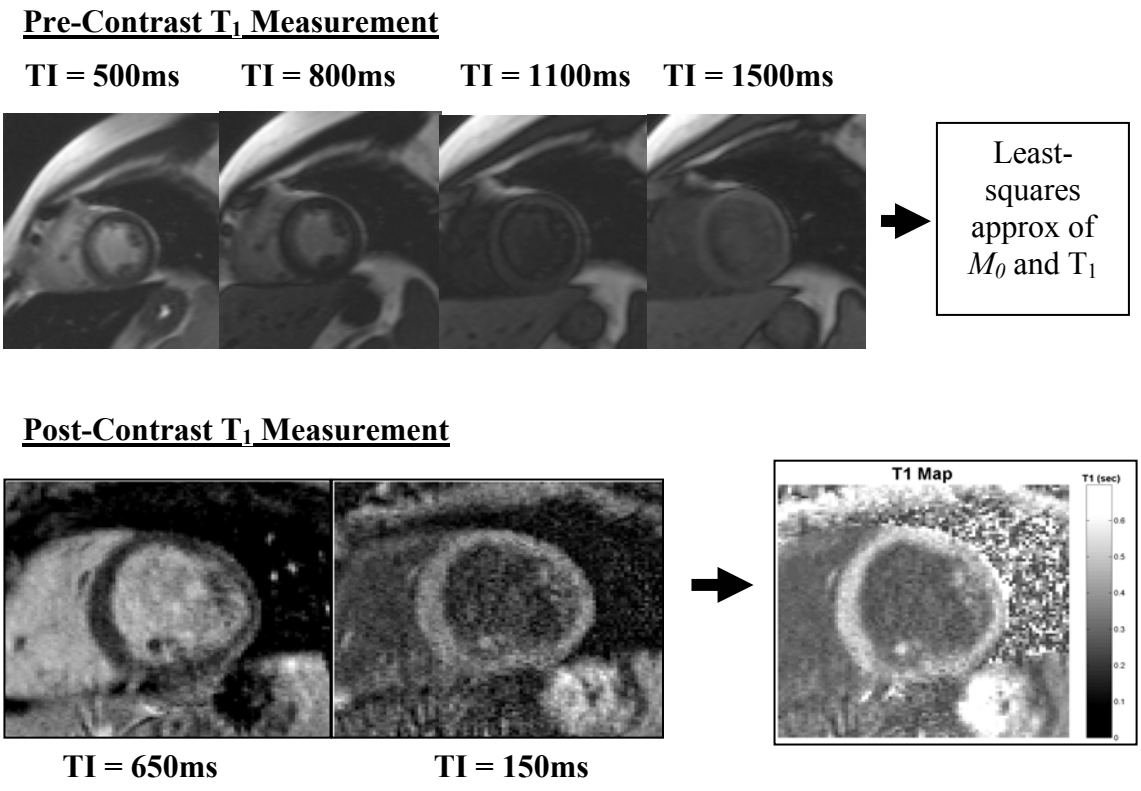

Figure 6.3. *In vivo T_1 measurement techniques.*

Table 6.1. T_1 Values of Blood and Myocardium in Normal Volunteers at 1.5T and 3T.

Dose (mmol/kg)	Time point (min)	1.5T		3T	
		Blood	Myocardium	Blood	Myocardium
0.1	0	1.58 ± .14[a]	1.07 ± .02	1.69 ± .03[a]	1.20 ± .10
	5	0.36 ± .08[a]	0.51 ± .08	0.40 ± .04[a]	0.54 ± .05
	10	0.40 ± .08[a]	0.56 ± .06	0.47 ± .03[a]	0.60 ± .03
	15	0.44 ± .08[a]	0.59 ± .07	0.51 ± .06[a]	0.63 ± .03
	20	0.48 ± .08[a]	0.62 ± .06	0.54 ± .06[a]	0.65 ± .02
	25	0.51 ± .08[a]	0.63 ± .05	0.56 ± .06[a]	0.67 ± .04
	30	0.54 ± .08	0.64 ± .06	0.59 ± .06[a]	0.70 ± .03
	35	0.55 ± .08[a]	0.66 ± .06	0.62 ± .06[a]	0.71 ± .03
0.2	0	1.58 ± .14[a]	1.05 ± .03	1.63 ± .07[a]	1.24 ± .03
	5	0.22 ± .06[a]	0.38 ± .05	0.28 ± .04[a]	0.42 ± .07
	10	0.28 ± .05[a]	0.44 ± .06	0.31 ± .07[a]	0.48 ± .06
	15	0.31 ± .06[a]	0.49 ± .05	0.34 ± .07[a]	0.49 ± .06
	20	0.33 ± .07[a]	0.50 ± .04	0.42 ± .07[a]	0.57 ± .04
	25	0.36 ± .07[a]	0.51 ± .05	0.44 ± .08[a]	0.59 ± .06
	30	0.38 ± .07[a]	0.53 ± .04	0.44 ± .08[a]	0.59 ± .06
	35	0.39 ± .07[a]	0.54 ± .05	0.45 ± .07[a]	0.59 ± .06

[a] *$p<0.05$ vs. myocardium*

Blood and myocardium T_1 values pre- and post-contrast at 1.5T and 3T are summarized in Table 6.1. Pre-contrast T_1 values for blood (n = 10) were not significantly different between 1.5T and 3T, despite a mean increase (1.5T: 1.58 ± 0.13s and 3T: 1.66 ± 0.06s, $p>0.05$). Significant differences were observed between pre-contrast T_1 values for myocardium (1.5T: 1.07 ± 0.03s and 3T: 1.22 ± 0.07s, n = 10, $p<0.05$).

Following contrast injection, there was a significant decrease in blood and myocardium T_1 values at both field strengths. In general, the post-contrast T_1 values for blood and myocardium were higher at 3T compared to 1.5T by 5-10%; however, the increase was not significant over the 10 subjects ($p>0.05$). It was observed that the change in T_1 from 1.5T to 3T was greater pre-contrast than post-contrast. Figure 6.4 depicts the difference in T_1 between fields (T_1@3T – T_1@1.5T) for blood and myocardium pre- and post-contrast. As shown, the *difference* in myocardium T_1 between

1.5T and 3T seen prior to contrast injection (0.16 ± 0.06 s, n = 10) was reduced by 72% (0.04 ± 0.06s, n = 10, p<0.05) after 10 minutes. The amount of the reduction was almost constant over all time points and insensitive to dose. A similar trend was observed in blood, but the decrease was 30% after 10 minutes.

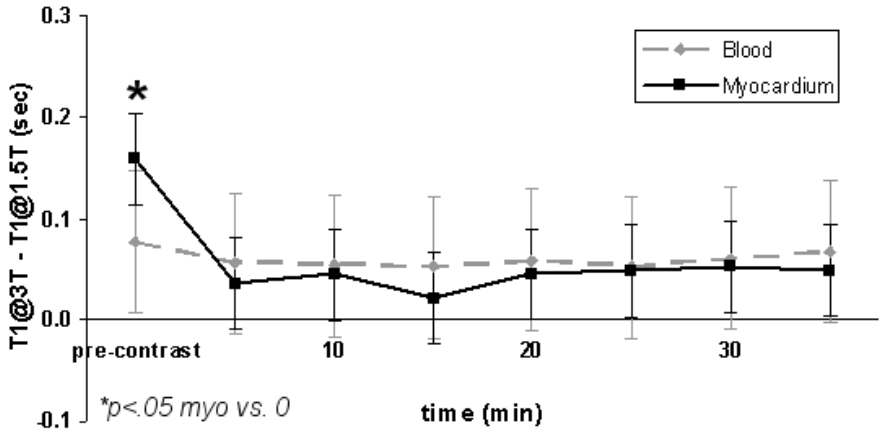

Figure 6.4. *T_1 difference between 1.5T and 3T before and after contrast in blood and myocardium.*

Contrast Agent Distribution and Relaxivities as a Function of Field Strength

Figure 6.5 shows the cumulative $\Delta R_{1myo}/\Delta R_{1blood}(t)$ values for 0.1mmol/kg and 0.2mmol/kg. A constant value of $\Delta R_{1myo}/\Delta R_{1blood}(t)$ existed at both 1.5T and 3T, which confirms a steady-state distribution of the contrast agent between blood and myocardium compartments. $\Delta R_{1myo}/\Delta R_{1blood}(t)$ was not significantly different between single and double dose (1.5T (single and double): 0.49 ± .05 and 0.44 ± .06; 3T: 0.56 ± .05 and 0.53 ± .07, p>0.05). Despite the constant value over time, a large difference was observed in $\Delta R_{1myo}/\Delta R_{1blood}(t)$ between 1.5T and 3T (0.46 ± .06 and 0.54 ± .06, n = 10, p<0.10),

which implies there may be a difference in compartmental contrast agent relaxivities (r_{1myo} and r_{1blood}) between field strengths (see Eq. [2]), assuming the ratio of compartmental extracellular volumes (λ_{myo}) did not change between 1.5T and 3T.

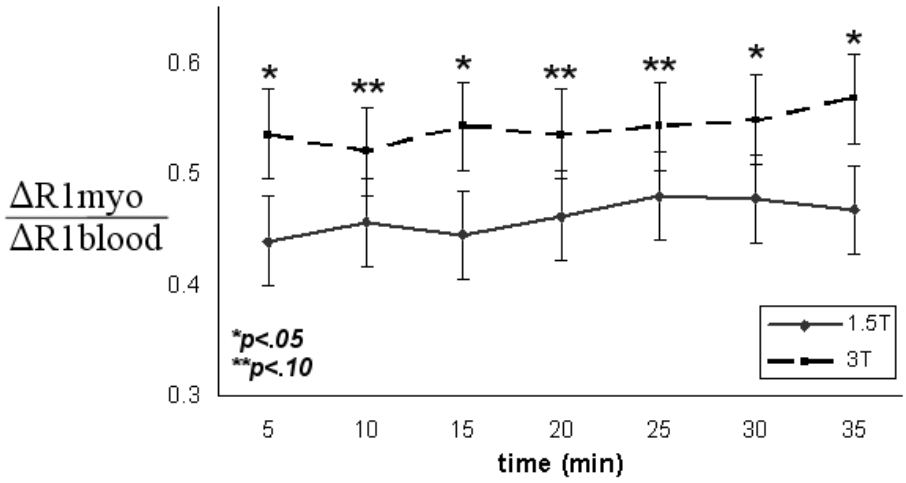

Figure 6.5. *Contrast agent distribution ($\Delta R_{1myo}/\Delta R_{1blood}$) as a function of time and field strength.*

$\Delta R_1(t)$ for blood and myocardium at both fields and doses was determined at each time point and used to determine $r_{1.5T}/r_{3T}(t)$ using the relationship given in Eq. [3]. These results are graphed temporally in Figure 6.6a for all subjects (n = 10), and showed that the ratio $r_{1.5T}/r_{3T}(t)$ averaged 1.01 ± 0.10 for myocardium over all time points (Figure 6.6b). *This result suggests that contrast agent relaxivity does not change with field strength in normal myocardium.* However, the average value of $r_{1.5T}/r_{3T}(t)$ in blood was 1.18 ± 0.20 over all time points. *This result implies that there was a decrease in contrast relaxivity in blood at 3T, relative to 1.5T.* High standard deviations were present in the data, which reflects the variation in contrast agent kinetics in different individuals.

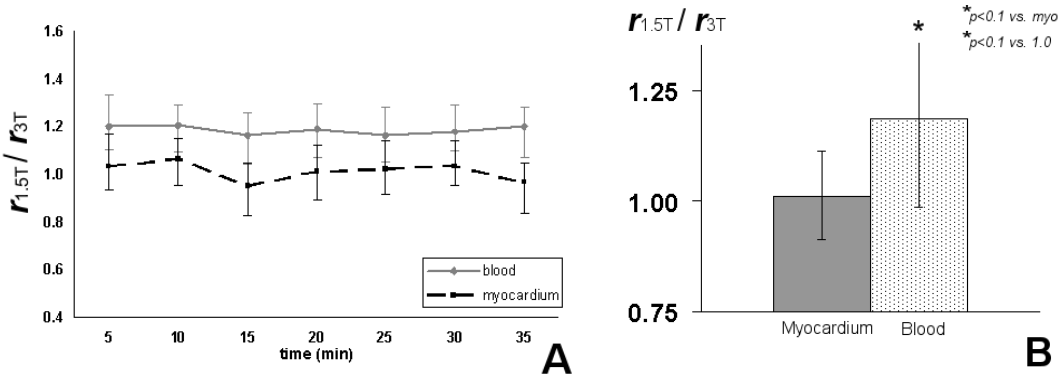

Figure 6.6. *Ratio of contrast agent relaxivities between 1.5T and 3T in blood and myocardium.*

Simulations of Myocardium Null-Point Inversion Time at 1.5T and 3T

The determination of the null-point *TI* using measured T_1 data at 1.5T and 3T was dependent on the segment number used to estimate the expected signal amplitude. The value of TI_{null} during the first segment was as much as 66% *longer* than the value during the 4th segment, when TI_{null} reached a steady-state value. This increase was less for 0.2mmol/kg doses and early post-injection time points, with an increase of approximately 20%. These trends confirm the results initially introduced in Chapter 3, stating that long segment repetition times (and shorter T_1 values) reduce the segment-to-segment signal variation during a scan. Stability of TI_{null} was revealed by the 4th segment, so final comparative analysis was performed using these values.

Figure 6.7 shows the change in TI_{null} from 5 to 35mins post-injection for 1.5T and 3T, and 0.1 and 0.2mmol/kg. One- and 2-heartbeat results are appropriately distinguished, and the *span* of TI_{null} at each time point is shown with vertical dashings, assuming ±5% deviations from the null-point magnetization of normal myocardium T_1

(see Methods). From the simulations, TI_{null} showed strong dependence on segment interval time ($p<0.05$), dose ($p<0.10$) and time post-contrast, while there was less dependence on field strength ($p>0.05$), with differences usually less than 10%.

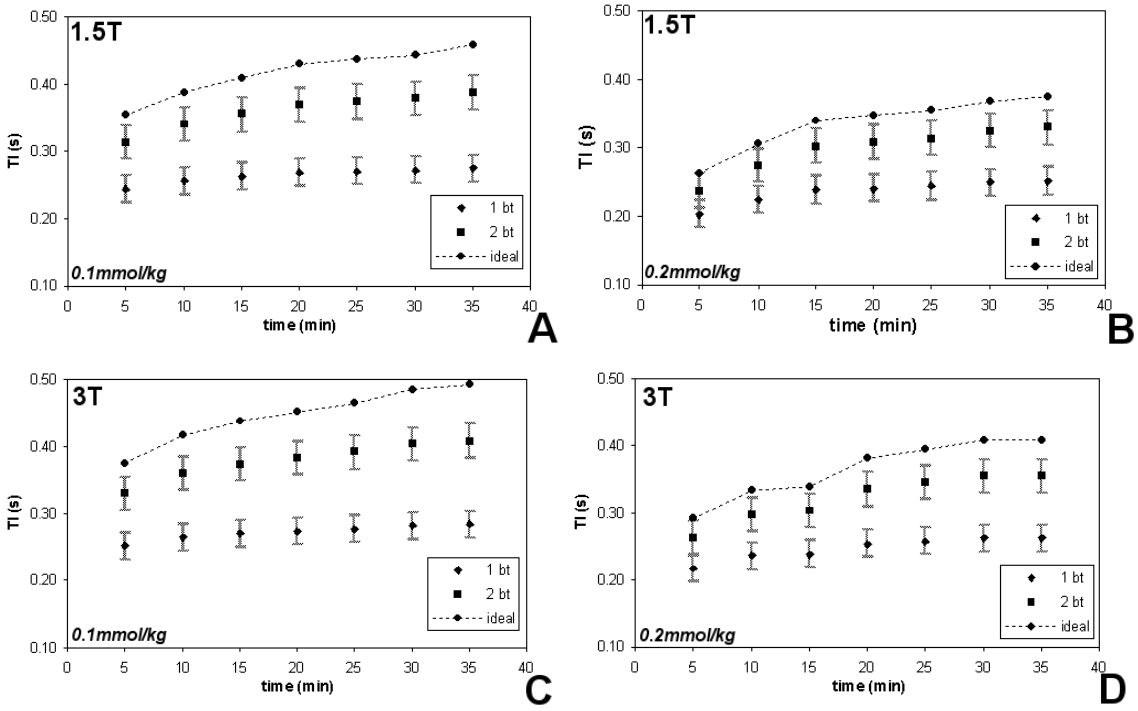

Figure 6.7. *The span of TI_{null} at 3T and 1.5T for 0.1 and 0.2mmol/kg.*

The "*ideal"* null-point *TI*, *which does not account for readout excitations and segment interval times*, accompanies the data in Figure 6.7. The ideal *TI* values were substantially higher than the simulation TI_{null} results, suggesting this simplistic evaluation of *TI* should be employed with caution if T_1 information is available. The separation of TI_{null} and ideal *TI* increased as the normal myocardium T_1 increased, with a maximum difference of 209ms (74%) for a 0.1mmol/kg 3T normal myocardium T_1 value of 710ms (35 min post). Generally, the ideal *TI* was over 30-70% greater than TI_{null} for 1-heartbeat interval data and 10-20% greater for 2-heartbeat intervals. The closest

correlation between the ideal *TI* and TI_{null} occurred for the lowest measured T_1 values and 2-heartbeat intervals (380ms; 0.2mmol/kg, 1.5T, 5mins post-injection).

The null-point *TI* values increased over time, relative to initial values measured 5 minutes post-injection. Over the span between 5 and 35 minutes post-injection, TI_{null} increased between 23 and 38% for 2-heartbeat segment intervals, while just 15 to 23% for 1-heartbeat intervals, implying that temporal user modification of the inversion time in delayed enhancement imaging is greater when 2-heartbeat interval IR-FLASH sequences are used. This has direct clinical significance since *a greater change in* TI_{null} *post-contrast places greater demand on user expertise to obtain high quality images*. There was also dose and field dependence, which had a primary effect on the T_1 of myocardium. This is also particularly significant since it suggests *a larger field strength (3T) will lessen the need for significant user modification of* TI_{null}*, making the study less operator-dependent.*

Discussion

The major findings of this chapter were: 1) the SNR and CNR of b-SSFP cine imaging were ~46 and ~21% higher, respectively, at 3T than 1.5T; 2) the T_1 of myocardium was 1.07 ± 0.03s at 1.5T and 1.22 ± 0.07s at 3T ($p<0.05$), but there was not a significant change in blood T_1; 3) the T_1 *difference* due to field strength (between 1.5T and 3T) was significantly reduced for myocardium post-contrast; 4) $\Delta R_{1myo}/\Delta R_{1blood}$ was different between 1.5T and 3T ($p<0.10$), suggesting field and tissue dependence of the contrast agent relaxivity; 5) the TI_{null} sensitivity over time was dependent on the segment

interval time and not substantially influenced by the field strength; and 6) there was large inter-subject variability of T_1 post-contrast.

The significance of B_0 inhomogeneity at 3T (initially described in Chapter 5) was most relevant with cine b-SSFP imaging (Figure 6.1), which is a common imaging technique in cardiac MRI. In addition to localized shimming, efforts should be made to reduce TR (TR < 3.5ms, either by maximizing bandwidth or FOV) to limit inter-pulse dephasing (due to the induced off-resonance precession angle), which is the predominant cause of signal loss in this sequence. There is also thought that reducing slice thickness will limit spin dephasing within the voxel, therefore reducing δB_0 artifacts [Reeder 1998]. Experience shows that artifacts in cine imaging can be reduced by using FLASH techniques, in which magnetization is repeatedly "spoiled" before each new TR.

Over all 10 subjects, the T_1 of myocardium was 1.07 ± 0.03 s at 1.5T and 1.22 ± 0.07s at 3T, while blood T_1 was 1.58 ± 0.13s at 1.5T and 1.66 ± 0.06s at 3T. The 3T values found in our study were roughly 8% higher than those reported by Noeske (1.55s for blood and 1.12s for myocardium at 3T) [Noeske et al. 2000], which may be due to different measurement techniques. Noeske utilized a partially re-focused gradient echo technique ("GRASS") to measure T_1 of myocardium and blood, but the methodology is unclear about the segment repetition time and the quantification method. The T_1 of blood at 1.5T was approximately 15-30% higher in our study compared to some previously reported values (1.20s [Greenman et al. 2003], 1.23s [Klein et al. 2004], 1.38s [Flacke et al. 2001], 1.34s [Saeed et al. 2000]), but these values can also be dependent on the measurement technique and flow characteristics. Klein [Klein et al. 2004] and Flacke [Flacke et al. 2001] utilized at modified "Look-Locker" technique, which is known to

measure T_1* [Pickup et al. 2004]. It is also known that blood T_1 at 1.5T depends strongly on hematocrit [Janick et al. 2001], with variations between 1.1s and 2.0s for hematocrit variations of 0.6 and 0.2. The b-SSFP readout module used with our method has been shown to be less sensitive to saturation effects than spoiled gradient-echo techniques (FLASH) due to the refocusing and reuse of transverse magnetization, making the sampling of free M_z recovery more accurate in inversion recovery experiments [Scheffler et al. 2001]. This is because the decay rate of magnetization *during* b-SSFP readout (E_1*) is *slower* than for FLASH [Scheffler 2003, Schmitt et al. 2004, Pickup et al. 2004] (also see Figure 4.3-4.5, Chapter 4). Due to this transient decay rate, the continuous sampling of the T_1 relaxation curve using either b-SSFP or FLASH requires appropriate correction of the *measured* T_1 relaxation time, with more significant corrections needed when FLASH is used. Since this present study samples T_1 with discrete *TI*s using (relatively) short readout times, the majority of the signal intensity at $k_y = 0$ evolves from the free inversion recovery preceding data acquisition, *making the measured T_1 an accurate estimation of the true T_1*. Furthermore, this measurement technique was assessed on phantoms of varying T_1 values and resulted in accurate measurements compared to reference T_1 values (Table 4.2, Chapter 4). The post-contrast T_1 values at 1.5T reported here are comparable to those reported previously using the Look-Locker method [Klein et al. 2004].

The average difference in pre-contrast T_1 between 1.5T and 3T was larger for myocardium than blood, 0.16 ± 0.06s vs. 0.08 ± 0.13s, respectively. The reason myocardium T_1 increased more than blood going from 1.5T to 3T could be attributed to the greater free water content and shorter molecular correlation times in blood

[Bloembergen et al. 1948], which would cause less field dependence on T_1, much the same way water and CSF T_1 appear almost insensitive to field change. The trend toward similar blood and myocardium T_1 values at high field strength may lower image contrast between blood and myocardium on T_1-weighted images.

A dose of 0.2mmol/kg caused T_1 values to be significantly lower than 0.1mmol/kg at both field strengths ($p<0.05$), as seen in Table 6.1. However, the measured $\Delta R_{1myo}/\Delta R_{1blood}$ and $r_{1.5T}$ / r_{3T} were not significantly different between single and double dose. As a result, the data was shown cumulatively. The partition coefficient (which is related to $\Delta R_{1myo}/\Delta R_{1blood}$) is not known to be dose dependent, since it is an inherent physiological property. Relaxivity also should not be dose dependent. Indeed, different doses of Gd-DTPA-BMA in solution yield specific R_1 values (see Figure 4.2), and the slope of this relationship is equal to the relaxivity, and assumed to be constant.

Post-contrast T_1 values showed a general increase in T_1 from 1.5T to 3T, but the change was neither significant nor constant over all subjects. Some subjects revealed marked T_1 change between fields (+0.15s), whereas others, at the same time point, experienced only subtle change (~0.06s). As a result, when data at each time point was analyzed cumulatively, there was not a significant difference in blood and myocardium post-contrast T_1 between 1.5T and 3T (Table 6.1). This observation reveals that the change in T_1 seen prior to contrast administration is obscured following injection, primarily as a result of distinct contrast kinetic behavior among subjects, or a substantial effect of T_2* at 3T during T_1 measurement. The former may be attributed to differences in glomerular filtration rate, left ventricular ejection fraction, or extracellular volumes among the subjects, while the latter may be due to field inhomogeneities and

susceptibility effects. Though scanning procedures were implemented to reduce T_2* dephasing (short TE) and dose was identical at both field strengths, it is possible that the concentration of the contrast agent in circulation at any given time point was not the same during both scans. A difference in Gd-DTPA-BMA concentration between scans could be related to a change in the glomerular filtration rate (GFR) day-to-day, which is largely controlled by food or fluid intake. Large differences in GFR were recently seen among humans and dogs [Kampa et al. 2003, Hackstein et al. 2003] and over day-to-day periods [Kampa et al. 2003]. This degree of variation in post contrast T_1 measurements *in vivo* has been seen previously [Sharma et al. 2003, Klein et al. 2004].

The ratio $\Delta R_{1\text{myo}}/\Delta R_{1\text{blood}}(t)$ at 1.5T was similar to values measured previously with MRI at 1.5T [Klein et al. 2004] and 2T [Wendland et al. 1997, Arheden et al. 1999]. These reports assumed that $\lambda_{\text{myo}} = \Delta R_{1\text{myo}}/\Delta R_{1\text{blood}}(t)$, which implies $r_{1\text{myo}} / r_{1\text{blood}} = 1$ (Eq. [2]). However, in the present study, there was an observable difference in $\Delta R_{1\text{myo}}/\Delta R_{1\text{blood}}$ (t) between 1.5T and 3T, which (from Eq. [2]) suggests there may be some tissue- and field-dependency of Gd-DTPA-BMA relaxivity (r_1). Previous investigations directly quantifying Gd-DTPA relaxivity have shown marginal decreases in r_1 *in vivo* and *in vitro* at high field strengths [Donahue et al. 1994, Bernstein et al. 2001, Takahashi et al. 2003]. Since explicit contrast agent concentrations were not determined in this study, relaxivity of Gd-DTPA-BMA in blood and myocardium ($r_{1\text{blood}}$ and $r_{1\text{myo}}$, respectively) could not be directly calculated using serial R_1 measurements (Eq [1]). Using approximate values of $fECV = 0.35$ and $Hct = 0.40$ [Wendland et al. 1997], $\lambda_{\text{myo}} = fECV / (1 - Hct) \approx 0.58$ in Eq. [2], making $r_{1\text{myo}}/r_{1\text{blood}}$ approximately 0.80 at 1.5T and 0.93 at 3T. It can be inferred from this data, therefore, that the relaxivity of Gd-DTPA-BMA may be greater in blood

than myocardium ($r_{1myo}/r_{1blood}(t) < 1$). This is paralleled by the observation that $r_{1.5T}/r_{3T}$ is 1.18 ± 0.15 in blood and 1.01 ± 0.10 in myocardium (Figure 6.6b), implying that the relaxivity in blood may be *decreasing* with field strength ($r_{1.5T}/r_{3T} > 1$), while the relaxivity in myocardium is remaining constant. However, due to the broad range of measured myocardial extracellular volumes (0.25 to 0.40 [Diesbourg et al. 1992, Arheden et al. 1999, Klein et al. 2004, Vinnakota et al. 2004]), there will be uncertainty in generalizing r_{1myo}/r_{1blood} and $r_{1.5T}/r_{3T}$ without precise measurements of *Hct* or λ_{myo}.

Longer T_1s will exist at higher fields for a given individual, even after injection of a contrast agent. Thus, for imaging sequences that rely on preparation pulses, such as inversion and saturation recovery, suppressing longer T_1s is simpler since the slope of magnetization recovery is shallower as it crosses or originates from zero, allowing some leeway in *TI* selection. But this may also detriment image contrast if another tissue of interest is also suppressed. From this discussion, a decrease in blood r_1 at 3T should produce lower image contrast between blood and myocardium post-contrast at 3T, *relative to 1.5T*. This may have significance in delayed enhancement imaging at 3T, as image contrast will likely decrease between blood and normal myocardium after normal myocardium is suppressed using inversion recovery. This may benefit image contrast between enhanced infarct tissue and blood for delineating subendocardial infarcts.

One of the direct outcomes of temporal T_1 data at 1.5T and 3T is the determination of the inversion times that would theoretically suppress the signal from normal myocardium. It has been shown in previous chapters that the mathematical representation of IR-FLASH closely approximates the null-point *TI* (TI_{null}) as determined by phantom T_1 experiments. In relation to delayed enhancement imaging at 3T, *this study*

has shown that TI_{null} is not significantly different than values at 1.5T ($p>0.05$). For both 0.1 and 0.2 mmol/kg doses, the T_1 of normal myocardium increased approximately 50ms from 1.5T to 3T, and remained constant over time. The reduction in T_1 difference post-contrast is the primary reason for the similarity of TI_{null} between 1.5T and 3T.

A more noteworthy discordance of TI_{null} simulations concerned the choice of the segment interval delay time. Two options are currently employed for IR-FLASH in delayed enhancement imaging: "1-heartbeat" segment intervals, which resembles a 3D delayed enhancement sequence, or "2-heartbeat" segment intervals, which typifies a 2D delayed enhancement sequence. From Figure 6.5, there is greater temporal TI_{null} sensitivity for 2-heartbeat intervals, meaning that TI_{null} must be modified to a greater extent between imaging time-points. It should be noted that TI_{null} with 2-heartbeat segment intervals are generally 20-40% longer than 1-heartbeat interval values.

Conclusions

In conclusion, T_1 increased from 1.5T to 3T, but more significantly for myocardium than blood. Following contrast administration, T_1 differences between 1.5T and 3T were obscured by individual variability between subjects, so there was not a significant difference in T_1 between fields following contrast injection. The ratio of contrast agent distribution ($\Delta R_{1\text{myo}}/\Delta R_{1\text{blood}}(t)$) exhibited some field dependence, which suggests possible field-dependence of contrast agent relaxivity. These observations may play a role in the reduced T_1 difference between 1.5T and 3T. The relevant effect of the reduction in post-contrast T_1 difference is the similarity of TI_{null} needed to suppress normal myocardium with delayed enhancement imaging at 1.5T and 3T.

CHAPTER 7

CONTRAST-ENHANCED IMAGING IN PATIENTS AT 1.5T AND 3T

Introduction

Until now, the discussion of image contrast and relaxation differences between 1.5T and 3T have been confined to customized imaging phantoms and healthy individuals (Chapters 4, 5, and 6). Several important conclusions concerning magnetic field effects, both positive and negative, were made based on these initial observations. But ultimately, the techniques developed and trends outlined must be transferable to clinical applications in order to establish a relevant method of improving the efficiency and/or quality of a clinical scan. Examining whether the limitations of 3T cardiac imaging are outweighed by the benefits can only be assessed by considering a quantitative comparison of delayed enhancement imaging in patients with prior myocardial infarction at both 1.5T and 3T.

The significance of this chapter in the scheme of this project is twofold. First, a detailed examination of T_1 relaxation differences between 1.5T and 3T of infarct tissue (to complement those of normal, or "remote" myocardium and blood) will provide data for contrast optimization algorithms, such as those outlined in Chapter 3. This will allow the selection of optimal imaging parameters, particularly *TI* and α. Furthermore, relaxation analysis in a selected patient population not only helps characterize the pharmacokinetics of contrast agent distribution (and excretion) in relation to standard values found in normal individuals, but also provides details of whether infarct tissue *relaxivity* is enhanced or depressed at higher field strengths. This latter fact is

instrumental in predicting whether heightened infarct visualization is achievable at 3T. The second objective is the impetus to examine image quality characteristics of delayed enhancement imaging at 1.5T and 3T. This "raw" comparison includes quantification of the signal- and contrast-to-noise ratio (SNR and CNR) gain at 3T in a clinical situation in the *same individuals*. This also requires observing and potentially reducing any severe image artifacts that may arise. In this basic analysis of image quality characteristics at 3T, parallels will be drawn with 1.5T imaging, along with recommendations to achieve the highest quality images at 3T.

To these ends, the overriding focus of this chapter is the measurement of longitudinal tissue relaxation times at 1.5T and 3T post-contrast administration. By including baseline measurements prior to contrast agent injection, a clear picture of the T_1 time course of three tissues (blood, normal myocardium and infarcted myocardium) can be obtained, along with contrast agent characteristics such as relative contrast effectiveness between field strengths. These aims are direct extensions of the experiments performed in Chapter 6 with "normal" (healthy) volunteers. It is expected that the T_1 trends of myocardium and blood will be similar to those measured in Chapter 6, with infarct T_1 enhancement being significantly greater than normal myocardium. *The question remains, however, whether infarct T_1 enhancement will be greater at 3T than 1.5T*, and whether the reduced cardiac function, which is common to this population subset, has a significant effect on post-contrast T_1 trends.

Methods

Seven persons with known myocardial infarction (MI) (6 male, 1 female, age range: 50-77yrs) participated in this study. The presence and location of the MI was confirmed by the referring physician from elevated cardiac enzymes (CK, CKMB, Troponin I), electrocardiogram (ECG) analysis, and prior catheterization/viability assessment. The protocol for MR imaging was approved by Emory's institutional review board and written informed consent was given by each subject prior to examination. The volunteers underwent two MRI scans, first at 1.5T (Philips Intera, Best, The Netherlands, 5 element cardiac phased array coil) to confirm the presence and location of the MI, and another at least three days (but no more than 10 days) later at 3T (Philips Intera 3T with a 6 element array cardiac coil, or Siemens Trio, Erlangen, Germany, 8 element torso phased array coil). ECG leads were placed on the subject's chest, and the tracings were visually confirmed at the imaging console.

Pre-Contrast T_1 Measurement

Following localization of a short-axis imaging plane containing the location of the MI, pre-contrast T_1 measurements of blood, infarcted myocardium and normal myocardium were performed using an inversion recovery (IR), single-shot fast gradient echo sequence (FLASH) using four inversion times (*TI*) at each field strength (1.5T: *TI* = 400-1400ms; 3T: *TI* = 500-1500ms). This pulse sequence was analyzed for pre-contrast T_1 measurements in Chapters 3 and 4 using a b-SSFP readout, but, as mentioned, a FLASH version was also useful with appropriate adjustments. Data acquisition parameters were 320×320mm field-of-view (FOV), 128×128 matrix with reduced data

sampling (60 phase encode lines acquired consecutively), 8mm slice thickness, TR/TE/α = 3.9/1.9ms/15°, linear acquisition order, and a bandwidth of 500 Hz/pixel. An additional scan was acquired without inversion preparation to serve as a reference image to standardize the image scaling due data acquisition parameters and proton density. As in previous chapters, rescaling was performed to compensate for differences in image gain. T_1 was calculated using a least-squares fitting method outlined in Appendix C for pre-contrast T_1 measurements.

Post-Contrast T_1 Measurement

Following contrast agent injection (0.2mmol/kg, Gd-DTPA-BMA, Omniscan, Amersham, Oslo, Norway), the T_1 of blood, infarcted tissue and normal myocardium was measured every 5 minutes for 30 minutes. T_1 relaxation was quantified from a single breath hold segmented FLASH-EPI "Look-Locker" sequence, which was programmed to acquire at least 46 cardiac frames over several heartbeats using a temporal resolution of approximately 40ms. An additional free relaxation period of 1000ms was installed after data acquisition to allow further T_1 relaxation before the next segment. Each image frame of the scan collected 128×96 pixels (reconstructed to 256 pixels) over a 300×300×8mm FOV imaging plane. Data was sampled with TR/TE/α = 7.6/4.1ms/10°, with 5 EPI data lines per TR, and 5 TRs per temporal frame. The scan duration was 14-18 seconds using 2 signal averages (NSA = 2). The Look-Locker technique was used in the current measurements due to its availability at 3T and its analysis of feasibility in Chapter 4. Recall that the 2-point ratio technique was used exclusively in Chapter 6, and post-contrast T_1 results showed close correlation with previous measurements in literature

using the Look-Locker method. Furthermore, the validation of both techniques over a broad range of T_1 warrants the interchangeability of both measurement techniques for evaluating post-contrast T_1.

The T_1 data was taken off-line for processing in Matlab computing software (MathWorks, Natick, MA). Regions-of-interest (ROI) were drawn for blood, normal myocardium, and infarcted tissue in each image frame, and the resulting re-scaled signal intensities, *S*, were fit to a three-parameter mono-exponential curve of the form:

$$S(nTI) = A(1 - B\exp(-nTI / T_1^*)), \qquad [1]$$

where *n* is the frame number, *TI* is the frame temporal resolution, T_1* is the *apparent* spin-lattice relaxation time, and *A* and *B* are constants. The true T_1 was related to T_1* by the methods outlined in Chapter 5 and in previous investigations [Pickup et al. 2004]. This relationship relies heavily on α and the expected T_1, as seen in Figure 7.1. But since α is low (10°) and the expected T_1 values are short, the error in true T_1 estimation is relatively low (Figure 7.1a). As in the phantom experiments in Chapter 5, a modulated α value of $\alpha' = 0.7\alpha$ was used in these corrections, which is a valid approximation of the *average* flip angle within the imaging slice [Diechmann et al. 1992].

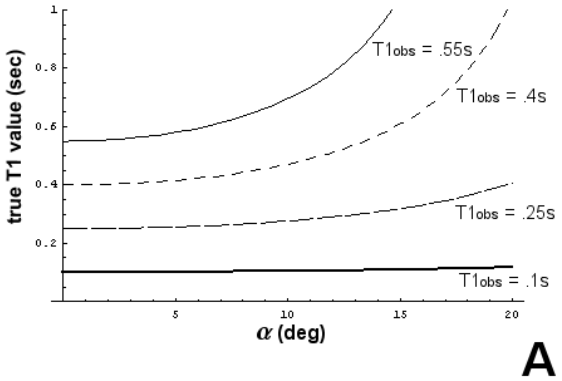

Figure 7.1. *Estimation of true T_1 value from a calculated T_1 (T_{1obs}) at a prescribed flip angle (α).*

Delayed Enhancement

Delayed enhancement imaging was performed at 1.5T and 3T on each subject at various time points between 5-30 minutes following contrast administration. The imaging plane was selected to best visualize the infarcted tissue (usually short-axis or long-axis views), and all data was collected in late diastole. All measurements of the signal intensity of the MI were evaluated with a 2D pulse sequence. A 3D pulse sequence was available at 1.5T, but not available at 3T for all subjects. Hence, *image quality comparisons between 1.5T and 3T were made exclusively with the 2D sequence*. The 2D single-slice imaging sequence was an IR, segmented-FLASH sequence with acquisitions every 2 heartbeats. Imaging parameters were: 320×300×10mm FOV, 256 matrix with 80% sampling, TR/TE/α = 4.5-5.0ms/1.6-2.3ms/15-20°, 16 lines/segment, bandwidth = 225-448Hz/pixel, and NSA = 1. The inversion times for the 2D sequence were determined from a Look-Locker image set preceding the scan. These *TI* values varied between 1.5T and 3T, but spanned 200-350ms over all scans. Exact inversion time ranges used in these scans are detailed in the Results section as part of the analysis.

SNR and CNR Measurements

Regions-of-interests (ROIs) from the blood pool, normal myocardium (septal and lateral), and infarcted tissue were measured in each delayed enhancement image. The mean signal (M) and standard deviation (σ_M) of background air were also measured. Since these latter quantities represent Rayleigh noise distribution in magnitude images, the true Gaussian distributed (white noise) standard deviation (σ_0) can be related to M (or σ_M) by considering the chi-squared probability distribution of M and the number of

elements in the receive coil, c [Constantinides et al 1997]. For c = 5, 6, and 8 used in this study, σ_0 is 0.32M, 0.29M, and 0.25M, respectively. The signal-to-noise ratio (SNR) of each tissue was then determined by dividing the average measured signal intensity of tissue (S_{ROI}) by σ_0: $SNR_\sigma = S_{ROI} / \sigma_0$. The contrast-to-noise ratio (CNR) of each tissue pair was determined from the absolute difference between the two corresponding SNRs: $CNR = Abs\left(SNR_1 - SNR_2\right)$. This CNR relationship is similar to the simulated $T_{1contrast}$ signal difference expression given in Chapter 3 (Eq. [3.24]), *without M_0 normalization*. The signal ratio ($SR = SNR_1 / SNR_2$) was also evaluated (infarct-to-blood) in order to express the *relative enhancement between two tissues*. This measurement was neglected in Chapter 4 because of the normalization procedures needed to compare the phantom results with simulation results. But it is convenient here since standardized images without IR pulses were not acquired with each delayed enhancement image post-contrast.

Since the scan parameters at each field strength could not be precisely matched (resolution and bandwidth), an empirical expression for SNR/voxel was quantified for each scan so that tissue SNR values could be compared between field strengths and scan types. This value was introduced in Chapter 6 and approximated by:

$$SNR/voxel \propto \Delta x \Delta y \Delta z \sqrt{\frac{N_x N_y N_z N_{acq}}{BW_{read}}}, \qquad [2]$$

where $\Delta x \Delta y \Delta z$ are the voxel dimensions (mm^3), N_x, N_y, N_z are the number of voxels in each dimension, N_{acq} is the number of signal averages, and BW_{read} is the readout bandwidth (Hz). For 2D imaging, Δz = slice thickness and N_z = 1. The additional SNR contributions due to minor TR and TE differences (< 1ms) were neglected.

Determination of Optimal Imaging Parameters from T_1

Optimal imaging parameters could not be derived before the delayed enhancement experiments described above. However, given the T_1 distribution in blood, normal myocardium and infarct tissue at 1.5T and 3T, simulations estimating the expected *transverse magnetization* were performed off-line to determine the optimal imaging parameters of IR-FLASH. Particularly, the magnitude of "$T_{1contrast}$" between normal and infarcted myocardium, using the strategies developed in Chapter 3 and 4, were simulated using the acquired T_1 information. (Recall that "$T_{1contrast}$" is the *expected image contrast determined mathematically*) The *optimal* $T_{1contrast}$ was determined (relative to the equilibrium longitudinal magnetization, M_0), and yielded values for the optimal flip angle (α_{opt}) and the optimal inversion time (TI_{opt}) from a 3D contour plot (see Figure 3.19). Also, based solely on the normal myocardium T_1 information, the null-point inversion time, TI_{null}, which describes the inversion time needed to produce zero magnetization for normal myocardium, was determined by simulating another IR-FLASH sequence. Concessions were also made during this calculation to provide a finite range for TI_{null} *at each time point* by assuming that the signal from normal myocardial is theoretically "nulled" when its magnetization level is less than ±5% of a FLASH sequence acquired without an IR pulse. Recall that this assumption was determined in Chapter 4 with phantom experiments and used with the simulations in Chapter 6. In these simulations, $M_0 = 1$ for all tissues initially. However, additional simulations were performed to account for the *increased proton sensitivity at 3T*, which would mathematically increase the value of M_0 in these simulations, relative to 1.5T. As determined experimentally in Chapter 4, the relative value of M_0 for a given tissue

increased approximately 33% at 3T. In Chapter 5, the gain in M_0 was also estimated, and showed that M_0 increased by at *least* 30% (30-97%). This increase in M_0 at 3T implies that the $T_{1contrast}$ is not solely dependent on the T_1 ratio between infarcted and normal myocardium, but also on the inherent signal elevation found at 3T.

The mathematical IR-FLASH simulation sequence was customized to resemble the imaging sequence used in the delayed enhancement studies in this chapter. For $T_{1contrast}$ simulations, the number of RF excitation pulses per segment acquisition was set to 16 for both 1- and 2-heartbeat cases, with an additional 5 pulses preceding the segment to represent the default "dummy" start-up excitations typically used. The "2-heartbeat" simulation resembles the 2D IR-FLASH imaging case, while the "1-hearbeat" simulation closely resembles a 3D IR-FLASH imaging case. In both sets of simulations, a quadratic variable flip angle sweep (VFS) was inserted during the first 13 pulses, in which the first pulse was set to 0, and the 13th pulse was set to α_{max}, which was the nominal, or "maximum", flip angle set by the user (Eq. [3.20]). Since a *linear* k-space acquisition order was used for imaging, the central pulse number in each segment (n = 13) was used to denote *the phase encode step that most described the $T_{1contrast}$ or signal information*, while the 3rd segment was used to represent the magnetization response that best describes the true $T_{1contrast}$ (see Figure 3.12). Other simulation parameters were TR = 5ms, and RR = 850ms (1-beat case) and 1700ms (2-beat case).

Contrast Agent Distribution

The pharmacokinetics of the contrast agent was evaluated for tissue compartmental (infarct and normal myocardium) distribution (ΔR_{1inf} / ΔR_{1blood} and

$\Delta R_{1myo} / \Delta R_{1blood}$) and relaxivity ($r_1$) differences between 1.5T and 3T. Recall from Chapter 6 that the expression $\Delta R_{1myo} / \Delta R_{1blood}$ quantifies the relative distribution of the contrast agent to myocardium (normal or infarcted) over blood distribution (Eq. [6.2]):

$$\Delta R_{1myo} / \Delta R_{1blood}(t) = fECV / (1.0 - Hct) \times r_{1myo} / r_{1blood}(t) . \quad [6.2]$$

Under the constraint that the contrast agent relaxivity is equivalent among compartments ($r_{1inf} = r_{1myo} = r_{1blood}$), $\Delta R_{1myo} / \Delta R_{1blood} = \lambda_{myo}$, which is the *partition coefficient of myocardium*. Otherwise, the partition coefficient of myocardium is, $\lambda_{myo} = fECV_{myo} / (1 - Hct)$, where $fECV_{myo}$ and Hct are the fraction of extracellular space in myocardium (or infarct) and hematocrit, respectively. These expressions are only valid under the assumption of steady-state extracellular contrast agent distribution and fast exchange between compartments, which can be validated by $\Delta R_{1myo} / \Delta R_{1blood}$ being constant over time post-contrast.

Without assigning any prior definition to hematocrit, or the fractional extracellular space, $\Delta R_{1myo} / \Delta R_{1blood}$ was calculated for myocardium and infarct tissue at each field strength by converting the T_1 measurements to R_1 ($R_1 = 1/T_1$), and evaluating $\Delta R_1 = R_{1post} - R_{1pre}$ at each time point. Since the contrast agent dose was kept the same between fields, the variation of $\Delta R_{1myo} / \Delta R_{1blood}$ between 1.5T and 3T was indicative of the relaxivity, r_1, possibly being field- and tissue-dependent.

For each time point, ΔR_{1myo} (infarct and normal) and ΔR_{1blood} was also related between field strengths, and the relative field-dependent r_1 ratio was determined from:

$$(r_1)_{1.5T} / (r_1)_{3T} = (\Delta R_1)_{1.5T} / (\Delta R_1)_{3T} . \quad [4]$$

This measure was used to reaffirm the posit introduced in Chapter 6 that compartmental relaxivity may *reduce* at higher fields. This feature of the contrast agent may explain the difference in image contrast of the delayed enhancement sequence between 1.5T and 3T.

Results

T_1 Measurements

Table 7.1 lists the T_1 values calculated for blood, normal and infarcted myocardium. Prior to contrast administration, the T_1 of blood was significantly different than both normal and infarcted myocardial tissues at both field strengths ($p<0.005$), as observed with the normal volunteers in Chapter 6. However, T_1 was not distinguishable between infarcted and normal myocardium, despite an average difference between the two tissues. Interestingly, the T_1 difference between pathology and healthy tissue in myocardium became increasingly *similar* at 3T, with infarct T_1 increasing by an average of 25% between 1.5T and 3T ($p<0.05$), while normal myocardium T_1 rising only 10%. At both field strengths, *infarct tissue was not visible on T_1-wieghted imaging prior to contrast administration.*

Table 7.1. Comparison of T_1 Values of Blood, Normal and Infarcted Myocardium at 1.5T and 3T.

Time post (min)	Blood		Normal		Infarct	
	1.5T	3T	1.5T	3T	1.5T	3T
pre	1.55±.10	1.64± .07	1.08± .06[a]	1.26± .06[a]	1.08± .06[a]	1.27± .06[a,b]
5	0.21±.03	0.23± .02	0.33± .04[ac]	0.34± .05[ac]	0.23± .04	0.25± .02
10	0.26±.02	0.28± .03	0.38± .02[ac]	0.38± .05[ac]	0.28± .02	0.26± .02
15	0.27±.02	0.31± .03	0.41± .04[ac]	0.41± .06[ac]	0.26± .02	0.30± .03
20	0.30±.03	0.35± .03	0.44± .03[ac]	0.48± .04[ac]	0.29± .05	0.33± .03
25	0.31±.03	0.37± .01	0.46± .03[ac]	0.51± .06[ac]	0.30± .05	0.35± .02
30	0.32±.04	0.35± .02	0.46± .04[ac]	0.56± .07[ac]	0.32± .05	0.37± .02

[a]$p<0.05$ vs. blood (same field strength); [b]$p<0.05$ vs. infarct 1.5T; [c]$p<0.05$ vs. infarct

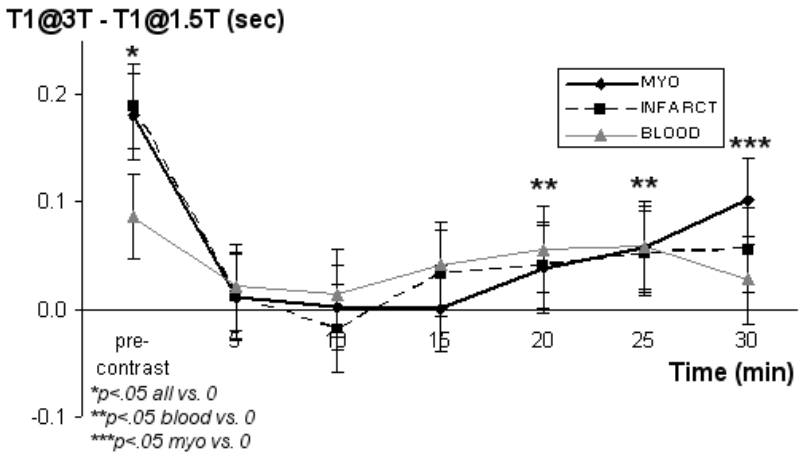

Figure 7.2. *Difference in T_1 between 3T and 1.5T over time post-contrast in patients.*

Following contrast administration of a total of 0.2mmol/kg Gd-DTPA-BMA, there was a significant decrease in baseline T_1 values in all tissues ($p<.001$). Over time post-contrast, T_1 began to rise due to contrast agent elimination ("wash-out"), but did not return to baseline T_1 values in the 30 minute time period of this study. To analyze the field-related T_1 behavior in each tissue, the *difference* in T_1 prior to contrast injection was propagated over time post-contrast, and is shown in Figure 7.2. It was found that the difference in T_1 between 1.5T and 3T (T1@3T – T1@1.5T) seen prior to contrast injection was significantly *reduced* ($p<0.05$) following contrast administration, and was *not significantly different from zero* for all tissues early after injection (< 15min) when the contrast agent concentration was highest. In contrast with the normal volunteer studies in Chapter 6, the T_1 difference for each tissue became larger at higher time points (> 20mins), indicating that there was a substantial T_1 difference between 1.5T and 3T *late after contrast administration*. Even though this trend was evident in all tissues, it was most revealing in normal myocardium, as the T_1 difference measured 30 minutes post-

contrast was approximately 100ms, which was closer to the pre-contrast difference between 1.5T and 3T (>180ms).

The average T_1-ratio between infarcted and normal myocardium, which, from the conclusions of Chapter 4, is predictive of image contrast in delayed enhancement imaging, was approximately *equal* at 1.5T and 3T over all time points (0.66±.06s vs. 0.69±.05s, respectively, p=NS), suggesting *similar expected image quality at both fields* (assuming no concession made to M_0). Furthermore, the average infarct-to-blood T_1-ratio, which is important for subendocardial infarct distinction, was also very similar between 1.5T and 3T (1.00 vs. 0.94, respectively, p=NS).

Delayed Enhancement

Two subjects did not complete the 3T examination, leaving 5 subjects with SNR and CNR measurements. The ranges of inversion times used in the 2D delayed enhancement FLASH sequences are listed in Table 7.2 for each subject, along with the time range at which the images were obtained.

Table 7.2. Inversion Times Used for Delayed Enhancement Imaging at 1.5T and 3T

	1.5T		3T	
subject	Time range (min)	Null-point Inversion Time (ms)	Time range (min)	Null-point Inversion Time (ms)
1	10-30	200-300	5-30	200-350
2	10-20	200-225	10-25	260-300
3	20-30	225-350	15-25	275-330
4	15-30	275-310	10-20	200-250
5	5-30	220-290	10-30	275-310

On average, the mean SNR of infarct tissue was higher at 3T (39.0±14.6 vs. 28.4±13.3, p>0.05), along with CNR between infarct and normal myocardium

(33.3±13.9 vs. 24.3±11.4, p>0.05) (Figure 7.3), but the data did not reach statistical significance. It was also observed that the mean infarct-to-blood signal ratio marginally favored 3T (1.63 ± 1.00 vs. 1.38 ± 0.35, p=NS), potentially enabling distinction of small subendocardial infarcts adjacent to the blood pool.

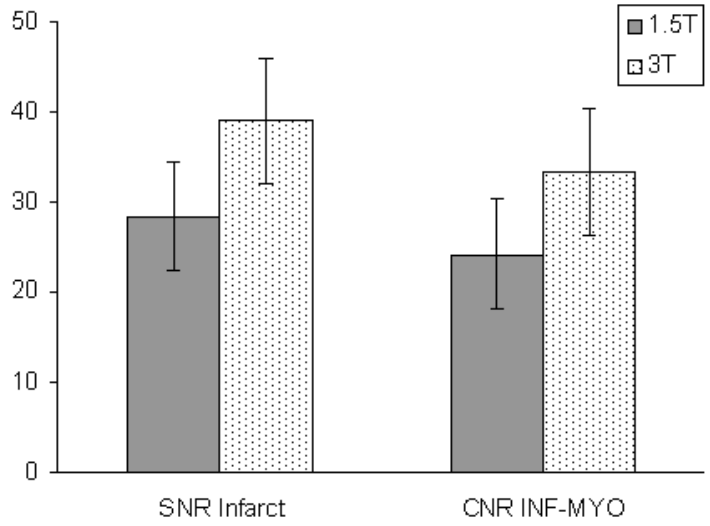

Figure 7.3. *Delayed enhancement SNR and CNR at 1.5T and 3T.*

An example of delayed enhancement imaging at 1.5T and 3T is shown in Figure 7.4. Precise localization of identical imaging planes was not achieved for the 2D comparison given in Figure 7.4a (1.5T) and b (3T). However, since a 3D sequence (15 slices) was also obtained at 1.5T, a similar slice to Figure 7.4b is given in Figure 7.4c. Despite different acquisition protocols, both images have the same resolution. The location of the small subendocardial infarct, especially relative to the blood pool, appears more defined at 3T than 1.5T (arrow). At both field strengths, this image contrast remained constant over time (>10 mins) with appropriate adjustments in *TI*.

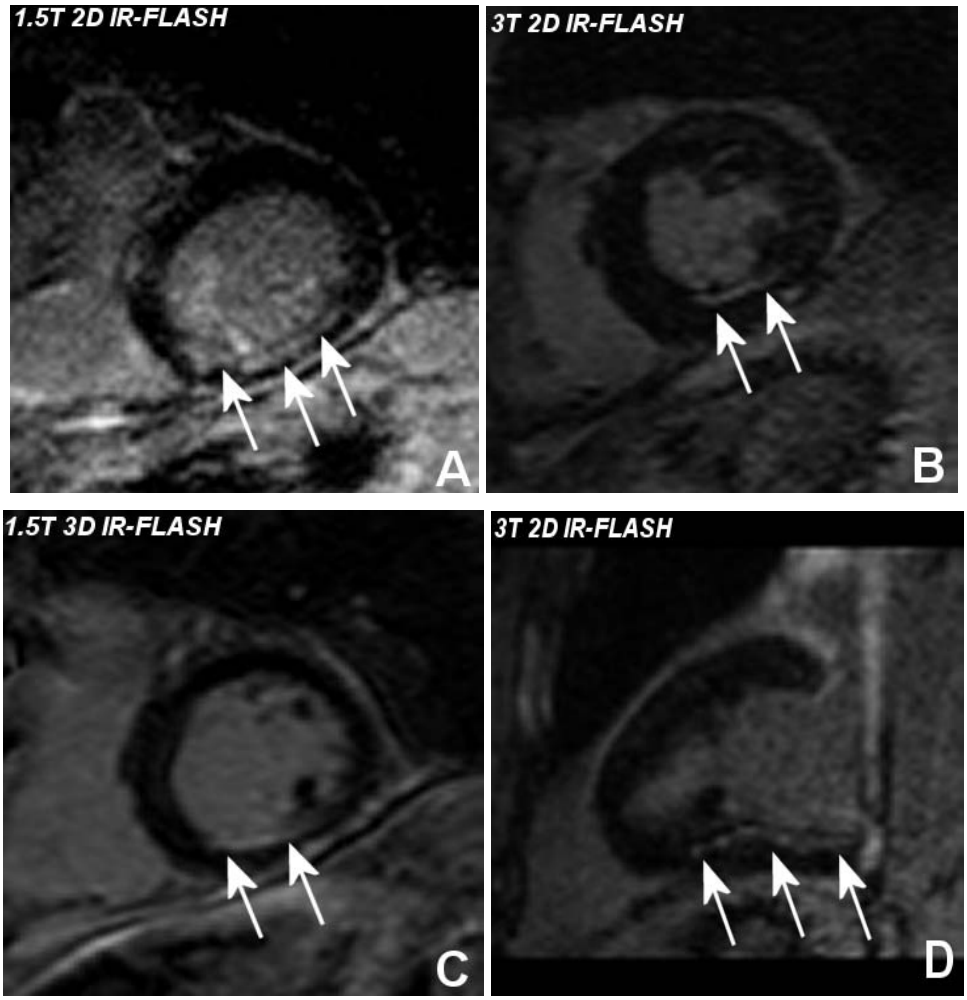

Figure 7.4. *Comparison of delayed enhancement at 1.5T and 3T.*

However, results varied widely subjects. Two subjects imaged at 3T produced less than ideal image quality. In one case, 3T delayed enhancement images lacked substantial enhancement compared to 1.5T (Figure 7.5a-b). This was possibly due to a very high contrast agent concentration, which may have induced significant intravoxel dephasing due to susceptibility effects or low T_2*, causing signal loss. In another case (Figure 7.5c-e), the blood pool exhibited inhomogeneous signal intensity (dashed arrow, Figure 7.5d-e), despite myocardial suppression (arrow heads). As a result of these signal variations, the enhanced subendocardial infarct tissue (solid arrow) could not be

distinguished from the blood pool using the 3D sequence. Although it is possible that inversion pulse inhomogeneity (as described in Chapter 5) may be the root of this problem, the exact cause of the blood pool signal variations was not determined, nor did they occur in other subjects. Further analyses of these particular results are revisited in the Discussion section.

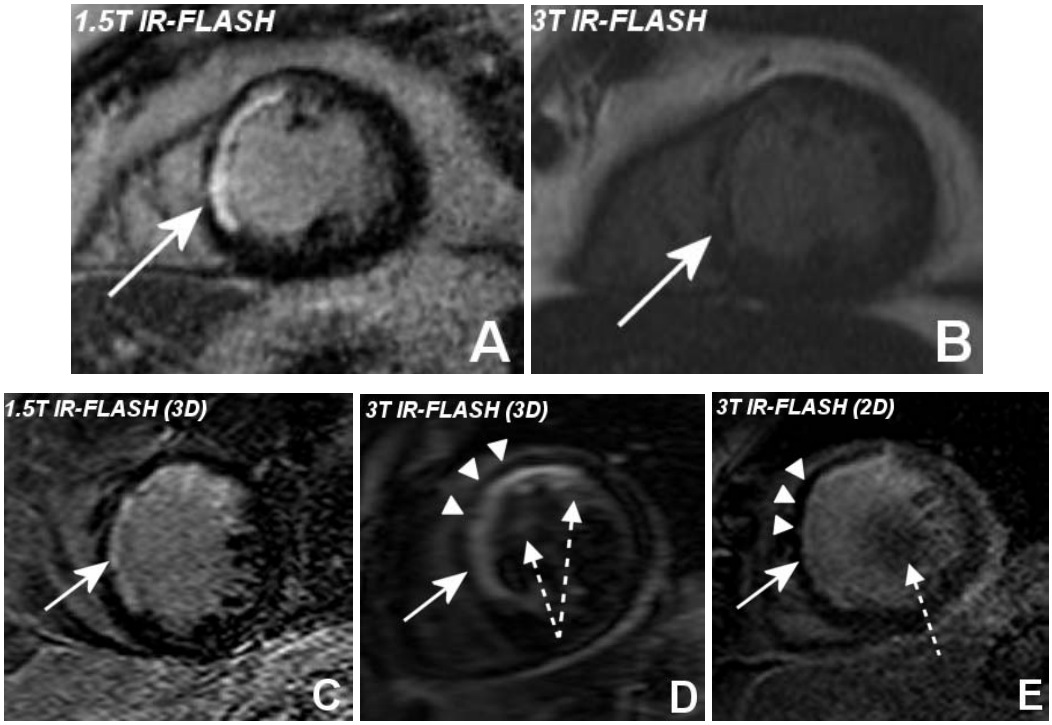

Figure 7.5. *3T delayed enhancement with poor image quality*

Determination of Optimal Imaging Parameters from T_1

$T_{1contrast}$ was mathematically determined from the difference between normal and infarcted myocardium transverse magnetization using the acquired T_1 information at both fields. The maximum $T_{1contrast}$ for both the 1- and 2-heartbeat imaging case, is shown in Figure 7.6. The values shown are relative to the equilibrium longitudinal magnetization, M_0, and, in all cases, the magnitude was less than 10% M_0. By assuming M_0 is equivalent at both 1.5T and 3T, the $T_{1contrast}$ was generally higher at 1.5T by virtue of the T_1

difference between infarct and normal myocardium being slightly higher at 1.5T. Recall that it was shown in Chapters 3 and 4 that the T_1-ratio was the most influential parameter determining heightened $T_{1contrast}$, when variations in M_0 were not considered to change. However, it was also experimentally observed in Chapter 4 and 5 that the magnitude of the equilibrium magnetization (determined from a short-TE, long-TR FLASH sequence) was stronger at 3T than 1.5T by approximately 30-97%. From this knowledge, additional simulations using M_0 = 1.33 at 3T (from Chapter 4) showed that the optimal $T_{1contrast}$ was larger at 3T than 1.5T (by 24.9%) over most time points post-contrast (Figure 7.6a). *This result was dependent on the assumed value of M_0*, but was consistent with the delayed enhancement imaging results given in the previous section, which, on average, showed a 37% increase in infarct-to-normal myocardium CNR. Therefore, *despite longer T_1s and a higher infarct: normal myocardium T_1-ratio at 3T, the increase in equilibrium magnetization sensitivity resulted in larger $T_{1contrast}$ between infarct and normal myocardium, compared to 1.5T.* This conclusion was true both theoretically (with simulations) and experimentally (from the imaging results).

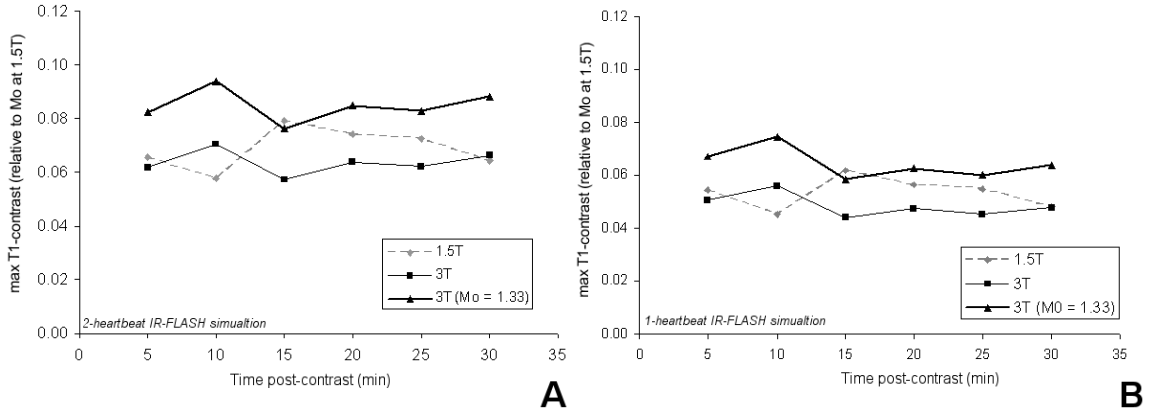

Figure 7.6. *$T_{1contrast}$ simulations using T_1 information at 1.5T and 3T.* ***A)*** *2-beat case, and* ***B)*** *1-beat case.*

When 1-beat sequences were simulated, the decrease in $T_{1contrast}$ was approximately 23% compared to the 2-beat case (Figure 7.6b). Although 3D delayed enhancement sequences have 1-heartbeat intervals between segments, the gain in the relative signal level over 2D sequences (by about 3.5-to-1) may compensate for the reduced $T_{1contrast}$ in imaging settings.

The optimal $T_{1contrast}$ shown in Figure 7.6 yielded an optimal readout flip angle (α_{opt}) and inversion time (TI_{opt}) for each T_1-pair. Table 7.3 lists TI_{opt} and α_{opt} at each time point at both field strengths for the 2-heartbeat sequence. The *simulated* null-point *TI* of normal myocardium is also given. Even though TI_{opt} was consistently longer than TI_{null}, the corresponding $T_{1contrast}$ was essentially equivalent (< 4% difference), which suggests $T_{1contrast}$ is maximal for a wide range of *TI* values, not only TI_{opt}.

Table 7.3. Optimal Contrast (T_1-contrast), Inversion Time (TI_{opt}) and Flip Angle (α_{opt}), and TI_{null} between Infarct and Normal Myocardium Calculated for 2-heartbeat IR-FLASH.

Time post (min)	1.5T				3T			
	Max T_1-contrast[a]	α_{opt} (°)	TI_{opt} (ms)	TI_{null}[b] (ms)	Max T_1-contrast[a]	α_{opt} (°)	TI_{opt} (ms)	TI_{null}[b] (ms)
5	.066	23.9	278	217 ±16	.082	23.8	291	225 ±17
10	.059	23.7	325	248 ±18	.094	23.7	315	250 ±19
15	.079	23.7	327	265 ±19	.076	23.6	351	267 ±20
20	.074	23.6	360	287 ±21	.085	23.5	404	309 ±23
25	.073	23.6	372	294 ±22	.083	23.4	432	326 ±24
30	.064	23.5	384	296 ±22	.088	23.3	465	351 ±25

[a] *Values represent the maximum difference in transverse magnetizations, relative to M_0 at 1.5T.*
[b] *The corresponding T_1-contrast produced using TI_{null} is roughly 4% lower than with TI_{opt}*

The optimal flip angle was approximately 23°-24° at both 1.5T and 3T (Table 7.3), and did not show sensitivity to time post-contrast. This flip angle was larger than those used in the delayed enhancement imaging experiments in this chapter, which used

15-20° flip angles. Using α = 15° in the simulations, the $T_{1contrast}$ was found to be approximately 10-20% lower than using α_{opt} = 23°. It must also be noted that α_{opt} is sensitive to TR and the number of phase encode steps per segment (lines/segment). Limiting α may be significant in 3D sequences at 3T, due to power deposition constraints and B_{1trans} inhomogeneity.

Since post-contrast blood T_1 was also measured at 1.5T and 3T, estimates of infarct-to-blood signal ratio were analyzed with IR-FLASH simulations using α_{opt} and TI_{opt}. Assuming the equilibrium magnetizations of blood and infarct tissue are equivalent, the average infarct-to-blood $T_{1contrast}$ ratio was 0.98 and 1.03 at 1.5T and 3T, respectively. But these were significantly lower than the signal ratio imaging results reported in the previous section (1.38 and 1.63, respectively), which suggests the equilibrium magnetization and/or proton density may be larger for infarct tissue in some cases. These results did not change significantly when TI_{null} was substituted in place of TI_{opt}.

Contrast Agent Distribution

$\Delta R_{1myo} / \Delta R_{1blood}$ at both 1.5T and 3T was evaluated to characterize the distribution of the contrast agent to each compartment and to investigate any changes in contrast agent relaxivity between field strengths. The use of this measure to describe the distribution is only valid if the exchange of contrast media is "steady" (or constant) between compartments. The results of $\Delta R_{1myo} / \Delta R_{1blood}$ (for both normal and infarcted myocardium), based on the measured T_1 values at 1.5T and 3T, are shown in Figure 7.7 over time for the 5 patients studied. As evident, $\Delta R_{1myo} / \Delta R_{1blood}$ was relatively constant over the time points studied (5-30 minutes), which affirms the contrast agent distribution

was in steady-state. $\Delta R_{1inf} / \Delta R_{1blood}$ was equivalent at 1.5T (0.91 ± .05) and 3T (0.96 ± .07), and was not significantly different from unity. This implies, therefore, the distribution volume (and partition coefficient) of infarcted myocardium is almost the same as blood in this particular patient population. In normal myocardium, $\Delta R_{1myo} / \Delta R_{1blood}$ was 0.50 ± .06 and 0.56 ± .06 at 1.5T and 3T, respectively, which was significantly lower than in infarct ($p<0.05$). This relationship is also shown by the upper-most curve in Figure 7.7, which depicts $\Delta R_{1inf} / \Delta R_{1myo}$. As seen, $\Delta R_{1inf} / \Delta R_{1myo}$ is approximately 1.87 ± .24 and 1.73 ± .14 at 1.5T and 3T.

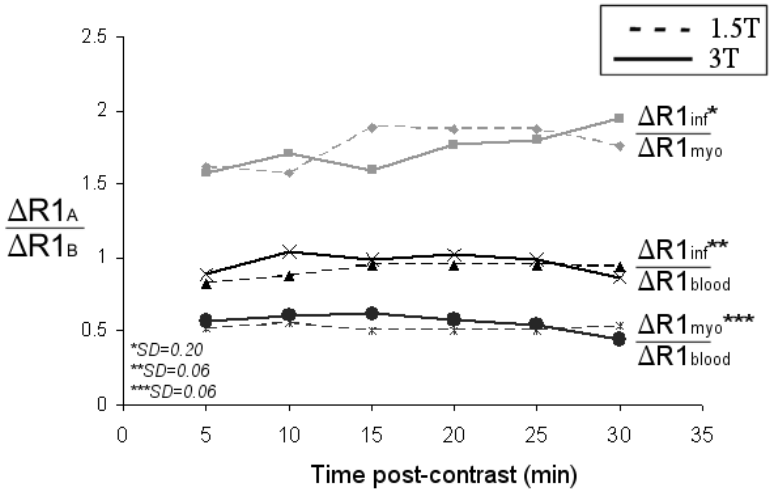

Figure 7.7. *Compartmental contrast agent distribution measured in vivo in patients at 1.5T and 3T.*

The values for $\Delta R_{1myo} / \Delta R_{1blood}$ were generally higher at 3T, but not significantly different between 1.5T and 3T ($p>.05$), indicating that the contrast agent relaxivity in each tissue compartment remained essentially the same between fields. This is revealed in Figure 7.8. On average, r_1 at 1.5T was larger by 8-10% than 3T for each tissue, but was only significant in blood ($p=0.026$). These results were generally consistent with those in

the normal volunteers (Chapter 6), which showed r_1 at 1.5T was as much as 18% greater than 3T.

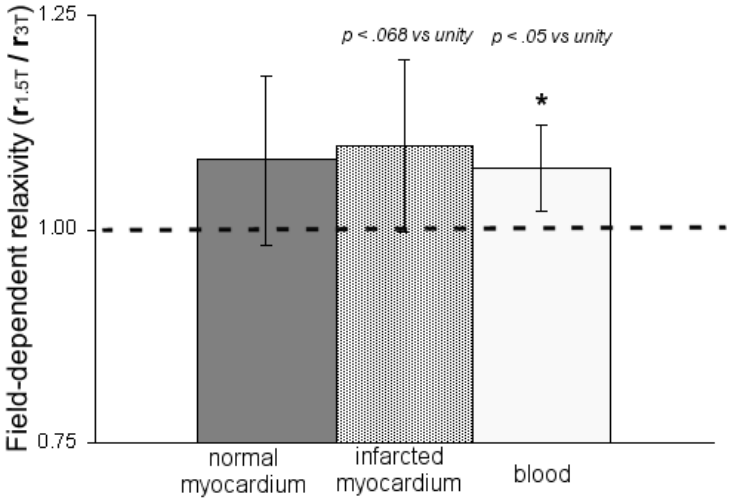

Figure 7.8. *Relative Gd-DTPA-BMA relaxivity in tissue between 1.5T and 3T in patients.*

Discussion

The primary objective of this chapter was to characterize the post-contrast T_1 values of blood, normal and infarcted myocardium in patients with prior myocardial infarction, which has only been previously considered at 1.5T [Klein et al. 2004]. The central motivation was to use the acquired information in computational simulations of the delayed enhancement pulse sequence to reveal the $T_{1contrast}$ benefits at 3T compared to 1.5T, and to outline the potential improvements of delayed enhancement image quality at both field strengths. Additionally, a direct SNR and CNR comparison was performed between 1.5T and 3T using standard IR-FLASH techniques, which enabled comparison to theoretical values. The improved contrast agent-related signal elevation was partly explained through the determination of tissue- and field-related r_1 changes.

The major findings in this chapter were: 1) Pre-contrast (native) T_1 values of blood, infarct and normal myocardium were significantly higher at 3T than 1.5T ($p<0.05$); 2) The T_1 difference between 1.5T and 3T in blood, infarct and normal myocardium was *not* significantly different *early* after contrast administration ($p>0.05$); 3) The SNR of infarct tissue and the CNR between infarct and normal myocardium were greater at 3T than 1.5T; 4) Mathematical simulation of IR-FLASH based on T_1 information correlated well with experimental CNR findings at 1.5T and 3T; 5) The optimal $T_{1contrast}$, achieved with TI_{opt}, was not significantly different than $T_{1contrast}$ attained using the null-point inversion time (TI_{null}); and 6) compartmental contrast agent relaxivity was significantly lower in blood at 3T ($p=0.026$), but showed a general decrease in all tissue compartments between 1.5T and 3T.

The T_1 values of blood, infarcted and normal myocardium measured post-contrast in this study at 1.5T were within experimental error with Klein [Klein et al. 2004] (~2% for blood, ~5% for infarct, and ~11% for normal myocardium). However, a slight increase in T_1 was observed for *normal myocardium* in this study over most time points (~11%), but was not deemed statistically significant ($p>0.05$) due to the standard deviation of the measurements in both studies (~30-60ms). One possible explanation for higher T_1s in this study is an increase Gd-DTPA concentration (and possibly poorer contrast agent clearance) in the myocardium at similar time points. Since it is known that the excretion rate of Gd-DTPA-BMA is tied to cardiac and renal function, which are both compromised in this patient population, it is possible that the lower T_1 values observed in earlier studies could be explained by the very low ejection fraction (EF) in their patient population (<35%). In general, our subjects were clinically stable with EF > 30% and not

considered in heart failure. Moreover, when compared to "normal" volunteer subjects (as in Chapter 6), normal myocardium and blood T_1s were substantially lower in these patients with prior infarction and reduced cardiac function, implying the close tie between Gd-DTPA-BMA clearance rate, cardiac function, and post-contrast T_1 values.

The point of most disagreement with some previous T_1 investigations was the pre-contrast T_1 values at 1.5T. In this study, blood T_1 was 1.55±.10s and myocardium T_1 was 1.08±.06s, which, on average, were higher than some earlier reports of blood T_1 (range: 1.20-1.80s [Barth et al. 1997, Wagenseil et al. 1999, Flacke et al. 2001, Storey et al. 2003, Klein et al. 2004]) and myocardium T_1 (range: 0.72-1.22s [Wacker et al. 1999, Wagenseil et al. 1999, Flacke et al. 2001, Foltz et al. 2002, Messroghli et al. 2003, Storey et al. 2003, Eriksson et al 2004, Messroghli et al. 2004, Klein et al. 2004]). Potential causes for these discordances were discussed in Chapter 6, where similar disagreements, particularly with blood T_1, were found. It has been shown that blood T_1 is highly dependent on hematocrit and oxygenation [Silvennoinen et al. 2003], ranging from 1350 to 1500ms at 1.5T. This is reflected in literature data, which reported T_1s of 1230 [Klein et al. 2004] and 1800ms [Wagenseil et al. 1999]. At 3T, the same dependency seems to exist, with T_1 varying between 1600 and 1750ms for arterial blood with physiologic hematocrit [Lu et al. 2004]. Measurements in the left ventricle have revealed a 3T blood T_1 of 1550ms [Noeske et al. 2000], but this needs to be substantiated with a larger subject population.

As noted, there is also a substantial range of reported myocardial T_1 values in the literature. In a review article in 1984, the mean myocardium T_1 at 1.5T (64 MHz) and 3T (128 MHz) were estimated as 867ms ± 16% and 1114ms ± 16%, respectively, using

fitted curves of the form $T_1 = A\ \omega^B$ [Bottomley et al. 1984]. This closely reflects some current 1.5T (721-771ms) [Messroghli et al. 2003] and 3T (1115ms) [Noeske et al. 2000] measurements. But the estimated standard deviation is quite large (± 16%), which is demonstrated by reported values as low as 720ms [Klein 2004] and as high as 1219ms [Wacker et al. 1999] at 1.5T. The T_1 of myocardium in this study (1.08±.06s) was within error of other measurements in humans [Flacke et al. 2001] and pigs [Wagenseil et al. 1999, Foltz et al. 2002, Storey et al. 2003]. The discrepancy between measurements may have significant dependence on the T_1 measurement technique, which is complicated *in vivo* due to cardiac and respiratory motion during image acquisition. One consistent finding, however, was that infarct tissue (and its T_1 value) was indistinguishable from normal myocardium pre-contrast injection on T_1-weighted sequences.

The change in T_1 between 1.5T and 3T (T1@3T – T1@1.5T) was determined in this chapter similarly to Figure 6.1 in Chapter 6. However, the behavior of myocardium and blood T_1 difference (Figure 7.2) did not coincide precisely with the results from the normal subjects, particularly early after contrast injection. From these patient studies, *there was no field-related T_1 difference early after contrast injection (0-15 minutes)*. The negligible T_1 difference early after contrast administration could be due to poor contrast agent clearance in these subjects, which would cause a maintenance of relatively high contrast agent concentration compared to "healthy" subjects, and thus a prolonged reduction of T_1 at *both* field strengths. According to Eq. [6.1] ($R_{1obs} = R_{1pre} + r_1 \times [Gd]$), very short T_1 values (and therefore large R_{1obs} values) imply the T_1 contribution from the contrast agent (i.e. $r_1 \times [Gd]$) dominates R_{1obs} to an extent that the T_1 measurement technique may not be sensitive enough to distinguish T_1 values at either field strength. At

later time points, as the contrast agent is eliminated, the contribution from the contrast agent diminishes and the T_1 difference between 1.5T and 3T becomes more apparent, and thus, more comparable to the findings from the "healthy" subjects.

Interestingly, the measurable disparity found in $\Delta R_{1myo} / \Delta R_{1blood}$ between 1.5T and 3T in "healthy" subjects (Chapter 6, Figure 6.3) was *not* observed in these patient studies, as depicted in Figure 7.7. The parameter $\Delta R_{1myo} / \Delta R_{1blood}$, which is customarily used to evaluate the partition coefficient (λ_{myo}) and the degree of cell loss in infarcted myocardium [Arheden et al. 1999, Klein et al. 2004], can also be used to characterize changes in contrast agent relaxivity, especially when a large $\Delta R_{1myo} / \Delta R_{1blood}$ difference is measured between field strengths. As shown with these present studies, the relative field-dependent change in r_1 ($r_{1.5T} / r_{3T}$) is minor, but does show significance in blood (Figure 7.8). It has been shown experimentally with field relaxivity studies in Chapter 4 and elsewhere [Donahue et al. 1994, Rinck et al. 1999] that Gd-DTPA r_1 *decreases with field strength*. Therefore, an $r_{1.5T} / r_{3T}$ greater than 1.0 was expected. In these patients, $r_{1.5T} / r_{3T}$ was 1.08 ± 0.14 in myocardium ($p>0.05$ vs. 1.0), 1.10 ± 0.11 in infarct ($p=0.07$), and 1.07 ± 0.06 in blood ($p<0.05$), whereas in "healthy" volunteers $r_{1.5T} / r_{3T}$ was 1.01 ± 0.10 in normal myocardium and 1.18 ± 0.15 in blood. A possible reason for this difference between patients and normal volunteers could be a wider variation in clearance rates among the "healthy" volunteers and between 1.5T and 3T experiments. Absolute values for r_1 were not calculated since contrast agent concentration was not explicitly determined at each time point post-contrast.

Apart from detailing the T_1 behavior post-contrast, and lending insight into the possible mechanisms for contrast enhancement, these results outlined the optimal

inversion times and flip angles needed to achieve maximum $T_{1contrast}$ (between infarcted and normal myocardium) in delayed enhancement imaging. It was found that there was a considerable difference between the TI_{opt} and TI_{null} (68-114ms at 3T and 60-88ms at 1.5T), where TI_{null} is the inversion time currently used in clinical practice. However, according to the corresponding $T_{1contrast}$ associated with these two *TI*s, *only a small difference was observed at both field strengths (maximum 4% difference)*. This finding correlates well with simulations using arbitrary T_1 values in Chapter 3 and phantom experiments in Chapter 5, *suggesting a large region of almost equivalent image contrast exists for a spectrum of inversion times (which is both time and T_1 dependent,* see Table 3). This conclusion has much to do with the definition of $T_{1contrast}$ used in this simulation. Since the normalized signal *difference* (Eq. [3.26]) was used as the figure-of-merit, the simulation was not biased to TI_{null}, which would have produced *infinite* image contrast if a signal *ratio* ($SI_{infarct}$ / SI_{myo}) was used as the figure-of-merit (since $SI_{myo} = 0$ at TI_{null}). Images comparing the contrast using TI_{opt} and TI_{null} could not be shown in these patients since TI_{opt} was determined off-line following the imaging experiments. Even so, this comparison was depicted in Chapter 4 (Figure 4.12), showcasing that despite a larger image contrast, TI_{opt} *does not always result in zero "normal myocardium" signal*, especially if normal myocardial T_1 is high (late post-contrast time points).

Since TI_{null} is generally used in practice, there is obvious speculation into the relevancy and utility of TI_{opt}. However, *there are two related reasons TI_{opt} is important, specifically to 3T delayed enhancement imaging*: 1) T_1 of normal myocardium at 3T is generally larger than 1.5T; and 2) TI_{null} is numerically close to TI_{zero}, which is the inversion time that produces zero contrast between normal and infarcted myocardium in

magnitude reconstructed images. An optimal *TI* is important in both of these issues since, from the earlier theoretical and phantom experiments, the $T_{1contrast}$ inherently decreases as T_{1myo} increases (as seen at 3T), while $TI_{zero} \leq TI_{null} < TI_{opt}$. Therefore, novel delayed enhancement techniques, such as phase-sensitive reconstruction [Kellman et al. 2002], which conserves the sign of the magnetization (thereby eliminating TI_{zero}), can be used to adapt TI_{opt} to resemble TI_{null}, thus producing maximum image contrast *and* nulling normal myocardium.

One of the most important findings in this study was that, on average, the CNR between normal and infarcted myocardium was higher (by 37%) at 3T compared to 1.5T (Figure 7.3). This was evident despite a key conclusion made in Chapter 4, which stated that image contrast (from phantom and mathematical experiments), was inversely proportional to the T_1-ratio between infarcted and normal myocardium, and (secondarily) the T_1 value of normal myocardium. However, this conclusion was made by assuming the equilibrium magnetization (M_0) was equal between 1.5T and 3T. Moreover, to precisely compare imaging results to mathematical results, which are presented with different intensity scaling, both needed to be normalized against a reference scan that approximated M_0. As shown throughout this thesis (see, for example, Determination of Field Dependency of M_0 (Chapter 5) and Delayed Enhancement at 1.5T and 3T in Phantoms (Chapter 4)), the increase in sensitivity was generally between 1.30-1.97 (due to some added T_1- and T_2-wieghting), which correlates well with previous reports on intrinsic SNR at 3T (1.50-1.60) [Wen et al. 1997] and brain tissue SNR at 3T (1.30-2.10) [Frayne et al. 2003]. Figure 7.6 depicts the $T_{1contrast}$ results using an M_0 at 3T that was 1.33-times greater than 1.5T, and reveals that *an increase in M_0 with field strength*

overcomes the lower $T_{1contrast}$ obtained with longer T_1s and generally smaller normal-to-infarct T_1 ratio at 3T.

There are additional issues pertaining to delayed enhancement image quality at 3T, however. As shown in Figure 7.5, there were instances when delayed enhancement imaging did not produce optimum results. *These differences are directly related to technical issues due to the increase in magnetic field*. These images certainly provide motivation for further investigation into image quality improvements at 3T. In one subject (Figure 7.5a-b), almost no enhancement was visualized in the area of the septal infarct (arrow, Figure 7.5b). At 1.5T, the area of scar tissue was almost completely transmural, and enhanced very intensely compared to the other subjects in the study (by +63%). This increased enhancement may have particular implications at 3T, since it implies the contrast agent concentration was very high. In addition to lowering T_1, paramagnetic contrast agents also lower T_2, but less significantly. When coupled with the fact that B_0 inhomogeneity is greater at 3T, it leads to very short T_2* values. At very high concentrations, therefore, T_2* may be short enough to cause signal loss even in short-TE, T_1-weighted gradient echo images. In fact, it can be shown that Gd-DTPA-BMA concentration in saline exceeding 12mM causes reduced signal intensity in spoiled gradient echo (FLASH) images at low and high field strength [Uematsu et al. 2003]. Our preliminary experiments (not shown) have revealed that concentrations between 5-10mM begin to show signal reduction in delayed enhancement sequences, implying there is a threshold above which Gd counteracts signal enhancement. From an analysis of extracellular volume in myocardium (~100mL) and assuming about 1% of the injected dose is in the myocardium [Prato et al. 1988], the concentration of Gd in the heart is

roughly 1.4mM, which is much lower than 5mM. However, in infarct tissue, where the partition coefficient is significantly higher (λ>0.90) and the residence time of Gd is longer, the concentration of Gd will be significantly higher, potentially approaching this threshold value of 5mM. More studies are needed to estimate the concentration in infarct tissue to determine the effect of T_2*-related signal loss in cases such as these. However, when a Look-Locker sequence was used to measure T_1 and locate the normal myocardium null-point time, as in Figure 7.9d, infarct tissue enhancement was attained. The essential difference in this particular case is that the Look-Locker sequence utilized a b-SSFP readout with a shorter TE than the standard IR-FLASH acquisition. This may have limited transverse dephasing and maintained high SNR compared to IR-FLASH. Even without inversion preparation, there seems to be signal loss in the infarct tissue core in this particular subject pre-contrast (Figure 7.9c) and late post-contrast (Figure 7.9b).

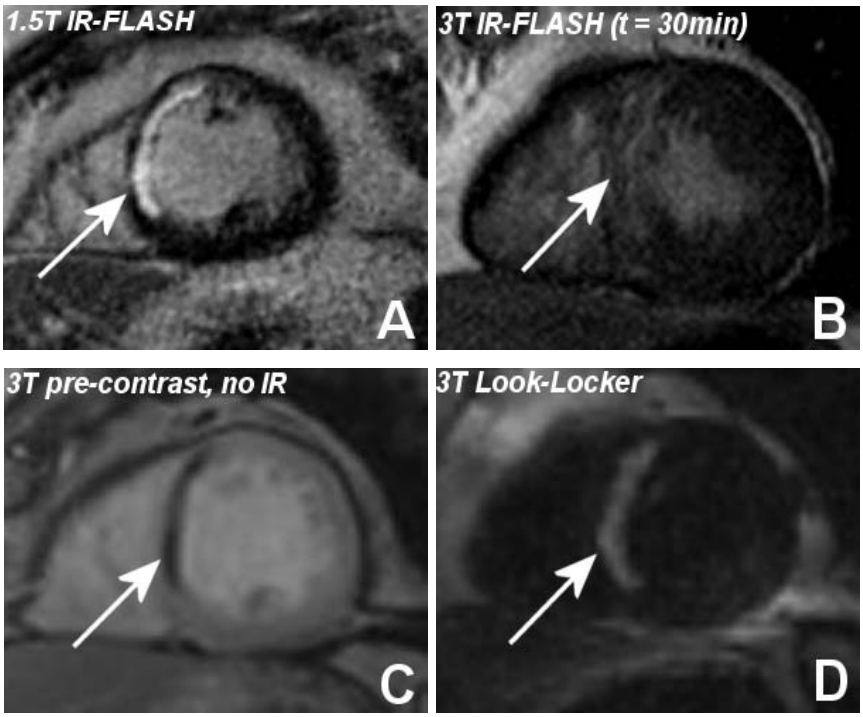

Figure 7.9. *One patient case resulting in poor infarct enhancement at 3T (**b**) compared to 1.5T (**a**), along with evidence of 3T infarct depiction using alternative methods (**c, d**)*

In another case, lack of signal homogeneity was observed in the blood pool at 3T (Figure 7.5d-e). From 1.5T, the infarct tissue is known to be located in the subendocardium along the postero-septal wall (Figure 7.6a). The lack of uniform signal in the blood pool compromised infarct visualization at 3T, since a distinct boundary is not apparent between enhanced myocardium and the blood pool. There are two possible reasons for this artifact. First, one must consider the inhomogeneity of the inversion pre-pulse or the B_{1trans} field across the FOV (and the slice). This is known to result in the well known field-focusing effect, whereby the B_{1trans} field is strongest in the middle of the FOV [Hoult 2000]. However, the effect did not seem to extend to other cardiac and extra-cardiac regions, nor was the variation identical among other slices, as found in phantom experiments. Another potential cause is flow-related. Though non-selective inversion pulses were used at 3T, blood initially away from the isocenter experiencing the 180° pulse may have been insufficiently prepared. This prepared magnetization enters the imaging slice with various amplitudes, causing the resulting image intensity to vary. Inversion pulse homogeneity in the sagittal plane was shown in a phantom at 3T to have an efficacy value of 0.94±.03 for adiabatic inversion pulses, which is comparable to 1.5T values (1.01±.04) (Chapter 5). However, the additional effect of inhomogeneous B_{1trans} may have still caused spatially variable signal intensities at 3T. From the corresponding images at 1.5T, the signal intensity in the blood pool should be elevated (Figure 7.5c). Evidence of this was found in regions near the myocardial wall at 3T (Figure 7.5d-e). There is also knowledge that background field variations (B_0 inhomogeneity) can cause "echo-shifting", which results in poor spatial frequency localization in *k*-space. The

consequence of this imprecise encoding is image distortion and signal variations where B_0 inhomogeneity is high [Haacke 1999].

Conclusion

This chapter focused on T_1 measurement and delayed enhancement imaging at 3T, compared to 1.5T, in patients with previous myocardial infarction. Though elevated T_1 values were found at 3T post-contrast, there was great similarity between T_1 values at 1.5T and 3T early after contrast administration (<10mins). Therefore, the range of TI_{null} values was also similar between the field strengths. Though these findings were different than those found in the "healthy" subjects, the discordance may be due to physiologic and pharmacokinetic differences between the two subject populations. Infarct enhancement was observed at 3T, and lead to cumulative CNR between normal myocardium being higher than 1.5T. Blood-to-infarct signal ratio also increased at 3T. However, both measures were within experimental error between fields. Using the T_1 information (and adaptations to M_0), the $T_{1contrast}$ simulations correlated well with the experimental findings. Though the optimal inversion time found through the simulations was different than TI_{null} in most cases, the $T_{1contrast}$ was not.

There remain field-related image artifacts at 3T that compromised diagnostic capability in many cases. These are most probably due to B_0 field inhomogeneity, T_2* (susceptibility) effects from contrast agent concentration, and B_{1trans} and inversion pulse inhomogeneity.

CHAPTER 8

CONCLUSIONS

The Problem Revisited

It is appropriate to revisit the major goals of this project before reviewing the significant findings. The problem statement, from Chapter 1, reads, "…*this thesis intends to outline the design criteria necessary for developing optimized pulse sequences for delayed enhancement imaging at two imaging field strengths, 1.5T and 3T."* The approach of the investigation centered around *mathematical optimization*, since it conveniently allowed analysis of multiple variables in the description of image contrast between infarct and normal myocardium ($T_{1contrast}$). From this stance, the method was validated with specifically designed MR phantoms, and subsequently used to investigate *in vivo* image contrast given T_1 values measured from volunteers and patients.

Overview of Findings

The core of theoretical development and experiments began in Chapter 3. Once the nature of the delayed enhancement sequence was developed for segmented IR-FLASH sequences, simulations were performed to determine optimal flip angle (α_{opt}) and optimal inversion time (TI_{opt}) given arbitrary T_1 values for normal and infarcted myocardium. In Chapter 4, the theoretical expressions for delayed enhancement were validated with a specific set of T_1 phantoms characteristic of 1.5T and 3T post-contrast myocardium and infarct T_1 values. The most significant findings from these two theoretical chapters are listed below.

1. Three distinct inversion times are noteworthy: a) TI_{zero}, the inversion time that produces *zero* $T_{1contrast}$ between infarct and normal myocardium; b) TI_{null}, the inversion time that produces *zero signal from normal myocardium*; and c) TI_{opt}, the inversion time that produces the *maximum* $T_{1contrast}$. These three inversion times are related in time by: $TI_{zero} < TI_{null} < TI_{opt}$.
2. TI_{null} converges to TI_{opt} as the T_1 difference between infarct and normal myocardium increases *and* as T_1 of infarct tissue decreases. The resulting $T_{1contrast}$ is highest for low infarct-to-normal myocardium T_1 ratio.
3. There is a broad region of high $T_{1contrast}$ in delayed enhancement imaging (Figure 3.19), which includes TI_{opt} and TI_{null}, but also a larger span of additional *TI*s. This span of *TI*s has the potential for making delayed enhancement imaging *TI*-insensitive while preserving high $T_{1contrast}$.
4. The optimal flip angle (α_{opt}) is approximately 20-23°, but should be < 40° to avoid significant signal saturation (driven equilibrium), and > 10° to avoid low signal amplitude (low SNR).

Also, for equivalent sequence parameters, the $T_{1contrast}$ increased as the segment interval delay (or, equivalently, the R-to-R wave interval) increased. There was also improved $T_{1contrast}$ by using variable flip angle sweeps over constant flip angles during the data acquisition period.

Next, the major differences between 1.5T and 3T imaging were revealed (Chapter 5) to quantify the potential challenges of 3T delayed enhancement imaging. The major findings were:

1. Frequency offsets (Δf) in the B_0 field was substantially higher at 3T, particularly in lateral and anterior wall. This causes accelerated spin dephasing (T_2* signal loss) and banding artifacts (in cine b-SSFP imaging). The average Δf in the heart can be reduced by using localized volume shimming.
2. The RF transmission field (B_{1trans}) is more inhomogeneous at 3T compared to 1.5T, causing the flip angle to be underestimated away from the isocenter.
3. The inversion preparation pulse, which is used in delayed enhancement imaging, is only accurate at 3T using *an adiabatic inversion pulse*. Other pulse types suffer from significant spatial inhomogeneity.
4. The proton sensitivity (or equilibrium magnetization, M0) increases at 3T by *at least* 30%, but spans (3T:1.5T) 1.30-1.97 for gradient and spin echo sequences.

From these conclusions, therefore, delayed enhancement imaging at 3T should be performed with an optimized adiabatic inversion pulse, with volume shimming, and short TE (to limit spin dephasing). RF inhomogeneity is inherent at 3T, but it can be limited by shimming the main field, using circularly polarized RF fields, and using lower flip angles (since the effective inaccuracy in flip angle will be less significant). The gain in M_0 at 3T provides compensation for the conclusion noted in the theoretical chapters (point #2) stating that the expected $T_{1contrast}$ will decrease as the difference in infarct-to-myocardium T_1 decreases.

In vivo contrast-enhanced experiments were performed in normal volunteers and patients at 1.5T and 3T to evaluate T_1 values. The knowledge that T_1 increases with field strength was confirmed pre-contrast (10-18% for normal myocardium; 5-6% for blood; and 25% for infarct tissue). However, the magnitude of this increase was significantly

depressed after the contrast agent was administered (5-10% for normal volunteers; and 0-20% for patients). The other main findings from the *in vivo* experiments were:

1. The post-contrast T_1-difference between 1.5T and 3T was not significant, particularly early after contrast injection (< 10 minutes). Therefore, the inversion times to null the signal from normal myocardium (TI_{null}) were almost the same. The T_1-difference became larger > 20min in patients, but not for normal volunteers.
2. There was some field dependence in the measure of contrast agent distribution, $\Delta R_{1myo} / \Delta R_{1blood}$, which suggested a possible change in contrast agent relaxivity. $\Delta R_{1myo} / \Delta R_{1blood}$ was lower at 1.5T than 3T, which implied the *contrast agent relaxivity was higher at 1.5T than 3T*. This has significance in contrast agent concentration quantification, and also plays a role in the expected post-contrast T_1-difference between fields.
3. The signal-to-noise ratio (SNR) of infarct tissue and the contrast-to-noise ratio (CNR) between infarct and normal myocardium increased by approximately 37% at 3T. CNR ratio between infarct and blood was 1.63 and 1.38 at 3T and 1.5T, respectively, indicating that infarct tissue is potentially more distinguishable from the blood pool at 3T.
4. TI_{opt}, α_{opt}, and TI_{null} were determined from *in vivo* T_1 values. The simulated gain in $T_{1contrast}$ (24.9%, using compensation for M_0 increase (+33%) at 3T) closely corresponded with *in vivo* measurements of contrast-to-noise ratio (CNR).

5. Significant field-related issues were susceptibility signal loss in regions of high contrast agent concentration (infarct and blood pool). This may limit SNR of some chronic myocardial infarction when using long echo times.

The breadth of these conclusions indicates that *delayed enhancement imaging is feasible at 3T*. Overall, there was marked gain in SNR and CNR at 3T. The theoretical framework has shown that optimization is tenable and closely reflects *in vivo* measurements. Both TI_{opt} and TI_{null} are dependent on T_1, which itself varies with time post-injection. The 1.5T and 3T values for TI_{null} and TI_{opt} are not very different since post-contrast T_1 values are similar.

Future Work

There are several areas of future work that may extend the current research. First, it is important to recruit a greater population of patients with myocardial infarction for delayed enhancement imaging at 3T. Given the initial conclusions of this project, there is obvious optimism for greater SNR and CNR at 3T for delayed enhancement. Furthermore, this venture will allow continued evaluation of the immediate influence of field effects on image degradation.

Second, the theoretical framework of delayed enhancement imaging can be advanced. Particularly, a factor may be included to account for image noise, so that one may obtain immediate estimations of SNR and CNR. Ideally, the user should be allowed to assign various imaging parameters such as resolution and bandwidth (just as one would at the imaging console), while also specifying the field strength of the experiment. As such, the data output could be incorporated into a simulation software package, and

would naturally allow SNR and CNR estimates for a variety of other MR applications and pulse sequences.

There must also be investigation into new pulse sequences (or reconstruction methods) to take advantage of the $T_{1contrast}$ gain afforded by the optimal solutions of TI_{opt} and α_{opt}. In parallel, there is a need to develop a *TI*-insensitive, fast delayed enhancement sequence with sufficient spatial resolution. Though there is ongoing progress towards this feat [Kellman 2005], delayed enhancement imaging at 3T may soon be the focus of such pursuits due to the improved CNR and SNR. With knowledge of T_1 time courses post-contrast given in this project, new pulse sequences incorporating a combination of preparation pulses may be able to take advantage of the trends to provide consistent image contrast over the duration of the exam, while providing arrhythmia insensitivity [Sharma 2003]. Also, a more global optimization timing routine needs to be investigated that addresses both suppression and enhancement of particular T_1s.

Final Thoughts

It is likely that 3T imaging systems will gain more leverage in cardiac viability imaging as they become more widespread. Furthermore, it is anticipated that these results will further additional research into new pulse sequences to overcome the inherent difficulties of delayed enhancement imaging of myocardial infarction. The use of preparation pulses is a valuable asset to enable controlled contrast in images. With greater experience, the image contrast benefits should make delayed enhancement imaging routinely successful at 3T. The combination of magnetization prepared MRI with the higher sensitivity of high field scanners makes this particular area of research bountiful.

APPENDIX A

ANALYSIS OF CONSTANT TRANSVERSE MAGNETIZATION

Constant transverse magnetization is beneficial in short-TR, spoiled gradient echo techniques, such as FLASH, since it reduces image ghosting and blurring associated with magnetization's gradual approach to steady-state levels. In the case when the flip angle in a repeated series of RF pulses is constant, the steady-state level is usually not achieved during image data acquisition. Consequently, it is desirable to prescribe a specific set of flip angles that generates constant transverse magnetization. The purpose of this derivation is to express a relationship between the current flip angle (α_n) and the previous flip angle (α_{n-1}) under the requirement that the transverse magnetization is constant.

The underlying constraint of constant transverse magnetization in FLASH is expressed as $M^+_{xy(n-1)} = M^+_{xyn}$. Knowing that the initial transverse magnetization is $M_0 \sin\alpha_0$, the constraint says that all subsequent transverse magnetization must be equivalent to this first value. In other words:

$$M^+_{xyn} = M^-_{zn} \sin\alpha_n = M_0 \sin\alpha_0 \quad . \qquad [A1]$$

This equation is true for any value *n*. It is evident that there is a dependency on longitudinal magnetization as well, which in turn places dependency on T_1 and *TR*. To fully view this relationship, it is helpful to observe the relaxation of longitudinal magnetization between RF pulses:

$$M_{zn}^{-} = M_{z(n-1)}^{-} \cos\alpha_{n-1} \cdot ER + M_0(1-ER), \qquad \text{[A2]}$$

where $ER = \exp(-TR/T_1)$. Equation [A2] can be written in terms of the transverse magnetization, using the constraint of Eq. [A1] and the fact $M_{zn}^{-} = M_0 \sin\alpha_0 / \sin\alpha_n$:

$$M_0 \frac{\sin\alpha_0}{\sin\alpha_n} = M_0 \frac{ER \cdot \sin\alpha_0 \cos\alpha_{n-1}}{\sin\alpha_{n-1}} + M_0(1-ER). \qquad \text{[A3]}$$

Equation [A3] can be simplified by eliminating M_0 and noting that $\sin\alpha_n / \cos\alpha_n = \tan\alpha_n$, resulting in the final equation determining the flip angles needed to produce constant transverse magnetization:

$$\frac{\sin\alpha_0}{\sin\alpha_n} = \frac{ER \cdot \sin\alpha_0}{\tan\alpha_{n-1}} + (1-ER) \qquad . \qquad \text{[A4]}$$

The current flip angle in the set is dependent on both the initial flip angle and the previous flip angle, in addition to T_1 and *TR*. It can be shown that the flip angle increases with *n*, which also tends to saturate longitudinal magnetization. If *n* is large (~20 to 30), even a flip angle of 90 degrees is often unable to maintain constant transverse magnetization. This occurs when $M_{zn}^{-} < M_0 \sin\theta_0$.

APPENDIX B

FLASH IMAGING WITH NON-CONSTANT FLIP ANNGLES

The general form of longitudinal magnetization in the FLASH sequence subject to *n* constant flip angle is given in Eq. [3.10]. However, there is no requirement for a constant set of flip angles. A similar general equation in the same recursive fashion can be derived assuming each flip angle is unique.

As before, the derivation begins with the equation for T_1 relaxation between two successive pulses:

$$M_{z2}^{-} = M_{z1}^{-} ER \cos\alpha_1 + M_0(1+ER) \qquad \text{[B1]}$$

Since the second pulse (α_2) is different from the first, it must be treated uniquely. Therefore, the magnetization just prior to the third pulse:

$$\begin{aligned} M_{z3}^{-} &= \left[M_{z1}^{-} ER \cos\alpha_1 + M_0(1+ER) \right] ER \cos\alpha_2 + M_0(1+ER) \\ &= M_{z1}^{-} ER^2 \cos\alpha_1 \cos\alpha_2 + M_0(1-ER)\left[ER\cos\alpha_2 + 1 \right] \end{aligned} \qquad \text{[B2]}$$

If the process is continued, a general trend becomes apparent, similar to the constant flip angle case. This trend can be manifested if the expression is simplified into the form given in Eq. [B2]. Then, an equation can be determined for each part of Eq. [B2]. The first part of Eq. [B2] ($M_{z1}^{-} ER^2 \cos\alpha_1 \cos\alpha_2$) is simply the product of all the previous RF pulses, coupled with an exponentially increasing *ER* term and the original longitudinal magnetization. Hence, for an arbitrary number of pulses *n*, the first part of the general equation for FLASH with non-constant α-pulses (designated M_{An}) will be:

$$M_{An} = M_{z1}^{-} ER^{n-1} \prod_{i=1}^{n-1} \cos\alpha_i \,. \qquad \text{[B3]}$$

The second term of Eq. [B2] (designated M_{Bn}) is more complex, but appears to contain both a product series and a summation series. In the simplification of Eq. [B2], the $M_0(1-ER)$ term can always be factored from the bracketed term (even for future pulses). Hence, it will not influence the general equation. Consequently, focus should be placed on the recursive nature of the bracketed term. This can be observed by noting the change in value of the bracketed term as *n* is increased:

$n = 1 \quad 0$

$n = 2 \quad 1$

$n = 3 \quad ER\cos\alpha_2 + 1$

$n = 4 \quad ER^2 \cos\alpha_3 \cos\alpha_2 + ER\cos\alpha_3 + 1$

$n = 5 \quad ER^3 \cos\alpha_4 \cos\alpha_3 \cos\alpha_2 + ER^2 \cos\alpha_4 \cos\alpha_3 + ER\cos\alpha_4 + 1$

From this progression, the observed trends can be simplified into product and summation terms. A generalization that satisfies the progression depicted above is:

$$M_{Bn} = M_0(1-ER)\left[\sum_{i=1}^{n-2} ER^i \left(\prod_{j=1}^{i} \cos\alpha_{n-j}\right) + 1\right] \qquad \text{[B4]}$$

The overall equation for FLASH with non-constant α is: $M_{zn}^{-} = M_{An} + M_{Bn}$.

APPENDIX C

NUMERICAL METHODS AND T_1 MAP

The image processing involved to determine an estimate of T_1 using the 4-point single-shot technique (4pt-IRss) and the 2-point ratio method (2pt-IR) took place off-line using programs written in Matlab computing software (MathWorks, Natick, MA). These determinations were performed with numerical methods using the MR images on a pixel-by-pixel basis, such that a "T_1-map" of the region was produced. In a T_1-map, each pixel has a unique mean and standard deviation. The following briefly describes the image processing methodology from MR images to T_1-maps.

For 4pt-IRss (pre-contrast T_1 measurements), each source image (at each *TI*) was first imported into the program, and re-scaled using scan-specific scaling factors (from the Dicom header file). If scaling factors were not available, the mean background noise was used to re-scale each image. Using one of the images (usually the control image with $TI = 0$), a user-defined region-of-interest (ROI) was drawn to encompass the blood pool, normal myocardium, or infarct tissue (~500 pixels). This region specification enabled reduced computation time for the T_1 estimation and avoided unneeded calculations in air. The *TI*s for each image were compiled into a vector, and a least squares 2-parameter fit (M_0 and T_1) to an absolute valued mono-exponential curve ($\text{Abs}[M_0 * (1 - 2*\exp(TI / T_1))]$) was evaluated for each pixel within the ROI. Note that the 4 source MR images were registered since the trigger delay during acquisition was constant between the scans. In addition to M_0 and T_1 maps, the *residual norm* was computed into a separate map

($[FitData(TI) - PixelData(TI)]^2$). The process is summarized in Figure D1. Measurements of T_1 were made from the maps using ROIs in blood (~100 pixels), myocardium (~50 pixels), and infarct tissue (~10-25 pixels).

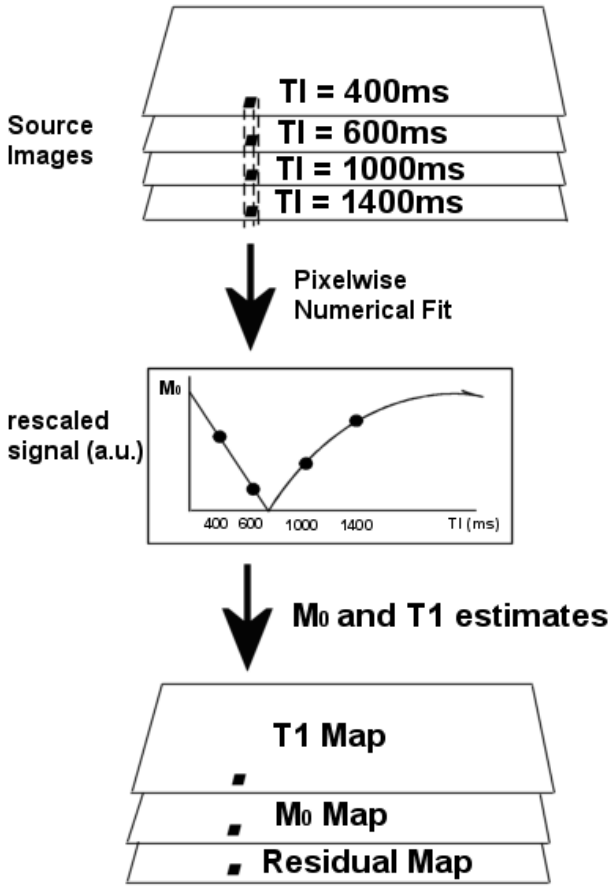

Figure C.1. *Method of pixelwise T_1 calculation in 4pt-IRss.*

The 2pt-IR method was computationally less demanding than the 4pt-IRss. Therefore, T_1-maps could be generated for the entire field-of-view. A graphical user interface (GUI) was created in Matlab to automate the T_1 process, which conveniently allowed the user to specify the source image files (dicom or raw data), *TI* times, and scaling values. The GUI is shown in Figure D2. The program also allowed input for the

color resolution of the ratio map, which is simply a division operation between the "HIGH TI" and the "LOW TI". The resolution (Max threshold) defines the dynamic range of the resulting ratio map. Once the ratio map is generated, a T_1 map can be produced after an ROI and the number of iterations is defined. This assignment determines the convergence rate of the numerical method (Newton-Rapshon Method). An initial guess of the expected T_1 is not needed since the program uses the *S* value of pixel (from the ratio map) and the low/high *TI*s (from source images) to provide an approximate first guess for the Newton-Rapshon method. Convergence is usually achieved with 10-20 iterations. Two resulting T_1 maps are produced: one assuming the ratio *S* value was positive, and one assuming the ratio *S* value was negative (see Eq. [3.26]). ROIs (rectangular and polygonal) or points can be assigned on the maps to determine the mean ± SD T_1 value of the specified region. Each pixel's true T_1 is determined using the criteria outlined in Chapter 3 for the 2-point method.

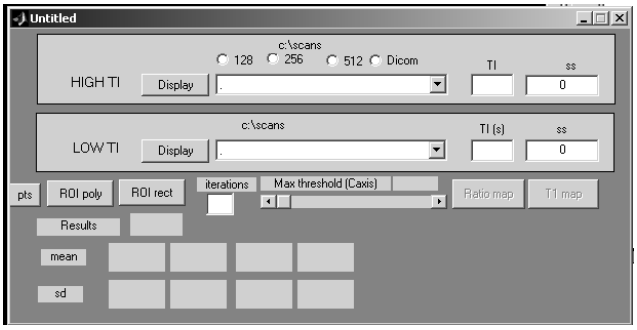

Figure C.2. *Screenshot of the Matlab GUI for the 2pt-IR method*

APPENDIX D

DIAGRAMS OF PULSE SEQUENCES

This section contains pulse sequence diagrams for some of the imaging sequences presented in the text. The sequences are given on a time-axis (from left to right), where the bottom-most schematic in each figure depicts the detailed sequence over one TR period, which consists of the RF pulse train, and the readout (x-direction) gradient. The other gradient directions, phase encode and slice-select, are not shown in the diagrams for simplicity. In brief, a slice-select gradient (z-direction) is associated with each RF pulse, and a phase encode gradient (y-direction) is incremented prior to each echo signal (the magnitude of which is dependent of the filling order of k-space).

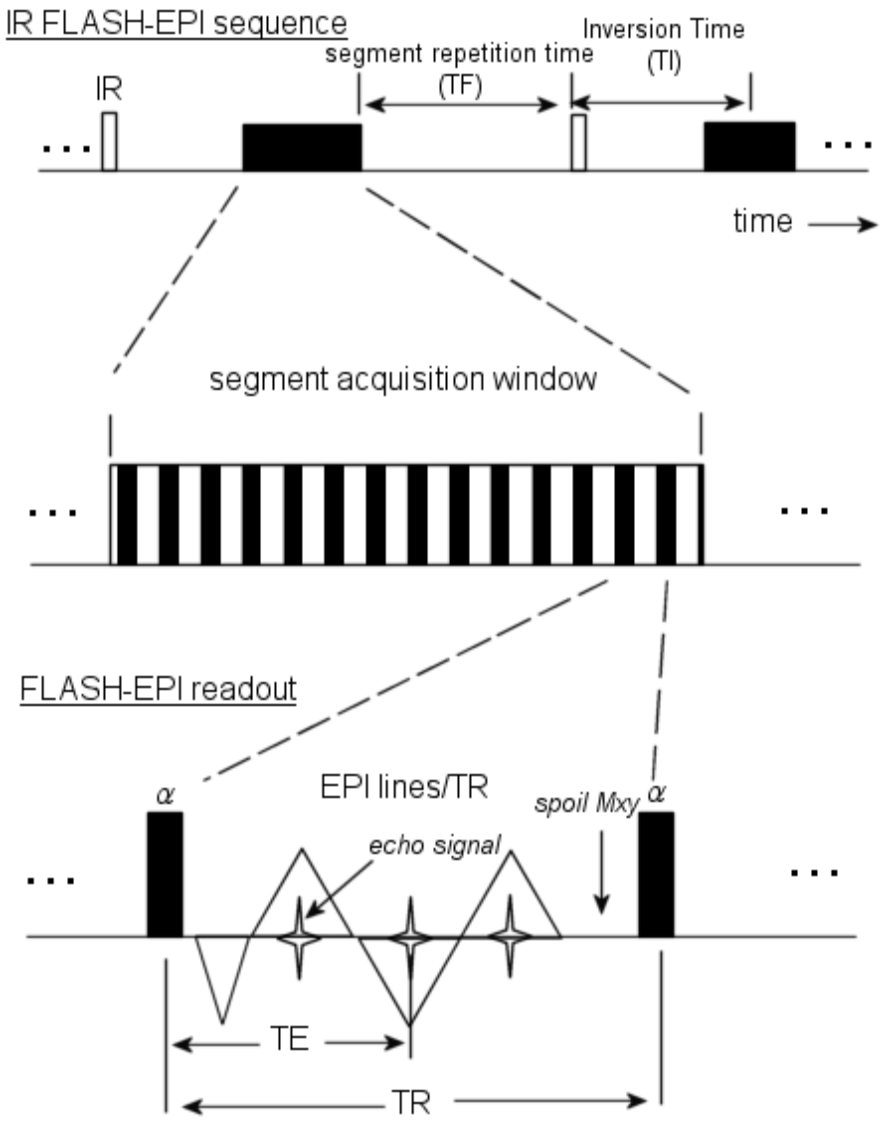

Figure D.1. *IR FLASH-EPI pulse sequence*

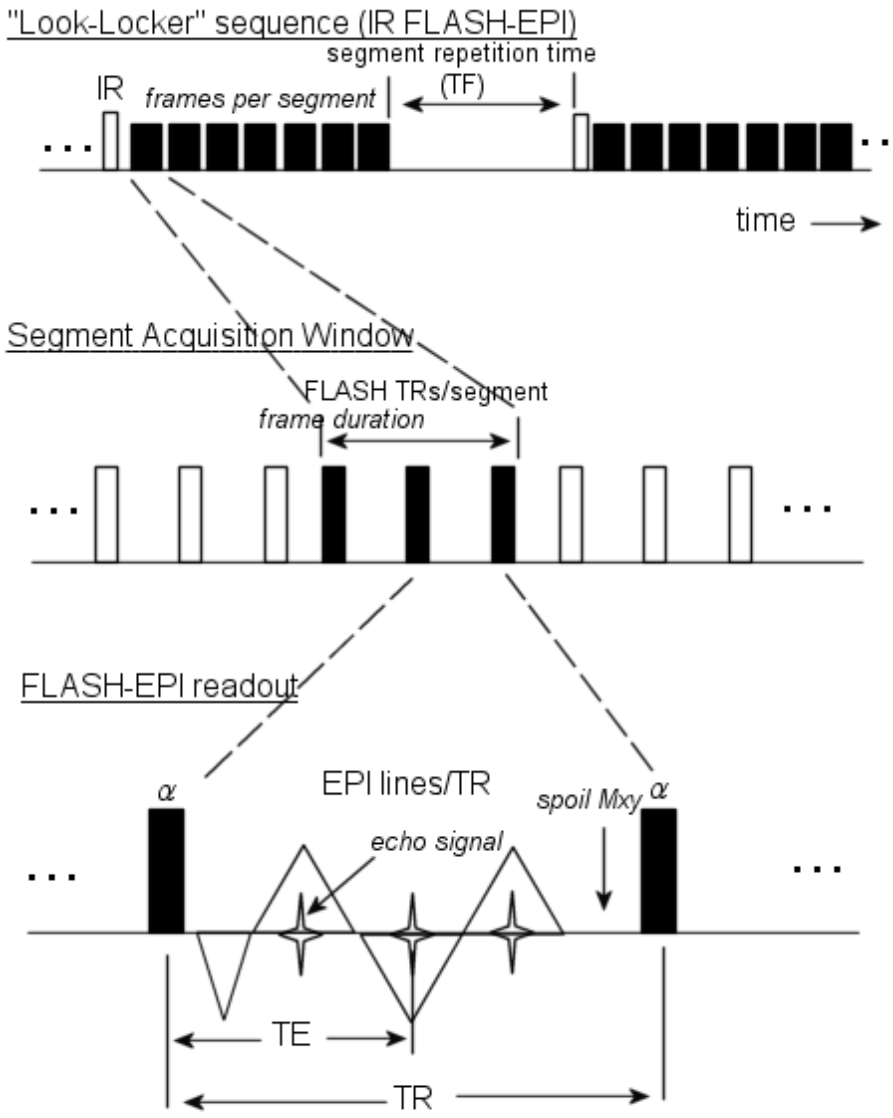

Figure D.2. *Look-Locker sequence (with FLASH-EPI readout)*

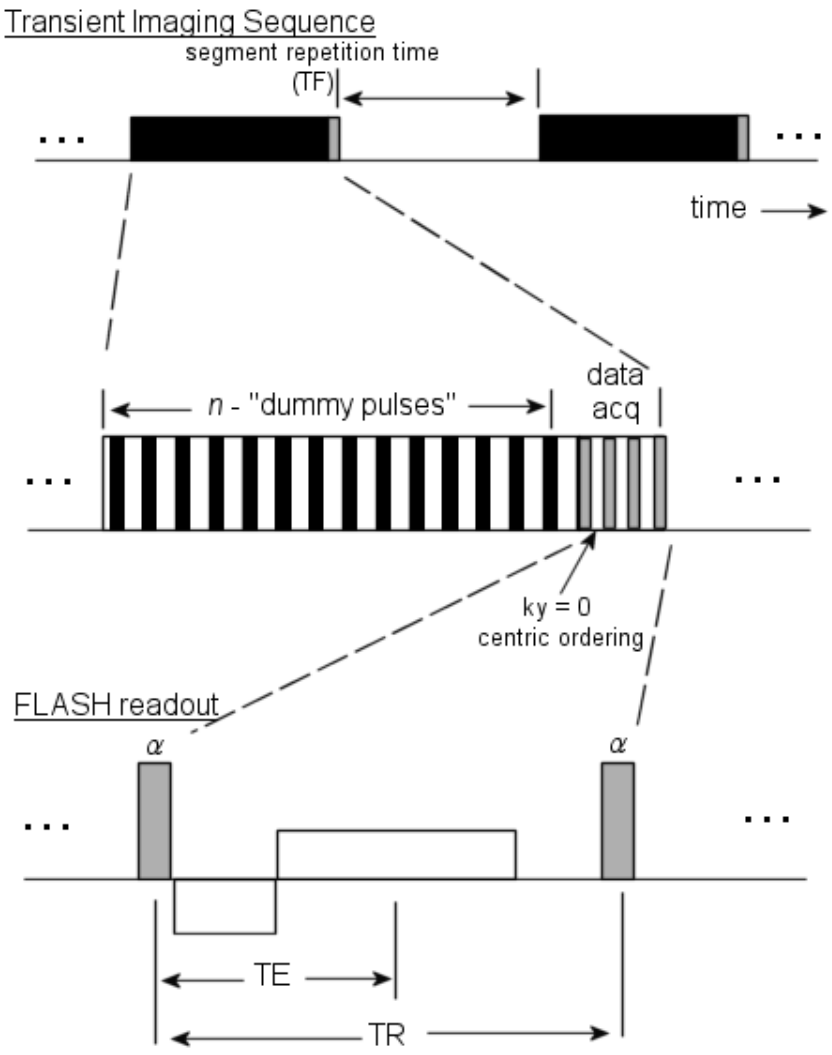

Figure D.3. *Transient imaging sequence.*

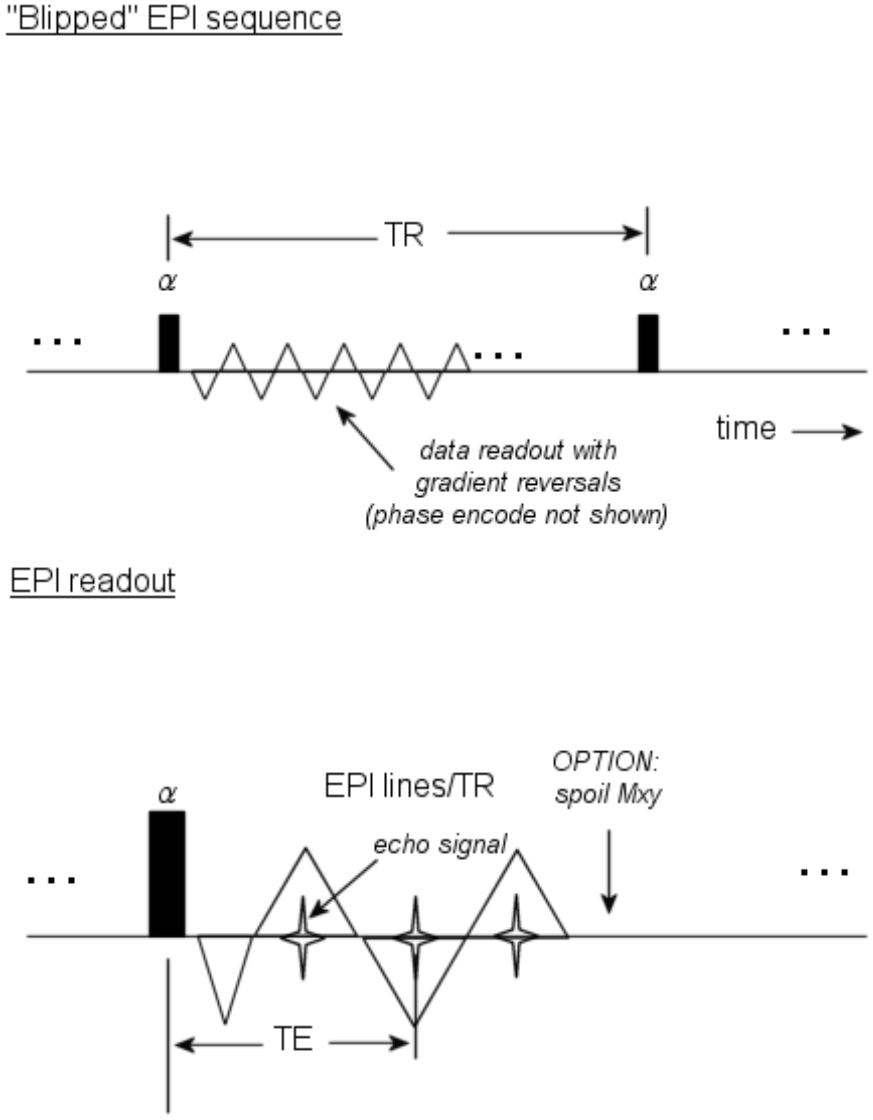

Figure D.4. *"Blipped" EPI pulse sequence*

REFERENCES

Alderman EL, Fisher LD, Litwin P, Kaiser GC, Myers WO, Maynard C, Levine F, Schloss M. Results of coronary artery surgery in patients with poor left ventricular function (CASS). Circulation. 1983;68(4):785-95.

Arheden H, Saeed M, Higgins CB, Gao DW, Bremerich J, Wyttenbach R, Dae MW, Wendland MF. Measurement of the distribution volume of gadopentetate dimeglumine at echo-planar MR imaging to quantify myocardial infarction: comparison with 99mTc-DTPA autoradiography in rats. Radiology. 1999;211(3):698-708.

Barilla F, Gheorghiade M, Alam M, Khaja F, Goldstein S. Low-dose dobutamine in patients with acute myocardial infarction identifies viable but not contractile myocardium and predicts the magnitude of improvement in wall motion abnormalities in response to coronary revascularization. Am Heart J. 1991;122(6):1522-31.

Barkhausen J, Ruehm SG, Goyen M, Buck T, Laub G, Debatin JF. MR evaluation of ventricular function: true fast imaging with steady-state precession versus fast low-angle shot cine MR imaging: feasibility study. Radiology. 2001;219(1):264-9.

Barth M, Moser E. Proton NMR relaxation times of human blood samples at 1.5 T and implications for functional MRI. Cell Mol Biol (Noisy-le-grand). 1997;43(5):783-91.

Becker LC, Levine JH, DiPaula AF, Guarnieri T, Aversano T. Reversal of dysfunction in postischemic stunned myocardium by epinephrine and postextrasystolic potentiation. J Am Coll Cardiol. 1986;7(3):580-9.

Berman DS, Kiat H, Friedman JD, Wang FP, van Train K, Matzer L, Maddahi J, Germano G. Separate acquisition rest thallium-201/stress technetium-99m sestamibi dual-isotope myocardial perfusion single-photon emission computed tomography: a clinical validation study. J Am Coll Cardiol. 1993;22(5):1455-64.

Bloch F, Hansen WW, Packard M. Nuclear Induction. Phys. Rev. 1946; 69:127.

Bloembergen N, Purcell EM, Pound RV. Relaxation effects in nuclear magnetic resonance absorption. Phys. Rev. 1948;73:679-710.

Bolli R, Zhu WX, Myers ML, Hartley CJ, Roberts R. Beta-adrenergic stimulation reverses postischemic myocardial dysfunction without producing subsequent functional deterioration. Am J Cardiol. 1985;56(15):964-8.

Bolli R. Myocardial 'stunning' in man. Circulation. 1992;86(6):1671-91.

Bottomley PA, Foster TH, Argersinger RE, Pfeifer LM. A review of normal tissue hydrogen NMR relaxation times and relaxation mechanisms from 1-100 MHz: dependence on tissue type, NMR frequency, temperature, species, excision, and age. Med Phys. 1984;11(4):425-48.

Braunwald E, Kloner RA. The stunned myocardium: prolonged, postischemic ventricular dysfunction. Circulation. 1982;66(6):1146-9.

Brundage BH, Massie BM, Botvinick EH. Improved regional ventricular function after successful surgical revascularization. J Am Coll Cardiol. 1984;3(4):902-8.

Bryant DJ, Payne JA, Firmin DN, Longmore DB. Measurement of flow with NMR imaging using a gradient pulse and phase difference technique. J Comput Assist Tomogr. 1984;8(4):588-93.

Busse RF, Riederer SJ. Steady-state preparation for spoiled gradient echo imaging. Magn Reson Med. 2001;45(4):653-61.

Chareonthaitawee P, Christian TF, Hirose K, Gibbons RJ, Rumberger JA. Relation of initial infarct size to extent of left ventricular remodeling in the year after acute myocardial infarction. J Am Coll Cardiol. 1995;25(3):567-73.

Chen C, Chen L, Fallon JT, Ma L, Li L, Bow L, Knibbs D, McKay R, Gillam LD, Waters DD. Functional and structural alterations with 24-hour myocardial hibernation and recovery after reperfusion. A pig model of myocardial hibernation. Circulation. 1996;94(3):507-16.

Christian TF, Miller TD, Hodge DO, Orszulak TA, Gibbons RJ. An estimate of the prevalence of reversible left ventricular dysfunction in patients referred for coronary artery bypass surgery. J Nucl Cardiol. 1997;4(2 Pt 1):140-6.

Chung YC, Kellman P, Lee D, Simonetti O. A fast, TI insensitive infarct imaging technique. JCMR 2003;5:40-41.

Cigarroa CG, deFilippi CR, Brickner ME, Alvarez LG, Wait MA, Grayburn PA. Dobutamine stress echocardiography identifies hibernating myocardium and predicts recovery of left ventricular function after coronary revascularization. Circulation. 1993;88(2):430-6.

Constantinides CD, Atalar E, McVeigh ER. Signal-to-noise measurements in magnitude images from NMR phased arrays. Magn Reson Med. 1997;38(5):852-7.

Dedieu V, Finat-Duclos F, Renou JP, Joffre F, Vincensini D. In vivo tissue extracellular volume fraction measurement by dynamic spin-lattice MRI relaxometry: application to the characterization of muscle fiber types. Invest Radiol. 1999;34(3):185-9.

Deichmann R, Haase A. Quantification of T1 values by SNAPSHOT-FLASH NMR imaging. J Mang Reson. 1992; 96: 608-612.

Deimling M, Heid O. Magnetization prepared true FISP imaging (abstract). In: Proc 2nd Annual Meeting ISMRM. San Francisco, 1994.

Depre C, Vanoverschelde JL, Melin JA, Borgers M, Bol A, Ausma J, Dion R, Wijns W. Structural and metabolic correlates of the reversibility of chronic left ventricular ischemic dysfunction in humans. Am J Physiol. 1995;268(3 Pt 2):H1265-75.

Depre C, Vanoverschelde JL, Gerber B, Borgers M, Melin JA, Dion R. Correlation of functional recovery with myocardial blood flow, glucose uptake, and morphologic features in patients with chronic left ventricular ischemic dysfunction undergoing coronary artery bypass grafting. J Thorac Cardiovasc Surg. 1997;113(2):371-8.

Diesbourg LD, Prato FS, Wisenberg G, Drost DJ, Marshall TP, Carroll SE, O'Neill B. Quantification of myocardial blood flow and extracellular volumes using a bolus injection of Gd-DTPA: kinetic modeling in canine ischemic disease. Magn Reson Med. 1992;23(2):239-53.

Donahue KM, Burstein D, Manning WJ, Gray ML. Studies of Gd-DTPA relaxivity and proton exchange rates in tissue. Magn Reson Med. 1994;32(1):66-76.

Elefteriades JA, Tolis G Jr, Levi E, Mills LK, Zaret BL. Coronary artery bypass grafting in severe left ventricular dysfunction: excellent survival with improved ejection fraction and functional state. J Am Coll Cardiol. 1993;22(5):1411-7.

Elster AD. How much contrast is enough? Dependence of enhancement on field strength and MR pulse sequence. Eur Radiol. 1997;7 Suppl 5:276-80.

Elster AD, Burdette JH. Questions and answers in magnetic resonance imaging. St. Louis: Mosby, 2001. 333p

Eriksson R, Johansson L, Bjerner T, Briley Saebo K, Ahlstrom H. Uptake of MnCl2 and mangafodipir trisodium in the myocardium: a magnetic resonance imaging study in pigs. J Magn Reson Imaging. 2004;19(5):564-9.

Fallavollita JA, Perry BJ, Canty JM Jr. 18F-2-deoxyglucose deposition and regional flow in pigs with chronically dysfunctional myocardium. Evidence for transmural variations in chronic hibernating myocardium. Circulation. 1997;95(7):1900-9.

Fedele FA, Gewirtz H, Capone RJ, Sharaf B, Most AS. Metabolic response to prolonged reduction of myocardial blood flow distal to a severe coronary artery stenosis. Circulation. 1988;78(3):729-35.

Flacke SJ, Fischer SE, Lorenz CH. Measurement of the gadopentetate dimeglumine partition coefficient in human myocardium in vivo: normal distribution and elevation in acute and chronic infarction. Radiology. 2001;218(3):703-10.

Flameng W, Suy R, Schwarz F, Borgers M, Piessens J, Thone F, Van Ermen H, De Geest H. Ultrastructural correlates of left ventricular contraction abnormalities in patients with chronic ischemic heart disease: determinants of reversible segmental asynergy postrevascularization surgery. Am Heart J. 1981;102(5):846-57.

Foltz WD, Huang H, Fort S, Wright GA. Vasodilator response assessment in porcine myocardium with magnetic resonance relaxometry. Circulation. 2002;106(21):2714-9.

Frayne R, Goodyear BG, Dickhoff P, Lauzon ML, Sevick RJ. Magnetic resonance imaging at 3.0 Tesla: challenges and advantages in clinical neurological imaging. Invest Radiol. 2003;38(7):385-402.

Gallagher KP, Matsuzaki M, Osakada G, Kemper WS, Ross J Jr. Effect of exercise on the relationship between myocardial blood flow and systolic wall thickening in dogs with acute coronary stenosis. Circ Res. 1983;52(6):716-29.

Glover GH, Hayes CE, Pelc NJ. Comparison of linear and circular polarization for magnetic resonance imaging. J Magn Reson. 1985; 1:339-53.

Greenman RL, Shirosky JE, Mulkern RV, Rofsky NM. Double inversion black-blood fast spin-echo imaging of the human heart: a comparison between 1.5T and 3.0T. J Magn Reson Imaging. 2003;17(6):648-55.

Grothues F, Smith GC, Moon JC, Bellenger NG, Collins P, Klein HU, Pennell DJ. Comparison of interstudy reproducibility of cardiovascular magnetic resonance with two-dimensional echocardiography in normal subjects and in patients with heart failure or left ventricular hypertrophy. Am J Cardiol. 2002;90(1):29-34.

Gruetter R. Automatic, localized in vivo adjustment of all first- and second-order shim coils. Magn Reson Med. 1993;29(6):804-11.

Haacke EM, Brown RW, Thompson MR, Venkatesan R. Magnetic resonance imaging: physical principles and sequence design. New York: John Wiley & Sons; 1999. 914p.

Haase A, Frahm J, Matthaei D, Hanicke W, Merboldt KD. FLASH imaging: rapid NMR imaging using low flip angles. J Magn Reson 1986 67;258-266.

Hackstein N, Heckrodt J, Rau WS. Measurement of single-kidney glomerular filtration rate using a contrast-enhanced dynamic gradient-echo sequence and the Rutland-Patlak plot technique. J Magn Reson Imaging. 2003;18:714-25.

Hanicke W, Merboldt KD, Chien D, Gyngell ML, Bruhn H, Frahm J. Signal strength in subsecond FLASH magnetic resonance imaging: the dynamic approach to steady state. Med Phys. 1990;17(6):1004-10.

Hargreaves BA, Vasanawala SS, Pauly JM, Nishimura DG. Characterization and reduction of the transient response in steady-state MR imaging. Magn Reson Med. 2001;46(1):149-58.

Hearse DJ. Stunning: a radical re-view. Cardiovasc Drugs Ther. 1991;5(5):853-76

Henriksen O, de Certaines JD, Spisni A, Cortsen M, Muller RN, Ring PB. In vivo field dependence of proton relaxation times in human brain, liver and skeletal muscle: a multicenter study. Magn Reson Imaging. 1993;11(6):851-6.

Heyndrickx GR, Millard RW, McRitchie RJ, Maroko PR, Vatner SF. Regional myocardial functional and electrophysiological alterations after brief coronary artery occlusion in conscious dogs. J Clin Invest. 1975;56(4):978-85.

Hinton DP, Wald LL, Pitts J, Schmitt F. Comparison of cardiac MRI on 1.5 and 3.0 Tesla clinical whole body systems. Invest Radiol. 2003;38(7):436-42.

Hoult DI, Phil D. Sensitivity and power deposition in a high-field imaging experiment. J Magn Reson Imaging. 2000;12(1):46-67.

Jaffer FA, Wen H, Balaban RS, Wolff SD. A method to improve the B0 homogeneity of the heart in vivo. Magn Reson Med. 1996;36(3):375-83.

Janick PA, Hackney DB, Grossman RI, Asakura T. MR imaging of various oxidation states of intracellular and extracellular hemoglobin. AJNR Am J Neuroradiol 1991;12:891-7.

Jezzard P, Duewell S, Balaban RS. MR relaxation times in human brain: measurement at 4 T. Radiology. 1996;199(3):773-9.

Jivan A, Horsfield MA, Moody AR, Cherryman GR. Dynamic T1 measurement using snapshot-FLASH MRI. J Magn Reson. 1997;127(1):65-72.

Kampa N, Bostrom I, Lord P, Wennstrom U, Ohagen P, Maripuu E. Day-to-day variability in glomerular filtration rate in normal dogs by scintigraphic technique. J Vet Med A Physiol Pathol Clin Med. 2003;50:37-41.

Kellman P, Arai AE, McVeigh ER, Aletras AH. Phase-sensitive inversion recovery for detecting myocardial infarction using gadolinium-delayed hyperenhancement. Magn Reson Med. 2002;47(2):372-83.

Klein C, Nekolla SG, Balbach T, Schnackenburg B, Nagel E, Fleck E, Schwaiger M. The influence of myocardial blood flow and volume of distribution on late Gd-DTPA kinetics in ischemic heart failure. J Magn Reson Imaging. 2004;20(4):588-93.

Look DC, Locker DR. Time saving in measurement of NMR and EPR relaxation times. Rev. Sci. Instrum. 1970;41:250-1.

Lu H, Clingman C, Golay X, van Zijl PC. Determining the longitudinal relaxation time (T1) of blood at 3.0 Tesla. Magn Reson Med. 2004;52(3):679-82.

Marban E. Myocardial stunning and hibernation. The physiology behind the colloquialisms. Circulation. 1991;83(2):681-8.

Messroghli DR, Niendorf T, Schulz-Menger J, Dietz R, Friedrich MG. T1 mapping in patients with acute myocardial infarction. J Cardiovasc Magn Reson. 2003;5(2):353-9.

Messroghli DR, Radjenovic A, Kozerke S, Higgins DM, Sivananthan MU, Ridgway JP. Modified Look-Locker inversion recovery (MOLLI) for high-resolution T1 mapping of the heart. Magn Reson Med. 2004;52(1):141-6.

Montgomery DD, Morrison WB, Schweitzer ME, Weishaupt D, Dougherty L. Effects of iodinated contrast and field strength on gadolinium enhancement: implications for direct MR arthrography. J Magn Reson Imaging. 2002;15(3):334-43.

Nayak KS, Cunningham CH, Santos JM, Pauly JM. Real-time cardiac MRI at 3 tesla. Magn Reson Med. 2004;51(4):655-60.

Noeske R, Seifert F, Rhein KH, Rinneberg H. Human cardiac imaging at 3 T using phased array coils. Magn Reson Med. 2000;44(6):978-82.

Okada RD. Kinetics of thallium-201 in reperfused canine myocardium after coronary artery occlusion. J Am Coll Cardiol. 1984;3(5):1245-51.

Oksendal AN, Hals PA. Biodistribution and toxicity of MR imaging contrast media. J Magn Reson Imaging. 1993;3(1):157-65.

Pickup S, Wood AK, Kundel HL. A novel method for analysis of TOMROP data. J Magn Reson Imaging. 2004;19(4):508-12.

Pickup S, Wood AK, Kundel HL. A novel method for analysis of TOMROP data. J Magn Reson Imaging. 2004;19:508-12.

Pierard LA, De Landsheere CM, Berthe C, Rigo P, Kulbertus HE. Identification of viable myocardium by echocardiography during dobutamine infusion in patients with myocardial infarction after thrombolytic therapy: comparison with positron emission tomography. J Am Coll Cardiol. 1990;15(5):1021-31.

Porter TR, Xie F, Kricsfeld A, Chiou A, Dabestani A. Improved endocardial border resolution during dobutamine stress echocardiography with intravenous sonicated dextrose albumin. J Am Coll Cardiol. 1994;23(6):1440-3.

Prato FS, Wisenberg G, Marshall TP, Uksik P, Zabel P. Comparison of the biodistribution of gadolinium-153 DTPA and technetium-99m DTPA in rats. J Nucl Med. 1988;29(10):1683-7.

Rahimtoola SH. The hibernating myocardium. Am Heart J. 1989;117(1):211-21.

Reeder SB, Faranesh AZ, Boxerman JL, McVeigh ER. In vivo measurement of T*2 and field inhomogeneity maps in the human heart at 1.5 T. Magn Reson Med. 1998;39(6):988-98.

Rehwald WG, Fieno DS, Chen EL, Kim RJ, Judd RM. Myocardial magnetic resonance imaging contrast agent concentrations after reversible and irreversible ischemic injury. Circulation. 2002;105(2):224-9.

Reimer KA, Jennings RB. The "wavefront phenomenon" of myocardial ischemic cell death. II. Transmural progression of necrosis within the framework of ischemic bed size (myocardium at risk) and collateral flow. Lab Invest. 1979;40(6):633-44.

Rinck PA, Muller RN. Field strength and dose dependence of contrast enhancement by gadolinium-based MR contrast agents. Eur Radiol. 1999;9(5):998-1004.

Ross J Jr. Myocardial perfusion-contraction matching. Implications for coronary heart disease and hibernation. Circulation. 1991;83(3):1076-83.

Saeed M, Higgins CB, Geschwind JF, Wendland MF. T1-relaxation kinetics of extracellular, intracellular and intravascular MR contrast agents in normal and acutely reperfused infarcted myocardium using echo-planar MR imaging. Eur Radiol. 2000;10:310-8.

Salustri A, Elhendy A, Garyfallydis P, Ciavatti M, Cornel JH, ten Cate FJ, Boersma E, Gemelli A, Roelandt JR, Fioretti PM. Prediction of improvement of ventricular

function after first acute myocardial infarction using low-dose dobutamine stress echocardiography. Am J Cardiol. 1994;74(9):853-6.

Scheffler K, Hennig J. T(1) quantification with inversion recovery TrueFISP. Magn Reson Med. 2001;45(4):720-3.

Scheffler K. On the transient phase of balanced SSFP sequences. Magn Reson Med. 2003;49(4):781-3.

Schmitt P, Griswold MA, Jakob PM, et al. Inversion recovery TrueFISP: quantification of T1, T2 and spin density. Magn Reson Med 2004;51:661-667.

Schulz R, Guth BD, Pieper K, Martin C, Heusch G. Recruitment of an inotropic reserve in moderately ischemic myocardium at the expense of metabolic recovery. A model of short-term hibernation. Circ Res. 1992;70(6):1282-95.

Schwitter J, Nanz D, Kneifel S, Bertschinger K, Buchi M, Knusel PR, Marincek B, Luscher TF, von Schulthess GK. Assessment of myocardial perfusion in coronary artery disease by magnetic resonance: a comparison with positron emission tomography and coronary angiography. Circulation. 2001;103(18):2230-5.

Segall G. Assessment of myocardial viability by positron emission tomography. Nucl Med Commun. 2002;23(4):323-30.

Shadowitz A. The electromagnetic field. New York: Dover Publications; 1975. 714p.

Sharma P, Patel S, Pettigrew RI, Oshinski JN. Measurements of relaxivity (R1) post contrast in patients with prior myocardial infarction (abstract). Proc Intl Soc Magn Reson Med 11 2003 p.144.

Shen YT, Vatner SF. Mechanism of impaired myocardial function during progressive coronary stenosis in conscious pigs. Hibernation versus stunning? Circ Res. 1995;76(3):479-88.

Sicari R, Varga A, Picano E, Borges AC, Gimelli A, Marzullo P. Comparison of combination of dipyridamole and dobutamine during echocardiography with thallium scintigraphy with thallium scintigraphy to improve viability detection. Am J Cardiol. 1999;83(1):6-10.

Silvennoinen MJ, Kettunen MI, Kauppinen RA. Effects of hematocrit and oxygen saturation level on blood spin-lattice relaxation. Magn Reson Med. 2003;49(3):568-71.

Slavin GS, Wolff SD, Gupta SN, Foo TK. First-pass myocardial perfusion MR imaging with interleaved notched saturation: feasibility study. Radiology. 2001;219(1):258-63.

Smart SC. The clinical utility of echocardiography in the assessment of myocardial viability. J Nucl Med. 1994;35(4 Suppl):49S-58S.

Stanisz GJ, Henkelman RM. Gd-DTPA relaxivity depends on macromolecular content. Magn Reson Med. 2000;44(5):665-7.

Storey P, Danias PG, Post M, Li W, Seoane PR, Harnish PP, Edelman RR, Prasad PV. Preliminary evaluation of EVP 1001-1: a new cardiac-specific magnetic resonance contrast agent with kinetics suitable for steady-state imaging of the ischemic heart. Invest Radiol. 2003;38(10):642-52.

Strich G, Hagan PL, Gerber KH, Slutsky RA. Tissue distribution and magnetic resonance spin lattice relaxation effects of gadolinium-DTPA. Radiology. 1985;154(3):723-6.

Stuber M, Botnar RM, Fischer SE, Lamerichs R, Smink J, Harvey P, Manning WJ. Preliminary report on in vivo coronary MRA at 3 Tesla in humans. Magn Reson Med. 2002;48(3):425-9.

Tannus A, Garwood M. Adiabatic pulses. NMR Biomed. 1997;10(8):423-34.

Thulborn KR, Boada FE, Shen GX, Christensen JD, Reese TG. Correction of B1 inhomogeneities using echo-planar imaging of water. Magn Reson Med. 1998;39(3):369-75.

Tweedle MF, Wedeking P, Telser J, Sotak CH, Chang CA, Kumar K, Wan X, Eaton SM. Dependence of MR signal intensity on Gd tissue concentration over a broad dose range. Magn Reson Med. 1991;22(2):191-4; discussion 195-6.

Uematsu H, Dougherty L, Takahashi M, Butler NS, Song HK, Ohno Y, Gefter WB, Schnall MD, Hatabu H. A direct comparison of signal behavior between 4.0 and 1.5 T: a phantom study. Eur J Radiol. 2003;45(2):154-9.

Vinnakota KC, Bassingthwaighte JB. Myocardial density and composition: a basis for calculating intracellular metabolite concentrations. Am J Physiol Heart Circ Physiol. 2004;286(5):H1742-9.

Vlaardingerbroek MT, Den Boer JD. Magnetic resonance imaging: theory and practice. New York: Springer, 2003. 481p.

Wacker CM, Bock M, Hartlep AW, Beck G, van Kaick G, Ertl G, Bauer WR, Schad LR. Changes in myocardial oxygenation and perfusion under pharmacological stress with dipyridamole: assessment using T2* and T1 measurements. Magn Reson Med. 1999;41(4):686-95.

Wagenseil JE, Johansson LO, Lorenz CH. Characterization of t1 relaxation and blood-myocardial contrast enhancement of NC100150 injection in cardiac MRI. J Magn Reson Imaging. 1999;10(5):784-9.

Walker PM, Marie PY, Mezeray C, Bessieres M, Escanye JM, Karcher G, Danchin N, Mattei S, Villemot JP, Bertrand A. Synchronized inversion recovery-spin echo sequences for precise in vivo T1 measurement of human myocardium: a pilot study on 22 healthy subjects. Magn Reson Med. 1993;29(5):637-41.

Watada H, Ito H, Oh H, Masuyama T, Aburaya M, Hori M, Iwakura M, Higashino Y, Fujii K, Minamino T. Dobutamine stress echocardiography predicts reversible dysfunction and quantitates the extent of irreversibly damaged myocardium after reperfusion of anterior myocardial infarction. J Am Coll Cardiol. 1994;24(3):624-30.

Weinmann HJ, Brasch RC, Press WR, Wesbey GE. Characteristics of gadolinium-DTPA complex: a potential NMR contrast agent. AJR Am J Roentgenol. 1984;142(3):619-24.

Wen H, Denison TJ, Singerman RW, Balaban RS. The intrinsic signal-to-noise ratio in human cardiac imaging at 1.5, 3, and 4 T. J Magn Reson. 1997;125(1):65-71.

Wilke NM, Jerosch-Herold M, Zenovich A, Stillman AE. Magnetic resonance first-pass myocardial perfusion imaging: clinical validation and future applications. J Magn Reson Imaging. 1999;10(5):676-85.

Xie D, Kennan RP, Gore JC. Measurements of the relaxivity of gadolinium chelates in tissue in vivo (abstract). 9th Proc Intl Soc Magn Reson Med. 2001; p.890.